Structural and magnetic properties of epitaxial rare-earth cobalt thin films

Strukturelle und magnetische Eigenschaften von epitaktischen Seltenerd-Kobalt dünnen Schichten
Zur Erlangung des akademischen Grades Doktor-Ingenieur (Dr.-Ing.)
genehmigte Dissertation von Shalini Sharma aus Meerut, Indien
Tag der Einreichung: 04.02.2020, Tag der Prüfung: 20.04.2020

1. Gutachten: Prof. Dr. Lambert Alff
2. Gutachten: Prof. Dr. Oliver Gutfleisch
Darmstadt – D 17

TECHNISCHE
UNIVERSITÄT
DARMSTADT

Materials and Earth Sciences Department
Institute of Materials Science
Advanced Thin Film Technology

Structural and magnetic properties of epitaxial rare-earth cobalt thin films
Strukturelle und magnetische Eigenschaften von epitaktischen Seltenerd-Kobalt dünnen Schichten

Doctoral thesis by Shalini Sharma

1. Review: Prof. Dr. Lambert Alff
2. Review: Prof. Dr. Oliver Gutfleisch

Date of submission: 04.02.2020
Date of thesis defense: 20.04.2020

Darmstadt – D 17

Bitte zitieren Sie dieses Dokument als:
URN: urn:nbn:de:tuda-tuprints-118121URL: http://tuprints.ulb.tu-darmstadt.de/11812

Dieses Dokument wird bereitgestellt von tuprints,
E-Publishing-Service der TU Darmstadt
http://tuprints.ulb.tu-darmstadt.de
tuprints@ulb.tu-darmstadt.de

Die Veröffentlichung steht unter folgender Creative Commons Lizenz:
Namensnennung – Nicht kommerziell – Keine Bearbeitungen 4.0 International
https://creativecommons.org/licenses/by-nc-nd/4.0/deed.de

Erklärungen laut Promotionsordnung

§8 Abs. 1 lit. c PromO

Ich versichere hiermit, dass die elektronische Version meiner Dissertation mit der schriftlichen Version übereinstimmt.

§8 Abs. 1 lit. d PromO

Ich versichere hiermit, dass zu einem vorherigen Zeitpunkt noch keine Promotion versucht wurde. In diesem Fall sind nähere Angaben über Zeitpunkt, Hochschule, Dissertationsthema und Ergebnis dieses Versuchs mitzuteilen.

§9 Abs. 1 PromO

Ich versichere hiermit, dass die vorliegende Dissertation selbstständig und nur unter Verwendung der angegebenen Quellen verfasst wurde.

§9 Abs. 2 PromO

Die Arbeit hat bisher noch nicht zu Prüfungszwecken gedient.

Darmstadt, 04.02.2020

S. Sharma

Dedicated to my parents

Abstract

With the ever increasing demand for beyond-state-of-the magnets, which could also serve in extreme conditions, it is crucial to reduce the dependence on the critical rare-earths and explore new materials or material designs. The cobalt rich compositions of the rare-earth (R) cobalt intermetallic systems offer the combined advantages of a strong magnetocrystalline anisotropy and a high saturation magnetization, well above room temperature. This work focuses on investigating thin films of R-Co intermetallics as model systems for designing the materials at the nanoscale, understanding the magnetic hardness mechanisms and developing more sustainable magnetic systems.

The technique of molecular beam epitaxy (MBE) is utilized to investigate the thin film phase diagrams of lesser critical (Y and Sm), and abundant (Ce) rare-earth cobalt based systems. The growth window of buffer-free (00l) oriented R_2Co$_{17}$ and RCo$_5$ thin films onto (001)-Al$_2$O$_3$ substrate are explored. With the manipulation of individual atomic beams, MBE enables a fine tuning of the stoichiometry, whereby it was possible to stabilize not only the individual phases of Y$_2$Co$_{17}$ and YCo$_5$ but also a nanocomposite of these phases. The Y$_2$Co$_{17}$ film has an easy-plane anisotropy matching well to bulk single crystal while the YCo$_5$ film exhibits a perpendicular anisotropy. As a result of exchange coupling of the Y$_2$Co$_{17}$ phase to the YCo$_5$ phase, the nanocomposite films also shows perpendicular anisotropy. The outcome of a uniaxial anisotropy induced in an easy-plane material of Y$_2$Co$_{17}$, and hence, the resulting coercivity, shows a potential way of broadening the class of materials useful for permanent magnets.

Furthermore, we were able to fabricate CeCo$_5$ thin films with a saturation magnetization of 500 emu/cm^3, a perpendicular anisotropy of 0.44 MJ/m^3 and coercivity of 2.74 kOe, which are the highest reported so far for the thin films. An extremely large perpendicular anisotropy of 1.67 MJ/m^3 is achieved SmCo$_5$ thin film without the use of any buffer layers. The atomic scale resolution of the film revealed that the SmCo$_5$ phase grows perfectly c-axis oriented on the (001)-Al$_2$O$_3$ substrate, however, with possible traces of the Sm$_2$Co$_{17}$. The result of a perpendicular anisotropy obtained in single layer of RCo$_5$ phase make them interesting for magnetic recording and spintronic applications.

In view of tuning the magnetocrystalline anisotropy of a compound by strain introduced by chemical substitution, thin films of yttrium substituted cerium (Y,Ce)Co$_5$ intermetallics are investigated. We observed that the structural and magnetic properties of (Y$_{1-x}$Ce$_x$)Co$_5$ films show a non-linear dependence on Ce content, x which is supposedly due to a varying chemical valence the Ce ion. The absolute values vary, but a similar trend in the lattice parameters and magnetization is also observed in the bulk single crystals.

Zusammenfassung

Mit der ständig steigenden Nachfrage nach Magnetwerkstoffen, die auch unter extremen Bedingungen funktionieren, ist es entscheidend, die Abhängigkeit von den kritischen Seltenen Erden zu verringern und neue Materialien oder Materialsystem zu erkunden. Die kobaltreichen Zusammensetzungen der intermetallischen Systeme aus Seltenerdmetallen (R) und Kobalt bieten die kombinierten Vorteile einer starken magnetokristallinen Anisotropie und einer hohen, weit über Raumtemperatur liegenden Sättigungsmagnetisierung. Diese Arbeit konzentriert sich auf die Untersuchung von dünnen Schichten aus intermetallischen R-Co-Schichten als Modellsysteme für das Materialdesign auf der Nanoskala, auf das Verständnis der Mechanismen der magnetischen Härte und auf die Entwicklung nachhaltiger magnetischer Systeme.

In dieser Arbeit wurde Molekularstrahlepitaxie (MBE) zur Untersuchung der Dünnschichtphasendiagramme von weniger kritischen (Y und Sm) bzw. häufigen (Ce) seltenen Erd-basierten Kobaltsystemen. Das Wachstumsfenster pufferfreier Kobaltsysteme als ($00l$) orientierter R_2Co_{17} und RCo_5 Dünnschichten auf (001)-Al_2O_3 Substraten wurde eingehend untersucht. Durch die Kontrolle der Molekularstrahlen ermöglicht MBE eine Feinabstimmung der Stöchiometrie, wodurch es möglich ist, nicht nur die einzelnen Phasen von Y_2Co_{17} und YCo_5 zu stabilisieren, sondern auch ein Nanokomposit beider Phasen herzustellen. Die Y_2Co_{17}-Schichten haben eine planare Anisotropie mit einkristallinen Kennwerten, während die YCo_5-Schichten eine senkrechte Anisotropie aufweisen. Aufgrund der Austauschkopplung zwischen der Y_2Co_{17}-Phase und der YCo_5-Phase entstehen Nanokomposit-Filme mit der gewünschten senkrechten Anisotropie. Diese induzierte uniaxiale Anisotropie impliziert eine deutlich erhöhte Koerzitivfeldstärke im Gesamtsystem. Insgesamt zeigt dieses Resultat eine neue Methode zur Erzielung maßgeschneiderter Permanentmagnete auf.

Außerdem konnten im Rahmen dieser Arbeit $CeCo_5$-Dünnschichten mit einer Sättigungsmagnetisierung von 500 emu/cm^3, einer senkrechten Anisotropie von 0,44 MJ/m^3 und einer Koerzitivfeldstärke von 2,74 kOe hergestellt werden, was die höchsten bisher berichteter Werte für dünne Schichten sind. In $SmCo_5$-Dünnschichten wurde eine extrem große senkrechte Anisotropie von 1,67 MJ/m^3 erreicht, und dies ohne die Verwendung von jeglichen Pufferschichten. Transmissionselektronenmikroskopie mit atomarer Auflösung an diesen Filemen ergab, dass die $SmCo_5$-Phase perfekt c-Achsen-orientiert auf dem (001)-Al_2O_3-Substrat wächst, jedoch mit möglichen Spuren von Sm_2Co_{17}. Das Ergebnis einer senkrechten Anisotropie, die in einer einzelnen Schicht der RCo_5-Phase erhalten wird, macht sie interessant für den Bereich der magnetischen Informationsaufzeichnung sowie für spintronische Anwendungen.

Zur Untersuchung der magnetokristallinen Anisotropie einer Verbindung mit gezielter chemischen Substitution wurden dünne Schichten aus Yttrium-substituierten Cerium (Y,Ce)Co_5 synthetisiert. Es wurde beobachtet, dass die strukturellen und magnetischen Eigenschaften von $(Y_{1-x}Ce_x)Co_5$-Schichten eine nichtlineare Abhängigkeit vom Ce Gehalt aufweisen, was möglicherweise auf eine gemischte Valenz des Ce-Ions zurückzuführen ist. Die absoluten Werte variieren zwar, jedoch wird ein ähnlicher Trend bei den Gitterparametern und der Magnetisierung auch bei Einkristallen beobachtet.

Contents

Abstract vii

Zusammenfassung ix

1 Introduction and motivation 1

2 Fundamentals 3
- 2.1 Magnetism . . . 3
  - 2.1.1 Diamagnetism . . . 5
  - 2.1.2 Paramagnetism . . . 5
  - 2.1.3 Ferromagnetism . . . 6
  - 2.1.4 Ferrimagnetism . . . 7
  - 2.1.5 Antiferromagnetism . . . 8
- 2.2 Permanent magnets . . . 8
  - 2.2.1 Coercivity mechanism . . . 9
- 2.3 Magnetic anisotropy . . . 11
  - 2.3.1 Magnetocrystalline anisotropy . . . 11
  - 2.3.2 Shape anisotropy . . . 12
  - 2.3.3 Surface or interface anisotropy . . . 12
  - 2.3.4 Perpendicular anisotropy . . . 13
- 2.4 Thin film growth . . . 14

3 Rare-earth cobalt intermetallics 17
- 3.1 Crystal structures . . . 20
- 3.2 Magnetic interaction . . . 22
- 3.3 Origin of magnetocrystalline anisotropy . . . 24
- 3.4 State-of-the-art thin films . . . 27
  - 3.4.1 Y-Co thin films . . . 27
  - 3.4.2 Ce-Co thin films . . . 27
  - 3.4.3 Sm-Co thin films . . . 28

4 Methods 31
- 4.1 Molecular beam epitaxy . . . 31
  - 4.1.1 Electron-beam evaporation . . . 31
  - 4.1.2 Growth rate monitoring . . . 33
- 4.2 X-ray diffraction . . . 34
  - 4.2.1 Diffractometer . . . 37
  - 4.2.2 Measurements . . . 38
- 4.3 Reflection high-energy electron diffraction . . . 40
- 4.4 X-ray photoelectron spectroscopy . . . 41
- 4.5 SQUID magnetometery . . . 42
  - 4.5.1 Magnetometer . . . 43
  - 4.5.2 Measurements . . . 44

4.6 Torque magnetometery 45
4.7 Transmission electron microscopy 48

5 Growth and characterization of Y-Co thin films 53
5.1 Gradual phase transition 53
  5.1.1 Growth temperature study 53
  5.1.2 Evaporation rate scan 53
  5.1.3 Microstructure of YCo_5 film 55
5.2 Controlled phase separation 55
  5.2.1 Evaporation rate scan 55
  5.2.2 Growth temperature study 57
  5.2.3 Microstructure of Y_2Co_{17} - YCo_5 nanocomposite film 59
5.3 Epitaxial relations 60
  5.3.1 Y_2Co_{17} on Al_2O_3 60
  5.3.2 YCo_5 on Al_2O_3 60
5.4 RHEED analysis 61
5.5 Magnetic properties 62
  5.5.1 Easy-plane anisotropy in Y_2Co_{17} film 62
  5.5.2 Perpendicular anisotropy in YCo_5 film 64
  5.5.3 Perpendicular anisotropy in Y_2Co_{17} - YCo_5 nanocomposite film 66
  5.5.4 Composition dependence on coercivity 67
  5.5.5 Growth temperature dependence on coercivity 67
5.6 Y_2Co_{17} - YCo_5 bilayers 68
  5.6.1 YCo_5 on Y_2Co_{17} on Al_2O_3 69
  5.6.2 Y_2Co_{17} on YCo_5 on Al_2O_3 71

6 Growth and characterization of Ce-Co thin films 73
6.1 Growth study 73
6.2 Epitaxy 73
6.3 Magnetization measurements 75
  6.3.1 Temperature dependence of coercivity 76
6.4 Anisotropy measurement 77
6.5 Thin film magnetic phase diagram 77

7 Growth and characterization of Sm-Co thin films 81
7.1 Growth temperature study 81
  7.1.1 Magnetization measurements 81
7.2 Evaporation rate study 81
  7.2.1 Decreasing cobalt rates 83
  7.2.2 Increasing samarium rates 83
7.3 Epitaxial relations 84
  7.3.1 Magnetization measurements 85
7.4 Anisotropy measurements 87
7.5 Electronic structure 89
7.6 Atomic structure analysis 92

8 Growth and characterization of (Y,Ce)Co_5 thin films 95
8.1 Structural analysis 95

8.2 XPS analysis . . . 96
8.2.1 YCo_5 film . . . 99
8.2.2 $CeCo_5$ film . . . 101
8.2.3 $(Y_{0.2}Ce_{0.8})Co_5$ film . . . 101
8.2.4 $(Y_{0.5}Ce_{0.5})Co_5$ film . . . 103
8.3 Magnetic properties . . . 105

9 Conclusions 109
9.1 Y-Co thin films . . . 109
9.2 Y_2Co_{17} - YCo_5 bilayers . . . 109
9.3 Ce-Co thin films . . . 110
9.4 Sm-Co thin films . . . 110
9.5 $(Y,Ce)Co_5$ thin films . . . 111

10 Outlook 113

List of Figures 115

List of Tables 121

Bibliography I

Academic Contributions XIII

Acknowledgments XV

1 Introduction and motivation

The research on magnetic materials is driven by the need to develop beyond state-of-the-art magnets which are key components of emerging green energy technologies such as electric vehicles, wind turbines, hydroelectric power generators and others. The strongest permanent magnets commercially used are based on NdFeB which has outstanding properties near room temperature. However, for high temperature applications, heavy rare-earths such as praseodymium, dysprosium, terbium are often added. With the ever increasing demand and the ongoing rare-earth crisis, it is crucial to reduce the dependence on these critical elements and explore new materials or material designs which could serve in extreme conditions as well.

Not only for permanent magnet applications, thin films of materials with high uniaxial anisotropy are important for ultra-high density magnetic storage devices. In magnetic random access memories, thin films exhibiting perpendicular anisotropy ensure a high thermal stability of magnetization states at reduced dimensions. The commonly known materials showing perpendicular anisotropy include multilayers of noble metals such as Pt, Pd which have high spin-orbit interaction that can cause spin-flips and increase the magnetization damping in spintronic devices. So, it is important to explore material systems not involving the use of expensive heavy metals and yet, maintaining the perpendicular anisotropy of the system.

This work focuses on investigating thin films of rare-earth cobalt intermetallics as model systems for understanding and proposing physical mechanisms to tailor the magnetic properties of a material. The technique of molecular beam epitaxy is utilized which not only allows fine tuning of the stoichiometry but also artificial designing of the microstructure. Thin film phase diagrams of lesser critical (yttrium and samarium), and abundant (cerium) rare-earth cobalt system are investigated. The $R\mathrm{Co}_5$ compositions are interesting candidates for permanent magnet because of the high Curie temperature, saturation magnetization and an extremely large magnetocrystalline anisotropy. The materials with an easy-plane anisotropy, on the other hand, generally results in a negligible coercivity as the magnetization rotates freely in the plane. However, a uniaxial anisotropy can be induced by exchange-coupling to the hard magnetic $R\mathrm{Co}_5$ phase. The experimental work described in this dissertation is based on these concepts and ideas.

Chapter 2 provides a brief account of the fundamental theories of magnetism and thin-film growth. A description of the characteristic properties of the *R*-Co compounds and a review of the available reports on the Y-Co, Ce-Co, Sm-Co thin films is given in chapter 3. In chapter 4, the experimental methods used in this work are described.

In chapter 5, the three main studies on the binary Y-Co system are described. First, a gradual transition from the $\mathrm{Y_2Co_{17}}$ to $\mathrm{YCo_5}$ phase as a result of decreasing cobalt evaporation rate is shown. Second, the approach for a controlled phase separation is described, whereby the soft magnetic $\mathrm{Y_2Co_{17}}$ is exchange-coupled to the hard magnetic $\mathrm{YCo_5}$ phase. Third, bilayers of $\mathrm{Y_2Co_{17}}$ and $\mathrm{YCo_5}$ phases are fabricated in an attempt to artificially build the microstructure as a bottom-up approach.

Chapter 6 details about the synthesis and characterization of $\mathrm{CeCo_5}$ thin films which had never been reported in the literature. In this work, the structural and magnetic properties of the films are described and a magnetic thin film phase diagram of the Ce-Co system is established.

The Sm-Co intermetallic compounds are technologically the most important class of cobalt based permanent magnets. Thin films of Sm-Co alloys have been investigated for number of application ranging from magnetic storage devices to micro-electro-mechanical-systems. In chapter 7, the evolution of magnetic anisotropy as a function of Sm and Co contents in buffer-free Sm–Co thin films is described. A detailed analysis of the atomic structure of the film is also provided.

One of the ways to enhance the magnetocrystalline anisotropy energy beyond the known limit is by introducing strain in a compound by mechanical means or by chemical substitution. Among all the rare-earths, cerium is one of the lowest priced and mined anyhow abundantly as part of the rare earth basket, thus, its use in applications is advisable. In view of tuning the magnetic anisotropy by rare-earth substitution, thin films of yttrium substituted cerium, $(Y,Ce)Co_5$, are investigated for the first time. In chapter 8, the effect of substitution on the structural and magnetic properties of the $(Y,Ce)Co_5$ thin films are described.

The main results of all the experiments are finally summarized in chapter 9 on conclusions. An account of the new research possibilities and directions is provided in the final chapter on outlook.

2 Fundamentals

2.1 Magnetism

The story of magnetism began with the discovery of a mineral, Fe_3O_4, which exhibited unique ability of attracting pieces of iron. It was named as magnetite after Magnesia, a place in modern Turkey where it was discovered. A properly shaped magnetite pointed towards north which gave it the name of lodestone. In the eighteenth century, compound steel magnets were made by rubbing (magnetizing) pieces of iron or steel with lodestone. Following the findings by Hans Christian Oersted in 1825 that magnetic fields can be produced by electric current, powerful magnetic fields could be made available with electromagnets. Permanent magnets, on the other hand, are a source of constant supply of magnetic field, without the continuous expenditure of electric power and generation of heat.

The magnetic property of a material is mainly due to the electrons. In an atom, an electron has two types of motion; orbital motion, in its own orbit around the nucleus, and spin motion, around its own axis. Each type of motion has an associated magnetic moment with it, the orbital angular momentum, **L**, and the spin angular momentum, **S**, respectively. The magnetic moments are vectors with the direction of orbital angular momentum perpendicular to the plane of the orbit and the spin angular momentum along the spin axis. The total magnetic moment of the atom, **J**, is the sum of orbital and spin angular momentum. When these moments cancel each other completely, the net moment is zero and the material is diamagnetic. When the magnetic moments cancel each other only partially, there is a net magnetic moment on the atom which form paramagnetic, ferromagnetic, antiferromagnetic and ferrimagnetic materials.

Magnetic field strength, **H**, is the measure of vector quantity that determines the ability of electric current or a magnetic material to induce magnetic field at a given point. Magnetic induction, **B**, is the magnetic field induced by a field strength, **H**, at a given point in vacuum and are related to each other as,

$$\mathbf{B} = \mu_0 \mathbf{H} \tag{2.1}$$

where μ_0 is the permeability (1.257×10^{-6} H/m or Vs/Am) and is defined as the degree of penetration of magnetic field lines in vacuum. Inside a material, **B** is given by the vector sum of the magnetic field strength, **H**, and resultant intrinsic induction termed as magnetization, **M**, or magnetic polarization, **J**. It can be expressed as the density of permanent or induced magnetic dipole moments in a material.

$$\mathbf{B} = \mu_0 \mathbf{H} + \mu_0 \mathbf{M} \tag{2.2}$$

The measure of responsiveness of a material to magnetic field is given by susceptibility, χ. The sign and magnitude of χ is a characteristic of each class of magnetic materials.

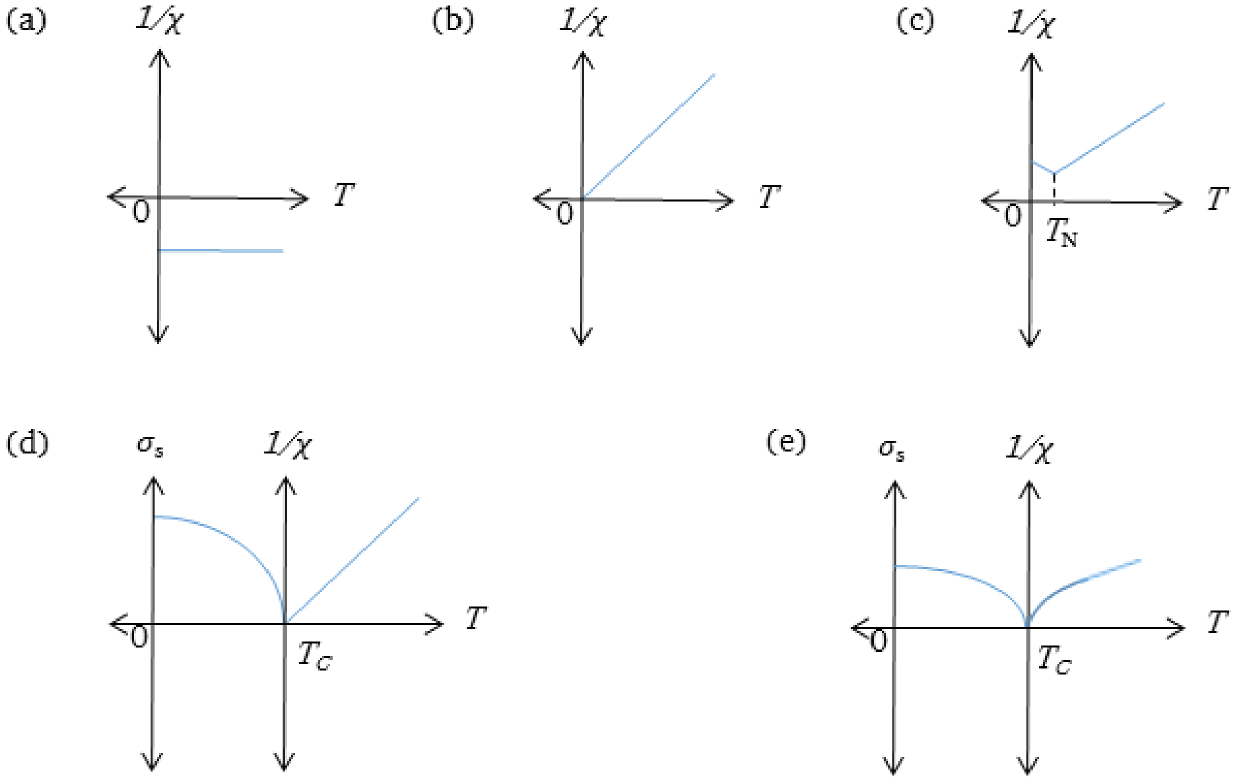

Figure 2.1: Plot of inverse susceptibility with temperature for (a) diamagnetic, (b) paramagnetic, (c) antiferromagnetic, (d) ferromagnetic, and (e) ferrimagnetic materials.

2.1.1 Diamagnetism

Diamagnetic substances have no un-paired electrons in their orbitals and therefore, no net magnetic moment of the atom. In the presence of a non-uniform magnetic field, these move from a region of high magnetic field to low magnetic field, i.e. the diamagnetic substances are repelled by a magnet. An external magnetic field accelerates or decelerates the orbiting electrons in such a way that their magnetic moment counteracts the external field giving rise to orbital diamagnetism. A torque on the magnetic moment induces a precessional motion of electrons around the applied magnetic field at the Larmour frequency. The mass susceptibility, χ, is independent of temperature as shown in Fig. 2.1(a). Some common examples of diamagnetic materials are Ag, Cu, superconductors etc. The $\mathrm{Al_2O_3}$ substrate used in this work is also diamagnetic with susceptibility of -37.0 $\times 10^{-6}$ emu/mol at 300 K.

2.1.2 Paramagnetism

Curie-type paramagnetic materials have atleast one unpaired electron that gives rise to magnetic moment. However, the net distribution of moment direction is random. In a typical paramagnetic salt, only one in about 10^9 moments is able to align with the field as thermal agitation disturbs this ordering of moments. The susceptibility of paramagnetic materials is positive but small in magnitude. It is inversely proportional to temperature as shown in Fig. 2.1(b) and is expressed by Curie's Law given by,

$$\chi = C/T \tag{2.3}$$

where C is the Curie constant. The Curie's law was explained by Langevin by assuming that the magnetic moments are influenced only by external magnetic field and thermal agitation. No interaction between the individual moments was considered.

The interaction among the individual moments, termed as the molecular field, was taken into account by Weiss to explain the magnetic behavior of most of the paramagnetic materials and postulated the Curie-Weiss Law given by,

$$\chi = C/(T - \theta) \tag{2.4}$$

A positive value of θ implies that the molecular field tends to align moments with each other and with the applied field and thereby, increases the susceptibility. Later on, the origin of this molecular field was found to be quantum mechanical exchange force by Heisenberg.

In Pauli paramagnets, the susceptibility is weak and independent of temperature. This phenomena is observed in metals when the conduction electrons occupy such energy levels that the applied field can reorient the spins of only small fraction of electrons.

In most of the solids expect the rare-earth elements, the electron orbits are strongly coupled to the crystal lattice which prevents the alignment of orbital magnetic moment into the field direction. The orbital moments are quenched in these cases and only spin paramagnetism is observed. However, the deep-lying localized $4f$ electrons in the rare-earths are screened by the outer electrons from the crystalline field of neighboring ions. Thus, the orbital magnetic moment of the f electrons are able to align with the external magnetic field.

2.1.3 Ferromagnetism

A ferromagnet, such as Fe, Co and Ni, is made up of small regions called domains in which the moments are spontaneously magnetized without any external applied field. The individual magnetization of domains cancel each other and the net magnetization of the material is zero. Above its Curie temperature, a ferromagnet becomes a paramagnet and follows Curie-Weiss law, as shown in Fig. 2.1(d). However, this transition is not sharp. The difference between paramagnetic and ferromagnetic Curie point is about 10-30 K.

The origin of the domains is the result of contributions from the exchange, anisotropy, magnetoelastic, and magnetostatic energy. The crystalline anisotropy energy makes the magnetization of a domain point along certain crystallographic directions known as the easy-axis of magnetization. In the saturated configuration, a single domain has a high magnetostatic energy which is minimized by dividing the crystal into two domains with opposite direction of magnetization. The subdivision continues until the energy required to form an additional boundary wall, is greater than the reduction in the magnetostatic energy [1]. The formation of a domain wall requires energy as the exchange forces favor parallel alignment of domains. The domain wall energy, E$_d$, is given by

$$E_d = \sqrt{AK} \tag{2.5}$$

and the wall thickness, D, is given by

$$D = \sqrt{A/K} \tag{2.6}$$

where A is the exchange coupling constant and K is the magnetocrystalline anisotropy constant and is described in Section 2.3 . These are two competing terms where A favors a parallel alignment of the spins with each other while K tends to align the spins with the crystal lattice.

The exchange energy is the energy of interaction between the neighboring atoms which tends to orient the electron spins of the atoms either parallel or anti-parallel depending on the algebraic sign of the exchange integral. It is of electroelastic origin and is given by,

$$E_{ex} = -2J_{ij}S_i.S_j \tag{2.7}$$

where J is the exchange integral connecting atoms i and j, S_i and S_j are the spin angular momenta. When J is positive, the energy for parallel orientation of spins is lowered than for antiparallel alignment. Hence, a positive value of J is a necessary condition for ferromagnetism. The Bethe-Slater curve shows the variation of J with the ratio,r_a/r_{3d} where r_a is the radius of an atom and r_{3d} is the radius of $3d$ shell of electrons. For larger ratios, J is small and positive. With decrease in the ratio, J increases, i.e. the interaction favoring parallel spins becomes stronger, to a maxima and then it decreases to zero. A further decrease in the interatomic distances, the spins must be antiparallel, J becomes negative and the material is antiferromagnetic.

An interplay of various energy contributions eventually leads to an energetically most favorable domain size for a given ferromagnetic material.

Theory of ferromagnetism

There are two main theories explaining ferromagnetism, (a) localized moment theory, and (b) band theory. In localized moment theory, which is also central to the molecular field theory given by Weiss and Heisenberg, the electrons contributing to moment of individual atom are localized at each atom. It could explain the variation of magnetization with temperature, but not the presence of a non-integral magnetic moment of atom, observed for metals.

According to the band theory, the electrons contributing to the magnetic moment are itinerant and can move from one atom to the other. The theory could well explain the non-integral values of magnetic moment but not the deviation of certain metals in the Slater-Pauling curve. The ferromagnetism in Fe, Co, and Ni is attributed to the partially filled $3d$ band. At low temperatures, strong exchange interactions between the electrons creates a difference in the spin-up and spin-down electrons. According to the itinerant electron model, there is an exchange splitting between two $3d$ sub-bands and hence, a magnetic moment, if the Stoner criterion is satisfied:

$$IN(E_F) - 1 \equiv I - 1 > 0 \tag{2.8}$$

where I is the effective Coulomb repulsion between the $3d$ electrons and $N(E_F)$ is the electron density at the Fermi level. The magnetic moment results from an equilibrium between normal tendency of the spins to align in anti-parallel arrangement (to occupy the lowest momentum and kinetic energy ranges in energy band) and the tendency of parallel alignment (because of positive exchange integral). The equilibrium magnetization depends on the temperature, number of electrons, the form of the band and the magnitude of exchange interaction [2].

Hysteresis

One of the most important characteristic of ferromagnets is the hysteresis in which the magnetic state of a system depends on its history as to how the magnetic field changed in the past. It is a result of non-equilibrium thermodynamics in which the magnetic induction lags behind changes in the magnetizing force causing it. The increase in the total magnetic moment of a ferromagnet upon application of external field takes place by two independent processes [1]. At low magnetic fields, the magnetization changes usually proceed by domain wall movements. The volume of the domains, which are favorably oriented with respect to the magnetic field, increases at the expense of the unfavorably aligned domains. At high fields, the magnetization usually changes by rotation of direction of magnetization.

2.1.4 Ferrimagnetism

Ferrimagnetic materials are also made up of magnetically saturated domains and exhibit magnetic hysteresis similar to ferromagnets below the Curie temperature. However, these are ceramic metal oxides and the arrangement of moments is different compared to ferromagnets. The inverse susceptibility graph is a hyperbola as shown in as shown in Fig. 2.1(e).

N$\acute{e}$el proposed a model to explain spontaneous magnetization, in which a ferrimagnetic crystal consists of two sublattices, one composed of A and the other of B ion occupying two different types of crystallographic sites. The direction of spontaneous magnetization on sublattice A is opposite to that on sublattice B. However, the magnitude of these magnetizations are not equal resulting in a net spontaneous magnetization on the crystal. The magnetic moments are localized on the magnetic ions and an exchange interaction occurs via oxygen ions by indirect (super-exchange) mechanism. The exchange force acting between an ion on *A* and *B* site, *AB*, is negative as in antiferromagnets. The *AA* and *BB* interactions are also weakly antiparallel.

Some of the ferrimagnetic materials include, γ-Fe_2O_3, ferrites, garnets and the heavy rare-earth cobalt intermetallic alloys, RCo_5. The ferrites exist in cubic and hexagonal, crystal structures. Ferrites of the type $MO.Fe_2O_3$, where M is a divalent metal ion, are cubic. Out of these, $CoO.Fe_2O_3$ is magnetically hard, rest others are soft. Some of the cubic ferrites have a spinel structure with divalent, M^{2+} ions at tetrahedral and the trivalent, Fe^{+3} at octahedral sites. Many others have an inverse spinel structure with the divalent ions at octahedral site and the trivalent ions equally divided between the two sites. Iron, cobalt and nickel ferrites have an inverse structure. Barium and strontium ferrites have a hexagonal crystal structure and are magnetically hard. In heavy rare-earth binary intermetallic alloys, RCo_5, where *R* starts from Gd to Tm, the cobalt moments are antiparallel to those of rare-earth.

2.1.5 Antiferromagnetism

Antiferromagnetic materials exhibit a spontaneous alignment of moments below a critical temperature. However, the moment on the neighboring magnetic ions are arranged in antiparallel fashion. The antiferromagnets can be considered to be made up of two interpenetrating and identical sublattices of magnetic ions with each sublattice being spontaneously magnetized to saturation in opposite directions at 0 K. Antiferromagnets obey the Curie Weiss law but with a negative value of θ.

$$1/\chi = T + \theta/C \tag{2.9}$$

With decrease in temperature, the magnetic susceptibility increases and reaches a maxima at N$\acute{e}$el temperature, T_N. The inverse susceptibility, $1/\chi$ vs T, is a straight line above which extrapolates to a negative temperature, as shown in Fig. 2.1(c). Below T_N, the susceptibility decreases with temperature. Cr, Mn, MnO, NiO, FeO are some common antiferromagnetic materials.

2.2 Permanent magnets

Permanent magnets are characterized by a large remanence as well as coercivity, giving rise to a large maximum energy product. The development of maximum energy density of the hard magnetic materials, developed in the twentieth century is shown in Fig. 2.2. The first class of permanent magnets was steels which are made up of iron and carbon. These are quenched to produce the metastable tetragonal martensitic structure that imparts hard magnetic properties. Alnico alloys contain substantial amounts of ferromagnetic Fe, Ni and Cu along with small amounts of Al and Cu and are free of carbon. The permanent magnet properties are achieved by the precipitation of a ferromagnetic phase of Fe and Co in a weakly magnetic Al and Ni matrix. The magnetization reversal in these single-domain precipitates takes place not by domain wall motion but instead by rotation against the shape anisotropy. Barium ferrite, $BaO.6Fe_2O_3$ ($BaFe_{12}O_{19}$), and strontium ferrite, $SrO.6Fe_2O_3$ ($SrFe_{12}O_{19}$), are the most important ferrimagnetic oxides commercially used. Ferrites are generally semiconductors and that is why these materials do not induce eddy currents in the presence of alternating magnetic fields and hence, the power losses due to eddy currents can be minimized. The coerciviy of the Alnico arise due to the shape anisotropy of single-domain particles of

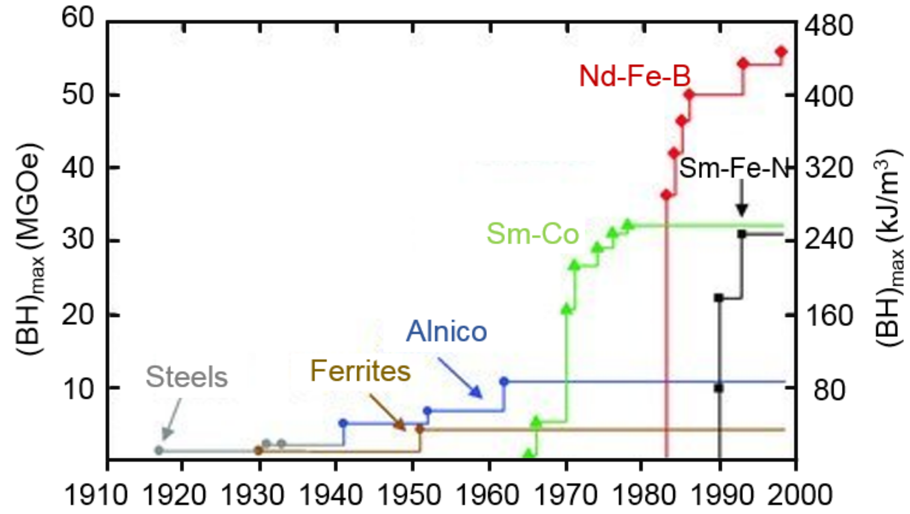

Figure 2.2: The development of maximum energy density of the hard magnetic materials developed in the twentieth century. Image adapted from [5].

Fe and Co. The hard ferrites exhibit a large magnetocrystalline anisotropy of $K_1 = 3.6 \times 10^5$ to roughly 5×10^5 J/m^3 for $SrFe_{12}O_{19}$ [3], however, with reduced magnetization. The need for a combination of high magnetization and high magnetocrystalline anisotropy led to the investigation of intermetallic compounds [4]. The strongest permanent magnets used commercially are the nucleation-type NdFeB magnets, which have outstanding properties near room temperature with the Curie temperature of NdFeB close to 350 °C. In the temperature range of 200-400 °C, the functioning of pinning-type $Sm_2(Co, Cu, Fe, Zr)_{17}$ magnets with significantly high Curie temperature outshines the utility of NdFeB-based materials.

2.2.1 Coercivity mechanism

Coercivity is an extrinsic property of a magnetic material and the underlying mechanism of coercivity depends on the size of smallest magnetic entity and the microstructure. In the simplest case of non-interacting, isolated, single domain particles with uniaxial anisotropy, the magnetization reversal takes place by coherent rotation process as explained by Stoner Wohlfarth model [6]. In this model, a rigid exchange coupling between the atomic spins is assumed which results in a parallel alignment of the spins in the system, at any time [7]. The reversal depends on the easy-axis distribution across the particle ensemble. This model is no longer applicable for large grained particles in which the magnetostatic interactions become important, leading to incoherent reversal of magnetization.

The Stoner Wohlfarth model predicts high values of coercivity equivalent to the anisotropy field for single domain particles provided they have intrinsically large values of anisotropy. However, the experimentally observed coercivity in a material is far below its anisotropy field, which is known as the Brown's paradox. The coercivity, H_c, is reduced to about $\alpha\ H_a$ where H_a is the anisotropy field and α is the Kronmüller factor and is related to nanostructural imperfections [8]. The presence of certain imperfections, like crystallographic defects, strain, secondary phases, magnetic and chemical inhomogeneities.

The nanocrystalline hard magnets can be broadly classified into the following three types depending on the microstructure:

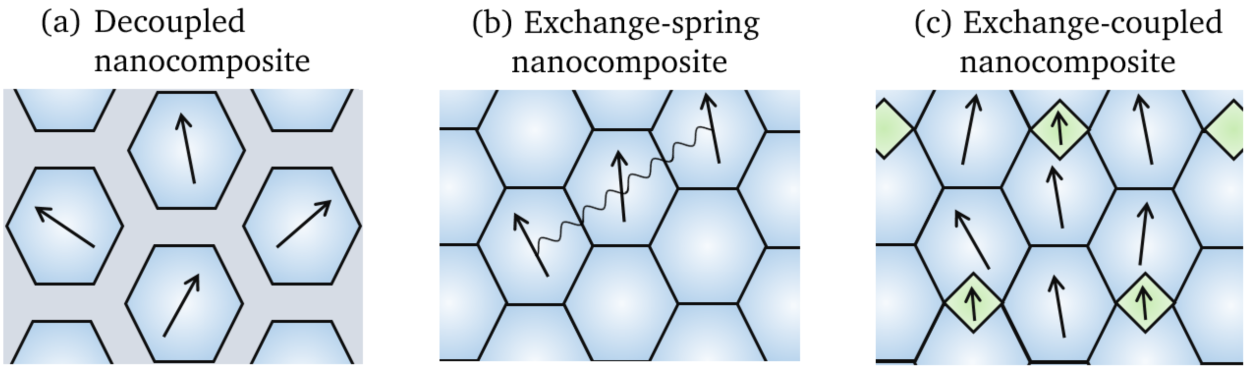
(a) Decoupled nanocomposite
(b) Exchange-spring nanocomposite
(c) Exchange-coupled nanocomposite

Figure 2.3: The different types of magnetic nanocomposites: (a) a decoupled nanocomposite, (b) an exchange-spring magnet, (c) an exchange-coupled magnet.

1. Decoupled magnet (excess rare-earth)

   In a typical decoupled magnet, the grains of a hard magnetic phase (50-200 nm) are isolated by an amorphous paramagnetic interlayer as shown in Fig. 2.3(a). These magnets comprise of an excess of rare-earth element. The easy-axes of the grains are isotropically distributed along the easy-direction determined by the magnetocrystalline anisotropy. In an example material system of $(\mathrm{Nd, Pr})_2\mathrm{Fe}_{14}\mathrm{B} +$ (Nd, Pr), the hard magnetic grains comprising of $R_2\mathrm{Fe}_{14}\mathrm{B}$ phase are enveloped by overstoichiometric rare-earths. Each grain behaves as an elementary permanent magnet and the reverse field has to overcome the crystal anisotropy of each magnet. Hence, decoupled magnets exhibit the highest coercivity.

2. Exchange-spring magnet (stoichiometric, single-phase magnet)

   In a stoichiometric magnet of $R_2\mathrm{Fe}_{14}\mathrm{B}$, the hard magnetic grains (average grain size of 20 nm) are in direct contact with each other. The exchange interaction among the grains aligns the magnetic moments with each other. In the remanent state, the magnetization cannot align parallel to the respective easy-axes as the spins are coupled to each other like a spring. Thus, there is a smooth transition of polarization from the easy-axis of one grain to the other and a magnetic texture is induced in a direction of the initially applied field. Only this exchange-coupled volume fraction brings about an enhanced remanence. In this case, exchange coupled magnets have lower coercivity than decoupled magnets as part of moments is rotated out of easy-axis [9].

3. Exchange-coupled magnet (overstoichiometric Fe, two-phase magnet)

   In a nanocomposite of hard and soft magnetic phases, the spins of the soft phase with a small anisotropy are coupled to the hard phase with an extremely large anisotropy as shown in Fig. 2.3(c). For an effective exchange, the size of the soft magnetic phase should be smaller than the exchange length of hard magnetic phase. Such magnets show an enhanced remanence more than that of the exchange-spring magnet because of the exchange-coupling between the grains as well as presence of soft magnetic phase with a high spontaneous polarization [10]. For example, magnets made up of NdFeB with an excess of Fe, the spins of Fe are coupled to NdFeB. There is an increase of energy product by a factor of two as compared to the conventional nanocrystalline decoupled magnet.

In the bulk magnets, the magnetization reversal takes place by nucleation of a reverse domain and the propagation of domain walls. In the nucleation type magnets, the magnetization reversal from the saturated state requires the nucleation of a reversed domain which occurs at high fields while the domain wall motion is relatively easy. Thus, in these type of magnets, the coercivity is controlled by the nucleation mechanism which most likely occur at those sites where the crystal anisotropy is locally lowered due to oxide formation, interface dislocations or localized distortions in the crystal [11].

On the other hand, in pinning-type magnets, the formation of a reversed domain is less energetic than its expansion in the grain. Generally, these should have a specially designed nanostructure made up of small inclusions of coherent phases. Local alterations of anisotropy and exchange energies appear near such precipitates which leads to a change of energy of the domain wall and eventually its pinning. Thus, the coercivity of pinning-type magnets is determined by the field required to move the domain wall across such pinning centers.

The technical realization of pinning-mechanism is based on a special feature in the phase diagram, i.e. decomposition-reaction of a high-temperature metastable multicomponent phase into neighboring phases, which are stable at lower temperatures. The addition of other elements promotes phase separation, elevates the phase stability ranges and hence, results in enhanced precipitation hardening. The hysteresis of exemplary pinning-type material $Sm_2(Co, Cu, Fe, Zr)_{17}$ has its origin in an intricate nanostructure comprising of $Sm(Co,Cu)_5$, $Sm_2(Co,Fe)_{17}$ and $Sm(Co,Fe,Cu,Zr)_{10-11}$ which results from a natural phase decomposition process [12, 13]. Upon complex heat treatment, an ordered nanocomposite is formed naturally in which domain wall pinning at specific sites is responsible for enhanced coercivity [14, 15].

2.3 Magnetic anisotropy

Magnetic anisotropy means that the magnetic properties of a material vary with direction. It is one of the most important intrinsic property of a magnetic material. The main sources of anisotropy are crystal structure, sample shape and atomic or micro-scale texture as described below:

2.3.1 Magnetocrystalline anisotropy

The magnetocrystalline anisotropy is a measure of the stability of the magnetization direction with respect to crystal axis. There are certain crystallographic directions along which when the magnetic field is applied, the saturation is achieved easily or at lower fields. These directions are called as easy-axes. While, when the magnetic field is applied along other directions, called as the hard-axes, a considerable amount of energy is required to orient the spins along these directions and bring the crystal to saturation. This energy is stored in the crystal in the form of anisotropy energy. Depending on the crystal structure, the magnetocrystalline anisotropy energy is given by:

$$\begin{aligned}
\text{Cubic}: E_a &= K_1c(\alpha_1^2\alpha_2^2+\alpha_2^2\alpha_3^2+\alpha_3^2\alpha_1^2)+K_{2c}(\alpha_1^2\alpha_2^2\alpha_3^2) && (2.10)\\
\text{Tetragonal}: E_a &= K_1sin^2\theta+K_2sin^4\theta+K_2'sin^4\theta cos4\phi+K_3sin^6\theta+K_3'sin^6\theta sin4\phi && (2.11)\\
\text{Hexagonal}: E_a &= K_1sin^2\theta+K_2sin^4\theta+K_3sin^6\theta+K_3'sin^6\theta sin6\phi && (2.12)
\end{aligned}$$

In a cubic crystal, let M_s make angles a, b, c with the crystal axes, then the cosine of these angles α_1, α_2, α_3 are the direction cosines. The anisotropy energy is expressed in terms of series expansion of the direction cosines of the saturation magnetization relative to the crystal axes. For tetragonal and hexagonal structures, the anisotropy energy is expressed in terms angle θ between M_s and the *c*-axis. For a hexagonal system, depending on the sign of K_1 and K_2, a material system shows easy-axis, easy-plane or an easy-cone anisotropy. The physical origin of magnetocrystalline anisotropy is discussed in Section 3.3

2.3.2 Shape anisotropy

The shape anisotropy originates from the demagnetizing field because of the shape of a material. A polycrystalline specimen having no preferred orientation of its grains, and therefore, no net crystal anisotropy. Within a material, the applied field, H_a, is reduced by the demagnetizing field, H_d. The demagnetizing field is proportional to the magnetization, M, as well as a demagnetization factor, N, which is defined through the geometry of the specimen:

$$H = H_a - H_d \tag{2.13}$$

$$H_d = NM \tag{2.14}$$

If a material is spherical in shape, the applied field will magnetize it to the same extent in all the directions. But if it is non-spherical, it is easier to magnetize it along a long axis than along a short axis. The lowest energy state is obtained when the dipoles are aligned along the long axis. The demagnetizing field along a short axis is stronger than along a long axis. The applied field along a short axis then has to be stronger to produce the same true field inside the specimen. In thin films long-range magnetic dipolar interactions between the moments can leads to different easy-axis than the intrinsic magnetic anisotropy, K. The shape anisotropy energy of a thin film is given by $2\pi\ M_\mathrm{s}^2$. If K is smaller than $2\pi\ M_\mathrm{s}^2$, then the easy-axis of magnetization lies in the film plane.

2.3.3 Surface or interface anisotropy

In ultra-thin films and multilayers, the symmetry at the surfaces, interfaces or atomic step edges is reduced leading to a large surface energy contribution known as the surface anisotropy [16, 17]. The different types of interfaces: an interface with substrate, an interface with atmosphere and an interface between layers in multilayers, lead to different contributions to surface anisotropy energy density, K_s. In addition, the lattice could be distorted due to the strain caused by lattice mismatch between the film and the substrate which contributes to magnetoelastic surface anisotropy. The contribution of the surface anisotropy energy is thickness dependent on the thickness of the film.

The effective anisotropy, K^{eff}, of a film with thickness, d, can be expressed as the sum of the effective volume anisotropy constant, K_v^{eff}, the shape anisotropy energy, $2\pi M_\mathrm{s}^2$ and the surface anisotropy energy density, K_s.

$$K^{eff} = K_v^{eff} - 2piM_s^2 + 2K_s^{eff}/d \tag{2.15}$$

$$K^{eff} \times d = (K_v^{eff} - 2piM_s^2) \times d + 2K_s^{eff} \tag{2.16}$$

The effective volume anisotropy constant, K_v^{eff} comprises of the magnetocrystalline and magnetoelastic contributions in the bulk of thin film [18]. In case of pseudomorphic growth below a critical thickness, the epitaxial strain due to the lattice mismatch between the film and the substrate, is thickness independent. In this case, K_V is not the same as the anisotropy energy of the bulk [19]. However, above this critical thickness, the strain is reduced by misfit dislocations and so the magnetostrictive anisotropy varies with thickness and should be taken into account with the thickness dependent effective surface contribution, although it is not originated from the surface.

2.3.4 Perpendicular anisotropy

It is energetically more favorable to magnetize a thin film along its plane because of the shape anisotropy. The alignment of the easy-axis of magnetization perpendicular to the film plane, known as perpendicular anisotropy, can be achieved when the perpendicular component of anisotropy overcomes the shape anisotropy [20]. Thin films with perpendicular anisotropy are important for ultra-high-density magnetic storage devices and spintronic applications [21]. In magnetic random access memories, the perpendicular anisotropy of the free layer permits stable magnetization states at room temperature and imposes a large energy barrier to the magnetization switching between up and down orientations in nanoscale devices. Moreover, these magnetization states can be readily altered using spin-transfer torque mechanism. Generally, the materials with high uniaxial magnetocrystalline anisotropy allow smaller and thermally stable media grains [22].

The common material systems exhibiting perpendicular anisotropy include multilayers of Co/(Pd, Pt), CoFeB/metal (Ta, Mg) oxides, rare-earth transition-metal alloys and $L1_0$-ordered (Co,Fe)-Pt alloys. There are different mechanisms leading to perpendicular anisotropy in these systems.

(i) Multilayers of Co/(Pd, Pt)

In multilayered systems with alternate layers of magnetic and heavy non-magnetic metals e.g., Co and Pt or Pd, with a particular orientation, interface anisotropy leads to a perpendicular orientation of magnetization. As the thicknesses of the individual layers decrease, the effect of surfaces and interfaces becomes so strong that the easy-axis can be rotated out of the film plane [23, 24]. In Co/Pt multilayers, perpendicular magnetic anisotropy is considered to be caused by the Co 3*d*- Pt 5*d* interfacial hybridization via enhanced orbital moment of cobalt [25].

(ii) CoFeB/ metal (Ta, Mg) oxides

The conventional material system of CoFeB-MgO is used in MTJs with an in-plane anisotropy as well as perpendicular MTJs [26] because of the high tunneling magnetoresistance ratio. Perpendicular magnetization in CoFeB/MgO multilayer system results in high-stability of magnetization at room temperature, important for long-term data storage [27]. The origin of perpendicular anisotropy at the interface between metallic oxides and ferromagnetic transition metals was predicted from the first-principle calculations. It is attributed to the overlap between O-p_z orbital of metallic oxides and d_{z^2} orbitals of transition metals hybridized with $d_{xz(yz)}$ [28].

(iii) $L1_0$-ordered (Co,Fe)-Pt, *R*Co$_5$ intermetallics

The *c*-axis textured growth of material system with extremely large uniaxial magnetocrystalline anisotropy greater than the shape anisotropy of the thin films results in perpendicular anisotropy. Some common examples are $L1_0$-ordered (Co,Fe)-Pt alloys and the class of *R*Co$_5$ (R = Sm, Y, Ce) compounds.

2.4 Thin film growth

The growth of thin films from incoming atoms in the gas phase is a non-equilibrium phenomena governed by both kinetic and thermodynamic processes. The most important kinetic processes include the arrival and adsorption of incoming atoms, their migration or diffusion on the surface, aggregation of atoms to form a nucleus, dynamics of a stable nucleus, atom attachment and detachment and inter-layer and intra-layer mass transport [29]. The incoming atoms generally adsorb where they land from vapor phase and reach a state of thermal equilibrium with the substrate at the site of impact. From then on, the thermally activated diffusion processes take place in the form of single adatoms movements between adjacent lattice sites. The energy barriers encountered by adatoms along their migration path define the diffusion rates and growth kinetics. The surface diffusion coefficient, D, is related to site-to-site hopping rate of an adatom, k_s, by

$$D = a^2 k_s \tag{2.17}$$

where a is the effective hopping distance between sites, and

$$k_s \propto \exp(-V_s/k_B T) \tag{2.18}$$

V_s is the potential-energy barrier from site to site, T, is the substrate temperature and k_B is the Boltzmann constant. In the initial stage of growth on flat surface, for a constant deposition rate, the diffusion coefficient, D, determines the average distance, l_D, covered by an adatom before being trapped,

$$l_D = \sqrt{D\tau} \tag{2.19}$$

where τ is the residence time before re-evaporation [30]. The adatoms from the gas phase diffuse on the substrate terraces before colliding with other diffusing adatom (intra-layer mass transport) and create a dimer. As the deposition proceeds, the number of dimers increases until their density is comparable to that of monomers. At this stage, the probability of a diffusing monomer encountering another monomer or a dimer is almost same and there is a competition between the growth of a cluster or the nucleation of a new one. As a result, the increase in the density of stable nuclei levels off until it saturates at a coverage of about 0.15 ML. At this point, the mean-free path of diffusing adatoms is equal to the average separation between the islands and any further increase in the leads to an island growth as all the adatoms reach existing islands and attach to them. At coverages beyond, 0.2 ML, the 2D clusters start to coalesce until the monolayer film percolates at about 0.55 ML. The adatoms also diffuse to a lower terrace also called as inter-layer mass transport. In this case, the atoms deposited on a top of an island reach the island edge and then diffuse to the lower layer. The rate of interlayer diffusion determines whether films are flat or 3D. In case of a limited intra-layer transport, the nucleation will occur on top of islands giving rise to growth of 3D clusters. For a faster interlayer diffusion, the island remain 2D until these coalesce, giving rise to layer-by-layer 2D growth of film [31].

The total energy of a thin film system comprises of the surface energy of the substrate, γ_S, the film, γ_F, the energy of the interface, γ_I, the misfit energy, E_{mis}. The growth modes are governed by the thermodynamic driving forces leading to the minimization of total energy. The three main modes used to describe the growth of a thin film are Frank-van der Merwe (layer by layer), Volmer-Weber (island growth) and Stranski-Krastanov growth mode.

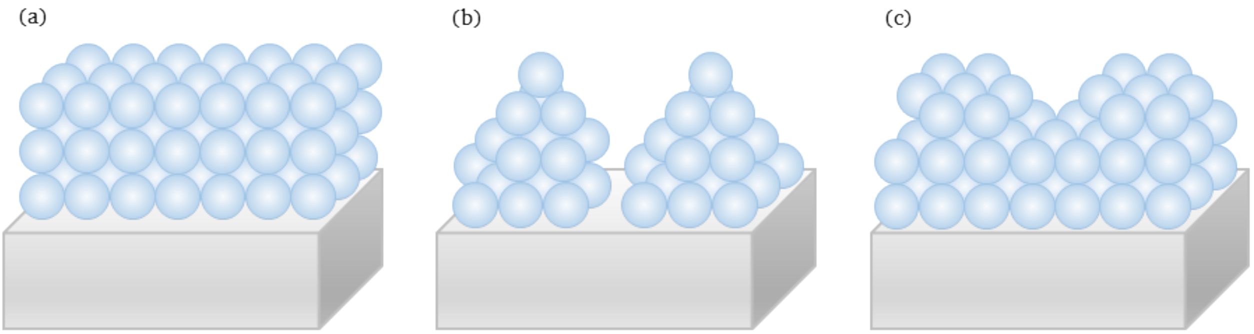

Figure 2.4: A schematic illustration of the (a) Frank-van der Merwe, (b) Volmer-Weber and (c) Stranski-Krastanov growth modes of thin films.

(a) Frank-van der Merwe growth mode

The 2-dimensional layer-by-layer Frank-van der Merwe growth mode occurs when the interaction between the incoming atoms and the substrate is much stronger than that between the adatoms. For a film composed of n layers, the criterion for a layer-by-layer growth is given by,

$$\gamma_{F(n)} + \gamma_{I(n)} < \gamma_S \tag{2.20}$$

In this case, the misfit energy is small and the sum of surface energy of the film and the interface is less than that of the substrate. It is schematically depicted in Fig. 2.4(a). The n dependence of γ_F indicates the variation caused by change in the lattice constant and/or the structure of the film.

(b) Volmer-Weber growth mode

A schematic illustration of the 3-dimensional Volmer-Weber island growth mode is shown in Fig. 2.4(b). In this case, the incoming atoms or molecules are more strongly bound to each other than to the substrate. This growth mode occurs when the sum of misfit energy and the surface energy of the film and the interface is greater than that of the substrate and is expressed as,

$$\gamma_F + \gamma_I + E_{mis} > \gamma_S \tag{2.21}$$

(c) Stranski-Krastanov growth mode

The Stranski-Krastanov growth mode is a combination of layer-by-layer and island growth and is illustrated in Fig. 2.4(c). When at the start of the deposition, E_{mis} and $\gamma_F + \gamma_I$ is smaller than γ_S, then the film grows layer-by-layer. However, since E_{mis} often increases with ongoing growth, the condition changes to smaller substrate surface energies in total and therefore, leading to island growth. The different energy contributions can be expressed as,

$$\gamma_F + \gamma_I + E_{mis} < \gamma_S \Rightarrow \gamma_F + \gamma_I + E_{mis} > \gamma_S \tag{2.22}$$

There are two possible reasons for this transition from 2D to 3D morphology. In the first case, the film material grows in the first few monolayers in a crystallographic structure different from its bulk. However, it adopts the bulk structure after a critical thickness. This induces an abrupt increase in free energy at the interface between two crystal structures and shifts the energy balance in favor of 3D growth. The second possibility is the strain release by formation of mounds so as to adopt to the bulk lattice constant. In some cases, misfit dislocations are created at or near the substrate-film interface to relieve the mismatch strain.

These growth modes refer to the morphology taken by a system grown close to thermodynamic equilibrium such that the morphology is given by the total energy, irrespective of the path taken by the film atoms in order to reach the minimum energy morphology. Often films are grown in conditions far away from equilibrium and their morphology is determined by kinetics, that is, it is the result of the microscopic path taken by the system during growth. The degree to which one is far away from thermodynamic equilibrium differentiates epitaxial thin film from crystal growth.

3 Rare-earth cobalt intermetallics

The lanthanides, La to Lu, as well as Y are known as rare-earth elements. The delocalized valence electrons ($5d^1$ and $6s^2$) are conduction electrons and, therefore, most of the rare-earth elements are trivalent in the metallic state. The deep-lying localized $4f$ electrons are responsible for the magnetic properties. The absence of $4f$ electrons, e.g. in La and Y, or their complete pairing, e.g. in Lu, and Yb, results in a diamagnetic behavior Gd which has the maximum number of unpaired $4f$ electrons is ferromagnetic. The heavier rare-earths with more than half-filled electrons, e.g. in Tb, Dy, Ho, Er, and Tm, are ferromagnetic below the Curie temperature and antiferromagnetic above it. The net magnetic moment, **J**, given by the sum of **L** and **S**,

$$\mathbf{J} = \mathbf{L} + \mathbf{S} \tag{3.1}$$

when $4f$ shell is more than half full, and by the difference

$$\mathbf{J} = \mathbf{L} - \mathbf{S} \tag{3.2}$$

when the $4f$ shell is less than half full. The rare-earths, with the exception of La, Lu, Y and tetravalent Ce, have a high magnetic moment per atom.

The combination of a rare-earth, R, with a $3d$ transition metal, M, gives rise to a number of intermetallic compounds where both elements occupy well defined crystallographic sites. The existence of a R-M intermetallic was predicted by Buschow in [32] with the condition that the heat of formation of the compound should be negative. The model proposed by Miedema [33] was used in which of the heat of formation depends on the composition, work function and the nearest-neighbor interactions described in terms of density of electrons at the boundary of Wigner-Seitz cell. Accordingly, the stability of a binary R-M compounds, is predicted to increase, from Mn to Ni for a given rare-earth and from La to Lu, for a given transition metal. The relative stability of the compounds of the same composition but with dissimilar structures, however, could not be derived using this model. A list of the binary R-M intermetallic compounds with their crystal structure and symmetry are given in Table. 3.1.

Within the scope of this work, the structural and magnetic properties of the binary compounds of Y-Co, Ce-Co and Sm-Co material systems are investigated. The equilibrium phase diagram of the Y-Co system as adapted from [34] is shown in Fig. 3.1. With decreasing content of cobalt, Y_2Co_{17} phase is formed within a range of 88.0-89.5 atomic % of Co, followed by YCo_5 formed within a range of 83.0-85.7 atomic % of Co. The other phases include Y_2Co_7, YCo_3, YCo_2, Y_2Co_3, YCo, Y_9Co_7, Y_8Co_5 and Y_3Co. In the Y-Co system, the Curie temperature of Y_2Co_{17} (1186 K), YCo_5 (987 K), Y_2Co_7 (639 K) and YCo_3 (305.5 K) exceeds room temperature. While Y_2Co_{17} is an easy-plane material with anisotropy of -0.33 MJ/m^3, YCo_5 exhibits a strong uniaxial magnetocrystalline anisotropy of 5.78 MJ/m^3 and corresponding anisotropy field of about 13 T [35, 36].

The equilibrium phase diagram of the Ce-Co system is shown in Fig. 3.2. All of the intermetallic compounds, Ce_2Co_{17}, $CeCo_5$, Ce_2Co_7, $CeCo_3$, $CeCo_2$ and $Ce_{24}Co_{11}$ exist as line phases. Unlike the Y-Co system, only the compositions, Ce_2Co_{17} and $CeCo_5$ are ferromagnetic at room temperature. Ce_2Co_{17} exhibits an easy-plane

Table 3.1: Binary R-M intermetallic compounds with lattice structure and symmetry

Compounds	Lattice symmetry	Structure type	M
R_3M	orthorhombic	Al_3Ni	Ni, Co
R_4M_3	hexagonal	Ho_4Co_3	Co
RM	orthorhombic	FeB or CrB	Ni
RM_2	cubic	$MgCu_2$	Fe, Ni, Co
RM_3	hexagonal	$CeNi_3$	Ni
	rhombohedral	$PuNi_3$	Fe, Ni, Co
R_2M_7	hexagonal	Ce_2Ni_7	Ni, Co
	rhombohedral	Gd_2Co_7	Ni, Co
R_6M_{23}	cubic	Th_6Mn_{23}	Fe
RM_5	hexagonal	$CaCu_5$	Ni, Co
R_2M_{17}	hexagonal	Th_2Ni_{17}	Fe, Co, Ni
	rhombohedral	Th_2Zn_{17}	Fe, Co, Ni
RM_{13}	cubic	$NaZn_{13}$	Co

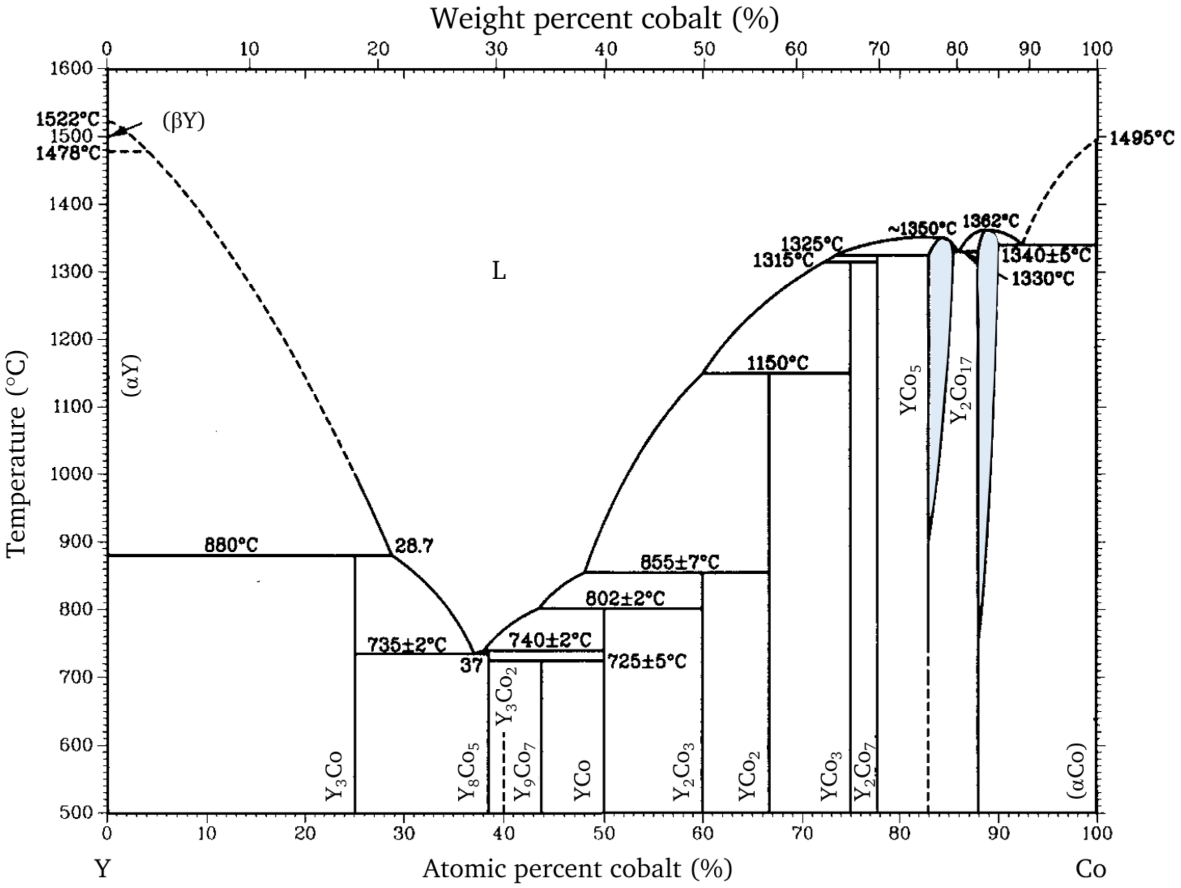

Figure 3.1: Equilibrium phase diagram of Y-Co system. Adapted from [34].

anisotropy with anisotropy field of 14 kOe and a Curie temperature of 1078 K. $CeCo_5$ single crystals exhibit an extremely large uniaxial anisotropy of 6.4 MJ/m^3 with anisotropy field of 210 kOe and a Curie temperature of 737 K [37, 38]. $CeCo_3$ is a Pauli paramagnet and Ce_2Co_7 has a low Curie temperature of 50 K [39, 40].

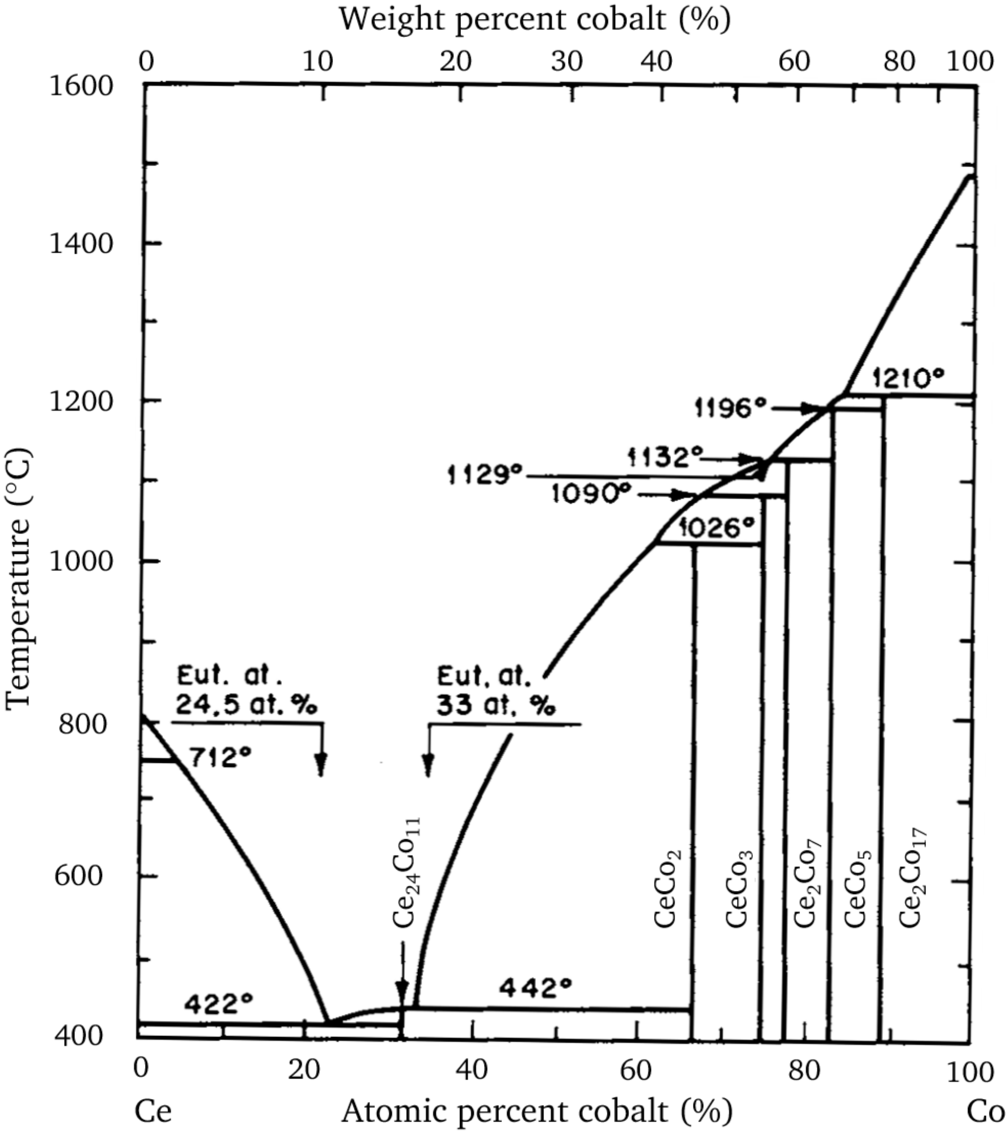

Figure 3.2: Equilibrium phase diagram of Ce-Co system. Adapted from [41].

The Sm-Co intermetallic compounds are technologically the most important class of cobalt based permanent magnets. The equilibrium phase diagram of the Sm-Co system is shown in Fig. 3.3. It is adapted from NIMS Atom Work and is based on [42]. The different intermetallic phases observed in the Sm-Co system are Sm_2Co_{17}, $SmCo_5$, Sm_2Co_7, $SmCo_3$, $SmCo_2$, Sm_5Co_2 and Sm_3Co. Sm_2Co_{17} and $SmCo_5$ are the primary flux producing phases making them important components of bulk as well as thin film magnets. $SmCo_5$ has the highest magnetocrystalline anisotropy of 11–20 MJ/m^3 and Curie temperature of 1020 K. Unlike Y_2Co_{17} and Ce_2Co_{17} which have a non-magnetic rare-earth, Sm_2Co_{17} exhibits a large uniaxial anisotropy of 3.2 MJ/m^3 and high Curie temperature of 1195 K (920 °C), thus, rendering them effective for high temperature applications. Sm_2Co_7 also shows ferromagnetism below 713 K [43].

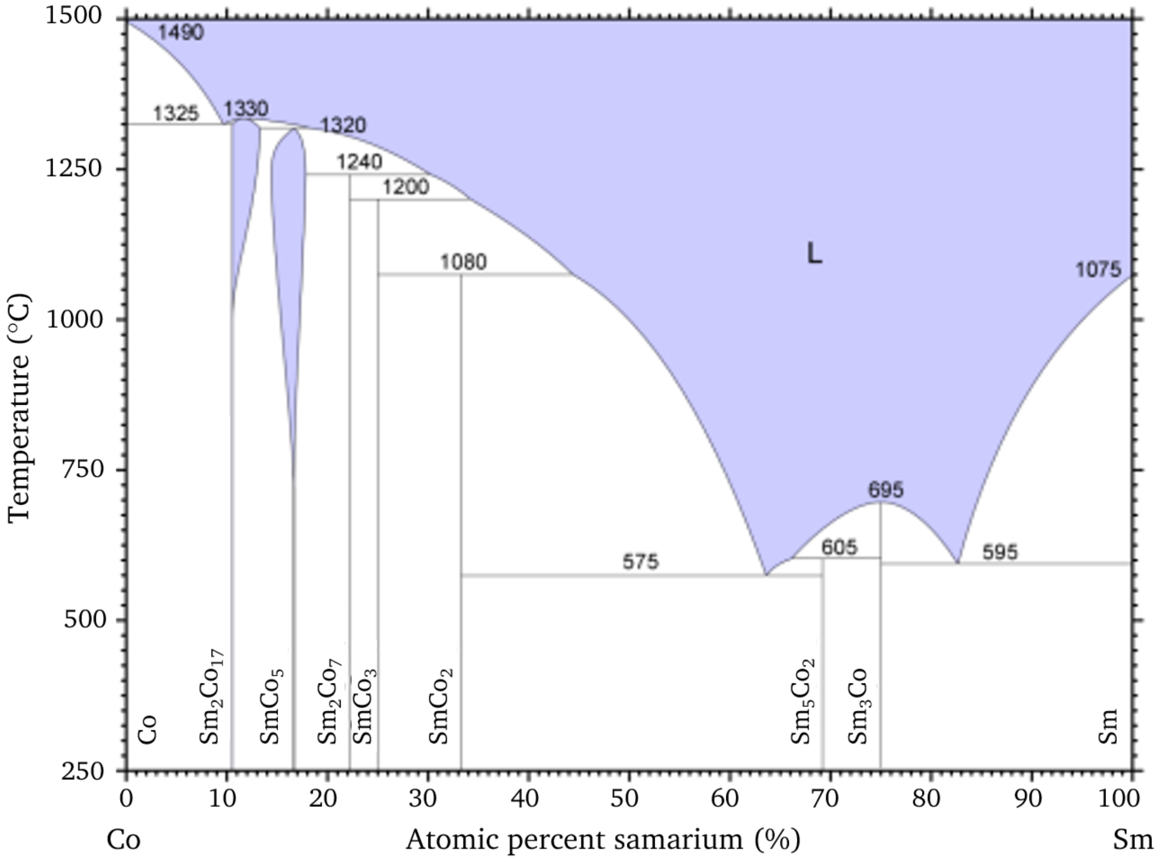

Figure 3.3: Equilibrium phase diagram of Sm-Co system. Adapted from [44].

3.1 Crystal structures

In this section, the crystal structures of various intermetallic compounds commonly observed in the equilibrium phase diagram are discussed. The intermetallics with composition of RCo_5 have $CaCu_5$ hexagonal crystal structure with parameters [45] given in Table. 3.2.

The unit cell of $CaCu_5$ structure comprises of one rare-earth and five cobalt atoms per unit cell as shown in Fig. 3.4(a). A schematic representation of the $CaCu_5$ unit cell with layered structure is shown in Fig. 3.4(b). The crystal structures are drawn using VESTA software [46]. The rare-earths occupy $1a$ (000) site, the Co atoms occupy two crystallographic sites, the $2c$ sites at (1/3, 2/3, 0), (2/3, 1/3, 0) in the plane containing the R atoms (represented as layer A) and $3g$ sites at (0, 1/2, 1/2), (1/2, 0, 1/2), (1/2, 1/2, 1/2) in the plane without R atoms (represented as layer B). The $CaCu_5$ crystal structure is the building block from which majority of other structures are derived through simple substitutions accompanied with layer shifts.

The R_2Co_{17} alloys exist in either Th_2Ni_{17}-type hexagonal (space group $P6_3/mmc$) or Th_2Zn_{17}-type rhombohedral (space group $R\bar{3}m$) structures. These are obtained from the $CaCu_5$ structure via replacement

Table 3.2: Crystallographic parameters of the $CaCu_5$ structure

Crystallographic parameters	$CaCu_5$
Strukturbericht Designation	$D2_d$
Pearson symbol	hP6
Stoichiometry	AB_5
Space group	$P6/mmm$
Nearest neighbours	A: $6B_1$, $12B_2$, 2A B_1: 3A, $3B_1$, $6B_2$ B_2: $4B_1$, $4B_2$, 4A

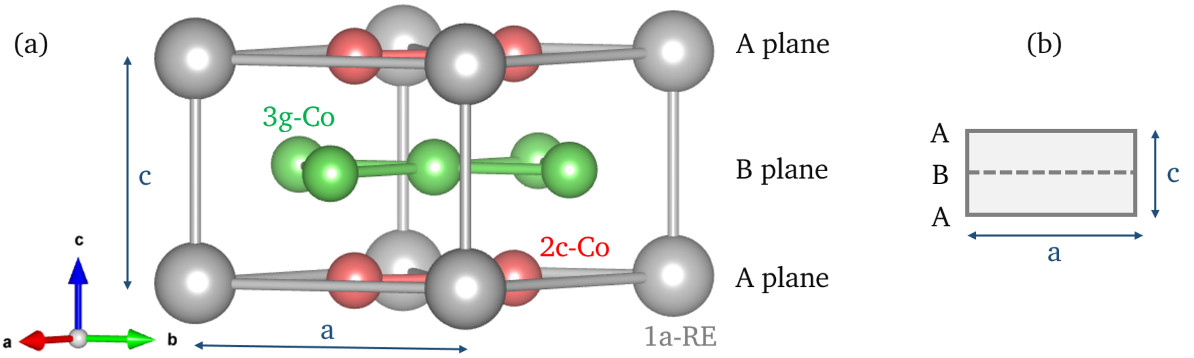
(a)
3g-Co
2c-Co
1a-RE
A plane
B plane
A plane
c
a
c
a
b
(b)
A
B
A
c
a

Figure 3.4: (a) The unit cell of RCo$_5$ compound with $CaCu_5$ structure where R at 1a site is shown in grey, Co at 2c site in red and Co at 3g site in green. (b) A schematic representation of the same $CaCu_5$ unit cell.

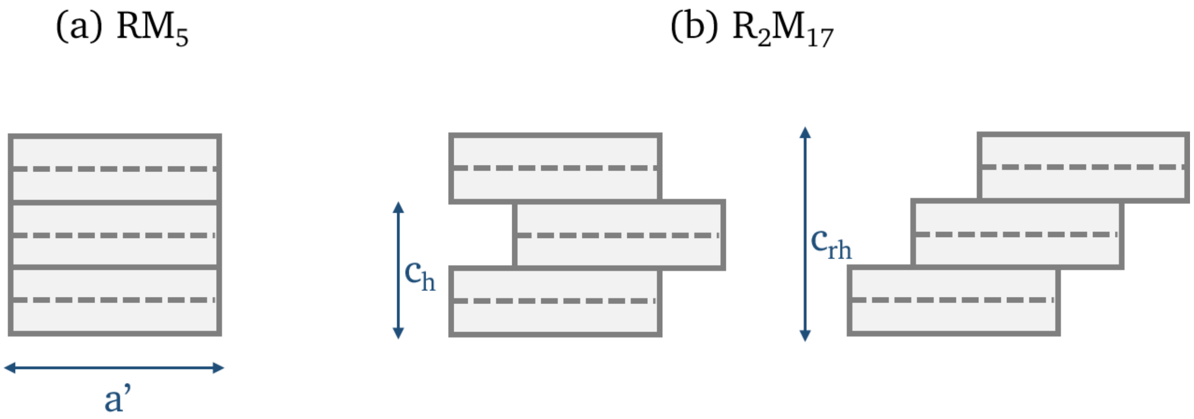

Figure 3.5: Schematic representation of the two types of stacking modes for R_2M_{17} derived from (a) RM_5, hexagonal $CaCu_5$ structure. (b) The two possible stacking modes leading to hexagonal and rhombohedral structure types of the R_2M_{17} intermetallic compounds.

of one-third of all *R* atoms by a cobalt dumb-bell [47, 48]. The unit cell edge in the basal plane is given by, $a' = a\sqrt{3}$, as shown in Fig. 3.5(a). The two possible stacking arrangements in the *c*-direction are schematically shown in Fig. 3.5(b).

If the *R* at site A in the basal plane is replaced by Co dumbbell, in the next layer of *R* atoms, the replacement occurs at site B. In the following layer of *R* atoms, depending on the location of replacement of *R* by Co dumbell, there are two possible structures. If the replacement of *R* occurs again at the same site A, a hexagonal Th_2Ni_{17}-type structure is obtained, as shown in Fig. 3.6(a). If the replacement of *R* occurs at a third site C, the Th_2Zn_{17}-type rhombohedral structure is derived, as shown in Fig. 3.6(b).

The R_2Co_7, RCo_3, and RCo_2 structures are also derived from the RCo_5 structure by replacement of Co by *R* atoms in RCo_5 compounds. A schematic representation of the stacking sequence in these compounds is shown in Fig. 3.7. The different stacking arrangements of RM_5 unit cells with *a* and *c* lattice constants give rise to the hexagonal and rhombohedral, R_2M_7, hexagonal and rhombohedral, RM_3, and cubic, RM_2 structures.

The rhombohedral, RCo_3 structure together with RCo_5 unit cell are shown in Fig. 3.8. In the RM_5 structure, in either the top or the basal plane of each second unit cell, the replacement of one of the two Co atoms by a *R* atom followed by a layer shift and minor rearrangements, lead to the RM_3 structure. The hexagonal R_2Co_7 together with RCo_5 unit cell are shown in Fig. 3.8.

3.2 Magnetic interaction

The magnetic interactions in rare-earth transition metal intermetallic compounds can be classified into: (i) interaction between rare-earths, *R*-*R*, (ii) interaction between metals, *M*-*M*, and (iii) interaction between a rare-earth and metal, *R*-*M*, as described in the following:

(i) *R*-*R* interaction

The interaction between the magnetic moments of the rare-earths is the weakest of all the interactions. As the 4*f* orbital wavefunction is localized, there is no direct overlap among neighboring rare-earths.

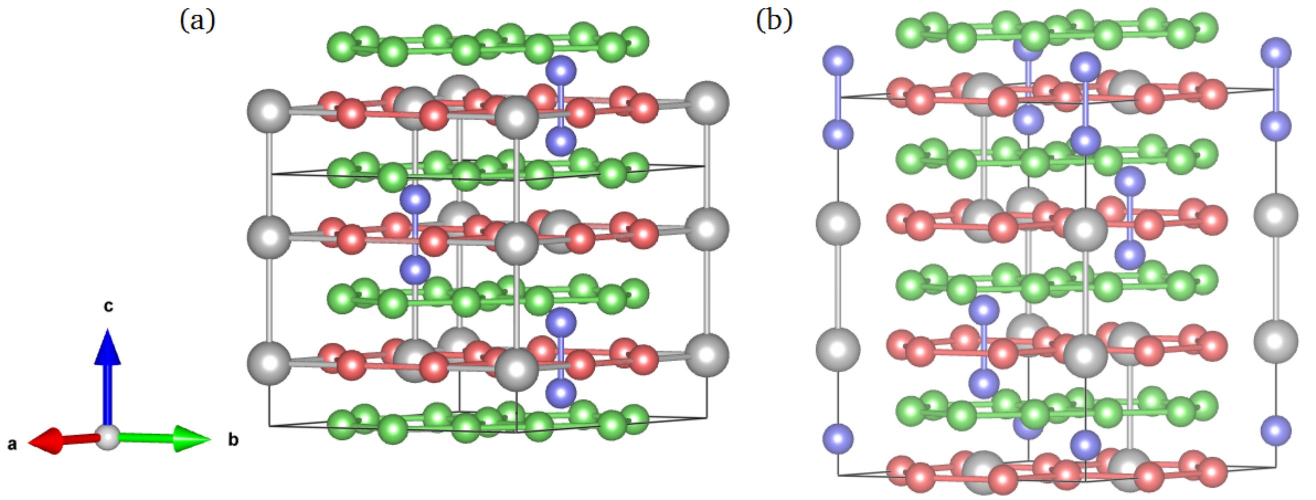

Figure 3.6: (a) The Th_2Ni_{17}-type hexagonal, and the Th_2Zn_{17}-type rhombohedral, structures of R_2Co_{17}. The R at $1a$ site is shown in grey, Co at $2c$ site in red, Co at $3g$ site in green and the Co dumbbell in blue.

Instead, the 4*f* moments in the crystal interact via spin polarization of the *s*-conduction electrons and orient themselves accordingly. This conduction-electron polarization oscillates and can lead to both parallel and anti-parallel coupling. The coupling strength depends on the crystal structure and the number of conduction electrons. This type of interaction is generally called as Ruderman-Kittel-Kasuya-Yosida (RKKY) interaction and the strength of this type of interaction decreases with increasing distance. In *R*-*M* compounds rich in transition metal content, this indirect *f*-*f* exchange is usually neglected [49].

(ii) *M*-*M* interaction

A strong overlap of spatially extended wavefunctions of delocalized 3*d* electrons result in this type of strong interaction which leads to a difference in the number of spin-up and spin-down electrons, given that the Stoner criterion is satisfied. The compounds in which the number of spin-up and spin-down electrons are equal, the net magnetic moment is zero as observed in YCo_2, YMn_2, $LaNi_5$, YNi_5 and $ThNi_5$ [48, 32]. For the *R*-Ni and *R*-Co compounds, the magnetic moments are due to one incomplete 3*d* sub band, whereas for the Fe compounds both the sub-bands are incomplete [50]. For R_2Co_{17} and R_2Ni_{17}, the Fermi level is situated somewhere between the top of one of $3d$ sub-band and the first main maximum in the density of states.

(iii) *R*-*M* interaction

The strength of this type of interaction is intermediate between the above two interactions. The spin angular momentum of the *R* atoms is antiparallel to the cobalt moment. However, the net magnetic moment, *J*, of the rare-earth sublattice is coupled ferromagnetically to the magnetization of the cobalt sublattice, in case of a light rare-earth (atomic number less than that of Gd). For a heavy rare-earth, an anti-parallel coupling exists between the rare-earth and cobalt sublattice as in ferrimagnets with characteristic compensation points. The Curie temperature in *R*-*M* compounds is largely determined by the *M*-*M* interaction. The *R*-*M* contribute to a precise correction to Curie temperature and stabilizes the rare-earth anisotropy against thermal excitations.

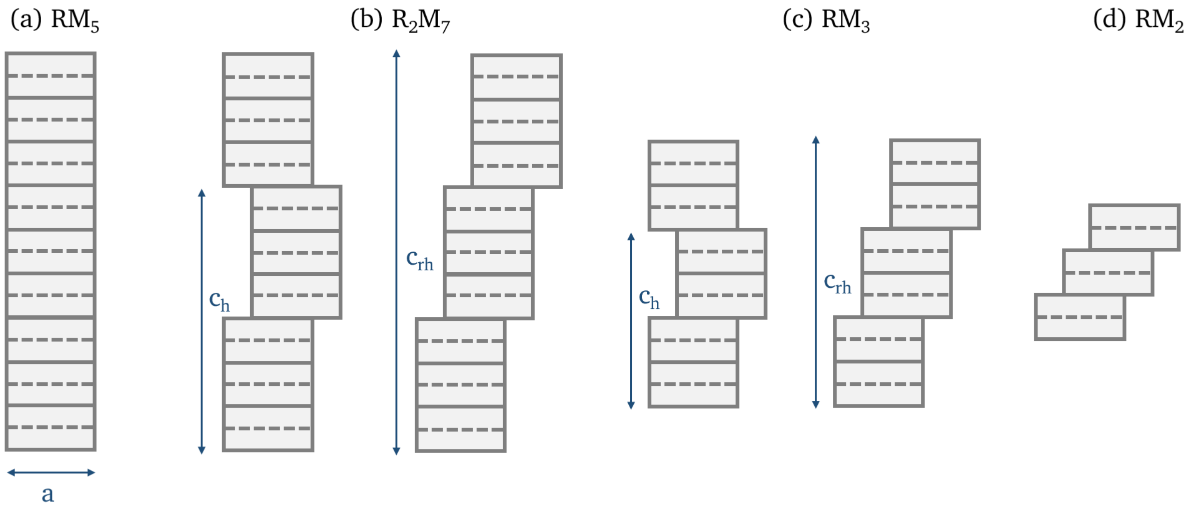

Figure 3.7: Schematic representation of (a) $R\text{M}_5$ unit cells with a and c lattice constants and the different stacking arrangements which lead to the (b) hexagonal and rhombohedral, $R_2\text{M}_7$, (c) hexagonal and rhombohedral, $R\text{M}_3$, and (d) cubic $R\text{M}_2$ structure.

3.3 Origin of magnetocrystalline anisotropy

The $R\text{Co}_5$ compounds are characterized by an extremely large magnetocrystalline anisotropy. The key parameters that contribute to the magnetocrystalline anisotropy are orbital moment of a magnetic ion, spin-orbit interaction, and interactions with the neighboring ions.

The orbital motion of electrons is affected by the spin-orbit coupling and the crystalline environment. The crystalline electric field (CEF) is the potential created at the magnetic ion site by the electric charge distribution in the rest of the crystal. The orbital motion interacts with the crystal lattice through electrostatic field and overlapping wave functions of the neighboring atoms. The spin motion of an electron interacts with its orbital motion via spin-orbit coupling. Thus, the spin-orbit interaction together with the crystalline electric field leads to the alignment of magnetic moment in specific directions in the crystal. The anisotropy of the orbitals can be explained using the following models:

1. Single-ion model

   In localized electron systems, the magnetocrystalline anisotropy arises from electrostatic interaction between asymmetric *d*- or *f*-charge cloud of the moment carrying electrons with the surrounding anisotropic crystalline electric field. The electron orbital preferentially orients with respect to the crystallographic direction that minimizes the CEF interaction energy and results in directional dependence of the energy (magnetocrystalline anisotropy energy) in the crystal field. The crystallographic direction associated with energy minimum determines the direction of easy-axis of magnetization [51, 10].

   The Steven coefficient describes the real shape of the ellipsoidal rare-earth 4*f* orbital. When the rare-earth ion is surrounded by a certain crystalline environment, the tip of the prolate preferentially points in interstitial directions rather than the negatively charged corner atoms [49]. This would determine if the ion has easy-axis anisotropy or easy-plane anisotropy. The single-ion anisotropy

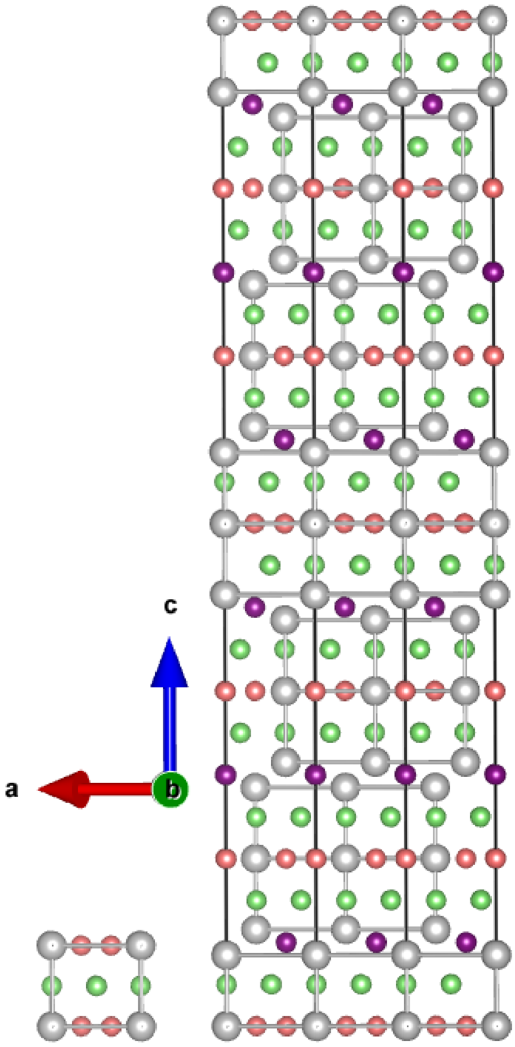

Figure 3.8: Crystal structure of rhombohedral, RCo$_3$, derived from the unit cell of RCo$_5$ with CaCu$_5$ structure. The R at 1a site is shown in grey, Co at 2c site in red, Co at 3g site in green and Co at 2a site of MgZn$_2$ structure in purple.

exists in compounds with lanthanides having localized 4*f*-electrons. The anisotropy of the rare-earth 4*f* orbital is decribed using this model.

2. Two-ion model

   The two-ion model is used to describe the magnetocrystalline anisotropy in light actinide intermetallics in anisotropic covalent bonding. It arises due to the interaction involving the delocalized 5*f*-electron wave functions with the overlapping 5*f* orbitals of the nearest neighbor ions (5*f*-5*f* interaction) and with valence-electron orbital of the ligands (5*f*-ligand hybridization).

In 3*d* transition metal systems such as Fe and Co, the orbital moments are quenched as these delocalized electrons are strongly affected by the local symmetry of the crystal. Thus, the spin-orbit coupling is small and the effective moment for many ions is given by the spin-only formula. The anisotropy of 3*d* systems arise because the electrons try to minimize the energy by adapting to the crystal.

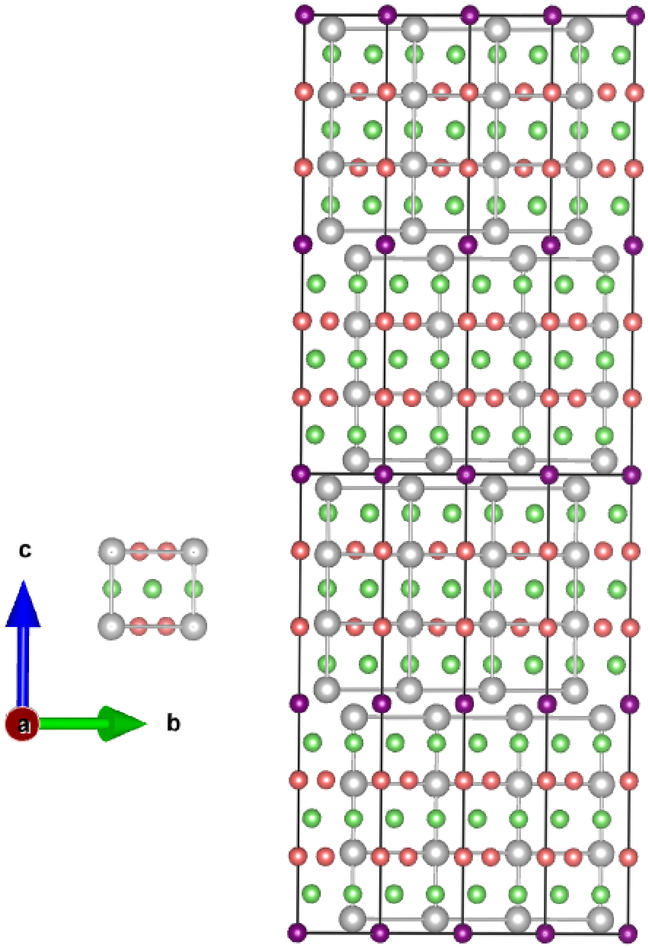

Figure 3.9: Crystal structure of hexagonal, $R_2\mathrm{Co}_7$, derived from the unit cell of $R\mathrm{Co}_5$ with CaCu_5 structure. The R at $1a$ site is shown in grey, Co at $2c$ site in red, Co at $3g$ site of CaCu_5 in green and Co at $2a$ site of MgZn_2 in purple.

The 4*f* shells in the rare-earth ions (R^{+3}) are well-screened from the crystalline environment giving rise to strong orbital moment and spin-orbit coupling. The anisotropy arises because of the effect of crystalline electric field on the 4*f* orbital of the rare-earth.

In *R*-*M* intermetallics, both the rare-earth and transition metal sublattices contribute to the anisotropy. However, 3*d* sublattice contribution is stronger in only *R*-Co compounds. The dominant contribution to the anisotropy is due to 4*f* orbital of the rare-earth. This could explain the large magnetocrystalline anisotropy in $R\mathrm{Co}_5$ compounds with *f* electrons such as SmCo_5 which has the highest magnetocrystalline anisotropy known. However, interestingly, there are no 4*f* electrons in yttrium and yet its anisotropy is more than 50 times larger than the elemental hcp cobalt and one order of magnitude smaller than the isostructural SmCo_5. This underlines the importance of cobalt sublattice to the anisotropy in $R\mathrm{Co}_5$ compounds.

In YCo_5, the dipolar contribution of *R* sublattice is of the same order as that of Co sublattice. The 2*c* and 3*g* cobalt sites give rise to an axial and planar contribution to the magnetocrystallline anisotropy, respectively. Thus, the overall axial anisotropy is the result of an equilibrium between different Co site contributions [52, 53, 54, 55]. Polarized neutron diffraction results on YCo_5 have shown that mainly Co(2*c*)

Table 3.3: Comparison of saturation magnetization, M_s, remanent magnetization, M_r, coercive field, H_c, in perpendicular direction, and first anisotropy constant, K_1, for YCo_5 thin films.

reference	method	buffer	M_s (emu/cm^3)	M_r (emu/cm^3)	H_c (kOe)	K_1 (erg/cm^3)
[59]	DC sputtering	Cu	300	270	5	1×10^7
[60]	MBE	Cu	normalized magnetization		< 1	-

sites contribute to the anisotropy. Based on neutron scattering experiments, Schweizer et al. have reported the existence of unusually large orbital moments on the Co sites in YCo_5 [56] which opens the possibility of a large cobalt orbital magnetic moments being responsible for the large anisotropy [57]. An excess of Co in the form of Co dumbbells at Co(2*c*) site e.g. in Y_2Co_{17}, leads to a reduction in symmetry of the site and thus, a decrease in the anisotropy [49].

The direction of magnetic easy-axis of RCo_5 and R_2Co_{17} compounds show a strong systematic dependence on the type of rare-earth and temperature. For YCo_5 and $CeCo_5$ in which the rare-earth is non-magnetic, an easy *c*-axis is observed for an entire temperature range from 4 K to a temperature slightly exceeding room temperature. In R_2Co_{17} compounds, the competition between the single-ion anisotropy of *R* and the Co sublattice gives rise to either a preferred *c*-axis or an easy-plane anisotropy. The R_2Co_{17} compounds with a magnetic rare-earth such as Sm, Er, Tm and Yb only have an easy-axis anisotropy and the rest exhibit an easy-plane anisotropy [58].

3.4 State-of-the-art thin films

3.4.1 Y-Co thin films

The magnetic properties of YCo_5 thin films have not been well studied so far. There are only few reports on YCo_5 thin films. Kubota *et al.* prepared Y-Co thin films with very low saturation magnetization at room temperature on a Cu underlayer using DC magnetron sputtering [59]. Yamada *et al.* described the preparation of YCo_5 thin films also on Cu buffer layers, however, without discussion of its magnetic properties [60]. The main results of these studies are summarized in Table 3.3.

The influence of the addition of Cu in the YCo_5 bulk alloy on magnetic and structural properties was studied by Téllez-Blanco *et al.* According to their findings, an increasing Cu concentration led to a decreasing saturation magnetization, anisotropy energy, and Curie temperature of the system [61]. These results for Y(Co,Cu) are in contrast to Sm(Co,Cu) alloys where the addition of Cu was found to be advantageous. Thus, in order to explore the intrinsic properties of the YCo_5 phase, it is important to avoid Cu diffusion. In this work, the Y-Co thin films were grown without the use of any buffer layer.

3.4.2 Ce-Co thin films

To our knowledge, the only available literature reports about electrodeposited soft magnetic Ce-Co thin films in which a majority of the deposit was an oxide instead of an alloy and, hence, a comparably low magnetic moment was observed [62]. The crystal structures of rare earth-transition metal alloy films were studied by Ohtake *et al.*, however, their magnetic properties were not described [63]. Apart from that, there are no studies on the structural and magnetic properties of the $CeCo_5$ films. There are few reports on $CeCo_5$ flakes and melt-spun ribbons. Zhang *et al.* prepared $CeCo_5$ flakes with a maximum coercivity of 3.3 kOe by a surfactant-assisted high-energy ball milling process [64]. Lu *et al.* prepared $CeCo_{5.4}$ melt-spun ribbons and obtained a maximum coercivity of 1.4 kOe [65].

3.4.3 Sm-Co thin films

$SmCo_5$ thin films have been extensively studied as compared to other material systems. The thin films exhibiting perpendicular magnetic anisotropy with high magnetic anisotropy energy (K_u greater than 1.2 MJ/m^3) are considered essential for realizing ultra-high density (1 Tb/inch^2) magnetic storage devices [22, 66, 67, 68, 69]. The Sm-Co thin films have also been investigated for various other relevant applications such as micro-electro-mechanical-systems [70, 71, 72], and electromagnetic microactuators [73]. An overview of the growth parameters and magnetic properties of the Sm-Co thin films is provided in Table 3.4. The main observations are summarized below:

1. Different buffer or seed layers such as Cu [66, 74], Ru [75], Cu/Ti [66, 68], Ni-W [76], Cu/Ta [77] and others, were used to promote *c*-axis texture in the $SmCo_5$ films. On the other hand, an in-plane texture of the film was observed with the use of Cr buffered MgO (110) [78].
2. Copper with a face-centered-cubic structure is the most commonly used buffer layer to synthesize $SmCo_5$ thin films with perpendicular anisotropy. The Cu films have a 111 texture which is the closest packed plane and has the lowest surface energy.
3. Cu is known to decrease the crystallization temperature of $SmCo_5$ thin films. It diffuses into $SmCo_5$ layer, substitutes cobalt to form $Sm(Co,Cu)_5$ alloy and increases the stability of $SmCo_5$ phase.
4. To reduce the thickness of Cu buffer layers, additional seed layers such as Ti, Ru, Ta are used. It not only reduces the roughness of Cu layer but also improves the 111 texture [79].

The use of buffer layers alters the intrinsic magnetic properties, e.g. magnetization and anisotropy of the material. It leads to interdiffusion and higher roughness, besides an obvious increased thickness of the overall device structure. In this work, the Sm-Co films have been grown directly on Al_2O_3 substrate without the use of additional buffer layer and yet, we were able to achieve a perfect *c*-axis texture.

Table 3.4: Review of growth parameters and magnetic properties of Sm-Co thin films.

Composition	Deposition Technique	Substrate	Temp. (°C)	Buffer (nm)	M_s (emu/cm^3)	H_c (kOe)	H_a (kOe)	K$_1$ (MJ/m^3)	References
$SmCo_5$	Sputtering	Glass	345	Cu 111 (100)	-	4.5	-	$\perp$	[80]
$Sm_{17.5}Co_{82.5}$	PLD	Al_2O_3	430	Cr (10)	-	11	-	$\perp$	[81]
SmCo	Sputtering and PLD	Si 100	450	Cr (100)	-	20	-	$\parallel$	[82]
$SmCo_5$	Sputtering	Glass	325	Cu 111 (10–500)/ Ti (25)	600	12	> 15	$\perp$	[83]
SmCo	Sputtering	MgO 100, 110	600	Cr 100 (20)	-	30	> 60	$\parallel$	[84]
$SmCo_5$	Sputtering	Si	350	Cu 111/ Ti (1)	600	12	> 50	$\perp$	[85]
$SmCo_5$	Sputtering	Glass	325	Cu 111 (10–500)/ Ti (25)	600	12	> 15	4.0, $\perp$	[66]
Sm_2Co_7, Sm_2Co_{17}	Sputtering	MgO 100	600	W 100 (20)	-	30, 10	> 90	$\parallel$	[86]
$SmCo_5$	PLD	MgO 100	400	Cr 100 (60)	676.41	30	> 90	$\parallel$	[78]
$SmCo_5$	Sputtering	MgO 100	400	Cr 100 (60)	-	17.5	30	$\parallel$	[77]
$SmCo_5$	PLD	Al_2O_3 001	700	Ru 001 (20)	787.82	13.5	> 40	7.6, $\perp$	[75]
$SmCo_5$	Sputtering	-	350	Cu 111 (200)	-	9.6	> 15	$\perp$	[74]
$SmCo_5$	Sputtering	Glass	530	Ni 111/NiW 211/W 110 (20/20/4)	450	15.5	> 20	$\perp$	[76]
$SmCo_5$	Sputtering	Glass	400	Ta 002 /Cu (4/50)	250	18	> 30	$\perp$	[79]

4 Methods

In this chapter, an overview of the experimental methods and techniques used for the synthesis and characterization of the thin films is provided. The *R*-Co films were grown by co-evaporation of elemental rare-earth and cobalt using molecular beam epitaxy (MBE) equipped with in-situ reflection high-energy electron diffraction (RHEED). The X-ray diffraction (XRD) technique for crystallographic structure analysis and the X-ray reflectivity (XRR) measurements for the thickness determination are described. The electronic structure of the films was investigated using X-ray photoelectron spectroscopy (XPS). The magnetic properties of the films were investigated using superconducting quantum interference device (SQUID) and torque magnetometry. Transmission electron microscopy was used (TEM) to study the morphology and atomic structure of the films.

4.1 Molecular beam epitaxy

The term epitaxy refers to the growth of crystalline layer upon (epi) on the surface of crystalline substrate which imposes a crystalline order (taxis) onto the thin film. Molecular beam epitaxy is a physical vapor deposition technique in which molecules or atoms are evaporated onto the substrate under ultra-high vacuum (UHV) conditions [87]. From the kinetic gas theory, the number, n, of gas atoms impinging on a unit area of substrate, in unit time, t, depends on the pressure, P, of the chamber, the atomic mass, m, of the gas atoms and the temperature, T, of the substrate, and can be expressed as

$$\frac{dn}{dt} = \frac{P}{\sqrt{2\pi mkT}} cm^{-2}s^{-1} \tag{4.1}$$

where k is the Boltzmann constant. A schematic of MBE chamber used in this work is shown in Fig. 4.1. It comprises of UHV growth chamber with a base pressure of upto 10^{-9} mbar and load lock (for substrate transfer) separated by a gate valve. A complete schematic of the valve board of the MBE system including the vacuum guages (IG: ion guage, VG: pirani guage) is shown in Fig. 4.2. The growth chamber is equipped with a 25 keV reflection high-energy electron diffraction system allowing in-situ monitoring of the film growth. A cryo shroud surrounding the chamber walls prevents desorption and maintains a low background pressure in the system. The substrate is mounted on an omicron holder using Ag paste and inserted in the manipulator equipped with a SiC heater. The temperature of substrate was calibrated using a special holder with a hole for inserting the thermocouple. The unit is equipped with three electron-beam evaporation sources (Hanks HM^2 single crucible e-Gun, Thermionics), an effusion cell and two rf activated gas radical sources (HD25, Oxford Applied Research). A computer interface using custom LabView program was used to control various parameters during the film growth.

4.1.1 Electron-beam evaporation

The required material to be deposited, in the form of pellets or rods, is placed in water cooled tungsten crucibles. In this work, elemental Y pellets (99.9% purity, Chempur), Co rods (99.95% purity, Kurt

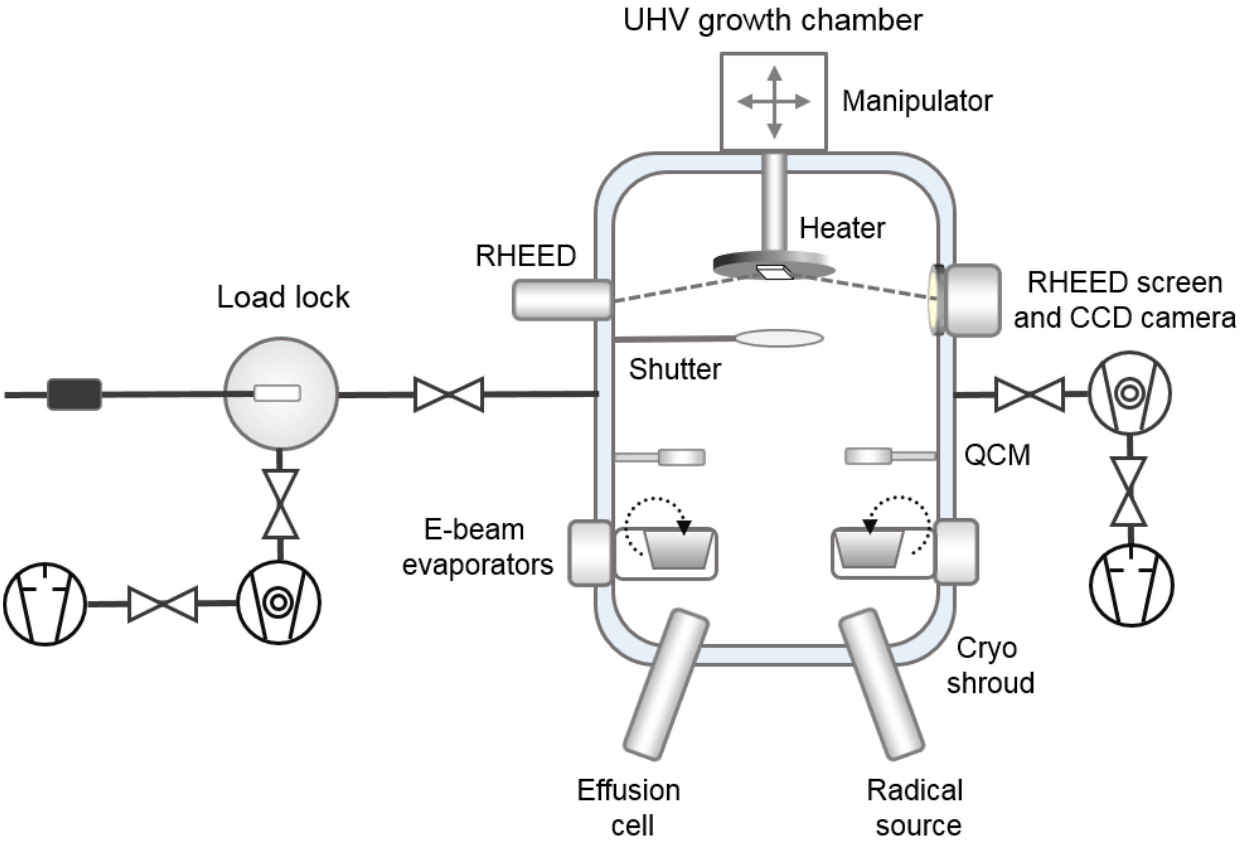
UHV growth chamber
Manipulator
Heater
RHEED
Load lock
RHEED screen
and CCD camera
Shutter
QCM
E-beam
evaporators
Cryo
shroud
Effusion
cell
Radical
source

Figure 4.1: Schematic of molecular beam epitaxy unit used in this work.

J. Lesker), Ce pellets (99.9% purity, Chempur) and Sm pellets (99.9% purity, Kurt J. Lesker) were used which were evaporated using electron beam in the vacuum chamber. As the rare-earth elements are strong oxygen getters, these are stored in hydrocarbon oil. The pellets are cleaned in heptane (or any hydrocarbon solvent) in an ultra-sonic bath multiple times to remove any traces of oil. The W crucibles are cleaned first, in heptane and then, in acetone atleast three times. After cleaning, the crucibles are filled with metal pellets upto 80% volume and then introduced to the vacuum chamber.

Inside the chamber, the beam of electrons is generated by a tungsten filament which is at negative potential (-10 kV) relative to the grounded crucible. The filament, heated by electric current, produces an intense electron cloud by the process of thermionic emission. Because of the high negative potential, the electrons are ejected from the filament and then bent by magnetic field (by 270°) in such a way that the electron beam is focused into the crucible. When the beam encounters the material, there is a discharge of energy (kinetic energy of electrons and thermal energy of filament) which raises the local temperature of the material in excess of 3500°C and evaporates it. To ensure uniform melting across the entire surface of the material, magnetic sweep coils are used to scan the electron beam in mutually perpendicular directions at a maximum frequency of 500 Hz. The evaporation rate of the material is controlled by the power supplied to the filament heater current. A change in the filament heater current modifies its temperature and thus, the emission current of the filament. However, because of the thermal inertia of the filament, there is unavoidable lag in response which could lead to fluctuation in the rate. Depending on the vapor pressure of individual element, fluctuations in the evaporation rate also arise during simultaneous operation of two or more sources.

4.1.2 Growth rate monitoring

To monitor the evaporation rates of the metals and hence, the resulting film thickness during the deposition, a quartz crystal microbalance (QCM) with a rate-deposition controller and a feedback loop is used. The sensor head of QCM is supported by two feedthroughs for cooling water and an electrical contact wire to connect to oscillator. A QCM comprises of a thin wafer of quartz with metal-film (Au) electrodes deposited on both sides. Quartz is a piezoelectric material which oscillates at its natural resonant frequency (5-6 MHz) when an oscillator is connected to it. This resonant frequency decreases when some material is deposited on to it and the resulting shift in frequency is directly proportional to the additional mass. The relation between this shift in frequency, δ_f, and the thickness, d, is given by,

$$d = \frac{\rho_q v_q \delta_f}{2\rho f^2} \tag{4.2}$$

where ρ_q, v_q, and f is the density, velocity of sound and initial resonant frequency of quartz and ρ is the density of the film. The resonant frequency of the QCM can also be affected by the temperature of the operating environment, gas pressure and film stress.

Inside the MBE chamber, there are in total four QCMs, three source QCMs, one above each individual source and one calibration QCM, which is adjacent to the substrate. Before beginning the deposition experiments, it is important to perform calibration in order to ensure accurate monitoring of the thickness. The tooling factor, a parameter in the LabView program, of each source is so adjusted that the thickness measured by the QCM above individual source is the same as that close to the substrate.

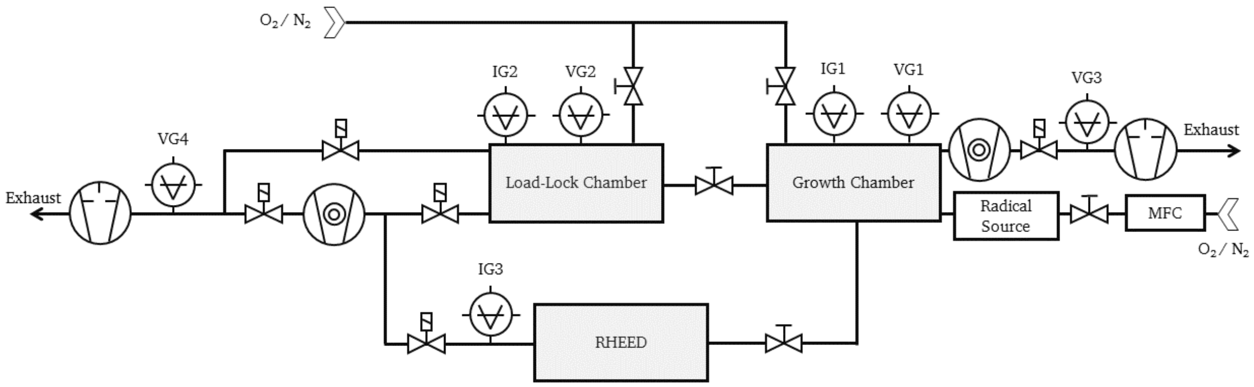

Figure 4.2: Schematic of the valve board of the MBE unit including corresponding vacuum guages, ion guage (IG) and pirani vacuum guage (VG).

4.2 X-ray diffraction

X-rays are electromagnetic radiations which are produced when electrons (or any electrically charged particle) with sufficient kinetic energy are rapidly decelerated on striking a target in an X-ray tube. The emitted radiation is a mixture of different wavelengths with the intensities depending on the accelerating/decelerating voltage. The X-ray spectrum is comprises of sharp peaks, which are characteristic of the target material, superimposed on a broad, continuous part called as the Bremsstrahlung.

Diffraction is a scattering phenomena which occurs when wave motion encounters regularly spaced scattering objects with the spacing of the same magnitude as the wavelength. The wavelength of X-rays, e.g. Cu $K_{\alpha 1}$ is 1.5406 Å, which is of the same order of magnitude as the interatomic distance in crystals. A periodic arrangement of the atoms creates a difference in the path length and thus, a phase difference, of the rays, upon scattering from different planes of the crystal. There will be certain crystallographic directions in which the scattered beam will be completely in-phase and reinforce each other leading to constructive interference. If the electric field vectors of two rays have the same magnitude and direction at the same instant and at any point, these are said to be in-phase and form the diffracted beam. Fig. 4.3(a) shows a set of parallel planes, normal to the plane of the paper and at a distance d apart. A beam of parallel, monochromatic X-rays of wavelength λ is incident on the crystal at an angle θ. There is no path difference for the rays scattered at θ by the atoms within a plane. However, the rays scattered from different planes will be in-phase if the path difference is a whole number of wavelengths, known as the Bragg's law, given by,

$$2d \sin\theta = n\lambda \tag{4.3}$$

where n is the order of reflection and is equal to the number of wavelengths in the path difference between rays scattered by adjacent planes. For fixed values of λ and d, there may be several angles of incidence for which the Bragg's law will be satisfied, corresponding to $n = 1, 2, 3$,..

The position of the atoms in a unit cell affect only the intensity of diffracted beam but not its direction. When an X-ray encounters an electron, the alternating electric field of the X-ray induces an oscillatory motion of the electron about its mean position. Because of the acceleration or deceleration of the electron, an electromagnetic wave is emitted. The process is known as scattering of X-rays where the scattered beam

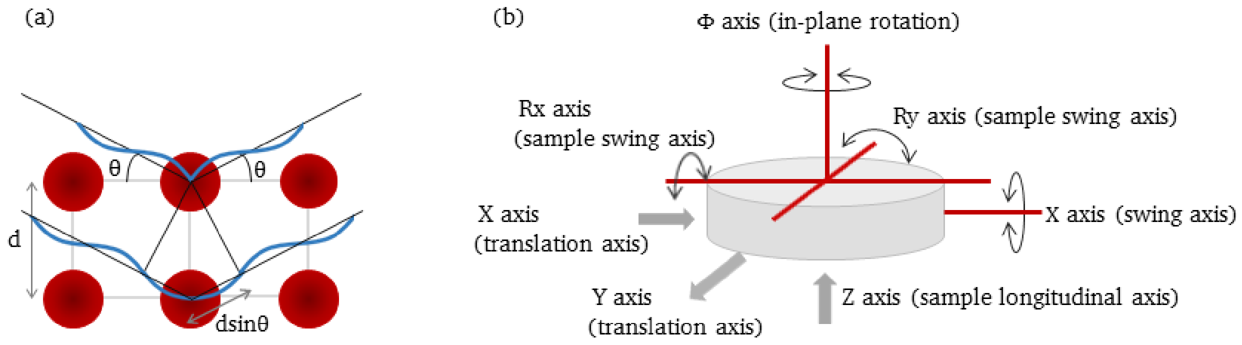

Figure 4.3: (a) The geometric relationship between incident and diffracted X-rays from the atomic planes with a spacing d, representing the Bragg's law. (b) The sample stage of the horizontal sample mount goniometer with all the possible movements along different axes.

refers to the wave radiated by the electron on interaction with incident X-rays. The scattered beam has the same wavelength and frequency as the incident beam with a definite phase relationship and is said to be coherent. The intensity of the scattered beam from the electron depends on the scattering angle. Using the Thomson's equation, the intensity of the scattered beam is found to be only a small fraction of the incident beam and is inversely proportional to the square of the distance from the scattering atom [88].

The electrons are mainly responsible for coherent scattering in an atom as the heavier nucleus does not oscillate to an appreciable extent. The efficiency of scattering of an atom in a given direction is represented by the atomic scattering factor, f, given by,

$$f = \frac{\text{amplitide of wave scattered by an atom}}{\text{amplitude of the wave scattered by one electron}} \tag{4.4}$$

f depends on the atomic number Z of the atoms and inversely on the quantity (sinθ / λ).

When a monochromatic X-ray beam strikes an atom both coherent and incoherent scattering takes place simultaneously in all directions. The coherent scattering, as described above, is caused by the tightly bound electrons while the loosely bound electrons results in incoherent scattering or the Compton effect. The coherently scattered beams from all the atoms in a unit cell reinforce in certain directions to give rise to the diffracted beam.

The resultant wave scattered by all the atoms in a unit cell is called as structure factor, F. For hkl reflection from a unit cell made up of N atoms with fractional coordinates uvw and scattering factor, f, the structure factor is given by,

$$F_{hkl} = \sum_{1}^{N} f_n e^{2\pi i(hu_n + kv_n + lw_n)} \tag{4.5}$$

F is a complex number with the absolute value, | F |, representing the amplitude of the resultant wave scattered by a unit cell, and the square of amplitude, $\mid \mathrm{F} \mid^2$, gives the intensity of the diffracted beam.

$$|F| = \frac{\text{amplitide of wave scattered by all the atoms of a unit cell}}{\text{amplitude of the wave scattered by one electron}} \tag{4.6}$$

The Bragg's law is a simple expression that could explain most of the diffraction effects but not complex phenomena such as diffused scattering at non-Bragg angles. Therefore, the concept of reciprocal lattice was introduced by a German physicist Ewald in 1921. Each point in reciprocal space is related to a set of planes in the crystal and represent the orientation and spacing between these planes using relation,

$$\mathbf{G}_{hkl} = h\mathbf{a}^* + k\mathbf{b}^* + l\mathbf{c}^* \tag{4.7}$$

where the $\mathbf{G}_{hkl}$ is the reciprocal space vector, drawn from the origin of the reciprocal lattice with unit vectors $\mathbf{a}^*$, $\mathbf{b}^*$, $\mathbf{c}^*$ to any point with coordinates hkl, is perpendicular to plane (hkl) in real crystal lattice. The magnitude of the reciprocal space vector is given by the inverse of spacing d of (hkl) planes,

$$G_{hkl} = \frac{1}{d_{hkl}} \tag{4.8}$$

The change in the wavevector, **k**, of the incident and scattered beam is called as the scattering vector. Laue expressed the necessary conditions for elastic scattering or diffraction to take place from a periodic lattice with vectors **a**, **b**, and **c** in terms of Laue's equations, given by,

$$\mathbf{k}.\mathbf{a} = h\lambda \tag{4.9}$$

$$\mathbf{k}.\mathbf{b} = k\lambda \tag{4.10}$$

$$\mathbf{k}.\mathbf{c} = l\lambda \tag{4.11}$$

The diffraction intensity is maximum when all the three conditions are simultaneously met which occurs when $\mathbf{k} = \mathbf{G}$. While Laue used the light optics approach to argue that the phase difference between the waves scattered by adjacent scattering centers is a whole number of wavelength, Bragg proposed that the waves behaved as these are reflected from atomic planes.

The Bragg's condition of diffraction can be expressed geometrically in the reciprocal space by Ewald sphere. It is a graphical construction to visualize the planes that satisfy the Bragg condition. Consider an incident wave vector, $\mathbf{k}_i$, with origin at the center of a sphere of radius $k_i = 1/\lambda$, incident at θ on (hkl). The terminal point of $\mathbf{k}_i$ is taken to be the origin of the reciprocal lattice. For diffraction from (hkl) to occur, a point with coordinates hkl in the reciprocal space lies on the surface of this sphere. The direction of the diffracted vector, $\mathbf{k}_{hkl}$, is given by the line joining the center of the sphere to the point. When this condition is fulfilled, the reciprocal space vector, $\mathbf{G}_{hkl}$, is given by,

$$\mathbf{k}_{hkl} - \mathbf{k}_i = \mathbf{G}_{hkl} = h\mathbf{a}^* + k\mathbf{b}^* + l\mathbf{c}^* \tag{4.12}$$

4.2.1 Diffractometer

A SmartLab X-ray diffractometer from Rigaku together with a control software, SmartLab Guidance, are used for the structural characterization of the films. The diffractometer is known as four-circle as it is equipped with four axes: ω for sample rocking, ϕ for in-plane rotation, χ for tilting and 2θ axis for scanning detector, as shown in Fig. 4.3(b). The SmartLab Guidance software allows an automatic and independent adjustments of all the components [89, 90]. The instrument is composed of the following main parts:

1. X-ray source

   A rotating 9 kW Cu anode with W filament is used to generate X-rays with K_α of 1.5406 Å.

2. Incident optical system

   The incident side of the diffractometer is made up of cross-beam optics (CBO) unit, incident optical unit and incident slit (IS) box. The CBO unit is mechanism for switching between the Bragg-Brentano (BB) parafocusing (for powder sample) and parallel beam (PB) geometry (for a thin film). A paraboloidal synthetic multilayer mirror is used to collimate (divergence of 0.04° vertically) and monochromatize (intensity ratio of K_α to K_β of 1000) a divergent incident beam, emitted from X-ray source. The focus of the X-ray tube is at the focus of the paraboloid with the thickness of each layer so adjusted that the Bragg condition for the incident X-rays is satisfied. Next to the CBO unit, a Ge channel-cut crystal monochromator is used in the incident optics to provide higher monochromatization and collimation (0.02°). In a Ge (220) 2-bounce monochromator, the X-rays incident at Bragg angle for Ge (220) at 22.6°, reflect twice and exit the crystal parallel to the incident beam. To restrict the size of the X-ray beam vertically and horizontally, width-limiting and length-limiting slit are used both at the incident and receiving side. In addition, a soller slit made up of a set of metal foils placed horizontally or vertically at regular intervals is used so as to extract only those X-rays that parallel to the gaps. The angular resolution depends on the intervals of the metal plates.

3. Goniometer

   The mechanical section of the horizontal sample mount X-ray diffractometer comprises of a sample stage as shown in Fig. 4.3(b), an axis for setting the angle of the X-ray source, θ_s, with respect to the sample, a detector axis for setting the angle of the detector, θ_d, with respect to the sample, and a χ cradle with tilt adjustment axes, Rx and Ry, attached to it.

4. Receiving optical system

   The receiving side consists of two receiving slit (RS) units, a soller slit and parallel slit analyzer, PSA, and an attenuator. A channel-cut crystal in the receiving optics, known as analyzer, restricts both the 2θ take-off angle and wavelength to enhance the resolution (0.01°) of the diffraction beam.

5. Detection system

   To measure the X-ray intensities, a scintillation counter is used which can withstand a counting rate of 0.1 cps to 800 thousand cps. For X-ray intensities exceeding detection limit, metallic foils known as attenuator is used to protect the detector. SmartLab is equipped with an automated mode in which the attenuators are automatically switched depending on the intensity.

4.2.2 Measurements

Different types of measurement methods are used to obtain various kinds of information about thin film sample as described below:

Out-of-plane, $2\theta - \theta$, measurement

To obtain information about the lattice planes that are parallel to the sample surface, $2\theta - \omega$ measurements are carried out while maintaining a fixed relation between the diffraction angle, 2θ and the incident angle, ω, $2\theta = 2\omega$. This type of measurement geometry is also known as symmetrical reflection method [91]. The measurement of sample in the diffractometer involves first aligning the sample using: (a) direct beam half-cut, and (b) surface normal alignment.

In the direct beam half-cut alignment, the 2θ-axis is set to 0° and the Z-axis is retracted to the bottom in order to measure entirely the intensity of the direct beam. Then, the Z-axis is scanned (-2.0 mm to -1.4 mm) and so adjusted at a position at which the incident X-ray intensity is halved. Then, the ω axis is scanned ($\pm 1^\circ$, absolute) and so adjusted to obtain maximum intensity of the alignment beam. The above two scans of the Z and ω axes are repeated three times to ensure that the sample surface and incident X-ray beam are parallel. In the surface normal alignment, the 2θ-axis is set to scattering angle of the substrate (41.67° for 0006 Al_2O_3) and then, a relative scan of Z-axis (± 0.2 mm) and ω-axis (($\pm 0.8^\circ$,) is carried out near the scattering angle of the substrate.

After aligning the sample, the general measurement is carried out. For high resolution, a Ge (220) 2-bounce monochromator, an open soller slit at the incident side and a soller slit of 5° at receiving side is used. For medium resolution, a soller slit of 5° is used at the incident and receiving side in addition to graphite monochromator. A width limiting slit of 2 mm is inserted at the incident side and height limiting slits are set to IS at 0.8 mm, RS1 at 1.2 mm and RS2, at 2 mm by the SmartLab Guidance software.

Rocking-curve, ω-scan

The information about preferred orientation or texture of the film can be quantitatively determined using a rocking-curve measurement. The detector is fixed at the diffraction angle, 2θ, of the reflection to be investigated and then ω is scanned $\pm 5^\circ$ relative to that peak. The distribution of preferred orientation is obtained from the full width at half maximum (FWHM) of the peak.

X-ray reflectivity measurement

The information about the thickness, roughness and density of the surface as well as different interfaces in the sample can be derived from an X-ray reflectivity profile. When the X-rays are incident at a grazing angle, ω, less than the critical angle, θ_C, total internal reflection occurs. The critical angle depends on the electron density or the refractive index, n, of the material, and is given by the relation,

$$\theta_C = \sqrt{2\delta} \tag{4.13}$$

$$n = 1 - \delta - i\beta \tag{4.14}$$

where δ is the dispersion and depends on the wavelength of the X-rays and the density of the film, and β is related to the X-ray absorption.

In case of a thin film deposited on a substrate, the X-rays reflected from the film-substrate interface and the film-atmosphere interface, interfere constructively or destructively. The interference pattern is visible as oscillations in the reflectivity profile, and are known as Kiessig fringes. The analysis (or fitting) of the oscillations using RCRefSim simulation software can yield different types of information. The period of the oscillation is inversely proportional to the film thickness. The density of the film is given by the amplitude as well as the critical angle for total internal reflection. The slope of the reflectivity profile is dependent on the surface or interface roughness. In case of a rough interface, a gradually varying electron density results in a rapid decrease of reflected X-rays [92].

For measuring a reflectivity profile, the sample alignment requires a fine tuning of the halving adjustment not only in direct beam but also in the total reflection range. The direct-beam half cut alignment is carried out as in $2\theta - \theta$ measurement as described before. For the surface normal alignment, the scattering angle is fixed at 0.5°, which is smaller than the critical angle. In this way, the surface of the sample behaves as a mirror and total internal reflection occurs.

In-plane measurements

To access the planes that are not parallel to the sample surface, in-plane measurements are performed by scanning the χ cradle in addition to the $2\theta - \theta$ axes. The normal to sample surface is aligned with ϕ rotation axis using Rx and Ry tilt-axes to avoid a precession motion of the scattering vector [93].

In order to determine the epitaxial relations, ϕ scans of the diffraction peak of the film with respect to the substrate is performed. It is important that the reflex has an in-plane component so as to monitor the change in scattering vector depending on the symmetry of the crystal structures and as well as the arrangement of lattice of the film on top of the substrate.

Pole-figure measurements

The pole figure measurement expresses the preferred crystallographic orientation of a material made up of small crystallites. The orientation of a plane in a crystal can be represented by a plane normal from a point in the crystal. If the center of a reference sphere is located at this point, then the plane normal intercept the surface of sphere to form a pole. The sphere with its poles can be projected onto a plane while maintaining the angular relationship among the pole position. Such a two-dimensional representation of the poles at the sphere on to a plane is called as pole figure.

In these measurements, the diffraction intensity distributions are measured by rotating the sample in all the directions while keeping the diffraction angle, 2θ, fixed. The pole figure axes, α corresponding to χ is scanned from 0° to 90°, and β corresponding to ϕ is scanned from 0° to 360°. The position of each pole on a stereographic projection plane is defined by χ and ϕ.

4.3 Reflection high-energy electron diffraction

The wave nature of a beam of electrons was first theoretically predicted by de Broglie in 1924 and experimentally observed by Davisson and Germer in 1927. A stream of electrons are diffracted by a periodic arrangement of scattering centers in a crystal in accordance with the Bragg's law. In the electron diffraction techniques, the wave nature of electrons is utilized to obtain information about the crystal. Depending on the energy, E, of the incident electron beam, there are three main characterization techniques: (a) low energy-electron diffraction (LEED) with $10\,\mathrm{eV} < \mathrm{E} < 300\,\mathrm{eV}$, (b) reflection high-energy electron diffraction (RHEED) with $10\,\mathrm{keV} < \mathrm{E} < 30\,\mathrm{keV}$ and (c) transmission electron microscopy (TEM) and diffraction with $120\,\mathrm{keV} < \mathrm{E} < 300$ keV. As the electrons are less penetrating than the X-rays, the transmission pattern can originate from thin specimens and the reflection patterns result from only the surface layer of the specimen.

In this section, the basic principle and working of RHEED is described. The MBE set up is equipped with an in-situ 30 kV RHEED gun with a base pressure of 10^{-8} mbar. The electron beam is incident at glancing angle of few degrees to the substrate. The diffraction pattern is recorded on a phosphor screen and is digitally captured by charge-coupled device (CCD) camera. The shape of the diffraction spots can be used to determine the surface structure. As the electrons are easily absorbed in air, the electron-beam source , the substrate and the detector, all are enclosed in high-vacuum.

A crystal is made up of a periodic arrangement of atoms with electron charge distributions around the ion core. In electron diffraction, the incident electron interacts with the periodic potential field which depends on the charge density. The strength of this electrostatic interaction is orders of magnitude stronger than that of the X-ray with a crystal. RHEED involves strong interaction of electrons with periodic potential of the lattice and can, therefore, not be described quantitatively by kinematic scattering theory where only single elastic scattering is assumed. However, for physical and qualitative description of RHEED, kinematic approach is commonly used. The amplitude of the wave vector, k_i, for the incident electrons with energy, E_{kin}, is estimated using

$$k_i = \frac{1}{\hbar}\sqrt{2m_0 E_{kin} + \frac{E_{kin}^2}{c^2}} \tag{4.15}$$

where m_0 is the rest mass of electron and c is the speed of light. At low angles of incidence, the surface normal component of incident wave vector is small and the diffraction occurs from the two-dimensional surface layer on the substrate. The reciprocal lattice depends only on the shape and size of the unit cell of the crystal lattice. As a result, the reciprocal lattice is a set of one-dimensional streaks, also called as truncation rods, perpendicular to the surface [94].

The diffraction condition is satisfied for the scattered wavevectors, $\mathbf{k}$, connecting the origin of $\mathbf{k}_i$ and reciprocal lattice rod in the Ewald sphere of radius $1/\lambda$. The Ewald sphere intercepts a sheet of reciprocal lattice rods in the form of rings called as the Laue zones. For clean and atomically flat, single crystalline substrate the diffraction spots lie on these concentric circles. Diffraction spots lying on zero$^{\mathrm{th}}$-order Laue circle refer to intersection of $(0k)$ rods with Ewald sphere.

The intensity of a diffraction spot is affected with Kikuchi lines which originate from the inelastically scattered electrons. The Kikuchi patterns, however, can be used to track the orientation of a crystal structure in space. These can be thought of as to be originated from point source of electrons within the diffracting medium. Kikuchi developed a 'two-event model 'to interpret the existence of these parallel line pairs. In this model, the incoming collimated and mono-energetic beam of electrons are diffused into the crystal, thus, creating sources of electrons traveling in multiple directions. These diffused electrons then undergo Bragg diffraction from the planes in the material [95].

The intensity oscillations of the specular or the primary beam can be used to monitor the thickness of the growing film. The intensity of the scattered beam from an initial atomically flat surface decreases with nucleation of the islands and rises again as these islands grow and coalesce to form a smooth layer again. Ideally, the oscillation period corresponds to the deposition of one crystal layer.

4.4 X-ray photoelectron spectroscopy

XPS is a surface sensitive technique in which soft X-rays with photon energy of 0.25 - 2 keV are absorbed by an atom, leading to its ionization and emission of a core electron. While the process of ionization by the X-ray photons take place from a depth of few micrometer, only the electrons originating from about 7-8 nm are emitted without energy loss. These emitted electrons produce photoemission peaks while the electrons that lose energy in inelastic process form the background. The emitted electrons are detected by a spectrometer according to their kinetic energy. Only those electrons with energy range within the pass energy can enter the analyzer.

When a photon of energy $h\nu$ interacts with an electron with binding energy, E_b, the entire photon energy is transferred to the electron and as result, it is ejected with kinetic energy, E_{kin}, given by,

$$E_{kin} = h\nu - E_b - \phi_s \tag{4.16}$$

where ϕ_s is the work function of spectrophotometer. The process of photoemission is shown in Fig. 4.4(b). An incident photon of energy $h\nu$, ejects photoelectron from $1s$ or K shell and leaves behind a hole in the shell. There are various electronic transitions that can occur after creation of hole. An electron from higher energy shell (L_1) fills this hole in K shell and either emits energy, $E_{L1} - E_K$, as characteristic X-ray, or it is sufficient to excite and emit higher energy electron, L_{23}, by the Auger process as shown in Fig. 4.4(a). The process is characterized by appearance of Auger line, KL_1L_{23}, which indicates that the initial vacancy is created in the K shell and a double vacancy in the L shells.

Each element has its characteristic spectrum which is a plot of number or count of electrons per second versus the kinetic energy [96]. The energy of the photoemitted electron is a representation of the difference between the initial or ground state and the final state configuration which may contain contributions from highly excited states. The valence-band photoemission spectra provides the density of states (DOS) modified by photoionization cross sections. The core-level spectra gives information on the charge transfers involved in chemical bondings from the measurement of peak positions and the chemical shifts. The quantification is performed from the peak areas. However, determining chemical shifts from observed spectra is not straightforward owing to final-state effects of photoemission involving f orbitals which complicate core-level spectra of lathanides.

Besides the photoemission process, the core-level spectra of metals is modified by various electron interactions. The scattering of the conduction electrons by the hole gives rise to asymmetry in the photoemission peak. Multiple plasmon, extrinsic and intrinsic, excitations also result in additional peaks in the photoemission spectra. Extrinsic plasmon is produced by a quantized energy loss because of the coupling of the electric field of a photoelectron with the electron density fluctuations from the site of excitation through

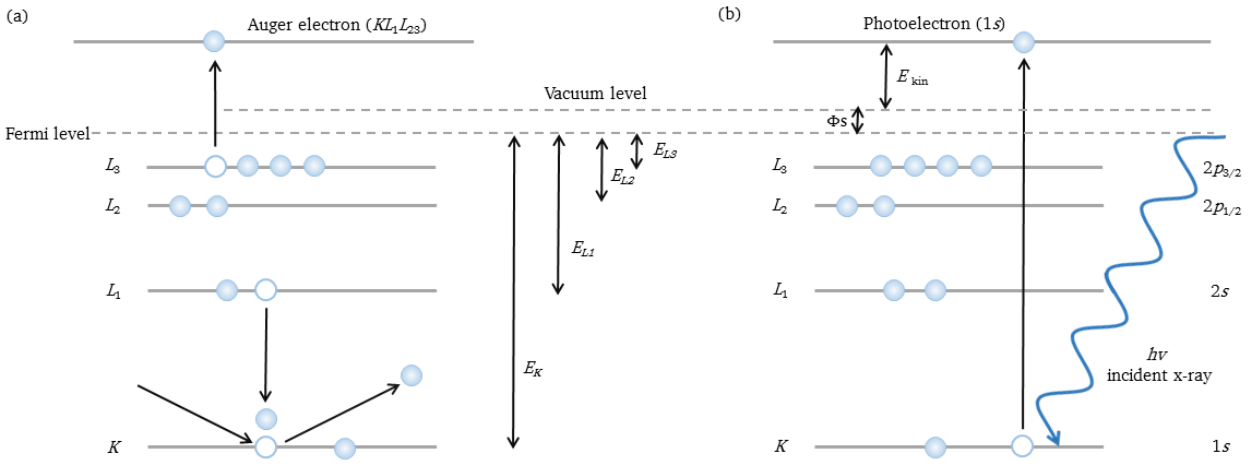

Figure 4.4: Schematic of electron emission processes in solids: (a) Auger process (b) photoemission process, upon irradiation with an X-ray photon.

the solid to the surface [97, 98]. Intrinsic plasmons result from the coupling of the core hole with the conduction electron gas at the instant of photoionization process. The intrinsic plasmon excitations appear in intrinsic or primary electron emission spectrum together with the main peak and its asymmetric tail. The photoelectrons which experienced extrinsic energy loss processes, including the extrinsic plasmon excitations, belong in an XPS spectrum to the background of inelastically scattered electrons.

Multiplet splitting arises when a core hole vacancy, created by photoemission from an s or p orbital, interacts with an unpaired valence electron. When a core hole is produced by the incident photon, the outer electron system is perturbed by the core-hole charge and screens it. Thus, the core hole induces a dielectric as well as magnetic response of the outer electron system [99].

In this work, the XPS measurements were performed with focused, monochromatic Al-K_α radiation with energy of 1486.6 eV using a PHI Versaprobe 5000 spectrometer. In addition, PULSE system Dynamic XPS measurement facility at SIGMA Surface Science GmbH, Germany, was utilized.

4.5 SQUID magnetometery

A Magnetic Property Measurement System (MPMS) from Quantum Design was used to measure the magnetic properties of the thin film samples in this work. It is equipped with superconducting quantum interference device (SQUID) which is the one of the most sensitive magnetic flux detector. The functioning of SQUID is based on two important physical phenomena: superconductivity and Josephson effect.

Superconductivity

Superconducting materials undergo a phase transition when cooled below a certain temperature in which these are characterized by zero resistance. The superconducting state is an ordered state of conduction electrons of the metal. According to the Bardeen-Cooper-Schrieffer (BCS) theory, phonon exchange between the electrons causes them to condense into weakly bound pairs (Cooper pairs) that can travel

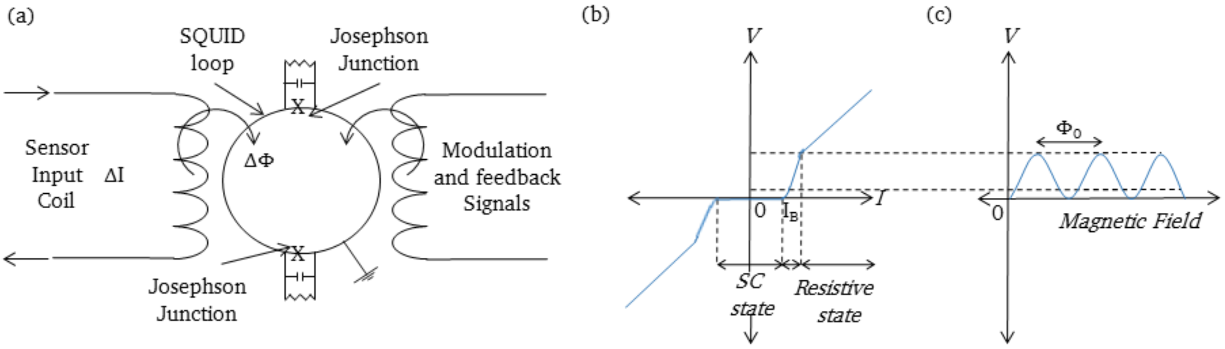

Figure 4.5: (a) Schematic of a DC SQUID. (b) $I - V$ curve showing the bias current (I$_B$) that puts the operational point midway between the superconducting (SC) and resistive regions. (c) Periodic change in voltage with externally applied flux at a constant bias current.

without scattering. The electrons in cooper pairs can be depaired by thermal (critical temperature), kinetic (critical current density) or magnetic (critical field) interactions. The transition temperature ranges from 92 K for $YBa_2Cu_3O_{6.9}$ to below 0.001 K for Rh. When a superconductor, placed in a constant magnetic field, is cooled down to below its transition temperature, the magnetic field lines are ejected from its interior. This phenomenon is known as Meissner Effect. If the superconducting material forms a ring, the flux ($\Phi = \int BdA$) interior to the ring is trapped. This flux is quantized and exists only in multiples of flux quantum ($\Phi_0 = 2.068 \times 10^{-15} T/m^2$). If the magnetic field is then turned off, a current is induced in the ring which keeps the flux inside constant. This current will continue to circulate as long as the ring is below its critical temperature.

Josephson effect

B.D. Josephson predicted that Cooper pairs can tunnel through a thin resistive barrier with no voltage drop from one superconducting region to the other [100, 101]. In DC Josephson effect, a DC current flows in the absence of any electric or magnetic field. In AC Josephson effect, a DC voltage applied across the junction causes RF current oscillations across the junction. Further, an RF voltage applied with DC voltage can cause a DC current to flow across the junction.

When a DC magnetic field is applied through a superconducting circuit containing two junctions, the supercurrent shows interference effects as a function of magnetic field intensity. This effect is an example of macroscopic long range quantum-interference which is used in SQUID magnetometer. A DC SQUID uses two Josephson junctions as compared to one in RF SQUID and is biased with a DC current [102].

4.5.1 Magnetometer

The SQUID magnetometer is made up of the following four main components:

1. Superconducting magnet

The magnet is in the form of a solenoid of a superconducting loop to generate large magnetic fields (upto 6 T). It is charged by a specific current and then operated in the persistent mode without any external power supply.

2. Superconducting detection or pick-up coils

   The magnetic moment of the sample is measured by moving it through the pick-up coils and measuring the local changes in the magnetic flux density produced. The pick-up coils are located at the center of the superconducting magnet but outside the sample space. These are wound in a set of three coils configured as second-order gradiometer with total length of approximately 3 cm. The upper coil (compensation coil) is a single turn wound clockwise, the center coil (signal coil) consists of two turns wound anti-clockwise, and the bottom (compensation coil) wound clockwise. The gradiometer measures the difference in the field ($\delta^2 B_z/\delta z^2$) between the signal coils and the compensation coils. The current induced by homogeneous magnetic field from a distant source are canceled out, whereas an inhomogeneous field will create different current in each coil, thus, making it sensitive to magnetic sample which is closer to pick-up coils than the compensation coils.

3. SQUID sensor

   A SQUID sensor is connected to the detection coil. It is based on the Josephson effect explained above. The schematic of a typical DC SQUID is shown in Fig. 4.5(a) where the input, feedback, and modulation coils are inductively coupled to the SQUID loop. It is biased with a dc current approximately equal to twice of critical current and develops a dc voltage across the junction [103]. This value of bias current puts the operational point between the superconducting and resistive regions in the I-V curve as shown in Fig. 4.5(b). At a fixed value of bias current, when an external magnetic flux is coupled into the SQUID loop, the voltage drop across the Josephson junctions will change. A change in the magnetic flux induces a wave function phase change that enhances the current through one Josephson junction and reduces the current through the other. As the external flux increases (or decreases), the voltage will change in a periodic manner with a period of Φ_0 as shown in Fig. 4.5(c). By monitoring the change in the voltage, the magnetic flux that was coupled to the SQUID loop can be determined. This periodic voltage is used to provide a feedback current that locks the SQUID at a unique point in the $V - \Phi$ curve. This current reflects the changes in flux applied to the SQUID. The SQUID, therefore, acts as a magnetic flux to voltage converter.

4. Superconducting magnetic shield

   It is a volume of low magnetic field around the SQUID that traps and stabilizes the ambient magnetic field.

4.5.2 Measurements

The MPMS is equipped with a MultiVu application software as an interface to control the hardware parameters. The magnetization and hysteresis curves were measured at temperatures from 5 K to 300 K. A clear plastic drinking straw with a low magnetic susceptibility (9×10^{-9} emu) is used to position and hold the sample. For in-plane measurements, a narrow straw is folded along its long-axis and the thin-film is placed, standing straight on its edge, parallel to length of the straw. This sample containing straw is inserted inside another straw gently such that the sample is in middle of the outer straw. For out-of-plane measurements, a larger straw is used and V-shaped grooves are cut. The thin-film sample is placed in such a way that it rests flat horizontally between the two capsules held by the grooves. Centering plugs or adapters are inserted at both ends of the straw to attach to the sample rod.

The position of the sample is adjusted such that it is at the center of SQUID pick-up coils. Otherwise, only a part of the magnetic moment is detected by the coils. Both DC and RSO measurements can be used to center the sample. The RSO centering is faster, higher sensitivity and is less susceptible to base-line drift. In DC centering, the full length of the sample transport vertical path is scanned. The steps involved in the DC centering are:

1. Initialize transport

   In this step, the RSO sample transport is initialized by first lowering it to the lower-travel-limit switch (zero position) and then raised to any position above this switch. The sample is placed far below the SQUID pick-up coils so that these do not detect any moment. At this position the transport can begin the sample centering.

2. Full DC scan

   The entire length (12.0 cm) of the transport motion is scanned while measuring 64 data points. Then a voltage response is generated by the SQUID when the sample is moved through the pick-up coils [104]. DC centering scan uses the scan length specified in the Set parameters tab. For example, if the scan length is set at 4 cm, the graph will display the range from 0 to 4 cm and will be centered at 2 cm. The signal from the sample may not show on the screen if the sample is not within few cm of being centered. In the centering scan, the sample transport moves up and down through the pick-up coils three times, while oscillating the sample around the center of the coils. The sample is centered when the peak of the large, middle curve is within 0.05 cm of the half way point of the scan length.

3. Adjust sample position

   It is used to more accurately center the sample if it is not within 0.05 cm of being centered within the scan.

After the sample is well centered, the sequence for measuring the magnetic moment of the sample can be started. While measuring the hysteresis curve, the hysteresis charging mode of the magnet in which the solenoid remains under constant power from the dc magnet supply. As a result the magnetic field is rapidly changed without taking the time to turn the magnet persistent heater on and off while making the measurements. In this case, the actual field is slightly different than the set field. In the no overshoot or oscillate charging mode, there is an iteration process in which the system tries to precisely set the field. The measurement of magnetic moment is performed using reciprocating sample option in which the sample is moved rapidly and sinusoidally through the SQUID pick-up coils. This sample transport is driven by servo motor that does not stop the sample movement for each data reading. A shaft encoder on the servo motor tracks the position of the sample and is recorded synchronous to the acquisition of the SQUID signal.

4.6 Torque magnetometery

The physical property measurement system (PPMS) from Quantum Design is equipped with a magnetic torque measurement option. In these measurements, a plot of the torque required to rotate the saturation magnetization away from an easy direction is obtained as a function of the angle of rotation. In the simplest case of a uniaxial crystal, such as a hexagonal crystal, the anisotropy energy can be expressed as,

$$E = K_1 sin^2\theta \tag{4.17}$$

where θ is the angle between the saturation magnetization and the easy *c*-axis. If the applied field is strong enough, the magnetization will be parallel to the field, and the angle θ is the same as that between the field and the *c*-axis. As the crystal is rotated, a torque, *L*, is exerted by the saturation magnetization, per unit volume of the crystal and is given by,

$$L = -\frac{dE}{d\theta} = -K_1 sin(2\theta) \tag{4.18}$$

According to the above equations, for positive K_1, at θ equal to 0° and 180°, the energy is minimum, corresponding to direction of easy-magnetization while at 90°, the energy is maximum corresponding to hard-axis of magnetization. The first anisotropy constant, K_1, is given by the amplitude of the measured torque curve. The above analysis is valid only if the field is strong enough so that the magnetization is aligned with the field for all angles of rotation. The shape, polarity and periodicity of the torque curve depends on the anisotropy of the sample. The Fourier analysis of experimental torque curve can reveal various contributions to the observed torque.

In the torque magnetometer, the thin film sample is mounted on a silicon, microfabricated, torque-lever chip, as shown in Fig. 4.6. Continuous piezoresistors are patterned on the legs of the torque lever in the region of high stress [105]. The torsion or twisting of the torque lever about its symmetry axis is measured using these piezoresistors. When a torque is exerted on the sample, there is a change in the resistance, which is measured by a Wheatstone bridge integrated on the chip. The sample size is limited to $1.5 \times 1.5 \times 0.5$ mm^3 and the maximum weight to 10 mg. A maximum torque of 5×10^{-5} Nm can be measured using this technique.

For the evaluation of torque curve measured for a thin film sample, different energy contributions need to be considered, the magnetocrystalline anisotropy, the shape anisotropy and the magnetostatic energy [106]. The intrinsic magnetocrystalline anisotropy energy for a hexagonal crystal is expressed by,

$$\frac{E_k}{V} = K_1 sin^2\theta + K_2 sin^4\theta \tag{4.19}$$

where K_1 and K_2 are the first and second-order anisotropy constants, θ is angle between saturation magnetization and the *c*-axis, which is normal to the film plane. The shape anisotropy energy, E_s, is given by

$$\frac{E_s}{V} = -2\pi M_s^2 sin^2\theta \tag{4.20}$$

Which has the opposite sign as the uniaxial anisotropy. The magnetostatic energy due to angle, α, between the field and magnetization direction is given by

$$\frac{E_{MH}}{V} = M_s H cos(\alpha - \theta) \tag{4.21}$$

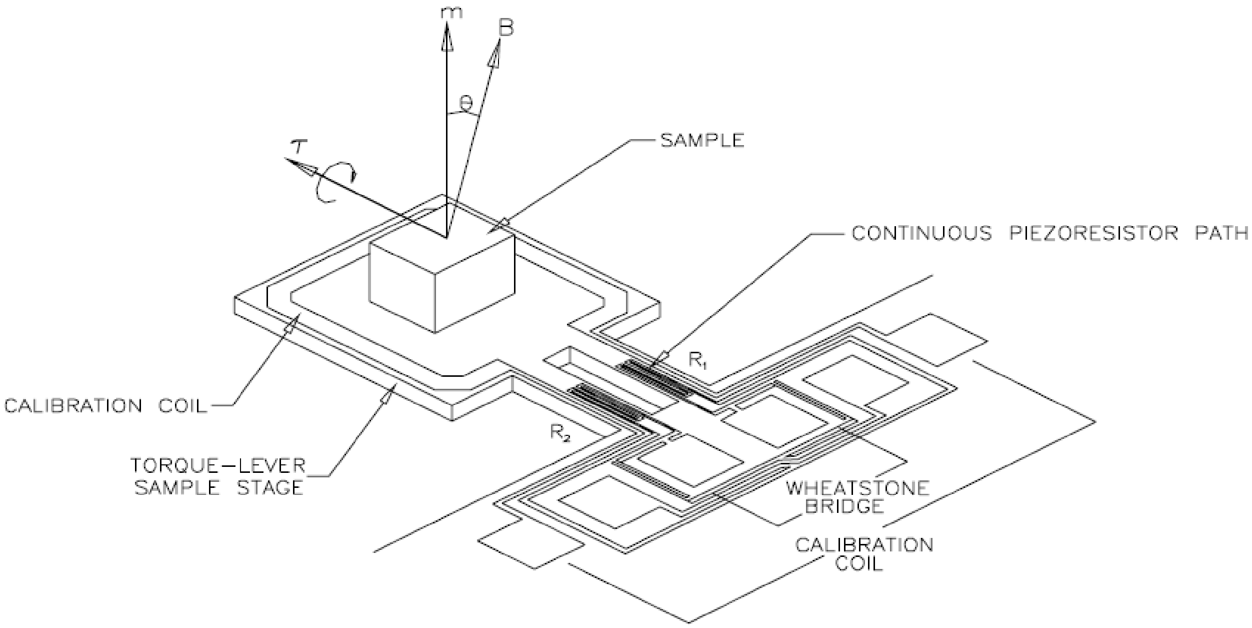
m
B
θ
τ
SAMPLE
CONTINUOUS PIEZORESISTOR PATH
R₁
R₂
CALIBRATION COIL
TORQUE–LEVER SAMPLE STAGE
WHEATSTONE BRIDGE
CALIBRATION COIL

Figure 4.6: A schematic of torque-lever-chip used to measure magnetic torque. Image taken from Quantum Design PPMS torque magnetometer option user's manual [105].

The total energy, E_t, is given by the sum of these contributions,

$$\frac{E_t}{V} = M_s H cos(\alpha - \theta) + (K_1 - 2\pi M_s^2) sin^2\theta + K_2 sin^4\theta \tag{4.22}$$

On differentiating the total energy with respect to θ, the torque per unit volume is given by,

$$\frac{L}{V} = A\sin(2\theta) + B\sin(4\theta) \tag{4.23}$$

$$A = K_1 + K_2 - 2\pi M_s^2 \tag{4.24}$$

$$B = -\frac{1}{2}K_2 \tag{4.25}$$

The coefficients A and B are found by fitting the torque curve to the Fourier expansion series where, A and B are the first-and second-order Fourier coefficients of sine-like torque curve, $L = f(2\theta)$. The applied field must be higher than the anisotropy field in order to force the magnetization in the field direction. As it is not possible to achieve higher fields in the laboratory, the coefficients obtained at different field are extrapolated to infinite field ($1/H = 0$). The above described analysis is used for determining the first and second-order anisotropy constants of the $R\text{Co}_5$ thin films investigated in this work.

4.7 Transmission electron microscopy

In an electron microscope, electrons are used to form an image of the object as visible light in an optical microscope. The resolution of visible-light microscope, according to Rayleigh criteria, is proportional to the wavelength. The smallest distance that can be resolved using visible light is a few hundred nanometers. The de Broglie wavelength of the electrons, λ, with kinetic energy, E, given by,

$$\lambda = \frac{1.22}{\sqrt{E}} \tag{4.26}$$

is of the order of few picometer for electrons with 200 keV. This shows that an atomic scale resolution is possible using electrons as probe. The incident electrons are scattered through different processes within matter giving rise to different types of signals depending on the depth and volume of interaction, as shown in Fig. 4.7. In transmission electron microscopy, the forward scattered electrons from a thin lamella are used to obtain structural and chemical information as well as morphology of the sample. In spherical aberration corrected (C_s-corrected) scanning transmission electron microscopy (STEM), a convergent electron beam is scanned on to the surface which enables atomic resolution imaging.

The incident beam of electrons is created by the Schottky process in which the electrons are emitted from a W filament which has a lowered work function due to the formation of Schottky barrier. The incoming electrons are scattered by both, electrons and nuclei, in the material which changes the spatial and angular distribution of the emerging electrons. Coulombic electron-electron electrostatic interactions with the local electron density result in low-angle scattering, while electron-nucleus interaction lead to high-angle scattering analogous to the Rutherford experiment. The scattering at low-angle can be described by considering the wave nature of electrons in which the atomic-scattering factor depends on the wavelength of electrons, λ, scattering angle, θ, and the atomic number, Z.

The image is formed either by direct electrons transmitted through the sample or the electrons scattered from the sample at an angle. Accordingly, there are following two main forms of amplitude contrast used: bright-field (BF) or dark-field (DF) depending on the type of electrons used for imaging, direct or scattered, respectively. Bright and dark refers to the number of electrons hitting the screen or the detector, for example vacuum transmits all electron in the direct beam, thus it appears bright in bright-field imaging. In TEM mode, the direct or scattered electrons are selected using objective aperture while in the STEM mode, it is done by inserting a BF on-axis or an annular DF (ADF) detector in the respective angular detection range of the reciprocal space. The TEM and STEM modes of operation for the formation of BF and DF images are shown in Fig. 4.8.

In BF STEM mode, the BF detector is inserted onto the optical axis of the microscope and it intercepts the direct-beam electrons (semi-angle of detection, θ = 0 - 10 mrad) independent of the position where the beam is scanning the specimen. The dark field image is formed by collecting the scattered electrons on ADF detector surrounding the BF detector (θ = 10 - 90 mrad). Another annular detector around ADF - or by virtually changing the camera length - collects the electons scattered at even higher angles (θ > 90 mrad), can be used in which the Rutherford scattering effects are maximized and diffraction-contrast are smoothed out [107]. In such high-angle annular dark field (HAADF) or the Z-contrast atomic resolution can be achieved. HAADF images are a direct representation of atomic density variation in the sample, whereas HRTEM images require phase reconstruction techniques in order to correlate the recorded contrast to atomic positions.

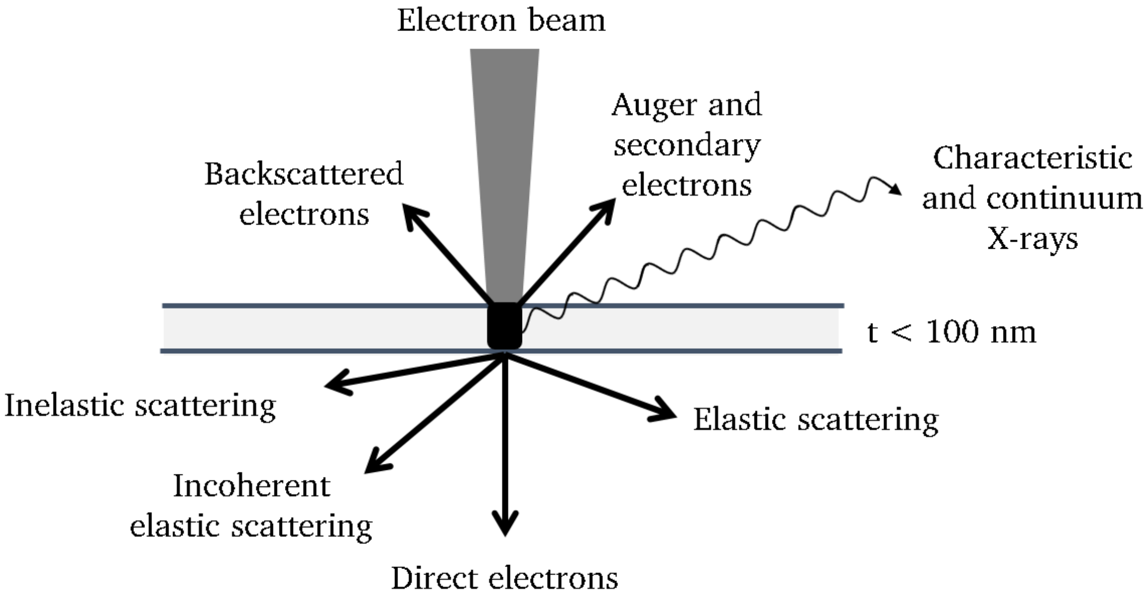
Electron beam
Auger and secondary electrons
Backscattered electrons
Characteristic and continuum X-rays
t < 100 nm
Inelastic scattering
Elastic scattering
Incoherent elastic scattering
Direct electrons

Figure 4.7: A schematic showing the different types of interactions of electrons with a thin sample.

In both bright- and dark-field images, the amplitude contrast always results from a variation in mass and/or thickness and diffraction as described in the following.

1. Mass-thickness contrast

   The electrons transmitted through the sample are scattered off-axis by elastic nuclear interactions known as Rutherford scattering. The Rutherford cross-section or probability of scattering depends on the electron beam energy, scattering angle, θ, and the atomic number, Z. It results in areas of the specimen with higher atomic number and/or larger thickness appear darker in bright-field and brighter in dark-field image.

2. Diffraction contrast

   The wave-nature of electrons gives rise to diffraction effects in which the scattering of electrons occurs at Bragg angles (θ = 0-90 mrad). For example the diffraction contrast arises as the variation in intensity of the direct beam (BF imaging), differentiating amorphous (high intensity, low diffraction) from crystalline (low intensity, high diffraction) regions.

Energy dispersive X-ray spectroscopy (EDS) was used for determining the composition of the thin film sample. The elemental quantification of two elements A and B is determined from their intensity, using Cliff-Lorimer equation,

$$\frac{I_A}{I_B} = k_{AB}\frac{C_A}{C_B} \tag{4.27}$$

where I_A, I_B are the characteristic intensities of elements A and B. C_A and C_B are the weight percents of each element. The term k_{AB} is the factor known as Cliff-Lorimer factor, which are tabulated and comparing

X-ray photon emission probabilities of two elements A and B. Here, Gatan Digital Micrograph's internal list of k-factors was used.

In this work bright-field and high-angle annular dark-field scanning transmission electron microscopy (BF and HAADF STEM) was performed on a JEOL JEM-ARM 200F operated at 200 kV acceleration voltage. Energy dispersive X-ray spectroscopy maps were recorded with a JEOL JED-2300T EDS detector. About 300 nm of Au was sputtered on top of the films to protect these during the lamella preparation by focused ion beam and thinning it to electron transparency. The multislice simulations of the HAADF STEM image were carried out using *Dr. Probe* software [108].

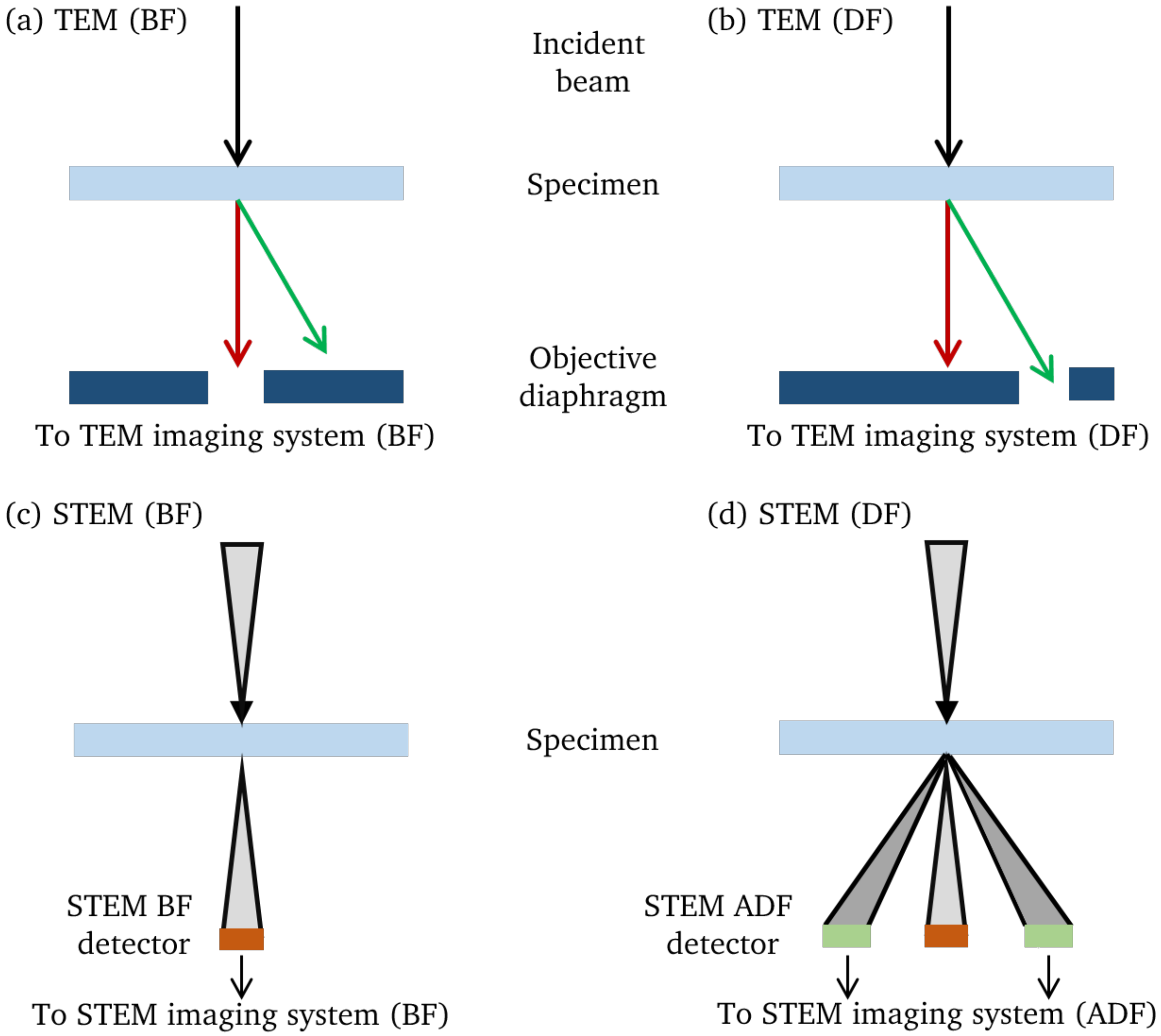
(a) TEM (BF)
Incident beam
(b) TEM (DF)
Specimen
Objective diaphragm
To TEM imaging system (BF)
To TEM imaging system (DF)
(c) STEM (BF)
(d) STEM (DF)
Specimen
STEM BF detector
STEM ADF detector
To STEM imaging system (BF)
To STEM imaging system (ADF)

Figure 4.8: Comparison of TEM and STEM modes of operation. In TEM mode, (a) direct or (b) scattered electrons are selected using aperture forming BF and DF images, respectively. In STEM mode, an (c) on-axis or (d) off-axis annular detector is used to perform equivalent operations.

5 Growth and characterization of Y-Co thin films

In this chapter, the three main studies performed on the binary Y-Co system are described. First, a gradual transition from the Y_2Co_{17} to YCo_5 phase as a result of decreasing cobalt evaporation rate is shown. Second, the approach for a controlled phase separation is described, where both Y_2Co_{17} and YCo_5 phases coexist coherently as a result of a natural phase decomposition reaction during the thin-film growth. Third, the bilayers of Y_2Co_{17} and YCo_5 phases are investigated in an attempt to artificially build the microstructure as a bottom-up approach.

5.1 Gradual phase transition

In this section, gradual phase transition from Y_2Co_{17} phase to YCo_5 is described as achieved by decreasing cobalt evaporation rate and hence, the cobalt content, in small steps.

5.1.1 Growth temperature study

For growing YCo_5 thin films by MBE, the required ratio of atomic flux of Y and Co was calculated by taking into account the atomic mass and density of the two elements, to be $R_{\mathrm{Co}} = 1.616 \times R_{\mathrm{Y}}$, where R_{Co} and R_{Y} are the growth rates of Co and Y respectively. Usually, reduced growth rates allow sufficient time for surface diffusion and result in higher film crystallinity. We selected the technically lowest possible rate of Y of 0.05 Å/s as starting point for the investigation. The corresponding rate of Co is 0.08 Å/s. First a temperature scan was performed at these Y and Co rates to determine the growth window for the formation of crystalline Y-Co phases.

The X-ray diffraction patterns of the Y-Co films grown at set temperatures from 400 °C to 750 °C is shown in Fig. 5.1. The first temperature scan showed that the Y-Co phase formation and improved crystallinity was favorable at a substrate temperatures from 550 °C to 600 °C. The maximum peak intensity was obtained at a set temperature of 600 °C corresponding to actual temperature of 530 °C from the temperature calibration. The following rate scan was then performed at 530 °C.

5.1.2 Evaporation rate scan

The experiments were started at the Co rich side, with a high Co rate of 0.19 Å/s, which was decreased stepwise for each new deposition down to 0.01 Å/s, while the rate of Y was held constant at 0.05 Å/s. The targeted thicknesses of the films were 30 nm. Fig. 5.2(a) shows the out-of-plane (θ–2θ) XRD patterns of the Y-Co thin films with the Co rate decreased from 0.19 to 0.10 Å/s in 9 steps. For this range of Co rates, besides the substrate 006 reflection at $41.67°$ and Ag capping layer 111 reflection at $38.18°$, film peaks at $44°$ could be attributed to (004) planes of $Y_2Co_{17\pm x}$ [109]. The intensity of this 004 reflection reached a maxima at a Co rate of 0.12 Å/s. No other crystalline phase was observed in this range.

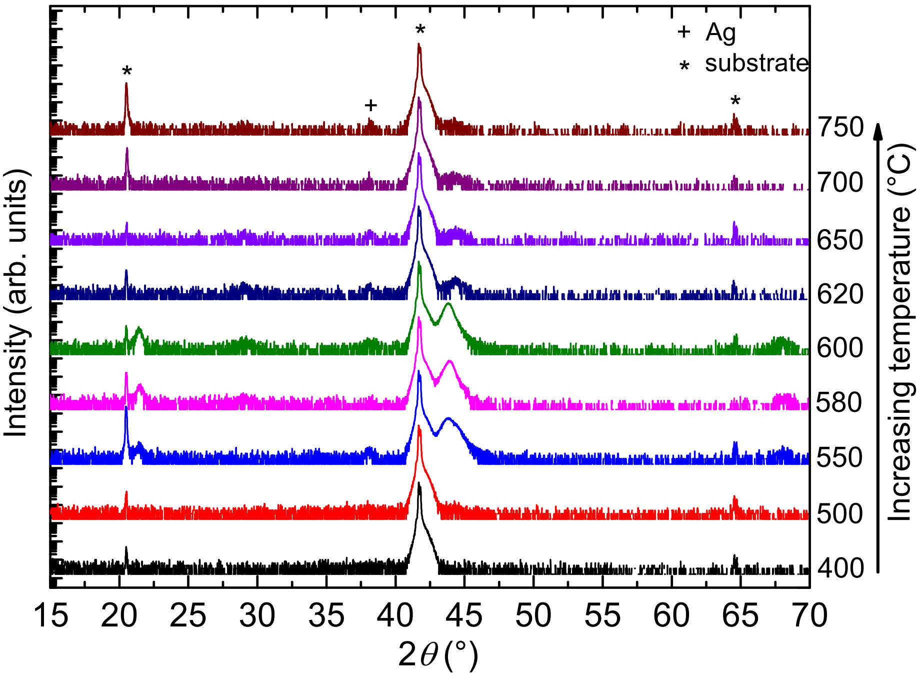

Figure 5.1: XRD patterns of 30 nm Y-Co films deposited at a rate of Y of 0.05 Å/s and Co rate of 0.08 Å/s with increasing growth (set) temperature from 400 °C to 750 °C.

In the Y-Co equilibrium bulk phase diagram, Y_2Co_{17} is followed by YCo_5 phase with decreasing atomic percent of cobalt. Therefore, we continued the reduction of the Co rate further from 0.09 to 0.01 Å/s while keeping the rate of Y constant at 0.05 Å/s as before. The corresponding XRD patterns are shown in Fig. 5.2(b). With decreasing Co rate, a continuous shift of the 004 reflection of Y_2Co_{17} to higher angles towards the 002 reflection of bulk YCo_5 was observed. The shift stopped at a Co rate of 0.05 Å/s, which corresponds to a rate ratio of Y to Co equal to 1. At these rates, the intensity of the 002 reflection at $44.50°$ was maximum. According to the ICDD database [110], this peak position corresponds to the 002 reflection of the sub-stoichiometric composition of $Y_{0.9}Co_{5.2}$. The appearance of the 002 reflection clearly suggested that the c-axis is perpendicular to film plane. Note, that only a very narrow growth window (Y 0.05 Å/s and Co 0.06-0.04 Å/s) existed in which phase pure YCo_5 thin films were obtained. A weak reflection of YCo_5 phase with 101 orientation started to appear at Co rate of 0.04 Å/s. On decreasing the Co rate from 0.04 to 0.01 Å/s, the intensity of the 002 reflection of YCo_5 started to decrease while the 100 reflection of Y at $29.12°$ started to become intense, indicating excess Y [111].

The dependence of the thin film properties on the absolute growth rate was studied by growing films at higher rates and repeating the rate scan (results not shown). With increasing Y to Co rate ratio (or decreasing Co rate), first, the Y_2Co_{17} phase is formed followed by the YCo_5 phase. At same deposition temperature, 002 oriented pure Co thin films are stabilized in its hexagonal symmetry on c-cut Al_2O_3 substrate. This hexagonal crystal structure is maintained throughout the entire range of Y and Co rates. With decreasing Co rate, the Co atoms are removed from the hexagonal crystal lattice in such a way that the hexagonal Y_2Co_{17} phase is transformed to the hexagonal YCo_5 phase. In all the Y-Co films grown throughout this work, the formation of YCo_5 phase was favorable at a Y to Co evaporation rate ratio close to unity.

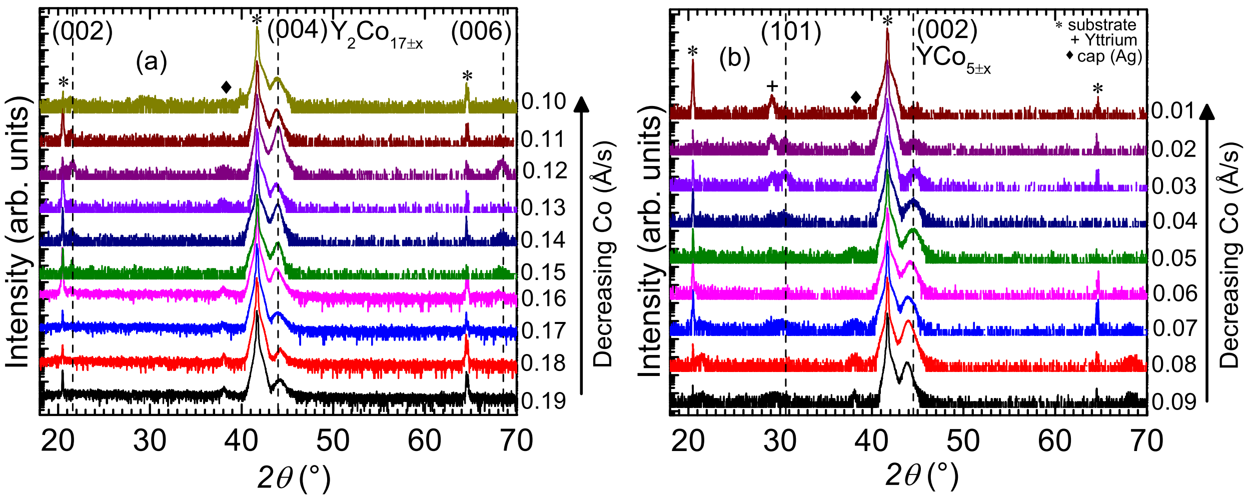

Figure 5.2: XRD patterns of 30 nm Y-Co films, deposited at a constant rate of Y of 0.05 Å/s and Co rate decreasing (a) from 0.19 Å/s to 0.10 Å/s and (b) from 0.09 Å/s to 0.01 Å/s .

5.1.3 Microstructure of YCo_5 film

The microstructure of the YCo_5 film was investigated using STEM as shown in Fig. 5.3. The composition integrated over the full layer refers to an atomic percent of Y of 17.57 ± 0.26 % and Co of 82.43 ± 0.28 % corresponding to YCo_5. An overview of the film morphology reveals an intricate microstructure. The single crystal Al_2O_3 substrate enables a layer-by-layer growth of highly crystalline YCo_5 phase upto a thickness of 10 nm. With increasing thickness, the layer-by-layer growth gives way to an island-type growth of Y deficient $Y_{1-\delta}Co_5$ grains. The grains are *c*-axis textured with stacking faults as indicated by the vertical lines in the FFT shown as inset of Fig. 5.3. A narrow thermodynamic stability of YCo_5 phase, epitaxial and/or thermal strain, accompanied by a strong oxygen affinity of Y lead to the growth of defect rich YCo_5 phase in the grains. The damage on the top of thin film sample could also be during the lamella preparation by FIB.

5.2 Controlled phase separation

In this section, the growth conditions are identified where both Y_2Co_{17} and YCo_5 phases coexist as a result of a natural phase decomposition reaction during the thin-film growth.

5.2.1 Evaporation rate scan

Fig. 5.4(a) shows the XRD patterns of the Y-Co thin films grown at 590 °C with an increasing ratio of evaporation rates of Y and Co. The Co rate is kept constant at 0.25 Å/s while the Y rate is increased from 0.18 Å/s to 0.25 Å/s. The films are about 30 nm thick. The reflections corresponding to the 006 Al_2O_3 substrate at 41.67° (along with its lower and higher order peaks) and 111 Ag cap layer at 38.18° are marked by asterisk and plus signs, respectively.

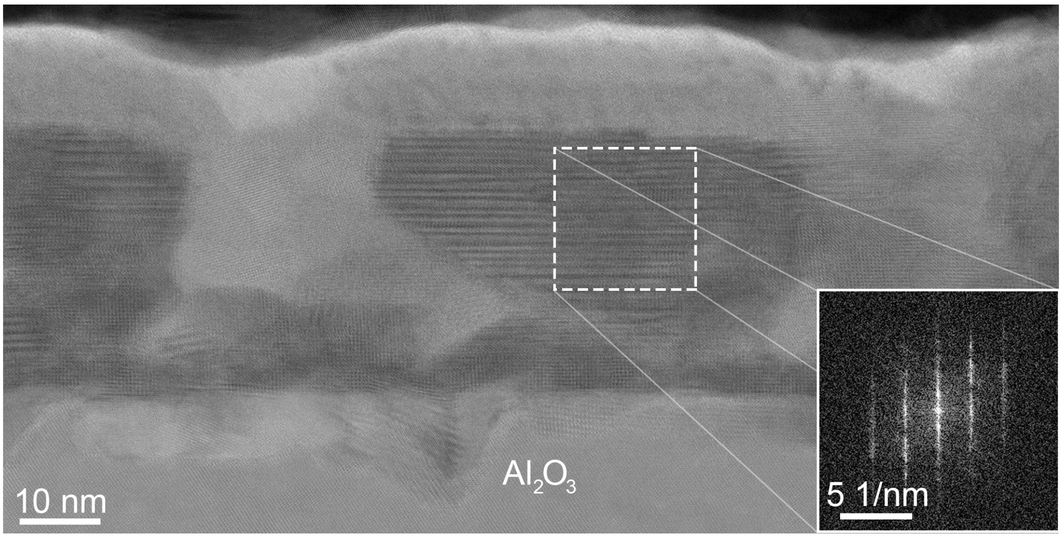

Figure 5.3: (a) The cross-sectional BF image of the YCo$_5$ film grown on (001)-oriented Al$_2$O$_3$ substrate. The inset shows the fast fourier transformation (FFT) map of YCo$_5$ grain.

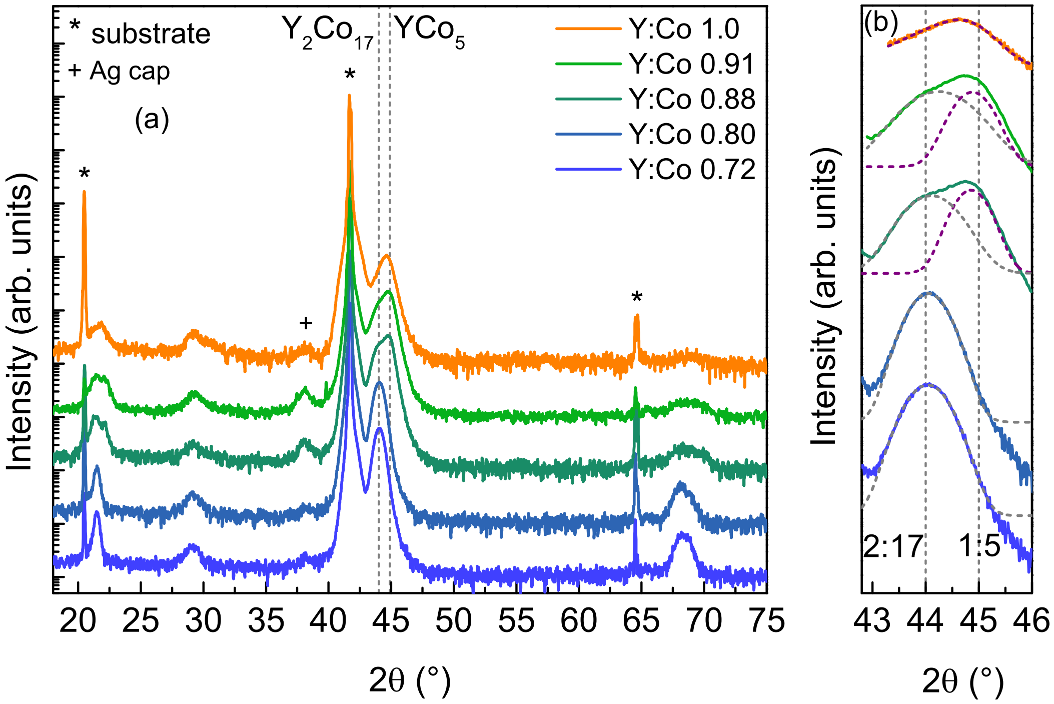

Figure 5.4: (a) X-ray diffraction patterns of Y-Co thin films grown onto (001)-oriented Al$_2$O$_3$ substrates at 590 °C. The evaporation rate of Y is increased from 0.18 Å/s to 0.25 Å/s while the Co rate is fixed at 0.25 Å/s. (b) Magnified view of the film peaks between 42.9° and 46° with fitting using Gaussian distribution function. The positions of the 004 Y$_2$Co$_{17}$ (2:17) and 002 YCo$_5$ (1:5) Bragg reflections are marked by vertical dashed lines.

Table 5.1: Average grain size of Y_2Co_{17} ($d_{2:17}$) and YCo_5 ($d_{1:5}$) in the Y-Co films in the nanocomposite films.

rate ratio (Y:Co)	$d_{2:17}$ (nm)	$d_{1:5}$ (nm)	size ratio ($d_{2:17}$:$d_{1:5}$)
0.88	7.33	11.13	0.658
0.91	5.87	10.44	0.563

A magnified view of the film peaks between 42.9° and 46° with increasing Y to Co ratio from bottom to top is shown in Fig. 5.4(b). The (001)-oriented Al_2O_3 substrate promotes the growth of *c*-axis textured films as indicated by the appearance of $00l$ reflections. For the films grown with Y to Co ratio of 0.72 and 0.80, Y_2Co_{17} phase is formed. The peak at about 44° corresponds to the 004 reflection of the Y_2Co_{17} phase [109]. It is symmetric and a single Gaussian distribution function is used to fit the peak. The lower order 002 and higher order 006 reflections are also observed at 21° and 68°, respectively.

With an increase in the ratio between 0.88 and 0.91, the peak at 45° corresponding to 002 reflection of YCo_5 phase is additionally observed [112]. In this case, the region between 42.9° and 46° is fit with two Gaussian peaks. At these growth conditions, both Y_2Co_{17} and YCo_5 phases are stabilized simultaneously. In these films, double lower order peak around 21° and a broad higher order reflection around 68° are also observed.

A natural phase decomposition during the film growth results in separation and self-arrangement of Y_2Co_{17} and YCo_5 phases as in a nanocomposite. The (001)-oriented Al_2O_3 substrate aligns the *c*-axes of both Y_2Co_{17} and YCo_5 phase parallel to each other favoring a coherent growth of the two phases.

With further increase in the Y to Co ratio to 1, a single asymmetric peak slightly shifted from the 002 reflection of the YCo_5 phase is observed. Additionally, traces of Y_2O_3 at about 29° are observed at all compositions.

The average grain size of Y_2Co_{17} ($d_{2:17}$) and YCo_5 ($d_{1:5}$) phases in the nanocomposite film is estimated from the Bragg angle (2θ of 004 of Y_2Co_{17} and 002 of YCo_5) using Scherrer equation given by,

$$d = (0.9 \times \lambda)/(\beta \cos(\theta))$$

where λ is the wavelength of Cu-K_α X-ray radiation and β represents the full width at half maximum (FWHM). The grain sizes are provided in Table 5.1.

It can be seen that the average grain size of both the hard and soft magnetic phases is in the range of 10-15 nm. Such nanoscale dimensions of the two phases are considered favorable for an effective exchange-coupling as exchange is a short-range interaction [113].

5.2.2 Growth temperature study

Fig. 5.5(a) shows the $\theta-2\theta$ scans of Y-Co films grown at Y and Co rate of 0.20 Å/s corresponding to a ratio of 1 at temperature increasing from 490 °C to 660 °C. The reflections corresponding to the Al_2O_3 substrate and the Ag cap layer are marked by asterisk and plus signs, respectively. A magnified view of the film peaks

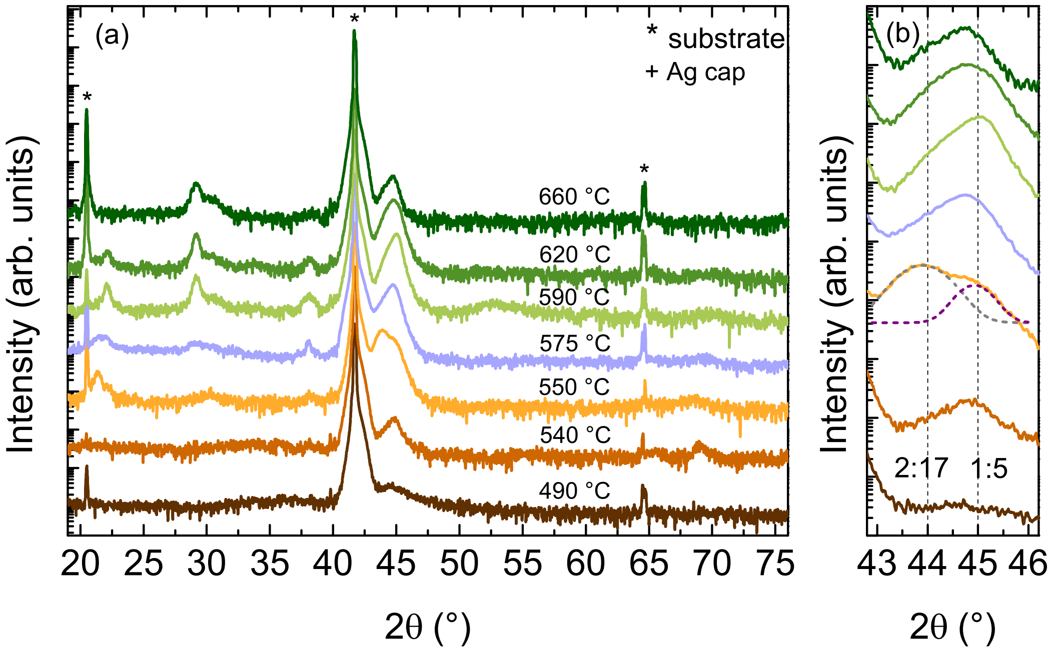

Figure 5.5: X-ray diffraction patterns of Y-Co thin films grown onto (001)-oriented Al_2O_3 substrates with increasing temperature from 490 °C to 660 °C for Y:Co of 1. (b) Magnified view of the film peaks between 42.9° and 46° with fitting using Gaussian distribution function. The positions of the 004 Y_2Co_{17} (2:17) and 002 YCo_5 (1:5) Bragg reflections are marked by vertical dashed lines.

in the region from 42.9° to 46° is shown in Fig. 5.5(b). The positions of the 004 Y_2Co_{17} (2:17) and 002 YCo_5 (1:5) Bragg reflections are marked by vertical dashed lines.

It can be seen that the film peaks become intense with increase in deposition temperature. At the lowest growth temperature of 490 °C, it can be seen that the 002 peak of YCo_5 phase is quite broad and diminished indicating that the film is nanocrystalline or amorphous. At 550 °C, there are two peaks observed, corresponding to Y_2Co_{17} and YCo_5. The region between 42.9° and 46° is fit to two symmetric Gaussian peaks: one at 43.90° corresponding to 004 reflection of Y_2Co_{17}, and the second at 44.93° corresponding to the 002 reflection of YCo_5 phase. At 575 °C, a single symmetric peak corresponding to YCo_5 phase at 44.64° is observed. With further increase in temperature from 590 °C, a single asymmetric peak at 45.16° corresponding to the YCo_5 phase is observed, however, with simultaneous increase of Y or Y_2O_3 around 28°. At the highest growth temperature of 660 °C, the intensity of 002 reflection of YCo_5 is considerably reduced.

The temperature study shows that the crystallization of the Y-Co phases is improved with the growth temperature. The oxidation of yttrium also increases with temperature. The Y_2Co_{17} and YCo_5 phases can be stabilized at intermediate temperature of 550 °C. The optimum temperature for the growth of YCo_5 phase is observed to be 575 °C at which an intense and symmetric 002 reflection is present accompanied with no or less observable contribution from the oxide.

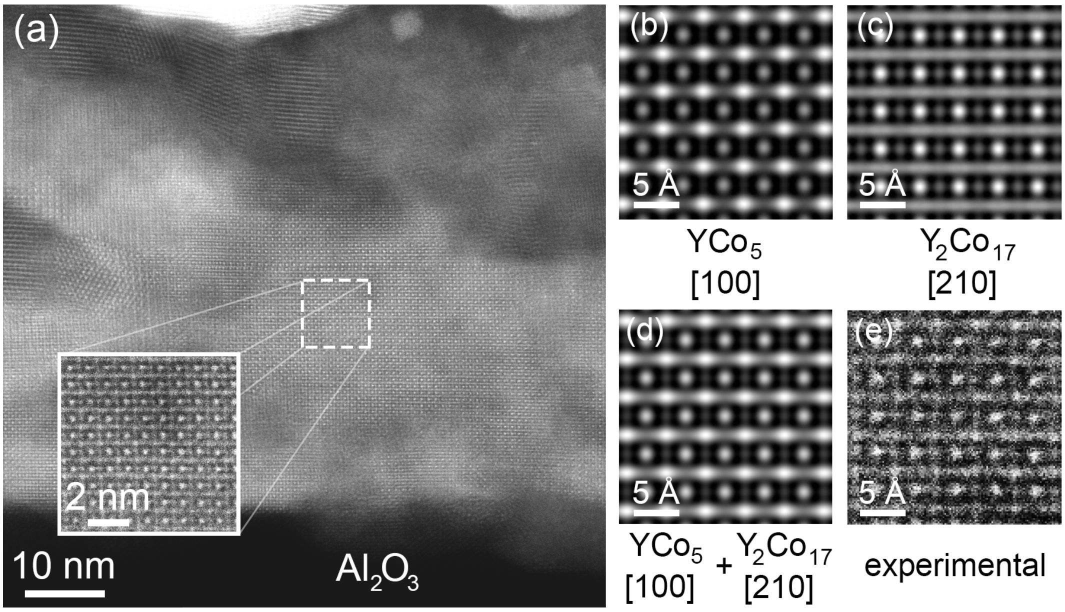

Figure 5.6: (a) The cross-sectional high resolution HAADF-STEM image of the Y-Co film grown on (001)-oriented Al_2O_3 substrate. Multislice simulations of a 15 nm slab of (b) YCo_5 crystal viewed along the [100] direction, (c) Y_2Co_{17} crystal along [210] viewing direction, and (d) a supercell of combined YCo_5 [100] and Y_2Co_{17} [210] cells. (e) Experimental atomic-resolution HAADF-STEM image of the crystalline area marked in (a).

5.2.3 Microstructure of Y_2Co_{17} - YCo_5 nanocomposite film

The cross-sectional high-resolution HAADF-STEM image of the Y_2Co_{17}-YCo_5 nanocomposite film grown at Y to Co rate ratio of 0.91 on (001)-Al_2O_3 substrate is shown in Fig. 5.6(a). The cross-section was cut along the [100] zone-axis of the Al_2O_3 substrate, in order to achieve on-axis observation conditions for high-resolution imaging. A set of crystal faces whose lines of intersection are parallel is called a zone. The direction parallel to the lines of intersection is the zone-axis [114].

It can be seen that the film has regions with well defined atomic contrast and highly crystalline structure. The inset shows a magnified view of the indicated area. In order to confirm the phase of the crystalline layer, multislice simulations were carried out. Fig. 5.6(b) shows a simulated image of the YCo_5 phase viewed along [100] direction and Fig. 5.6(c) shows the simulated image of the Y_2Co_{17} phase viewed along [210] direction. For both phases, the c-axes are parallel to the film growth direction. The observed HAADF high-resolution contrast resembles either of the pure phases or their combination. As a model structure, a supercell of the two phases was created preserving the projection orientation. The supercell represents a stack of equal volume ratio of 1:5 and 2:17 unit cells resulting in a micrograph shown in Fig. 5.6(d). The generated image matches well with the experimental STEM image of the film shown in Fig. 5.6(e). The model supports the nanocomposite nature of the film in close agreement with the XRD data shown in Fig. 5.4(a).

Self-assembly in the nanocomposite or the coherent precipitation is facilitated by the closely matching lattice constants, atomic species and crystal symmetry. The here described nanostructured magnet comprises of coherently interlinked Y_2Co_{17} and YCo_5 structures with c-axis oriented growth directed by the substrate. Such nanoscale architecture directly influences the magnetic properties.

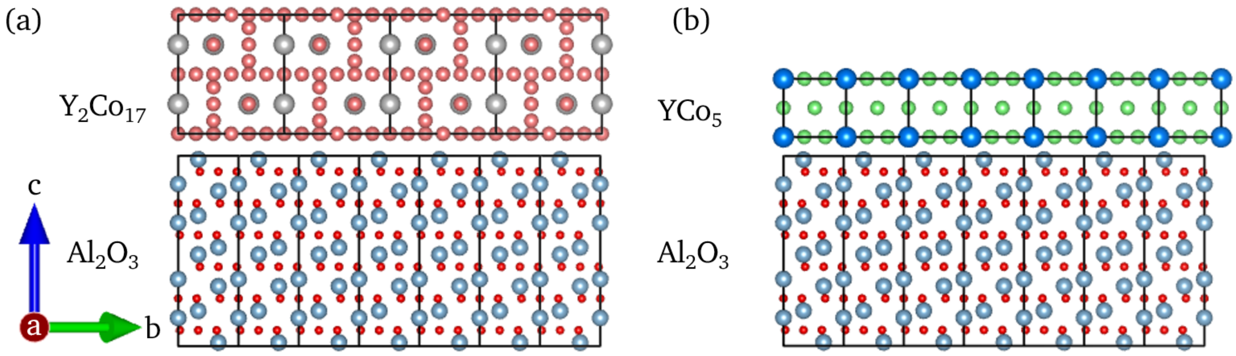

Figure 5.7: The atomic arrangement of (a) four unit cells of Y_2Co_{17} and (b) seven unit cells of YCo_5 in the ab plane upon seven unit cells of Al_2O_3 substrate.

5.3 Epitaxial relations

5.3.1 Y_2Co_{17} on Al_2O_3

The ϕ-scan of 222 reflection of Y_2Co_{17} at $2\theta = 48.97°$ and $\chi = 62.76°$, is shown in Fig. 5.8. The appearance of six peaks confirms the hexagonal crystal structure of the Y_2Co_{17} phase in the thin film. The observed reflections are: 222, $\bar{4}22$, $\bar{2}\bar{2}2$, $\bar{2}42$, $2\bar{4}2$, $4\bar{2}2$. The following epitaxial relation is derived;

Y_2Co_{17} (001) $\|$ Al_2O_3 (001); Y_2Co_{17} [100] $\|$ Al_2O_3 [100]

The out-of-plane lattice constant, c, of Y_2Co_{17} film as measured from the 004 reflection is 8.2263 Å. The in-plane lattice constant, a, is derived from 222 reflection to be 8.335 Å corresponding to c/a of 0.987. Bulk Y_2Co_{17} crystal has c of 8.12 Å and a of 8.36 Å with c/a of 0.9869 [109].

There are following two possible arrangements of Y_2Co_{17} on Al_2O_3 substrate. In the first case, four unit cells of Y_2Co_{17} are stacked upon seven unit cells of Al_2O_3 in the ab plane as shown in Fig. 5.7(a). Such an arrangement results in a small lattice mismatch of 0.39%. Thus, Y_2Co_{17} grows almost relaxed on Al_2O_3. In the second case, one unit cell of Y_2Co_{17} expand to fit with two unit cells of Al_2O_3. This arrangement results in a large mismatch of 12.16 % which creates tensile strain in the lattice. As the lattice constants of Y_2Co_{17} film measured from XRD match closely to the bulk crystal, it is most likely that Y_2Co_{17} lattice is not strained and it grows according to the atomic arrangement shown in Fig. 5.7(a).

5.3.2 YCo_5 on Al_2O_3

A ϕ-scan of (001)-oriented YCo_5 film (orange) on a (001)-oriented Al_2O_3 substrate (grey) is shown in Fig. 5.9(a). The ϕ-scan of the 104 reflection ($2\theta = 35.05°$, $\chi = 36.23°$) of Al_2O_3 which is rhombohedral, shows three peaks indicating three-fold symmetry. The three peaks are $\bar{1}14$, $0\bar{1}4$ and 104. The ϕ-scan of 201 reflection of YCo_5 ($2\theta = 48.59°$, $\chi = 62.33°$) shows six-fold symmetry which confirms the hexagonal crystal structure. The six peaks observed are: 201, $\bar{2}01$, 021, $0\bar{2}1$, $2\bar{2}1$ and $\bar{2}21$. It shows that film grows epitaxially on the Al_2O_3 substrate. The following epitaxial relation is derived;

YCo_5 (001) $\|$ Al_2O_3 (001); YCo_5 [100] $\|$ Al_2O_3 [100]

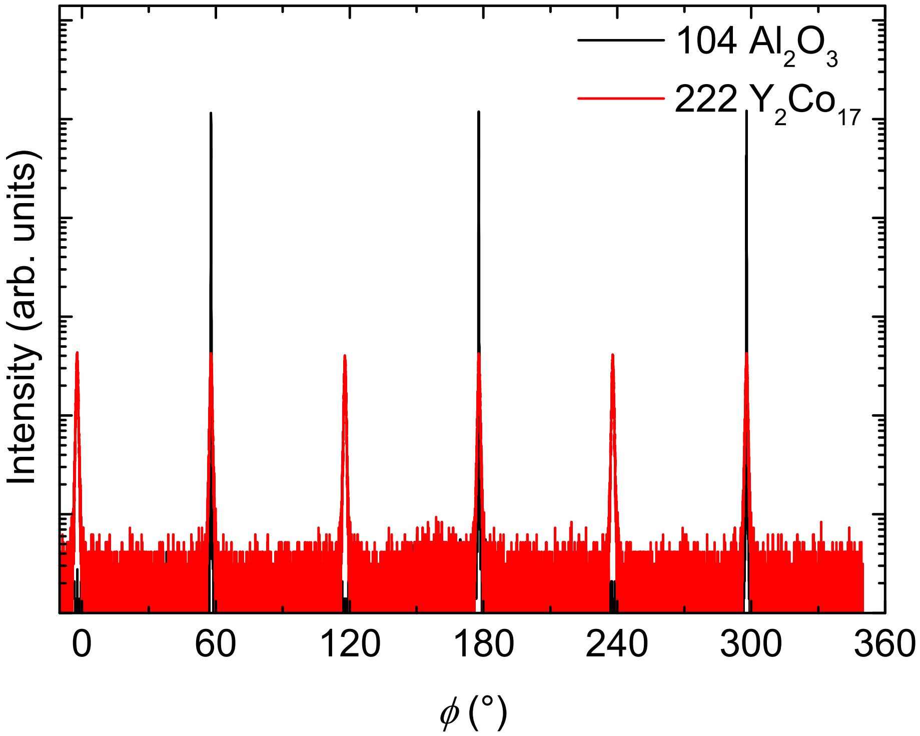

Figure 5.8: (a) ϕ-scan of 222 reflection of Y_2Co_{17} (red) with respect to 104 reflection of Al_2O_3 substrate (black).

Additionally, pole figure measurement of the 201 reflection of YCo_5 is performed in which the diffraction intensity distributions are measured on rotating and tilting the sample (scanning χ and ϕ) at constant diffraction condition ($2\theta = 48.59°$). The tilt angle χ is scanned from 0° to 90° and the in-plane rotation angle, ϕ, is scanned from 0° to 360° around the sample surface as shown in Fig. 5.9(b). The intense reflections corresponding to the 201-type Bragg peaks are shown in orange while the other less intense peaks in grey. A narrow distribution of the 201-equivalent reflections indicate the film is highly crystalline and strongly textured.

The atomic arrangement of unit cells of YCo_5 on Al_2O_3 substrate is shown in Fig. 5.7(b). The stacking of one unit cell of YCo_5 on Al_2O_3 substrate results in a lattice mismatch of 4.022 % which creates a compressive strain in the lattice. The bulk YCo_5 crystal has a of 4.95 Å and 3.97 Å with a volume of 84.24 Å^3. In the thin film, a compressed a lattice constant of 4.8743 Å and an elongated c lattice constant of 4.05662 Å, is obtained resulting in c/a ratio of 0.832 and a volume of 83.4678 Å^3.

5.4 RHEED analysis

Fig. 5.10 shows the RHEED patterns of (a) Al_2O_3 (001) substrate along [11-20] azimuth, and of (00l) oriented films of (b) Y_2Co_{17} and (c) YCo_5 along the same azimuth. The RHEED pattern of the as-deposited films showed streaky behaviour indicating an atomically flat surface. The different surface arrangement of atoms on Y_2Co_{17} surface leads to the appearance of 1/3 and 2/3 ordered streaks as shown by arrows in Fig. 5.10(b).

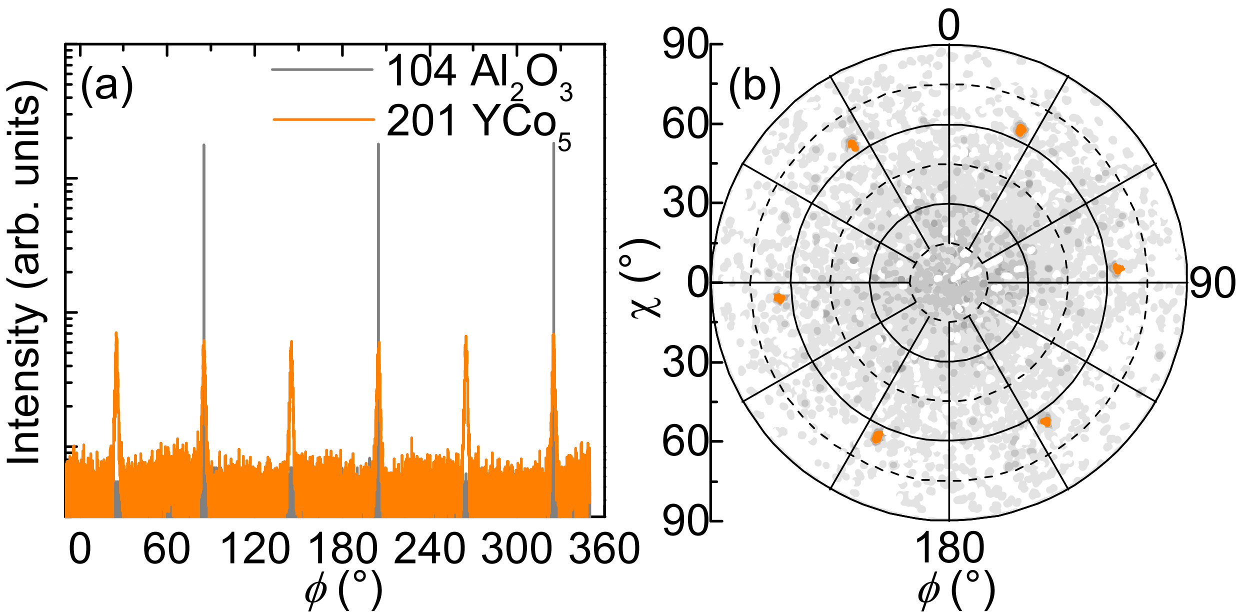

Figure 5.9: (a) ϕ-scan of 201 reflection of YCo_5 (orange) with respect to 104 reflection of Al_2O_3 substrate (grey). (b) Pole figure measurement of 201 reflection of YCo_5 where the film peaks are shown in orange and the less intense background in grey.

The real space lattice parameter was estimated from the horizontal distance between the RHEED streaks. For Y_2Co_{17}, the corresponding in-plane lattice spacing was determined to be 8.31 Å, matching closely to the in-plane lattice constant of 8.33 Å, as obtained using XRD. For YCo_5, a real space lattice parameter of 4.85 Å is also in close agreement with the in-plane lattice parameter determined previously by XRD.

5.5 Magnetic properties

The magnetic hysteresis curves measured at room temperature, perpendicular ($\perp$, orange spheres) and parallel ($\|$, grey diamonds) to the film plane are shown in Fig. 5.11. The following three instances are described: (a) the film grown at Y to Co ratio of 0.72 at which Y_2Co_{17} phase is formed, (b) the film grown at a ratio of 1 at which YCo_5 phase is formed, and (c) the film grown at a ratio of 0.88 at which both Y_2Co_{17} and YCo_5 phases co-exist.

5.5.1 Easy-plane anisotropy in Y_2Co_{17} film

The magnetic hysteresis curves of Y_2Co_{17} measured at room temperature, perpendicular ($\perp$, orange spheres) and parallel ($\|$, grey diamonds) to the film plane are shown in Fig. 5.11(a).

The Y_2Co_{17} film is characterized by a soft ferromagnetic behaviour with the highest magnetization of 772.63 kA/m and a small coercivity. The shape of the curves suggest that the easy direction of magnetization lies in the film plane while the hard-axis is perpendicular to the film [115]. After subtraction of the shape anisotropy contribution, the first magnetocrystalline anisotropy constant, K_1, is derived to be -0.243 MJ/m^3 from the field at which the hard-axis saturates.

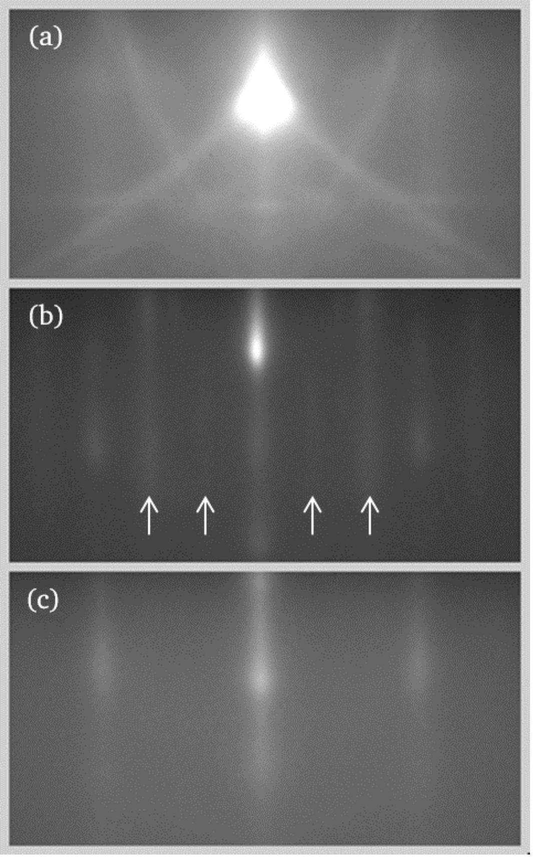

Figure 5.10: RHEED patterns of an (001)-oriented Al_2O_3 substrate along [11-20] azimuth, and 30 nm thick films of (b) Y_2Co_{17} and (c) YCo_5 along the same azimuth.

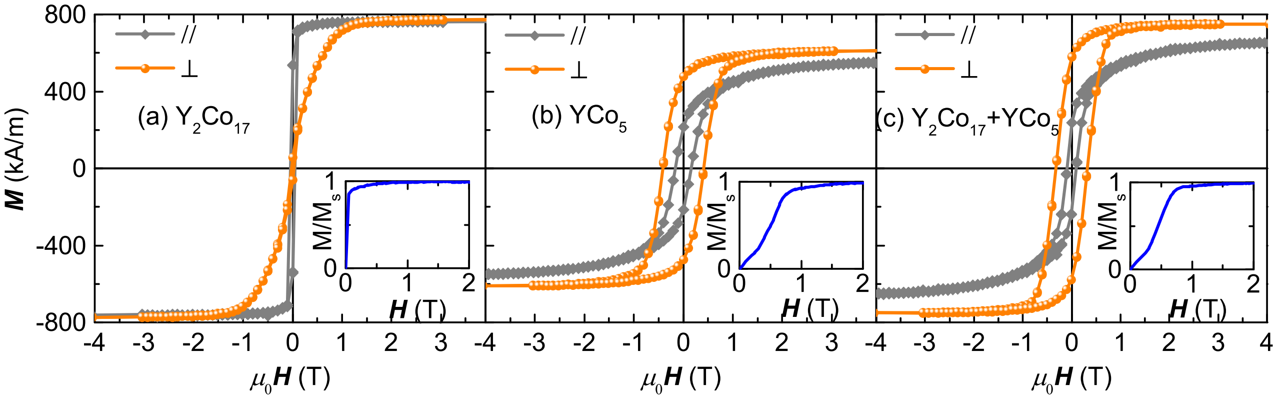

Figure 5.11: Room temperature hysteresis curves measured perpendicular (⊥, orange spheres) and parallel (∥, grey diamonds) to the plane of (a) Y_2Co_{17}, (b) YCo_5 and (c) Y_2Co_{17} and YCo_5 films grown at 590 °C. The corresponding initial magnetization curves are shown in the inset.

Bulk single crystals of Y_2Co_{17} show an easy-plane anisotropy with K_1 of -0.33 MJ/m^3. The value of K_1 obtained for our thin film is in good agreement to the bulk single crystal and W buffered thin film of Y_2Co_{17} reported in literature [35, 115]. Thus, the Y_2Co_{17} phase in the thin film is stabilized with the magnetization and anisotropy matching well to the bulk single crystal.

The virgin magnetization curve of the film is shown in the inset of Fig. 5.11(a). A steep rise in the magnetization under a small applied field shows that the domain walls move easily resulting in a high permeability. Such a behaviour is attributed to nucleation-controlled reversal of magnetization.

5.5.2 Perpendicular anisotropy in YCo_5 film

The hysteresis curve of the YCo_5 film is shown in Fig. 5.11(b). The film is magnetically hard with magnetization of 610.98 kA/m. The hysteresis curve measured perpendicular to the film is larger than the in-plane hysteresis curve and has a higher remanence and coercivity indicating that the major component of magnetization is perpendicular to the film plane. The origin of perpendicular anisotropy is considered to be uniaxial magnetocrystalline anisotropy associated with the *c*-axis textured growth of YCo_5 phase normal to the film plane. The microstructure of the film shows that it is made up of a thin single crystalline layer as well as aligned grains of high anisotropic phase of YCo_5. Ideally, large fields are required to bring remanent magnetization to zero, however, the presence of stacking faults in the grain results in reduced coercivity. The virgin magnetization curve of the YCo_5 film provided inset of Fig. 5.11(b) shows a gradual rise of magnetization with applied field. Such a behaviour is expected for isolated single domain particles in which the magnetization reversal takes place by coherent or incoherent rotation process [116, 117].

It can be also be seen that the hard-axis of magnetization does not fully approach the easy-axis of magnetization, and a gap continues to exist beyond saturation. This effect is known as anisotropic magnetization and was reported in RCo$_5$ intermetallic compounds including YCo_5 by Alameda *et al* [118, 119]. The magnetization anisotropy was described by Callen and Callen [120, 121]. There are several theories concerning the origin of the magnetization anisotropy. One possible explanation is the influence of magnetocrystalline anisotropy on the atomic moments. In the direction of easy magnetization, the anisotropy tends to keep the individual spins aligned forming a narrow cone along the easy-axis, and

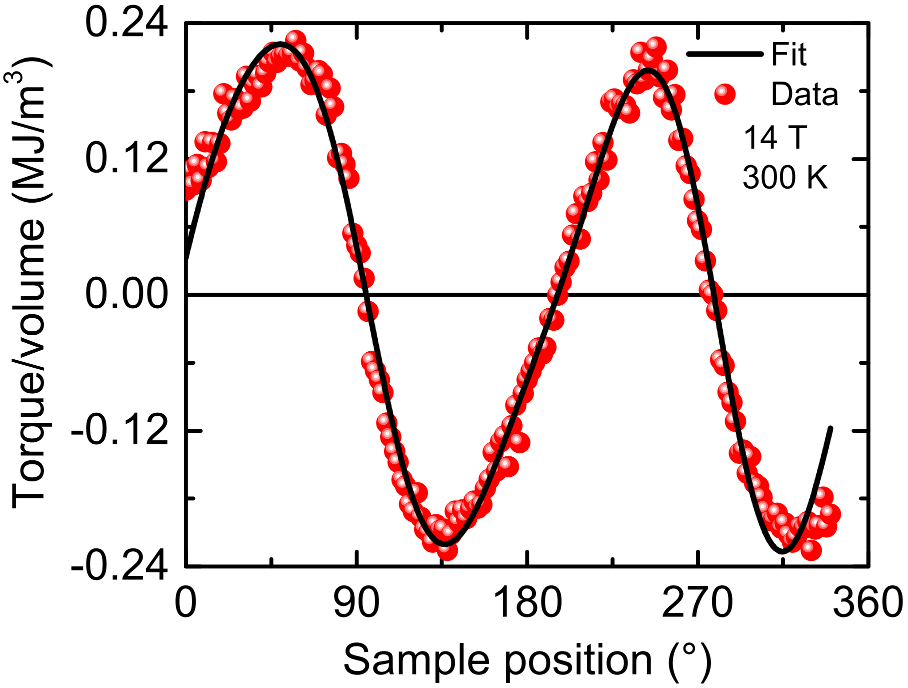

Figure 5.12: Torque measurement of a 30 nm YCo_5 thin film showing the actual data points and the refined curve, at 14 T and 300 K.

thereby, increases the magnitude of the magnetization. In contrast, in the hard direction the anisotropy enhances the angular deviation of the spins forming a wider cone along the hard-axis which decreases the magnitude of the magnetization.

The first anisotropy constant, K_1, of the optimized YCo_5 thin film was calculated from a magnetic torque measurement. The sample was rotated from $0°$ to $340°$ in the presence of a constant magnetic field. At $0°$, the sample surface plane is perpendicular to the applied field and at $90°$, it is parallel. The torque curves were measured at 300 K in fields from 2 to 14 T. Fig. 5.12 shows the angular dependence of torque per unit volume of YCo_5 at 14 T after subtraction of the signal from the bare substrate. The two-fold symmetry of the torque curve indicates two-fold symmetry of the axis of magnetization (easy and hard). These experimental torque curves obtained at different fields were Fourier transformed. Then, the coefficients of the two-fold symmetry component ($sin(2\theta)$) and the four-fold symmetry component ($sin(4\theta)$) terms for a hexagonal system were extrapolated to infinite field ($1/H = 0$) in order to estimate the value of K_1 [106]. Accordingly, K_1 as calculated from the torque measurement is 0.53 MJ/m^3.

Admittedly, there is still one order of magnitude for tuning K_1 towards values for bulk single crystal. The various factors which could lead to a reduced anisotropy of the thin film as calculated from the torque measurement are listed below:

1. Degree of texture

   The torque measurement gives an accurate measure of the anisotropy for perfectly aligned single crystals in which K_1 is equal to K_u. However, it can be clearly seen from the rocking curve and the small coercivity in the in-plane hysteresis curve that there is a misorientation of the grains. The microstructure of the film also shows stacking faults in the film growth direction. A deviation of the *c*-axis from the normal of the film plane results in reduced value of anisotropy, and K_1 in this case, is a measure of the perpendicular component of the anisotropy of the films.

2. Strain

   Pressure or epitaxial strain in thin-films is known to sensitively affect the magnetic properties of the intermetallic compounds [122]. As discussed previously, a lattice mismatch of 4.022 % creates a compressive strain in the YCo_5 lattice. Thus, the lattice constants of the thin film vary from the bulk which can affect the magnetocrystalline anisotropy. While in the case of Y_2Co_{17}, with a small lattice mismatch of 0.39%, the anisotropy of the film matches well to the bulk crystal.

3. Impurity

   The phase purity of the film is affected due to surface oxidation, interface layers, and amorphous/-nanocrystalline residuals undetectable in X-ray diffraction, which can affect the magnetic properties of the film. The microstructure of the film shows that there is some inter-diffusion at the film-substrate interface which is most likely due to reaction at high temperature during the film growth.

4. Stoichiometry

   The magnetocrystalline anisotropy of the different phases is related to the cobalt concentration. The cobalt sub-lattice anisotropy strongly depends on the stoichiometry. According to the phenomenological models, both with increasing and decreasing Co content with respect to the Y:Co = 1:5 composition will reduce anisotropy [123].

5.5.3 Perpendicular anisotropy in Y_2Co_{17} - YCo_5 nanocomposite film

Now, we describe the magnetic properties of nanocomposite film of the soft Y_2Co_{17} and the hard YCo_5 ferromagnetic phases. The corresponding hysteresis curves measured at room temperature are shown in Fig. 5.11(c). Similar to YCo_5, the nanocomposite film also shows perpendicular anisotropy. There is an overall enhancement in the remanence, as compared to YCo_5, as well as coercivity, as compared to Y_2Co_{17}. Since the magnetocrystalline anisotropy of the Y_2Co_{17} phase is small, its magnetization is pinned to the high anisotropic phase of YCo_5 leading to a hard magnetic behaviour. The hysteresis curves measured both perpendicular and parallel to the film, are continuous without a kink indicating a strong-exchange interaction between the phases. The grain size of Y_2Co_{17} phase (Table 5.1), is less than twice the domain-wall thickness of YCo_5 of 5.5 nm [124], in both the nanocomposite films. Such nanoscale architecture of the film enables an effective exchange-coupling, well in agreement to the exchange-hardening mechanism proposed for nanostructured two-phase magnets [125, 126].

The initial magnetization of the film shown in the inset of Fig. 5.11(c) rises gradually with the applied magnetic field. The Y_2Co_{17} - YCo_5 nanocomposite film comprises of gradually varying structural and magnetic properties. The gradients in concentration as well as alterations of both anisotropy and exchange energies, changes the energy of domain-wall and hence, hinders its movement pointing towards a pinning-type of mechanism.

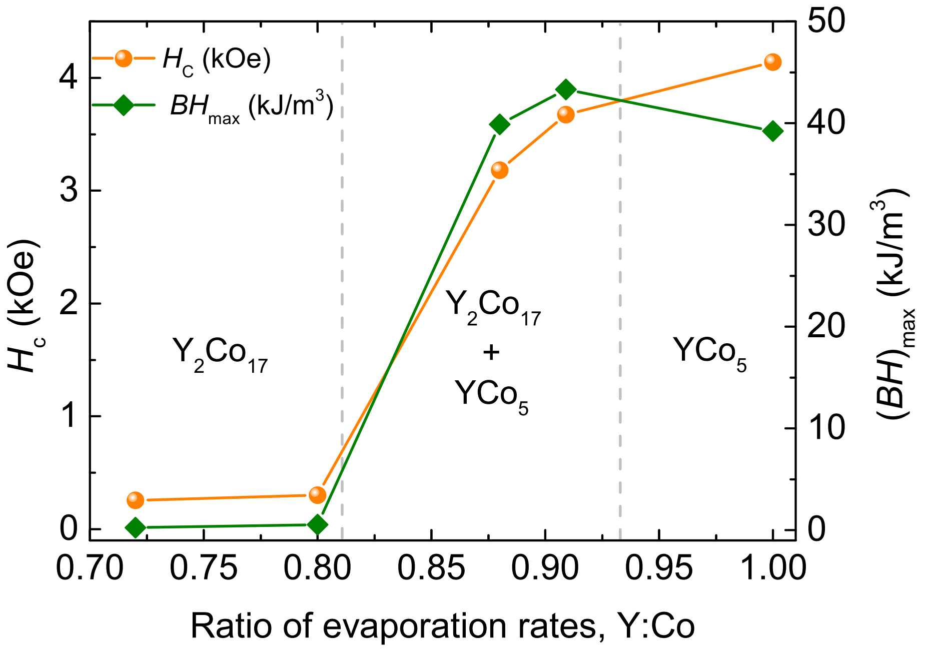

Figure 5.13: Coercive field, H_c, and maximum energy product, $(BH)_{max}$, versus ratio of evaporation rates of Y to Co. The three regions correspond to the growth of Y_2Co_{17}, YCo_5 and a nanocomposite of Y_2Co_{17} and YCo_5 phases.

5.5.4 Composition dependence on coercivity

A plot of the composition dependence of coercive field, H_c and the maximum energy product, $(BH)_{max}$, measured perpendicular to the film plane, is shown in Fig. 5.13. Here, vertical dashed lines mark different regions corresponding to Y_2Co_{17}, YCo_5, and a nanocomposite of Y_2Co_{17} and YCo_5 phases. The Y_2Co_{17} films are soft ferromagnetic with a small coercivity and energy product.

Then there is a sharp increase in the coercivity and energy product in the nanocomposite where both Y_2Co_{17} and YCo_5 phases co-exist as magnetically exchange-coupled system. The combined high magnetization of the soft Y_2Co_{17} and large coercivity of the hard YCo_5 phase gives rise to peak in the $(BH)_{max}$.

The third region corresponds to YCo_5 film with the highest coercivity of 4.14 kOe. The film exhibits a $(BH)_{max}$ of 39.22 kJ/m^3 which is the highest reported so far for thin films and is comparable to melt-spun ribbons and ball-milled nanopowders [59, 60, 127, 128].

Thus, the coercivity of the films increases from Y_2Co_{17} to YCo_5 phase while a maxima in $(BH)_{max}$ is obtained in the self-assembled nanostructured magnet of Y_2Co_{17} and YCo_5.

5.5.5 Growth temperature dependence on coercivity

The dependence of H_c, and $(BH)_{max}$ of the Y-Co films on the growth temperature is shown in Fig. 5.14. All the films were grown at Y to Co ratio of 1 at which YCo_5 phase is formed. The coercivity as well as $(BH)_{max}$ increase with temperature with a maxima at 575 °C above which it decreases sharply. Similar trend of coercivity on the substrate temperature has been observed in $SmCo_5$ thin films [80, 75].

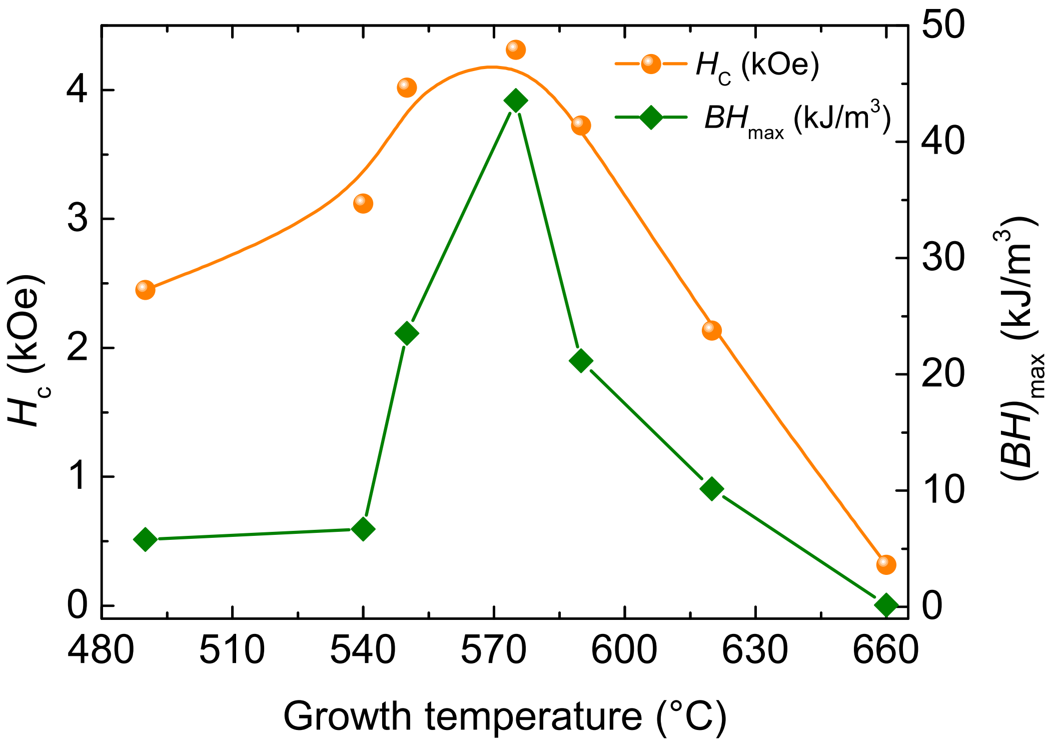

Figure 5.14: Coercive field, H_c, and maximum energy product, $(BH)_{max}$, versus the growth temperatures from 490 °C to 660 °C of Y-Co thin films grown at Y to Co ratio of 1.

The growth temperature dependence on the coercivity of the films is explained as follows. At the lowest temperature of 490 °C, a considerable coercivity of 2.45 kOe originates from the nanocrystalline, randomly oriented highly anisotropic YCo_5 grains. With increase in temperature, the crystallization or the nucleation of YCo_5 grains is enhanced upto a temperature of 575 °C. An increased number of YCo_5 grains results in an increase in the coercivity. With further increase in the temperature above 575 °C, when the number of grains become constant, the growth of grains occurs resulting in reduced coercivity [129]. At the highest growth temperature of 660 °C, the coercivity drops to the lowest value of 0.32 kOe. Besides, the given growth temperature might be additionally too high for a reaction between Y and Co to form YCo_5. Furthermore, the presence unreacted Y or Y_2O_3 in the films with temperature is observed to reduce the coercivity. The dependence of grinding time or the size of YCo_5 particles obtained in a high-speed vibratory mill shows similar behaviour [4].

5.6 Y_2Co_{17} - YCo_5 bilayers

So far, there are no reports available in the literature on the synthesis of bilayers of Y_2Co_{17} and YCo_5 phases. In this work, we investigate for the first time, the magnetic properties of the thin film heterostructures of Y_2Co_{17} and YCo_5 phases. Bilayers of Y_2Co_{17} and YCo_5 phases were grown with varying thicknesses on Al_2O_3 substrate. Depending on the order of growth of the two phases, there are two categories of bilayers. First, Y_2Co_{17} is grown directly on Al_2O_3 substrate and then YCo_5 is grown on top, i.e. $YCo_5 \parallel Y_2Co_{17} \parallel Al_2O_3$, as shown in Fig. 5.15(a). Second, YCo_5 is grown directly on Al_2O_3 substrate and then Y_2Co_{17} is grown on top, i.e. $Y_2Co_{17} \parallel YCo_5 \parallel Al_2O_3$, as shown in Fig. 5.15(b).

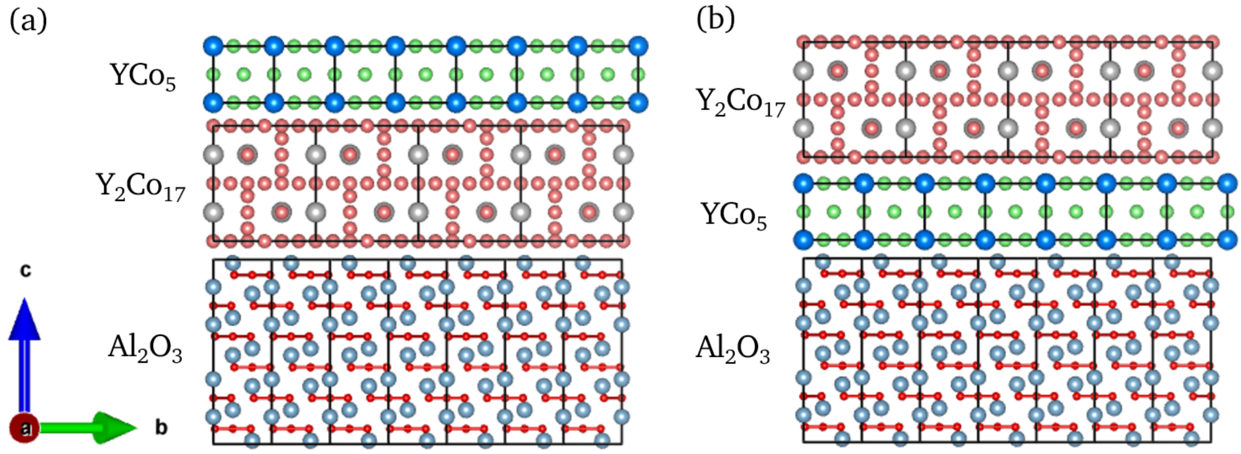

Figure 5.15: The arrangement of unit cells of YCo_5 and Y_2Co_{17} on Al_2O_3 in the bilayers: (a) YCo_5 ∥ Y_2Co_{17} ∥ Al_2O_3, (b) YCo_5 ∥ Y_2Co_{17} ∥ Al_2O_3

5.6.1 YCo_5 on Y_2Co_{17} on Al_2O_3

Fig. 5.16(a) shows the $\theta - 2\theta$ scans of the bilayers with Y_2Co_{17} grown directly on Al_2O_3 and then YCo_5 phase on top. The total thickness of the stack is 30 nm with the thickness of the Y_2Co_{17} layer increasing from 5 to 15 nm from bottom to top. The following three bilayers are synthesized: (a) Y_2Co_{17} (5 nm) and YCo_5 (25 nm), (b) Y_2Co_{17} (10 nm) and YCo_5 (20 nm), and (c) Y_2Co_{17} (15 nm) and YCo_5 (15 nm).

Magnified view of the Y-Co film peaks is shown in Fig. 5.16(b) with vertical dashed lines indicating the Bragg angle of 004 Y_2Co_{17} (2:17) and 002 YCo_5 (1:5) phases. It can be seen that in all the three cases, the position of the $(00l)$ reflection of the bilayer system is close to the 004 reflection of Y_2Co_{17} phase. This suggests that when Y_2Co_{17} film is grown first on the substrate, the lattice of the YCo_5 phase adjusts itself to the lattice of the Y_2Co_{17} phase beneath in such a way that a c spacing corresponding to only Y_2Co_{17} phase is observed.

There are two possible arrangements of YCo_5 unit cells on Y_2Co_{17}. In the first case, seven unit cells of YCo_5 are arranged on four unit cells of Al_2O_3 resulting in a mismatch of 3.618% as shown in Fig. 5.15(a). This creates a compressive strain in the YCo_5 lattice. In the second case, two unit cells of YCo_5 compress in the ab plane upon one unit cell of Y_2Co_{17}. There is a mismatch of 18.42% in this arrangement. Because of a smaller lattice mismatch, the former arrangement of the unit cells of the two phases is suggested.

The room temperature hysteresis curves of the bilayers: (a) Y_2Co_{17} (5 nm) and YCo_5 (25 nm), (b) Y_2Co_{17} (10 nm) and YCo_5 (20 nm), and (c) Y_2Co_{17} (15 nm), and YCo_5 (15 nm) are shown in Fig. 5.17. The hysteresis curves are measured perpendicular (orange spheres) and parallel (grey diamonds) to the substrate plane.

With decreasing thickness of highly anisotropic YCo_5 phase, the area of hysteresis curve measured perpendicular to the film decreases. All these bilayers exhibit an overall in-plane anisotropy. The saturation magnetization of the bilayer heterostructure increase, as expected, with increase in the thickness of Y_2Co_{17} layer. In all the cases, the phases are magnetically exchange coupled as indicated by smooth and continuous magnetization curves.

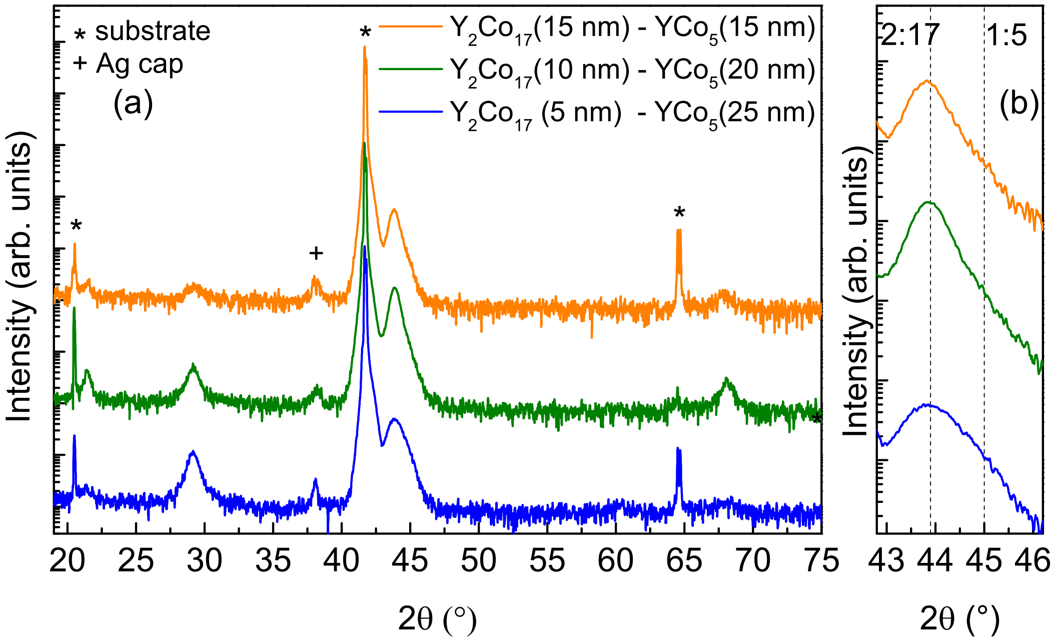

Figure 5.16: (a) $\theta - 2\theta$ scans of Y_2Co_{17} - YCo_5 bilayers with Y_2Co_{17} grown directly on Al_2O_3 substrate and then YCo_5 layer on top. (b) Magnified view of the Y-Co film peaks with vertical dashed lines indicating the Bragg angle of 004 Y_2Co_{17} (2:17) and 002 YCo_5 (1:5) phases.

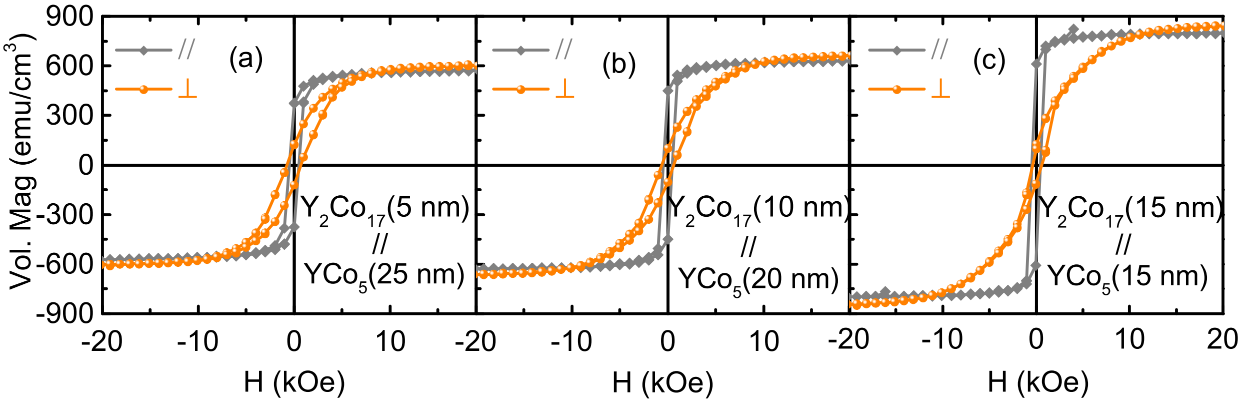

Figure 5.17: Room temperature hysteresis curves of Y_2Co_{17} - YCo_5 bilayers measured perpendicular (orange) and parallel (grey) to substrate with thicknesses: (a) Y_2Co_{17} (5 nm) and YCo_5 (25 nm), (b) Y_2Co_{17} (10 nm) and YCo_5 (20 nm), and (c) Y_2Co_{17} (15 nm) and YCo_5 (15 nm).

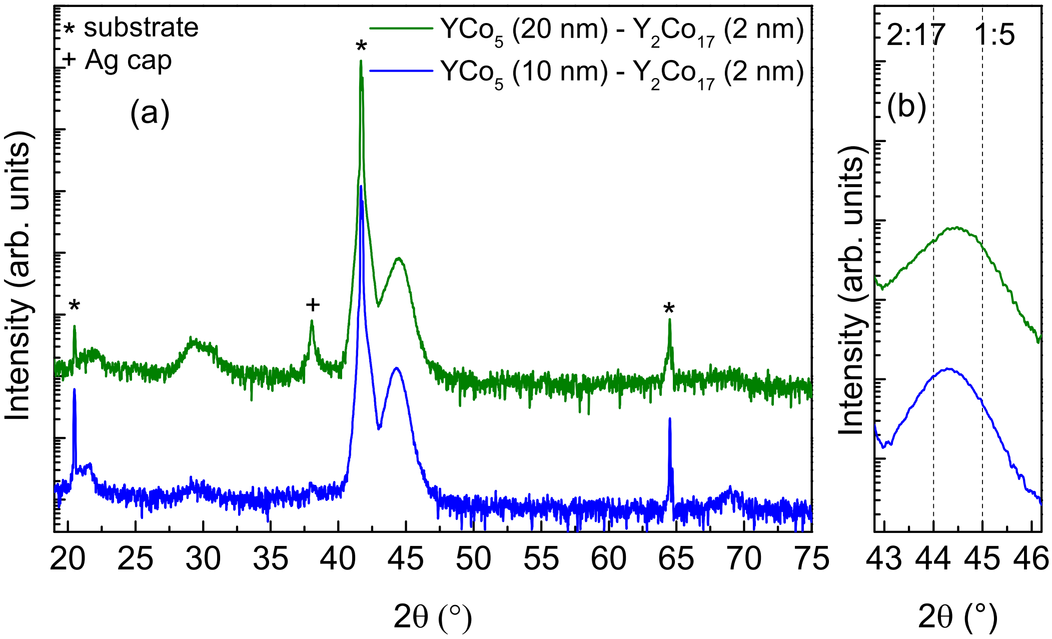

Figure 5.18: (a) X-ray diffraction scans of YCo_5 - Y_2Co_{17} bilayer stack with YCo_5 grown directly on Al_2O_3 substrate and then Y_2Co_{17} layer on top. (b) Magnified view of the Y-Co film peaks with vertical dashed lines indicating the Bragg angle of 004 Y_2Co_{17} (2:17) and 002 YCo_5 (1:5) phases.

5.6.2 Y_2Co_{17} on YCo_5 on Al_2O_3

Here, YCo_5 phase is synthesized directly on Al_2O_3 substrate and then Y_2Co_{17} layer is grown above it. Two bilayer hetrostructures with different thicknesses of hard magnetic layer are grown: (a) YCo_5 (10 nm) and Y_2Co_{17} (2 nm), and (b) YCo_5 (20 nm) and Y_2Co_{17} (2nm). Fig. 5.18 shows $\theta - 2\theta$ scans of YCo_5 - Y_2Co_{17} bilayers. A magnified view of the film peaks in the region between 42.9° and 46° is shown in Fig. 5.18(b) with vertical dashed lines indicating the Bragg angle of 004 Y_2Co_{17} (2:17) and 002 YCo_5 (1:5) phases.

It is observed that the position of the $00l$ reflection of the bilayer is in between that of Y_2Co_{17} and YCo_5 phases with the peak shifted to the 002 reflection of YCo_5 phase with increasing YCo_5 thickness. In both the films, a single c-lattice constant is obtained indicating that when YCo_5 film is grown initially on the substrate, the lattice of the Y_2Co_{17} phase adjusts itself to the lattice of YCo_5 phase beneath in such a way that a single c spacing is observed or the thickness of Y_2Co_{17} layer is so small that it cannot be detected in XRD.

The hysteresis curves of the bilayers: (a) YCo_5 (10 nm) - Y_2Co_{17} (2 nm), (b) YCo_5 (20 nm) - Y_2Co_{17} (2 nm) are shown in Fig. 5.19(a) and Fig. 5.19(b), respectively. These were measured perpendicular ($\perp$, orange spheres) and parallel ($\|$, grey diamonds) to the film plane at room temperature.

It can be seen that in both the films, the hysteresis curve measured perpendicular to the bilayers is larger than the in-plane hysteresis curve. Thus, the major component of magnetization is normal to heterostructure. The magnetization of the Y_2Co_{17} phase tends to align with YCo_5 phase resulting in an overall perpendicular anisotropy. The magnetization curves are smooth and continuous indicating a strong exchange-interaction between the two phases and these switch simultaneously with applied field. The coercivity of the bilayer stack increases with thickness of hard magnetic phase of YCo_5.

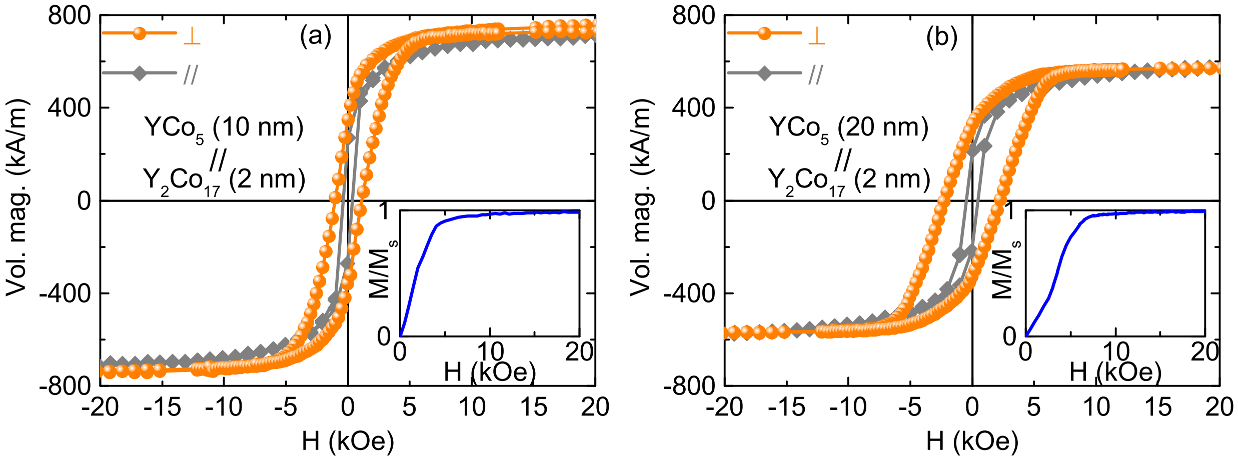

Figure 5.19: Room temperature hysteresis curves measured perpendicular (⊥, orange spheres) and parallel (∥, grey diamonds) to the bilayers: (a) YCo_5 (10 nm) - Y_2Co_{17} (2 nm) (b) YCo_5 (20 nm) - Y_2Co_{17} (2 nm). The corresponding virgin magnetization curves are shown in the insets.

The thickness of the soft magnetic phase is 2 nm which is smaller than the hard magnetic layer as well as the exchange length. Therefore, the magnetization of the Y_2Co_{17} aligns with YCo_5 phase and a perpendicular magnetization is induced in Y_2Co_{17} by exchange-coupling through the epitaxially grown interface.

The initial magnetization curves are shown in the insets of Fig. 5.19(a) and Fig. 5.19(b). A gradual increase in the magnetization indicate that the domain wall movement is impeded during magnetization reversal. However, it is important to look at the microstructure of the bilayers to understand the coercivity mechanism and confirm the layer-by-layer growth of the two phases.

6 Growth and characterization of Ce-Co thin films

In this chapter we describe, the structural and magnetic properties of $CeCo_5$ thin films grown by co-evaporation of cerium and cobalt by molecular beam epitaxy.

6.1 Growth study

To explore the favorable growth conditions for $CeCo_5$ thin films, the deposition temperature and evaporation rates of Ce and Co were systematically varied in a series of experiments. The targeted thickness of the films was $30\,\mathrm{nm}$. Similar to the Y-Co system, the formation of $CeCo_5$ phase was achieved at an evaporation rate ratio 1 between the rare-earth and cobalt.

Fig. 6.1 shows the out-of-plane (θ-2θ) XRD pattern of an optimized $CeCo_5$ thin film. The film was grown at rates of Ce of 0.10 Å/s and Co of 0.10 Å/s at a temperature of $500\,^{\circ}\mathrm{C}$. The film peak at 44.44° is attributed to 002 reflection of $CeCo_5$ [130, 131]. Its lower and higher order reflections are also observed. The appearance of strong 00*l* reflections indicates that the film is *c*-axis oriented. Other reflections corresponding to the substrate, Al_2O_3 006 at 41.67° and the cap layer, Ag 111 at 38.18° are also observed. At the used elevated temperature of $500\,^{\circ}\mathrm{C}$, Ce reacts with oxygen from the substrate or residual oxygen in the chamber to form CeO_2 and Ce_2O_3. Such nanocrystalline inclusions give rise to broad peaks at about 28° and 52°. The rather good crystallinity of the Ce oxides suggests oxidation through the substrate as also reported for Nd-Fe-B and Sm-Co thin films [69, 132, 133]. A possible way to suppress oxide formation could be an increase of the deposition rate.

The inset (a) of Fig. 6.1 shows the rocking curve of the 002 reflection giving information about film mosaicity. A small mosaic spread characterized by a FWHM of 0.21° suggests a strong degree of (00*l*) texture. A closer look at the line shape reveals two contributing features, a sharp and narrow central peak of high intensity superimposed on a broad peak of low intensity with long tails. The sharp peak is attributed to the epitaxial layer giving rise to coherent scattering of X-rays, while the broad peak is due to dislocation induced diffused scattering of X-rays. The film thickness and roughness were determined by fitting the XRR fringes (not shown). The film thicknesses varied between 30 and 31 nm, and the RMS roughness was below 1 nm. Such low roughness is consistent with streaky RHEED patterns observed during growth as shown in inset (b) of Fig. 6.1.

6.2 Epitaxy

To determine the epitaxial relationship between film and substrate, ϕ-scans of the film 201 reflection ($2\theta = 48.76^{\circ}$, $\chi = 62.72^{\circ}$) and of the substrate 104 reflection ($2\theta = 35.13^{\circ}$, $\chi = 38.23^{\circ}$) were performed. Fig. 6.2 shows a ϕ-scan of a (001) oriented $CeCo_5$ film (orange) on a (001) oriented Al_2O_3 substrate (green). As Al_2O_3 is rhombohedral, the 104 reflection shows three-fold symmetry. The three peaks are $\bar{1}14$, $0\bar{1}4$ and 104. The presence of a six-fold symmetry of the 201 peak of $CeCo_5$ confirms its hexagonal crystal structure

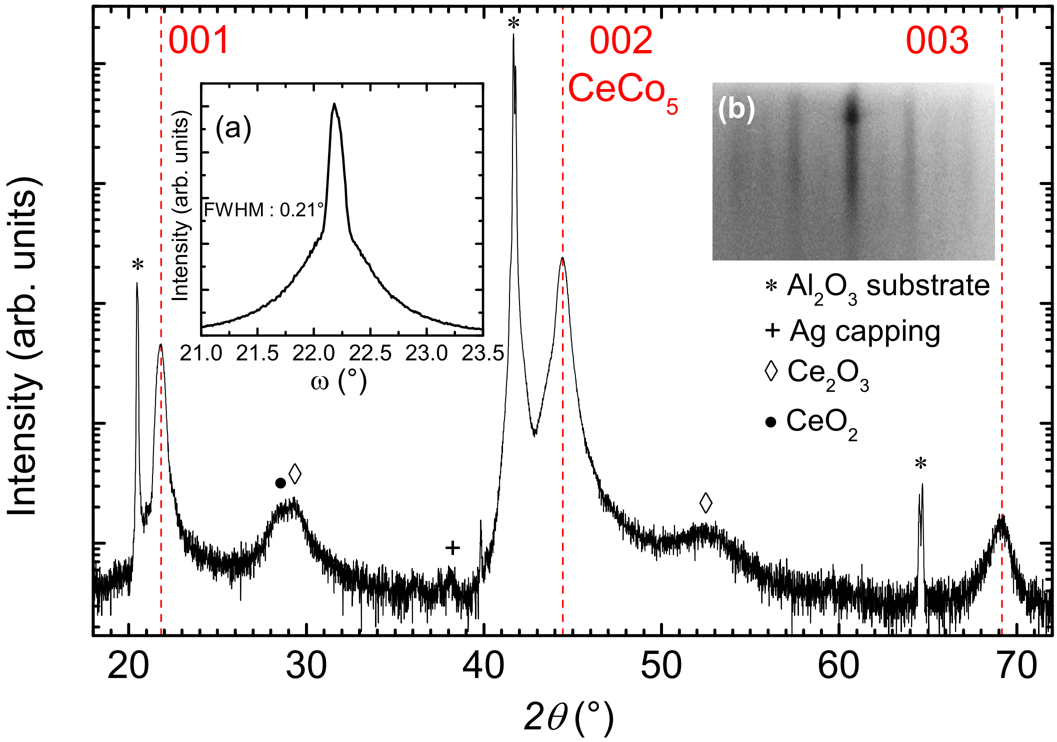

Figure 6.1: X-ray diffraction pattern of a 30 nm (001)-oriented $CeCo_5$ film grown onto a (001) Al_2O_3 substrate at $500\,°C$. The evaporation rates of Ce and Co were 0.10 Å/s. The inset (a) shows the rocking curve of the 002 Bragg peak, and (b) shows the RHEED pattern of the corresponding film at the end of deposition along the Al_2O_3 [11-20] azimuth.

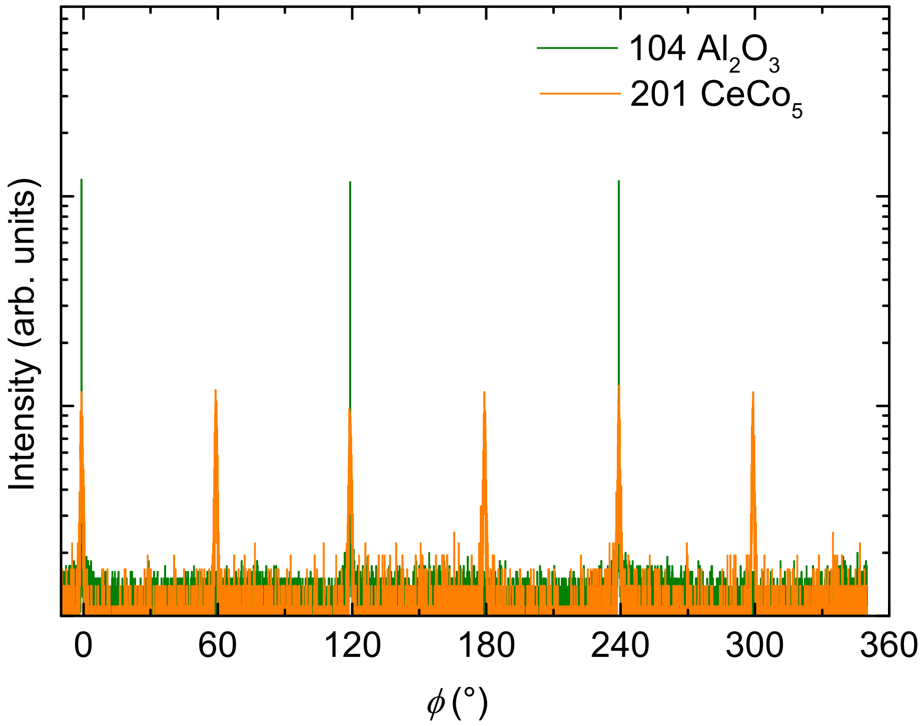

Figure 6.2: ϕ-scans of the 201 $CeCo_5$ and the 104 Al_2O_3 reflections.

with the c-axis perpendicular to film plane. The six peaks observed are: 201, $\bar{2}01$, 021, $0\bar{2}1$, $2\bar{2}1$ and $\bar{2}21$. The following epitaxial relation is derived;

$CeCo_5$ (001) || Al_2O_3 (001); $CeCo_5$ [100] || Al_2O_3 [100]

Furthermore, the out-of-plane lattice constant, c, was calculated from the 002 reflection to be 4.072 Å, and the in-plane lattice constant, a, was determined from the 201 reflection to be 4.837 Å. As a is smaller and c larger than the corresponding bulk values, the thin film was under compressive strain due to the lattice mismatch of 3.42 %. Small deviations from the exact stoichiometry in the $R\mathrm{Co}_5$ compounds can also lead to varying lattice constants.

6.3 Magnetization measurements

The magnetization, M, was measured as a function of applied field, H, in two directions, perpendicular and parallel to the film plane at temperatures from 5 K to 300 K. Fig. 6.3(a) and Fig. 6.3(b) show the M-H curves measured both, perpendicular (solid blue spheres) and parallel (open green diamonds) to the film plane at 5 K and 300 K, respectively. It can be seen that perpendicular to the film plane, the saturation magnetization, remanent magnetization, and coercivity are higher than along the film plane. This shows that the easy-axis of magnetization is aligned perpendicular to the film plane, i.e. it is parallel to the structural c-axis. However, still a small coercivity is observed in the in-plane hysteresis curve. This can be attributed to a slight misorientation of the grains, as apparent from the rocking curve (see inset (a) of Fig. 6.1). Another noticeable feature is the magnetization anisotropy which is the difference of magnetization of the easy and hard axis after saturation. It is characterized by $p = (M_{\mathrm{easy}} - M_{\mathrm{hard}})/M_{\mathrm{s}}$,

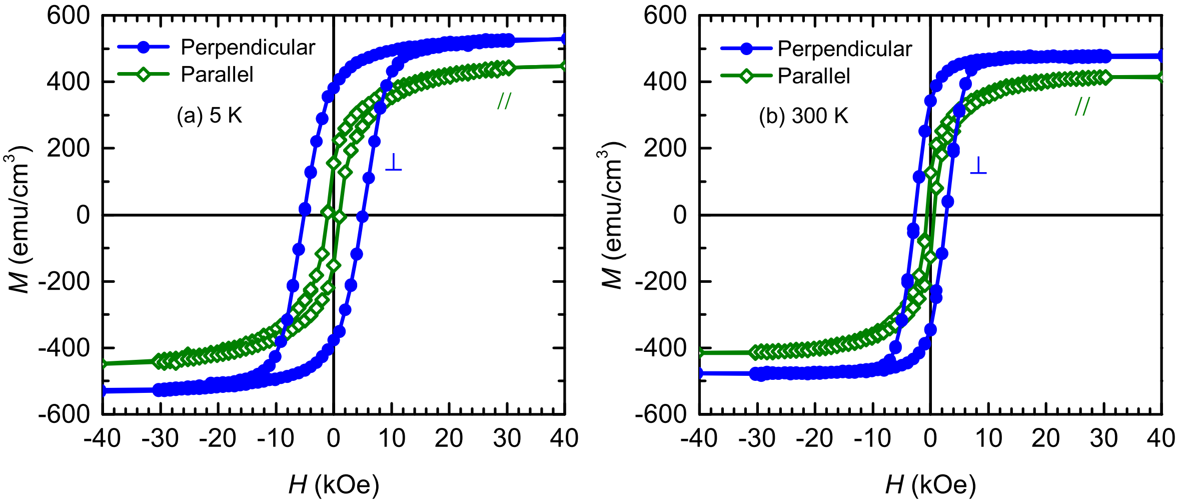

Figure 6.3: Magnetization, M, versus applied field, H, measured perpendicular (solid blue spheres) and parallel (open green diamonds) to the film plane at (a) 5 K and (b) 300 K.

where M_{easy}, M_{hard}, and M_{s} are easy axis, hard axis, and saturation magnetization, respectively. Callen *et al.* first predicted this phenomenon of magnetization anisotropy, and it was observed in various intermetallic systems including YCo_5 and $CeCo_5$ [120, 121, 119, 38].

In our experiments on $CeCo_5$ thin films, the highest observed M_{s} was 527 emu/cm^3 with $p = 15.50\,\%$ at 5 K (see Fig. 6.3(a)) and 476.03 emu/cm^3 with $p = 13.05\,\%$ at 300 K (see Fig. 6.3(b)), both perpendicular to the film plane. Bulk single crystals are reported to have a slightly higher magnetization of 612 emu/cm^3 at room temperature [37]. The presence of amorphous/nanocrystalline oxide residuals obviously lowers the magnetization of the thin films. Bartashevich *et al.* measured a smaller p for bulk single crystals of about 12 % at 5 K and 9 % at 300 K [38]. They attributed this temperature dependence of p to mixed-valent states of Ce. It is remarkable that the thin films have an enhanced magnetization anisotropy as compared to single crystals. The reduction of p as a function of temperature is consistent with literature indicating the temperature driven change in occupation number of the Ce $4f$ states.

6.3.1 Temperature dependence of coercivity

The temperature dependence of coercivity is plotted in Fig. 6.4, both perpendicular (solid blue spheres) and parallel (open green diamonds) to the film plane, from 5 to 300 K. At all temperatures, the coercivity measured perpendicular to the film plane is larger than parallel to the film plane which signifies perpendicular magnetic anisotropy. Adding further, it can be seen that the coercivity decreases with increase in temperature from 5.16 kOe at 5 K to 2.74 kOe at 300 K. The thermal stability of coercivity is expressed by the temperature coefficient which is defined as $\beta = [H_{\text{c}}(T) - H_{\text{c}}(300)]/[H_{\text{c}}(300) \times (T - 300)]$, where $H_{\text{c}}(300)$ and $H_{\text{c}}(T)$ represent the coercivity at 300 K and a temperature T, respectively. A negative temperature coefficient, β of -0.304 %K^{-1} in perpendicular direction and -0.153 %K^{-1} in parallel direction was measured within the temperature range of 5 - 300 K.

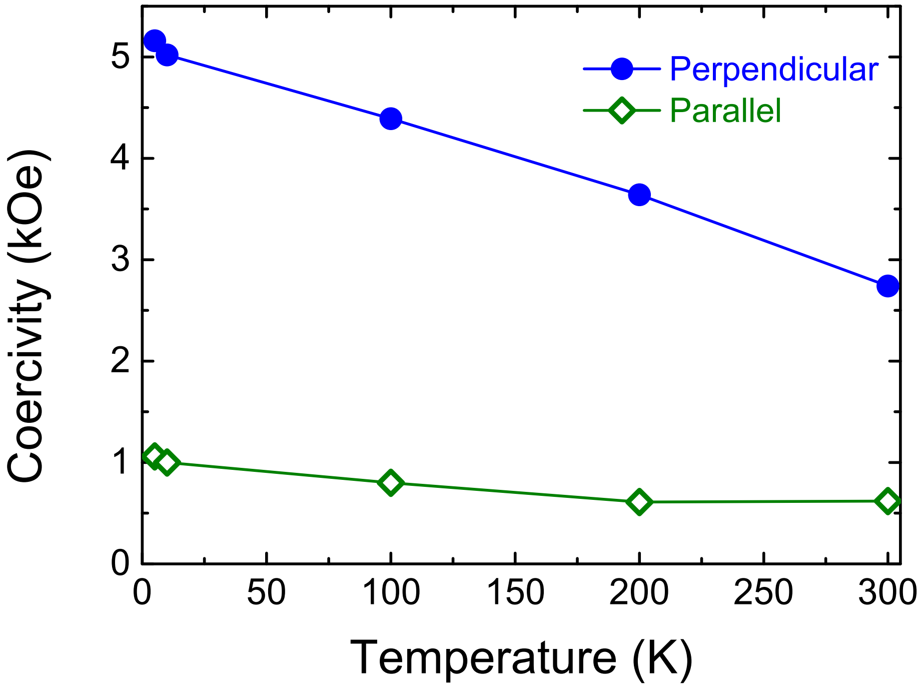

Figure 6.4: Temperature dependence of coercivity, perpendicular (solid blue spheres) and parallel (open green diamonds) to the film plane.

6.4 Anisotropy measurement

Angular dependent magnetic torque measurements were used to determine the value of the first anisotropy constant and the anisotropy field from 10 K to 300 K. Fig. 6.5 shows the torque measured while a 30 nm thin film sample was rotated from 0° to 360° under an external magnetic field of 14 T at 300 K. At 0°, the film is aligned normal to the applied field and at 90° it is aligned parallel. The measured torque curve is a slightly distorted sine wave. The two-fold symmetry of the torque curve indicates two-fold symmetry of the axis of magnetization (easy and hard). The torque per unit volume curves obtained at fields from 2 to 14 T, are fitted by a Fourier series. The Fourier coefficients (amplitudes) of the two-fold symmetry component ($sin(2\theta)$), *A'*, and the four-fold symmetry component ($sin(4\theta)$), *B'*, which are relevant for a hexagonal system, are extrapolated to infinite field ($1/H = 0$). As described by Worst *et al.*, from these extrapolated coefficients, *A* and *B*, the values of K_1 and K_2 were derived using $A = K_1 + K_2 - 2\pi M_s^2$ and $B = -1/2K_2$ where -$2\pi M_s^2$ is the shape anisotropy energy term [106]. We obtained $K_1 = 0.44\,\mathrm{MJ/m^3}$ at 300 K corresponding to an anisotropy field of 18.48 kOe, and $K_1 = 0.82\,\mathrm{MJ/m^3}$ at 10 K corresponding to an anisotropy field of 32.94 kOe.

6.5 Thin film magnetic phase diagram

The results on the growth and magnetic properties of the Ce-Co thin films are summarized in the form of a magnetic phase diagram is shown in Fig. 6.6. The saturation magnetization and coercivity (in the perpendicular direction) of 30 nm Ce-Co thin films grown at $500\,^\circ\mathrm{C}$ are plotted as a function of deposition rate ratio Ce to Co [134]. The magnetization of bulk (*B*) $CeCo_5$ and Ce_2Co_{17} single crystals are marked

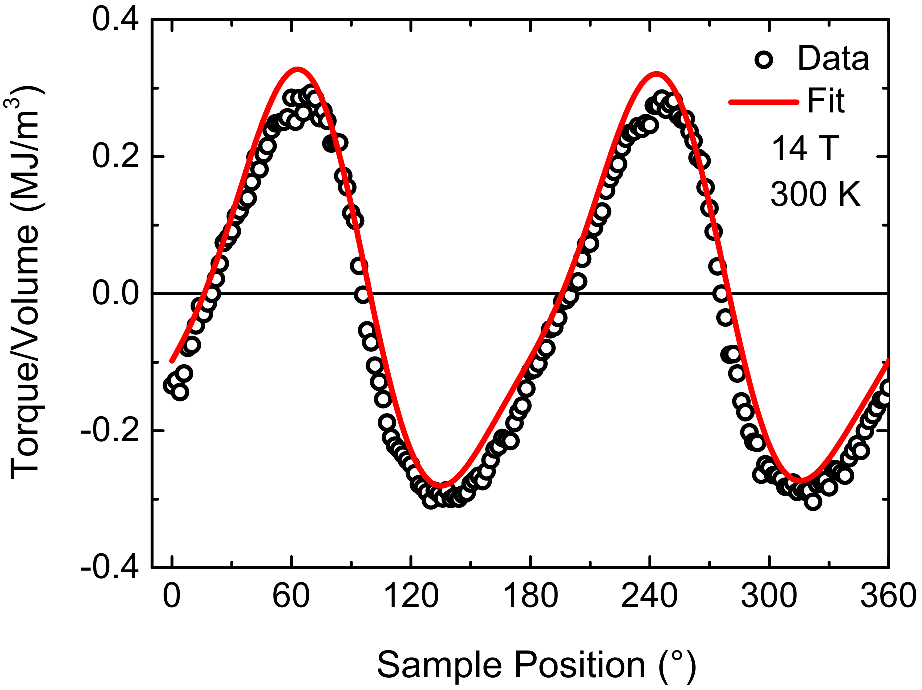

Figure 6.5: Angular dependence of torque per unit volume measured at 300 K and 14 T with actual data points (open black circles) and fit (red line).

with arrows on the magnetization axis. Taking into account the mass and density of Ce and Co, the ratio of the rates of Ce to Co required to obtain the 1:5 phase in MBE is calculated to be 0.625 (marked by an arrow on the ratio axis). Experimentally, the 1:5 phase is formed at a higher rate ratio. This indicates that incorporation probability of Ce into the crystal structure is below 1. A part of the excess Ce contributes to the observed oxide formation. With increasing Ce to Co ratio from 0, the soft magnetic Ce_2Co_{17} phase (bulk H_A of 14 kOe) forms first, followed by the highly anisotropic $CeCo_5$ phase (bulk H_A of 210 kOe [43]). With further increase in the ratio from 1 onwards, the magnetization as well as coercivity drops dramatically due to the progressing dilution of the Co system.

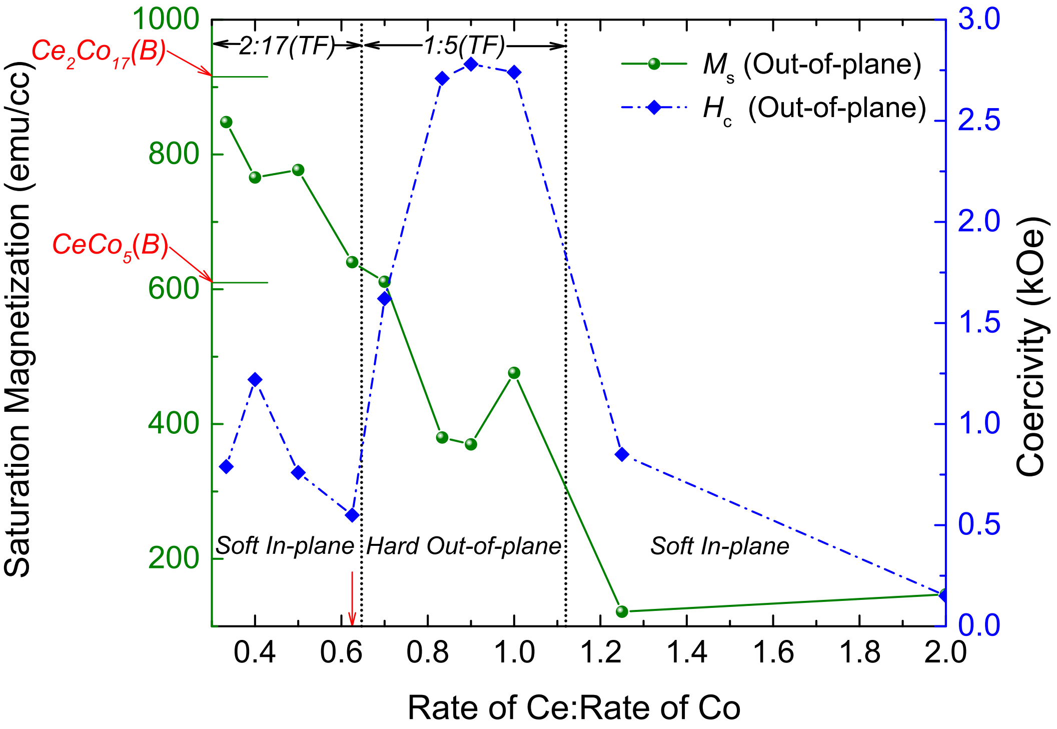

Figure 6.6: Magnetic phase diagram with saturation magnetization and coercivity of Ce-Co thin films (TF) as a function of rate ratio of Ce to Co [134]. The magnetization of bulk (B) $CeCo_5$ and Ce_2Co_{17} single crystals are marked with red arrows on magnetization axis (y-axis). The calculated ratio for $CeCo_5$ phase is marked with red arrow on ratio axis (x-axis).

7 Growth and characterization of Sm-Co thin films

In this chapter, the structural and magnetic properties of buffer free Sm-Co thin films are investigated. The effect of growth temperature and evaporation rates of samarium and cobalt are studied. A detailed analysis of the atomic structure of the film is also provided.

7.1 Growth temperature study

For growing $SmCo_5$ thin films by co-evaporation, the required ratio of atomic flux of Sm and Co was calculated by taking into account the atomic mass and density of the two elements, to be $R_{\mathrm{Co}} = 1.655 \times R_{\mathrm{Sm}}$, where R_{Co} and R_{Sm} are the growth rates of Co and Sm respectively.

To estimate the growth temperature window for $SmCo_5$ films, the first temperature scan was carried at evaporation rates of Co of 0.1 Å/s and Sm of 0.165 Å/s. Fig. 7.1 shows the Sm-Co thin films grown at calibrated substrate temperatures from 300 °C to 700 °C.

The reflections corresponding to the 006 Al_2O_3 substrate at 41.67° (along with its lower and higher order peaks) and the 111 Ag cap layer at 38.18° are marked. It can be seen that at 300 °C and 400 °C, there is no reflection corresponding to Sm-Co phase observed. A highly crystalline Sm-Co phase with weak oscillatory peaks corresponding to Laue oscillations is formed at 600 °C. At 700 °C, the intensity of the peak is reduced. Thus, 600 °C was selected as the optimum temperature for the growth of Sm-Co thin films.

7.1.1 Magnetization measurements

The magnetic hysteresis curves of the Sm-Co films measured at room temperature, perpendicular (out-of-plane, OP) and parallel (in-plane, IP) to the films are shown in Fig. 7.2. It can be seen in Fig. 7.2(a), that at 500 °C, the hysteresis curves measured perpendicular and parallel to the film plane are similar indicating that the magnetic properties are isotropic. The Sm-Co film grown at 600 °C, has the highest magnetization, as shown in Fig. 7.2(b). From the hysteresis curves, it can be seen that the easy-axis of magnetization is perpendicular to the film plane and the hard-axis lies in the film plane with a large anisotropy field greater than 5 T.

From combined XRD and magnetization measurements, the highest crystallinity and anisotropy was achieved at 600 °C. Thus, a thorough scan of the evaporation rates of Sm and Co was performed at 600 °C.

7.2 Evaporation rate study

In the bulk Sm-Co equilibrium phase diagram, starting from the Co rich side, the Sm_2Co_{17} phase is formed first followed by the $SmCo_5$ phase with decreasing Co or increasing Sm content. To realize this in our experiments, we deposited thin films using both the approaches. In the first approach, the evaporation rate

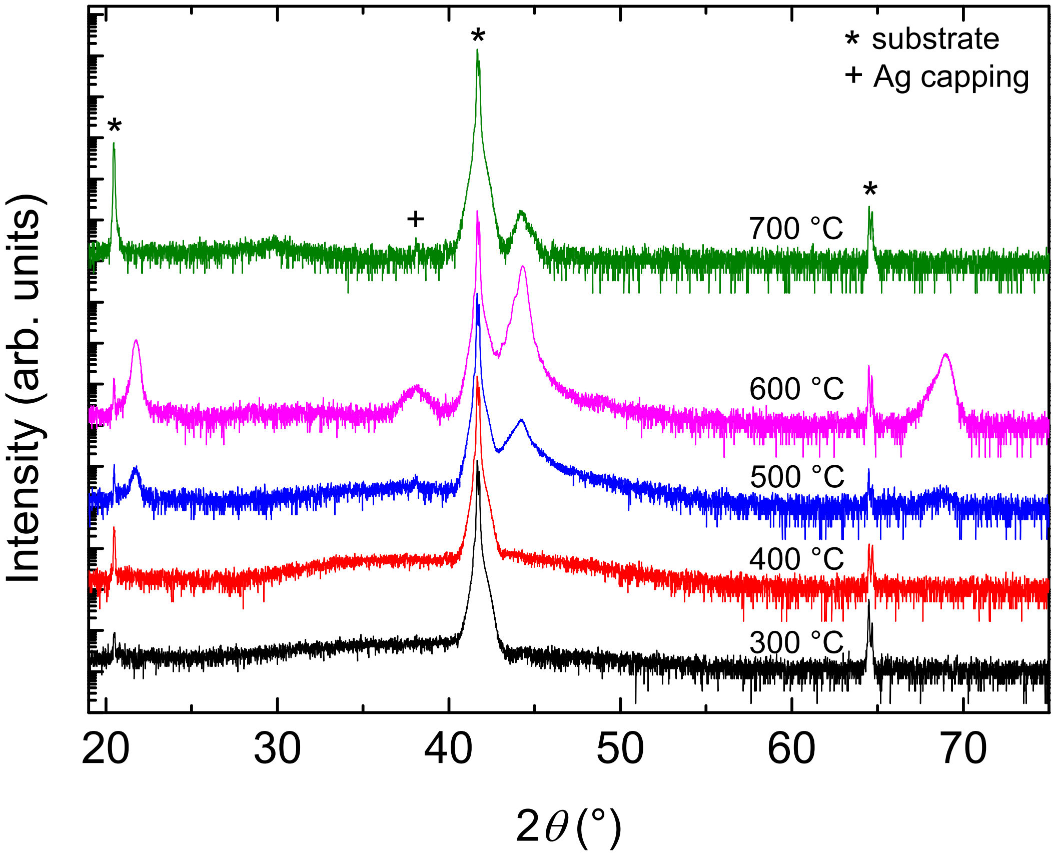

Figure 7.1: X-ray diffraction patterns of Sm-Co thin films grown onto (001)-oriented Al_2O_3 substrate at temperatures from 300 °C to 700 °C at evaporation rate of Sm of 0.10 Å/s and Co rate of 0.165 Å/s.

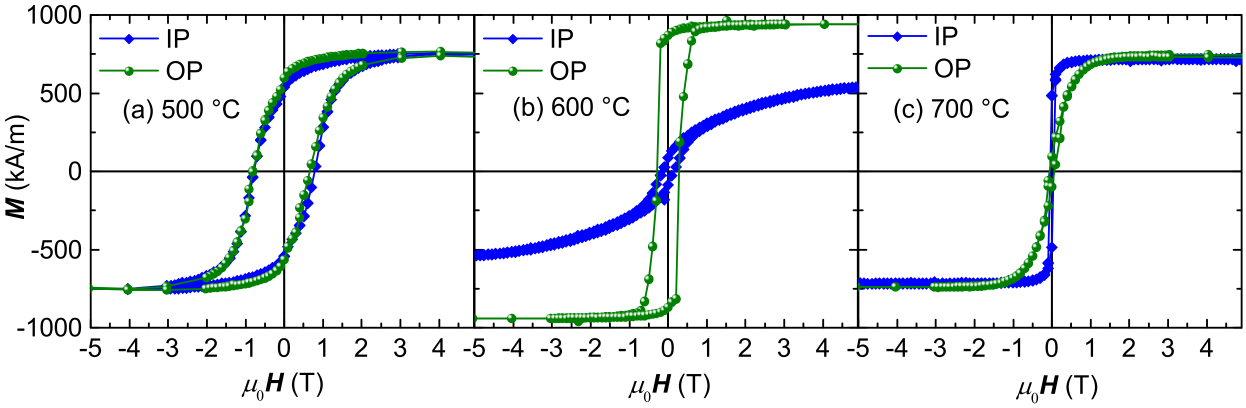

Figure 7.2: Room temperature M-H curves measured perpendicular (green spheres) and parallel (blue diamonds) to the plane of Sm-Co films deposited at growth temperatures increasing from (a) 500°C (b) 600°C, and (c) 700°C.

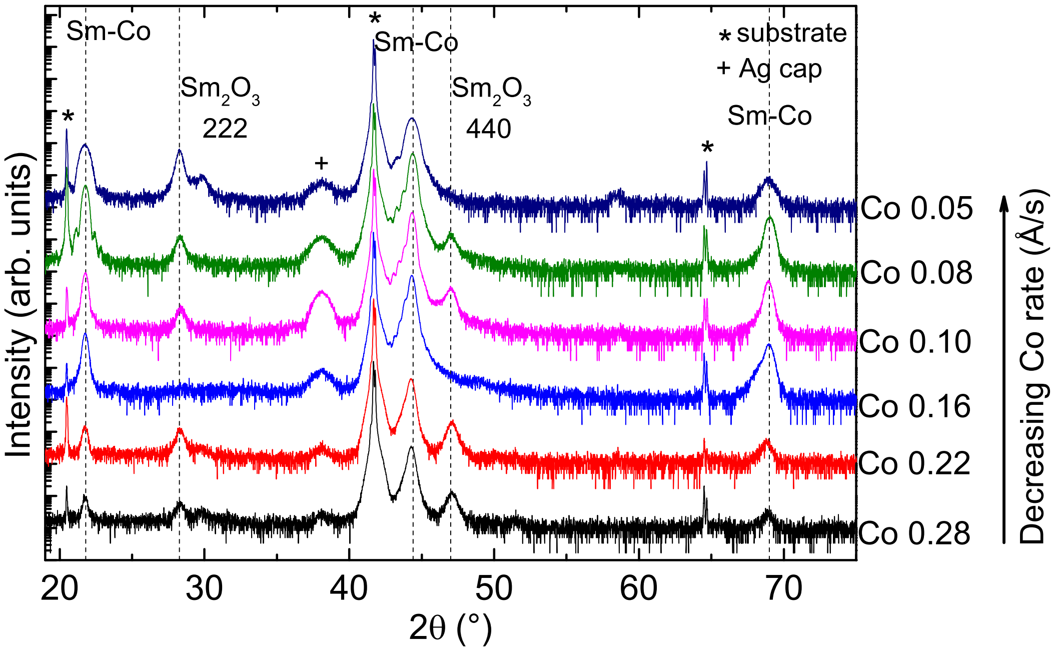

Figure 7.3: X-ray diffraction patterns of Sm-Co thin films grown onto (001)-oriented Al_2O_3 substrates at $600\,°C$. The evaporation rate of Sm is fixed at 0.1 Å/s while the Co rate is decreased from 0.28 Å/s to 0.05 Å/s.

of Sm is kept constant and the Co rate is gradually decreased. In the second approach, the Co rate was kept constant while the Sm rate is gradually increased.

7.2.1 Decreasing cobalt rates

Fig. 7.3 shows X-ray diffraction patterns of the Sm-Co thin films grown at 600°C in which the evaporation rate of Sm is fixed at 0.1 Å/s while the Co rate is decreased from 0.28 Å/s to 0.05 Å/s. With decreasing Co evaporation rate, there is no systematic trend observed in the peak position around 44.3° corresponding to intermetallic Sm-Co phase as the films are not phase pure. Additional peaks corresponding to oxidized form of Sm; 222 reflection at 28.26° and 440 reflection at 47° of Sm_2O_3 are present [135]. Thus, in order to approach $SmCo_5$ phase, the evaporation rate of samarium is increased as described in the next section.

7.2.2 Increasing samarium rates

After fine tuning of the growth temperature in a series of experiments, the samarium rate scan was performed at the optimized temperature of $540\,°C$. Fig. 7.4 shows the XRD patterns of the Sm-Co films deposited at $540\,°C$ with increasing Sm rate from 0.04 Å/s to 0.75 Å/s at a fixed Co rate of 0.25 Å/s. The thickness of the films varied between 30 and 31 nm, as determined by fitting the XRR fringes. The (001)-oriented single crystalline Al_2O_3 substrate promotes the growth of $(00l)$ oriented films which are marked by plus signs in the graph [136].

The appearance of strong $(00l)$ reflections indicate that the Sm-Co films are c-axis oriented. For Sm rates from 0.04 Å/s to 0.10 Å/s, the film peak (around 44°) shifts to lower angles. This is due to the expanding c

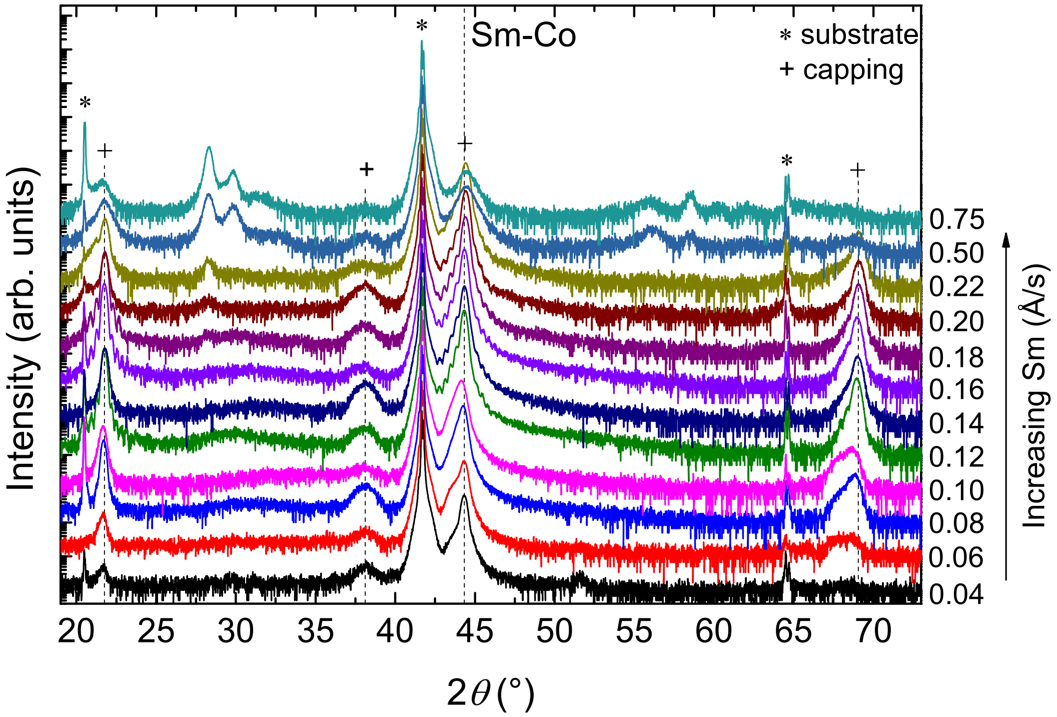

Figure 7.4: X-ray diffraction patterns of Sm-Co thin films grown onto (001)-oriented Al_2O_3 substrates at 540 °C. The evaporation rate of Sm is increased from 0.04 Å/s to 0.75 Å/s while the Co rate is fixed at 0.25 Å/s.

lattice constant of the strained film (due to lattice mismatch) when structure evolves from almost pure Co to Sm_2Co_{17} [137, 138]. With further increase in the Sm rate from 0.12 Å/s onwards, this peak shifts to higher angles which is due to the shrinkage of the lattice when the structure evolves from Sm_2Co_{17} (compressive strain of 1.2%) into the $SmCo_5$ phase (compressive strain of 5.1%). The high crystal quality of the films (for Sm rates from 0.12 Å/s to 0.22 Å/s) is demonstrated by the appearance of Laue oscillations for $00l$ reflections. The corresponding RHEED patterns of the films consistently were streaky, indicative of atomically smooth film surface. The peak positions for the films deposited at Sm rates of 0.18-0.20 Å/s are close to 44.40° which can be attributed to the 002 reflection of the $SmCo_5$ phase. However, these are still lower than that for bulk $SmCo_5$ [139, 140]. From a Sm rate of 0.20 Å/s, the intensity of the Sm peak (at 28.31° and 29.83°) started to increase, indicating an excess of Sm in the films. The films grown at Sm rates of 0.50 Å/s and 0.75 Å/s become polycrystalline with appearance of additional peaks between 55° and 60°. Therefore, the rate of Sm is not increased beyond 0.75 Å/s. The respective 2θ value of the ($00l$) type reflection around 44° for all the Sm-Co films is shown in Fig. 7.5. A detailed structural characterization of the optimized $SmCo_5$ film is shown in Fig. 7.6.

7.3 Epitaxial relations

The X-ray diffraction pattern, $\theta-2\theta$ scan of the optimized $SmCo_5$ film grown onto (001)-Al_2O_3 substrate at 540°C is shown in Fig. 7.6(a). The film is grown at evaporation rate of Sm of 0.16 Å/s and Co rate of 0.25 Å/s. (b) $\theta-2\theta$ measurement showing the 002 $SmCo_5$ reflection with Laue oscillations with the

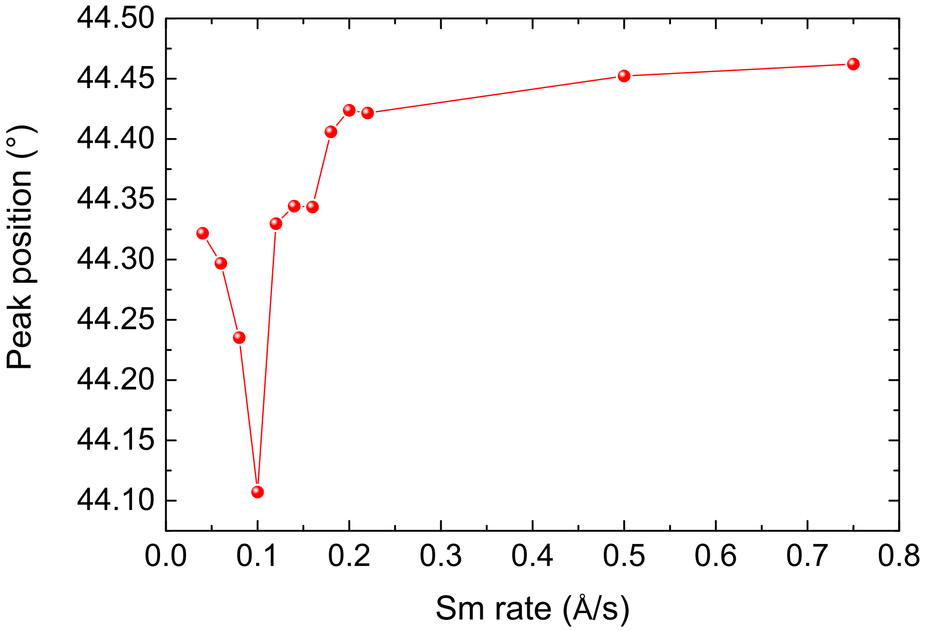

Figure 7.5: 2θ value of the (00l) type reflection around 44° for Sm-Co thin films as a function of Sm rate.

corresponding rocking curve is shown inset.

A ϕ-scan of $(00l)$-oriented $SmCo_5$ film (green) on a (001)-oriented Al_2O_3 substrate (grey) is shown in Fig. 7.6(c). The ϕ-scan of the 104 reflection ($2\theta = 35.0304°$, $\chi = 38.027°$) of Al_2O_3 which is rhombohedral, shows three peaks indicating three-fold symmetry. The three peaks are $\bar{1}14$, $0\bar{1}4$ and 104. The ϕ-scan of 201 reflection of $SmCo_5$ ($2\theta = 48.7791°$, $\chi = 63.022°$) shows six-fold symmetry which confirms the hexagonal crystal structure. The six peaks observed are: 201, $\bar{2}01$, 021, $0\bar{2}1$, $2\bar{2}1$ and $\bar{2}21$. It shows that film grows epitaxially on the Al_2O_3 substrate. The following epitaxial relation was derived:

$SmCo_5$ (001) $\|$ Al_2O_3 (001); $SmCo_5$ [100] $\|$ Al_2O_3 [100]

The pole figure measurement of the 201 reflection of $SmCo_5$ at $2\theta = 48.7791°$ is shown in Fig. 7.6(d). The tilt angle χ is scanned from 0° to 90° and the in-plane rotation angle, ϕ, is scanned from 0° to 360° around the sample surface. The intense reflections corresponding to the 201-type Bragg peaks are shown in green while the other less intense peaks in grey. A narrow distribution of the 201-equivalent reflections indicate the film is highly crystalline and strongly textured.

7.3.1 Magnetization measurements

The magnetization, M, is measured with applied field, H, in two directions, perpendicular and parallel to the film plane at room temperature. Fig. 7.7 shows the M-H curves for increasing Sm rates from 0.04 Å/s (a) to 0.75 Å/s (l), perpendicular ($\perp$, green spheres) and parallel ($\|$, purple, diamonds) to the film plane.

The hysteresis curves show that for Sm rates of 0.04 Å/s (a) and 0.06 Å/s (b), the easy-axis of magnetization lies in the plane of the film and the hard-axis is perpendicular to it. The ratio of remanent magnetization, M_r, to saturation magnetization, M_s, describing the squareness ratio is far from one in the perpendicular

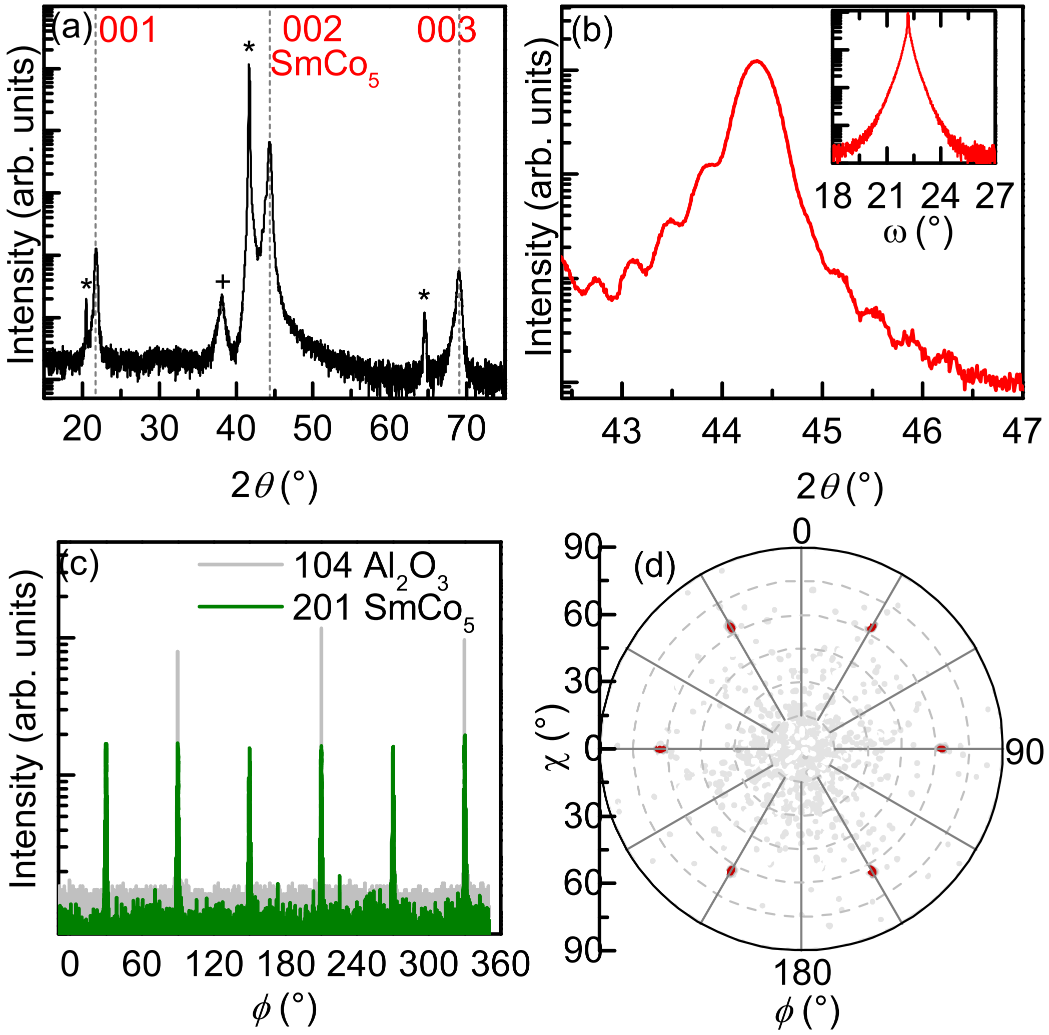

Figure 7.6: (a) X-ray diffraction pattern of Sm-Co thin film grown onto (001)-oriented Al_2O_3 substrate at 540°C. The film is grown at evaporation rate of Sm of 0.16 Å/s and Co rate of 0.25 Å/s. (b) $\theta - 2\theta$ measurement showing the 002 Sm-Co reflection with Laue oscillations and the corresponding rocking curve shown inset. (c) ϕ scans of 104 reflection of Al_2O_3 substrate (grey) and 201 reflection of $SmCo_5$ (green). (d) Pole figure measurement of 201 $SmCo_5$ reflection.

direction. The large magnetization of the films gives rise to large shape anisotropy energy ($2\pi M_s^2$). Therefore, in these films a dominating in-plane shape anisotropy is observed [136].

For Sm rates of 0.08 Å/s (c) and 0.10 Å/s (d), the out-of-plane hysteresis curve somewhat surpasses the in-plane hysteresis curve. Here, the perpendicular component of the anisotropy slightly exceeds the shape anisotropy of the film and, hence, a transition from in-plane to out-of-plane anisotropy is observed. The squareness ratio is slightly less than one.

With further increase in the Sm rate from 0.12 Å/s (e) onwards, there is a marked difference between the hysteresis curves measured in two directions. A larger out-of-plane hysteresis curve with higher M_r, M_s, and coercivity is observed as compared to the in-plane hysteresis curve. In these films, the easy-axis of magnetization is aligned normal to the film plane, i.e. it is parallel to the structural *c*-axis. Additionally, the squareness ratio is close to unity perpendicular to film plane. The origin of perpendicular anisotropy is considered to be uniaxial magnetocrystalline anisotropy associated with the *c*-axis textured growth of $SmCo_5$ normal to the film plane.

In Fig. 7.8, the saturation magnetization, M_s, and the first anisotropy constant, K_1, of the Sm-Co thin films are plotted as a function of Sm rate. The values for bulk (B) Sm_2Co_{17} and $SmCo_5$ single crystals are also marked [141, 37]. With an increase in Sm rate, the M_s of the films decreases. The Sm atoms substitute the Co atoms in such a way that the Sm_2Co_{17} phase gives way to the $SmCo_5$ phase [142]. For Sm rates between 0.16 Å/s and 0.18 Å/s, the saturation magnetization of the thin films is identical to that of bulk $SmCo_5$. As discussed in the previous section, from a Sm rate of 0.20 Å/s onwards, an excess of Sm in the films results in reduced magnetization.

The magnitude of K_1 of the thin films is derived using the formula, $K_1 = (M_s \times H_s)/2$ where H_s is the field at which the hard-axis magnetization curve saturates [143]. The general trend of anisotropy of Sm-Co thin films with increasing Sm rate can be clearly observed. From a Sm rate of 0.06 Å/s, there is a jump in the value of K_1, which increases further with increasing Sm rate. It reaches a maximum value of 2.38 MJ/m^3 for the films deposited at Sm rates of 0.14 Å/s and 0.16 Å/s. Such large anisotropy of the films corresponds to the formation of $SmCo_5$ phase. With further increase in the Sm rate from 0.18 Å/s onwards, the anisotropy declines because of an excess of residual Sm in the films.

7.4 Anisotropy measurements

The torque required to rotate the saturation magnetization away from the easy-axis is measured as a function of angle of rotation for the Sm-Co thin films. The thin film is rotated from 0° to 360° in the presence of a constant magnetic field. At 0°, the film plane is perpendicular to the applied field and at 90°, it is parallel.

Fig. 7.9 shows the torque curves measured for four films with increasing Sm rates of 0.08 (a), 0.16 (b), 0.20 (c), and 0.50 Å/s (d) at 14 T and 300 K. From the torque curve shown in Fig. 7.9(a), it seems that there is no definite magnetic texture in the film. This behavior is a result of competing anisotropies in the film. In the corresponding magnetization curve shown in Fig. 7.7(c), the area of the out-of-plane hysteresis curve is barely larger than that of the in-plane curve indicating that the magnetic properties are more isotropic. Apparently, in this case, the magnetocrystalline anisotropy is slightly greater than or comparable to the shape anisotropy of the films and, hence, a very small net torque per unit volume is observed. On the contrary, the torque curves shown in Fig. 7.9(b) and (c) are attributed to distinct perpendicular magnetic anisotropy. They are complementary to the magnetization data shown in Fig. 7.7(g) and (i). The two-fold

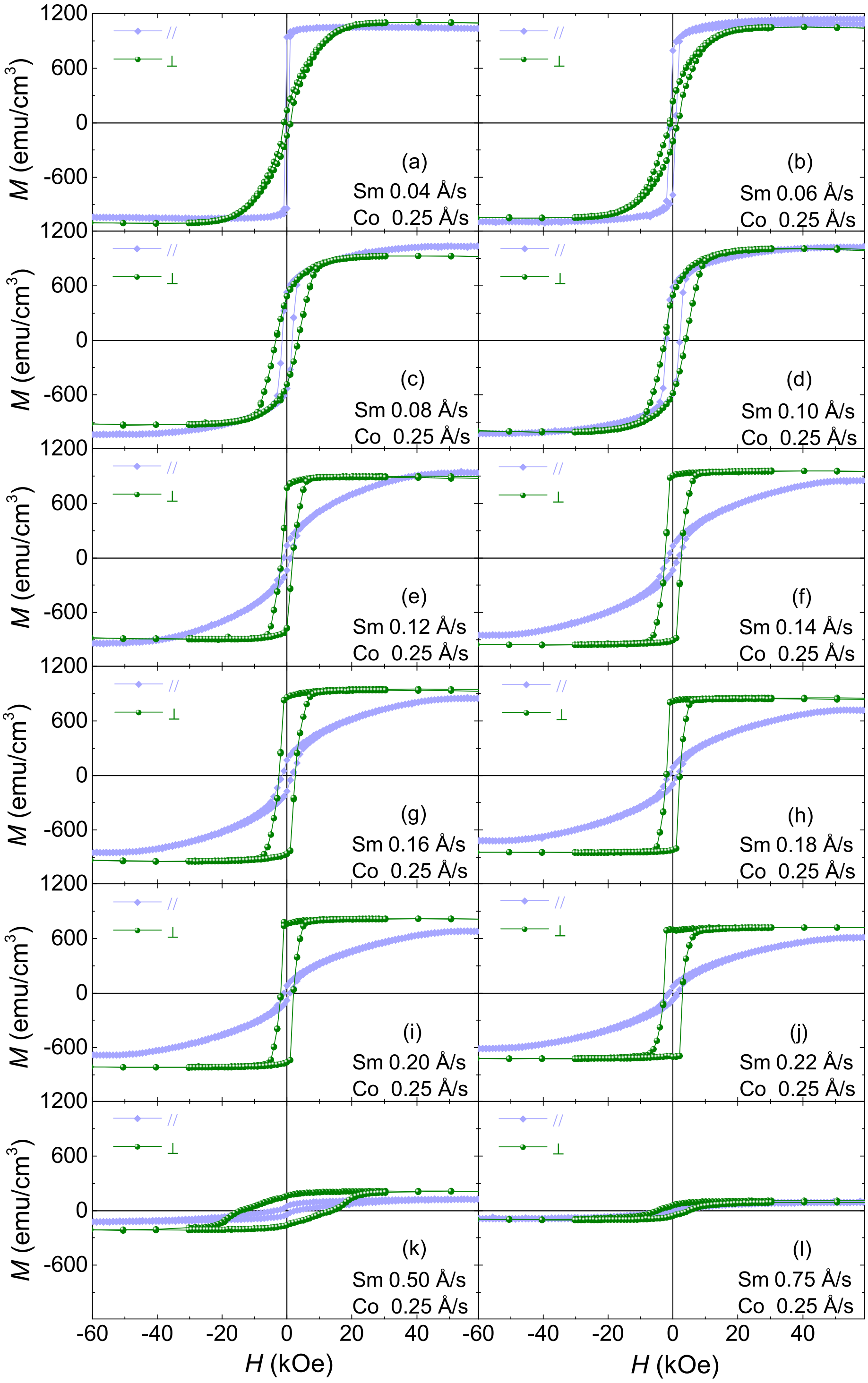

Figure 7.7: Room temperature M-H curves measured perpendicular ($\perp$, green spheres) and parallel ($\parallel$, purple, diamonds) to the plane of Sm-Co films deposited with increasing Sm rate from 0.04 Å/s (a) to 0.75 Å/s (l) and a fixed Co rate of 0.25 Å/s.

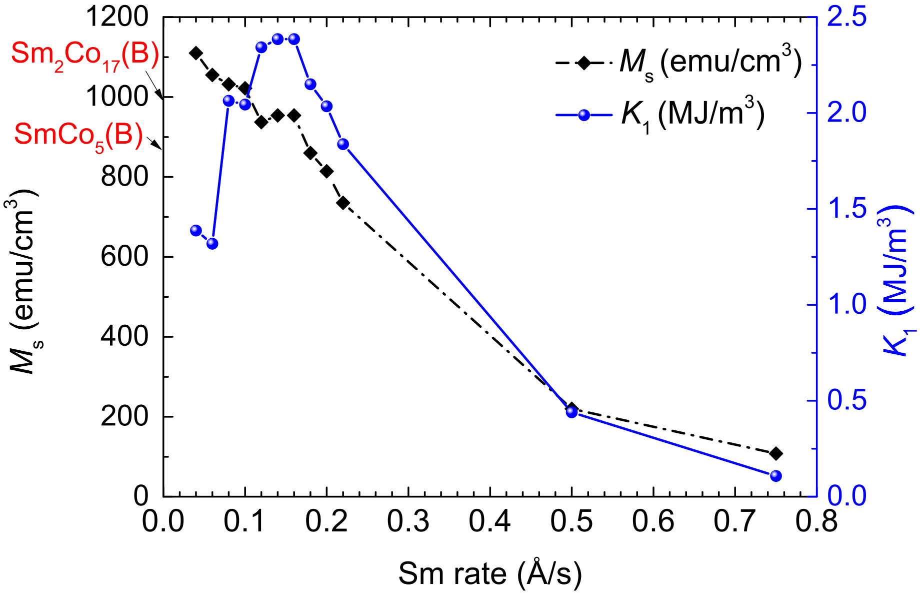

Figure 7.8: The saturation magnetization, M_s, of Sm-Co thin films and their respective first anisotropy constant, K_1, at 300 K, as a function of Sm rate. The magnetization of bulk (B) Sm_2Co_{17} and $SmCo_5$ are marked.

symmetry of the torque curves (with a period of about 180°) is characteristic of the uniaxial magnetic anisotropy with the easy-axis of magnetization perpendicular to film plane [144]. The torque curve shown in Fig. 7.9(d) is a kind of sawtooth wave with smaller perpendicular magnetic anisotropy. Although, the film has the largest coercivity of 14 kOe (see Fig. 7.7(k)), the magnetic anisotropy is small. This indicates that the coercivity is extrinsically induced by excess Sm which in turn reduces the net magnetic moment of the film. The presence of low-anisotropic phases (see the corresponding XRD pattern in Fig. 7.4) could in addition minimize the anisotropy of the film.

K_1 is calculated by fitting the torque curve to a Fourier series and by extrapolating the coefficients of the two-fold ($\sin(2\theta)$) and the four-fold ($\sin(4\theta)$) symmetry components to infinite fields ($1/H = 0$) [106]. A maximum value of K_1 of 1.67 MJ/m^3 is obtained for the film deposited at a Sm rate of 0.16 Å/s. The same film also exhibited the highest K_1 of 2.38 MJ/m^3 derived from the hysteresis measurements, as described in the previous section. However, this value of K_1 obtained from hysteresis curves is greater than the one determined from torque measurement. This is because of the overestimation of H_s on extrapolation of hard-axis magnetization curve to saturation.

7.5 Electronic structure

The Sm 3d spectrum shown in Fig. 7.10(a) is a superposition of $3d_{5/2}$ - $3d_{3/2}$ spin-orbit components corresponding to the metallic and oxidized state of samarium with different chemical environments. The position and relative intensities of the Sm 3d peaks are associated with various 4f final states created as a result of the photoemission process. In order to estimate the total amount of Sm in the film, the area under the Sm $3d_{3/2}$ component was used for quantification.

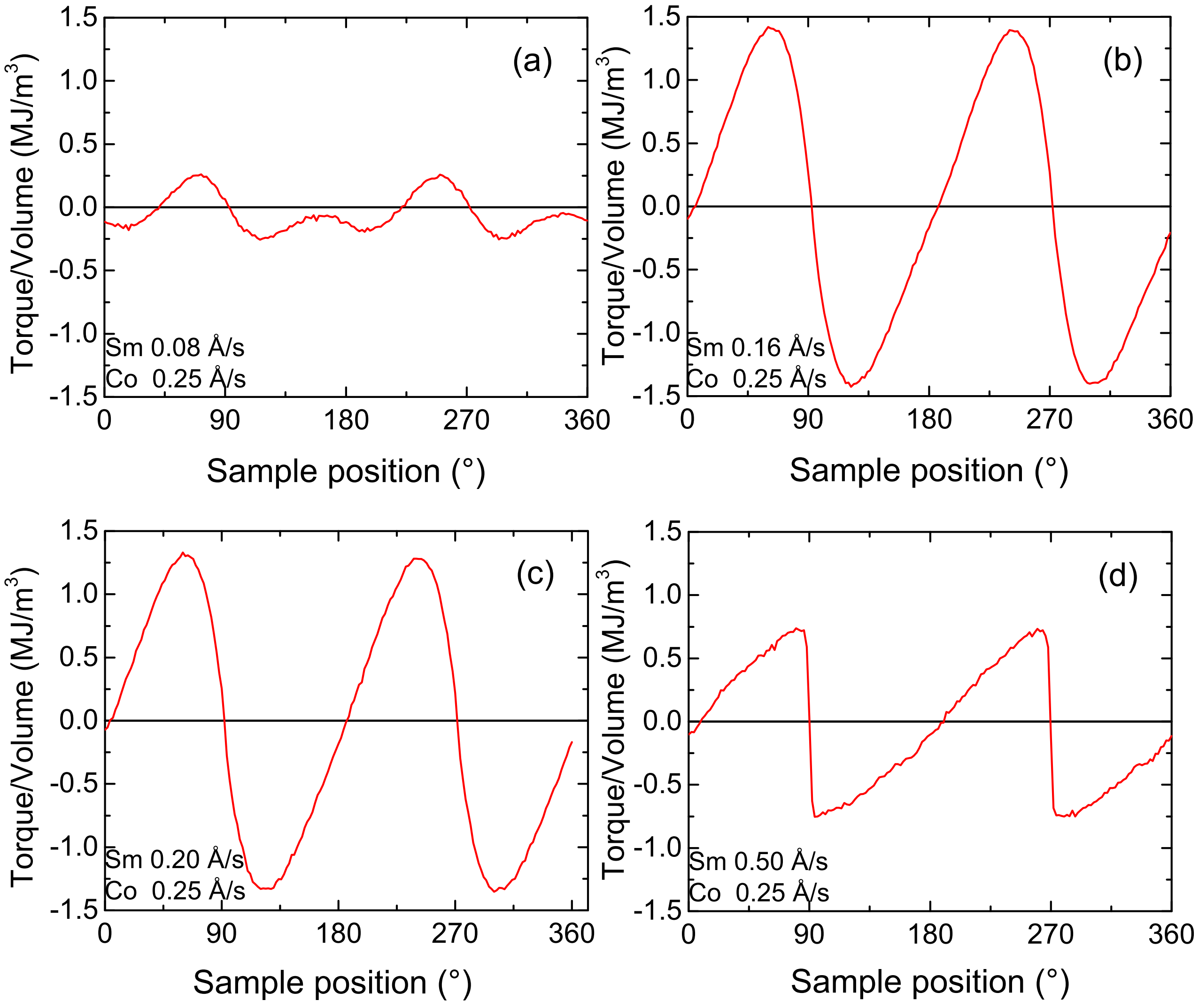

Figure 7.9: Magnetic torque curves measured for Sm-Co thin films deposited at Sm rate of 0.08 (a), 0.16 (b), 0.20 (c), and 0.50 Å/s (d) and Co rate of 0.25 Å/s at 14 T and 300 K.

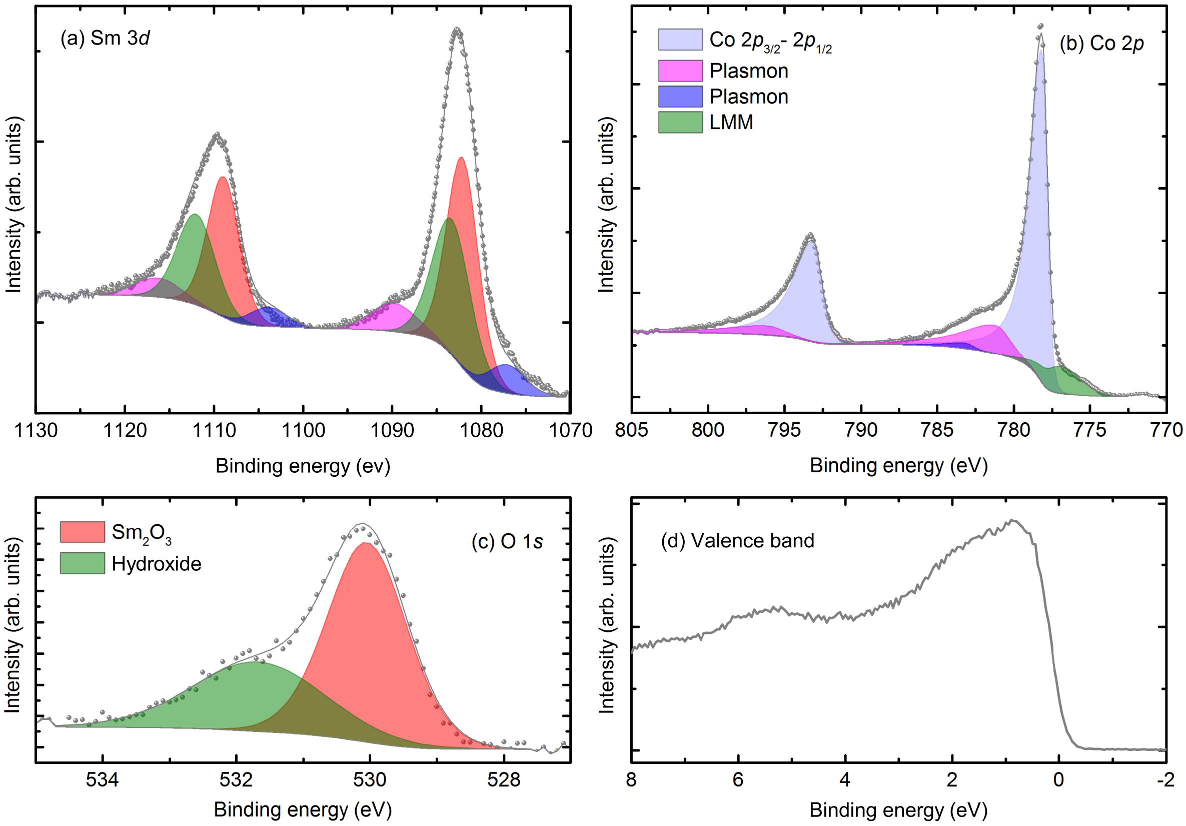

Figure 7.10: X-ray photoelectron spectra of (a) Sm 3d, (b) Co 2p, (c) O 1s levels and the (d) valence band spectrum measured for $SmCo_5$ film.

Fig. 7.10(b) shows the Co 2p photoelectron spectrum with spin-orbit doublets, $2p_{3/2}$ at 778.17 eV and $2p_{1/2}$ at 793.14 eV and a splitting of 14.97 eV. The peaks are fit with Lorentzian asymmetric function given by LA(1.2,5,5) as described in [97]. The position and asymmetric peak shapes are characteristic for metallic Co (Co^0) [145]. XPS studies on rare-earth cobalt intermetallic compounds have suggested that if there is a charge flow, it off the rare-earth sites to cobalt resulting in a small negative shift (0-0.2 eV) of the core level of the compound with respect to the cobalt element [146].

Additionally, two plasmon loss peaks at 3.0 eV and 5.0 eV higher binding energy than the main peak corresponding to the surface and bulk plasmons, respectively, and the Auger $L_3M_{23}M_{45}$ peak at 776.91 eV are also observed in the spectra. An interaction between the photoelectrons and conduction band electrons results in a quantized energy loss (plasmons) because of collective oscillation of the conduction electrons [97, 98].

The O 1s spectrum shown in Fig. 7.10(c) comprises of two components. The peak at higher binding energy of 531.67 eV corresponds to the hydroxide and the component at lower binding energy of 530.04 eV corresponds to Sm_2O_3.

Fig. 7.10(d) shows the valence band spectrum of the $SmCo_5$ film. Samarium contributes about three ($6s^25d^1$) and cobalt contributes about nine ($3d^9$) conduction electrons per atom. In pure Sm, three ($6s^25d^1$) electrons contribute to the valence spectrum from 0-3 eV while the spectrum from 5-10 eV originates from five $4f$ electrons. In $SmCo_5$, there are also five $4f$ electrons, however, in this case there are now 48 conduction electrons contributing to the valence band. Thus, the $4f$ intensity is less in the compound and the valence band spectrum originates mainly from d electrons.

The net concentration of Sm and Co was quantified from the total area under the Sm $3d_{3/2}$ and Co $2p_{1/2}$ peaks. The total Sm concentration in the film was estimated to be 12.03% and the total Co content is 87.97%. The ratio of Sm to Co corresponds to Sm_2Co_{17} phase, considering all of the samarium in the film reacts with cobalt.

7.6 Atomic structure analysis

The atomic structure of the Sm-Co film exhibiting the highest anisotropy was investigated using transmission electron microscopy. It is grown at Sm rate of 0.16 Å/s and Co rate of 0.25 Å/s on (001)-Al_2O_3 substrate. The HAADF-STEM image showing the overview of the Sm-Co film is shown in Fig. 7.11. The film is highly crystalline upto a thickness of 10 nm. Above that, no crystal order was observed. This amorphization of the film was most likely caused during the lamella preparation by focused ion beam. For further experiments, about 300 nm of Au was sputtered on top of the films, to be investigated in order to protect these from the ion beam.

The epitaxial relation of film with the substrate, as described previously, were used to map the crystallographic orientations of the thin film sample. The different crystal directions determined in the real space (grey) and reciprocal space (orange) for a hexagonal unit cell are shown in Fig. 7.12(a). A schematic of the thin film sample with corresponding crystallographic orientations is shown in Fig. 7.12(b). In order to determine the crystal structure of the films, the lamellas were prepared in two different directions indicated by 1 and 2 in Fig. 7.12(a). The position and orientation of the lamella 1 on the surface of the thin film sample was determined using scanning electron microscopy, as shown in Fig. 7.12(c).

The cross-sectional high resolution HAADF-STEM image of the Sm-Co films with lamellas cut in directions indicated by 1 and 2, are shown in Fig. 7.13(a) and Fig. 7.13(b), respectively. The atomic scale resolution

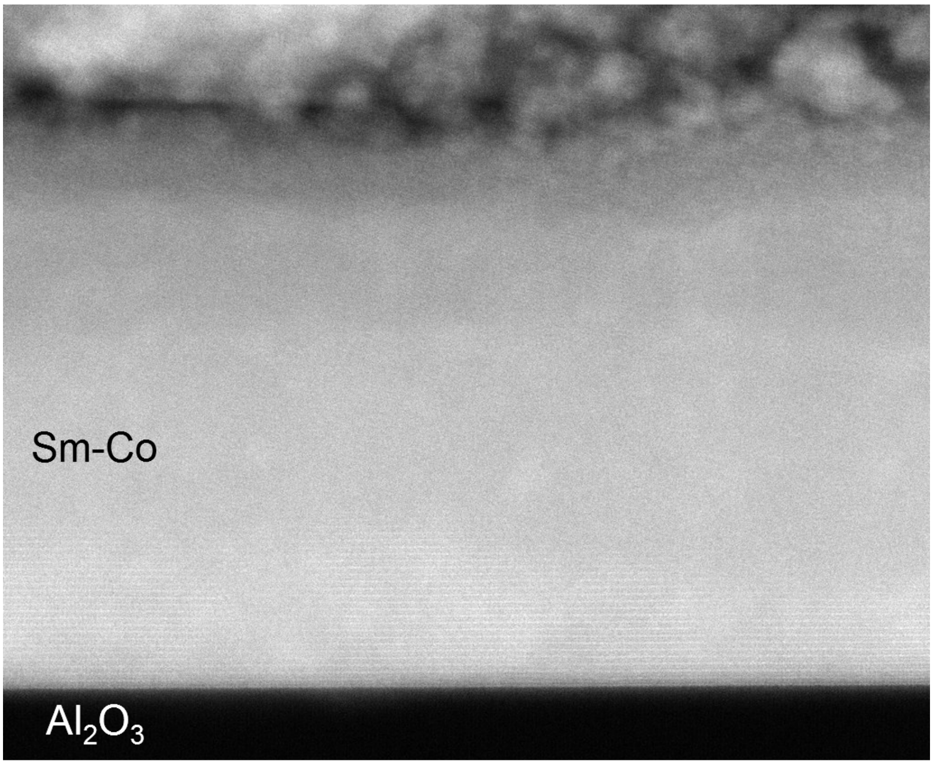

Figure 7.11: The HAADF-STEM image showing the overview of the Sm-Co film grown on (001)-oriented Al_2O_3 substrate.

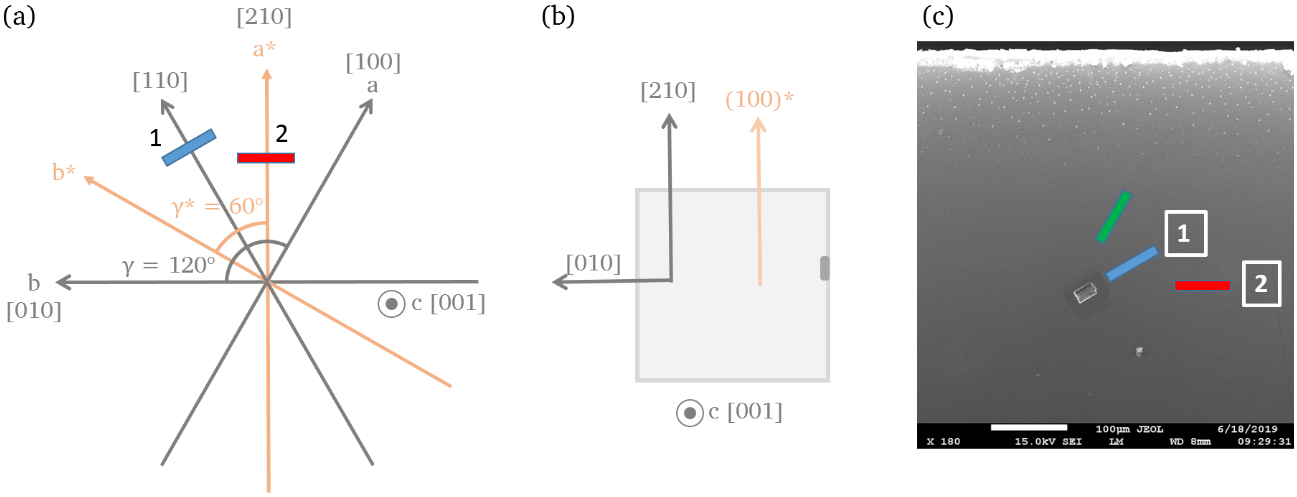
(a)
[210]
a*
[100]
a
[110]
1
2
b*
γ* = 60°
γ = 120°
b
[010]
c [001]
(b)
[210]
(100)*
[010]
c [001]
(c)
1
2
X 180
15.0kV SEI
100µm JEOL
LM
WD 8mm
6/18/2019
09:29:31

Figure 7.12: (a) The crystallographic directions in the real space (grey) and reciprocal space (orange) for hexagonal unit cell mapped for the Sm-Co thin film sample. (b) A schematic of the thin film sample with corresponding crystallographic orientations. (c) Scanning electron microscopy image with the position and orientation of lamella 1 on the surface of the sample.

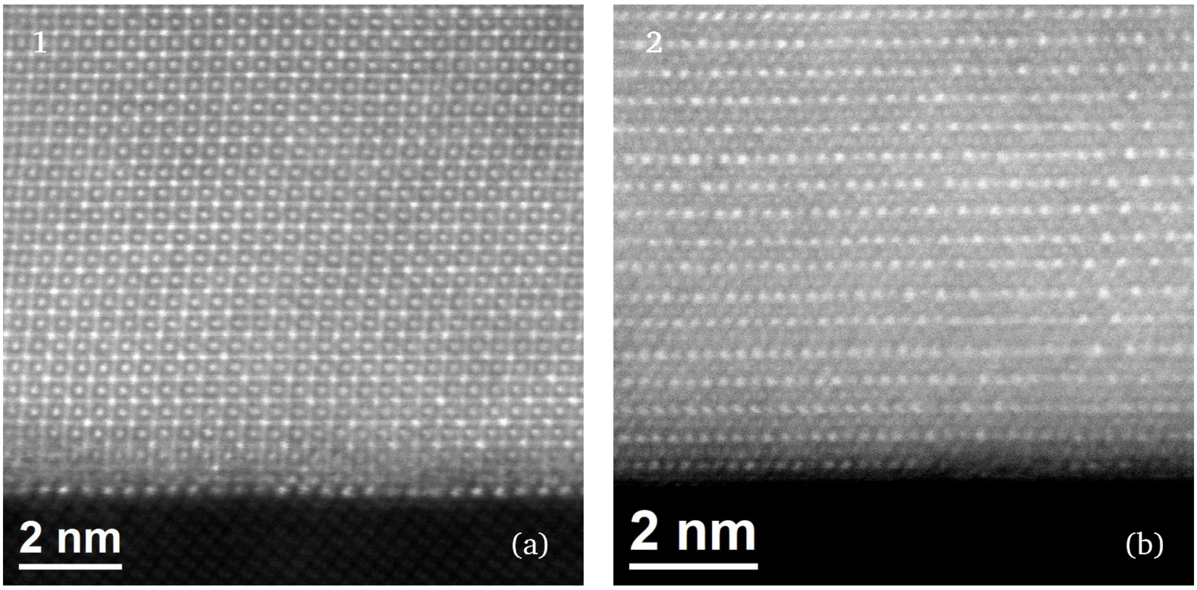

Figure 7.13: The cross-sectional high resolution HAADF-STEM image of the Sm-Co film in two directions, 1 and 2 at 30° to each other as indicated in Fig. 7.12(a).

revealed that the films grow perfectly *c*-axis oriented on the (001)-Al_2O_3 substrate without the use of additional buffer layers. The observed high-resolution contrast in Fig. 7.13(a) resembles strongly the atomic arrangement of *c*-axis oriented either $SmCo_5$ phase viewed along [100] zone-axis or Sm_2Co_{17} projected along [210] zone-axis. Such atomic arrangement was attributed to the $SmCo_5$ phase in [147]. However, the fact is that the crystal structures of the two phases show the same high resolution contrast when simulated along these directions using multislice software. The obtained high resolution contrast resembles either the $SmCo_5$ phase or the Sm_2Co_{17} phase. Other Sm-Co phases can be ruled out as these have an either zig-zag, or a non-linear stacking or doubling of Sm atoms. As it was hard to distinguish the phases in this direction, another lamella (indicated by 2 in Fig. 7.12(c)) was cut at 30° from the first one. Fig. 7.12(b) shows the cross-sectional high resolution HAADF-STEM image of the Sm-Co film viewed at 30° direction from lamella 1. In this case, the first 8 monolayers match perfectly to the $SmCo_5$ phase viewed along [210] zone axis. Above that there are possible traces of the Sm_2Co_{17} projected along the [100] zone-axis. Thus, we cannot completely rule out the presence of Sm_2Co_{17} phase in the film which has a lower anisotropy than the $SmCo_5$. However, STEM imaging can only provide information about a localized region in the sample.

According to the literature reports, thin films of $SmCo_5$ show large coercivity even though it is single phase. In our MBE grown films, there seems to be a trade off between perfect texture and phase purity. The Sm-Co film exhibiting the highest anisotropy is perfectly oriented, however, it is not entirely made up of $SmCo_5$ phase. The nature of arrangement of the two phases at a unit cell level, is still open for discussion. Adding to that, the film which exhibits the largest coercivity could only contain $SmCo_5$ phase, but without any texture. In order to confirm this model, the atomic structure of this particular Sm-Co film needs to be investigated.

8 Growth and characterization of (Y,Ce)Co_5 thin films

One of the ways to enhance the magnetocrystalline anisotropy energy beyond the known limit is by introducing strain in a compound by mechanical means or by chemical substitution. The partial replacement of a rare-earth with another rare-earth of different atomic size modifies the crystal structure and thus, can lead to an increase in the anisotropy energy [148]. In this work, we investigate the effect of substitution of yttrium with more abundant cerium in (Y,Ce)Co_5 intermetallics.

8.1 Structural analysis

Our results on tuning the composition in the *R*-Co system during co-evaporation, have shown that the growth of *R*Co_5 phase is favorable at evaporation rate ratio of 1 between the rare-earth and cobalt. As described in chapters 5 and 6, the high anisotropic phase of YCo_5 and $CeCo_5$ are formed at a ratio of 1 between Y and Co, and Ce and Co, respectively. Thus, for the growth of $(Y_{1-x}Ce_x)Co_5$ films, the ratio of evaporation rate between the rare-earth, Y and Ce, and Co is unity. The sum of the rates of Y and Ce, (Y + Ce), is kept constant at 0.2 Å/s while the individual rates of Y and Ce are varied. The Co rate is fixed at 0.2 Å/s for all the depositions.

The $\theta - 2\theta$ scans of 30 nm $(Y_{1-x}Ce_x)Co_5$ thin films grown on (001)-oriented Al_2O_3 substrate at 575°C are shown in Fig. 8.1. The reflections corresponding to the 006 Al_2O_3 substrate at 41.67° (along with its lower and higher order peaks) and 111 Ag cap layer at 38.18° are marked by asterisk and plus signs, respectively. The (00l)-type reflections corresponding to intermetallics, $(Y_{1-x}Ce_x)Co_5$, are marked by vertical dashed lines.

All the $(Y_{1-x}Ce_x)Co_5$ films crystallize in hexagonal structures as determined from the phi-scan of the films with the substrate. At elevated temperature, the rare-earths reacts with oxygen from the substrate or residual oxygen in the chamber and forms Y_2O_3, Ce_2O_3 and CeO_2. Such nanocrystalline inclusions of the rare-earth oxides give rise to broad reflections around 29° and 55°.

Fig. 8.2 shows the variation of (a) in-plane, *a*, and (b) out-of-plane, *c*, lattice constants of the $(Y_{1-x}Ce_x)Co_5$ intermetallics with Ce concentration, *x*. It can be seen that with increase in Ce content *x* from 0 to 1, *a* decreases and *c* increases, globally. There is a decrease of 0.59% in *a* and an increase of 0.26% in *c*, lattice parameter from YCo_5 to $CeCo_5$. However, this change is not linear and there is a sharp irregularity observed in both *a* and *c* at *x* of 0.6. Similar, trend in the lattice parameters has observed in the unpublished work on $(Y_{1-x}Ce_x)Co_5$ bulk single crystals.

There are different factors on which the lattice parameters depend such as crystal structure, chemical valence and the site where the substitution takes place. The distance between Y and the nearest Co atom along *a*-direction is 2.86 Åand along *c*-direction is 3.17 Å. As the Y-Co distance is smaller in the *a* direction, the effect of substitution is greater on *a* than on *c* lattice parameter. An irregularity in the trend could arise due to the mixed-valent state of cerium ion. The radius of Y^{+3} (1.16 Å) is in between that of Ce^{+3} (1.28 Å) and Ce^{+4} (1.11 Å). If the Y^{+3} are replaced by Ce^{+3} ions, we expect an increase in the c-lattice parameter, however, if Y^{+3} are replaced by Ce^{+4}, the *c*-lattice constant would be smaller. Thus, depending on the amount of Ce^{+3} and Ce^{+4} at each composition, the lattice constant also vary.

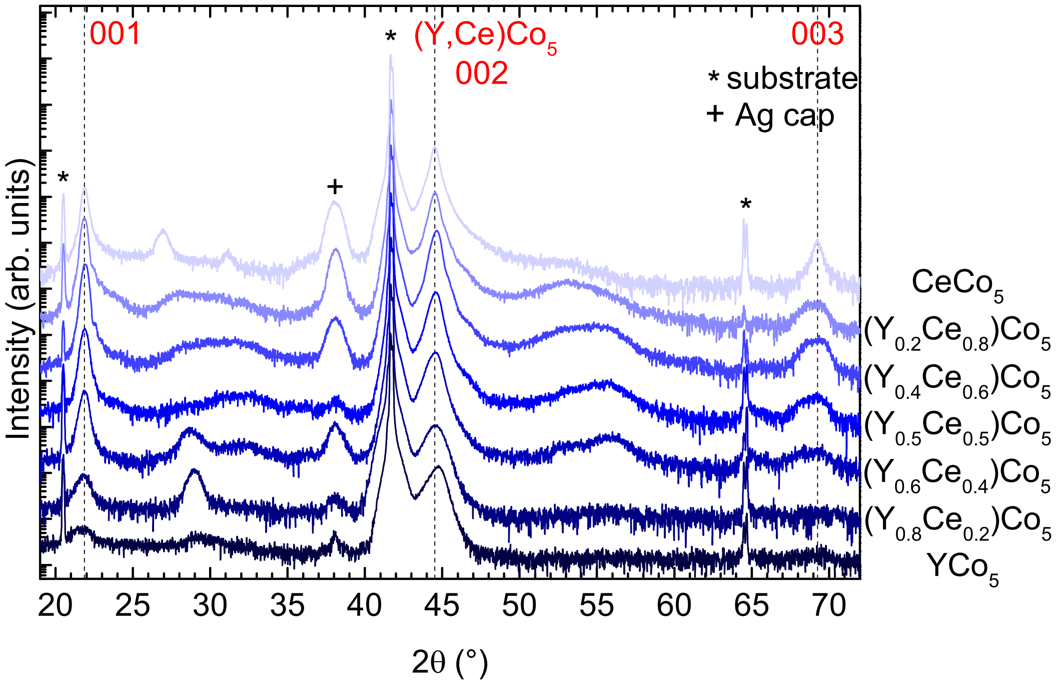

Figure 8.1: X-ray diffraction pattern of a 30 nm (00l)-oriented (Y$_{1-x}$Ce$_x$)Co$_5$ thin films grown at 575°C onto a (001)-oriented Al$_2$O$_3$ substrate.

Another factor which could lead to an irregularity in the lattice constants is the thermodynamic stability of a composition. As an example, if the parent compounds YCo$_5$ and CeCo$_5$ are more stable than a certain mixed composition, then most likely both YCo$_5$ and CeCo$_5$ phases would co-exist rather than the mixed compound. As the lattice constants of YCo$_5$ and CeCo$_5$ are quite close, it is hard to see a separation in the XRD peaks.

8.2 XPS analysis

In cerium, the 4f electron is rather weakly bound, despite the position of the f-shell deeper within the atomic core. According to the chemical environment, the 4f electron remains bound (trivalent), becomes fully itinerant (tetravalent) or resides in a mixed-valent/intermediate state [149]. The valence of Ce fluctuates between +3 and +4 at a frequency of about 10^{-13} Hz. The valence state of cerium in CeCo$_5$ was described to be between +3 and +4 using different techniques. A combined study of lattice parameters, magnetic properties and X-ray absorption (XRA) measurements suggests an almost tetravalent state [150]. A different analysis of the L_{III} XRA spectra estimates the cerium valence to be +3.29 [151]. Bartashevich *et al.* concluded from the temperature dependence of the magnetocrystalline and magnetization anisotropy of bulk CeCo$_5$ crystals that Ce is in a mixed-valence state between Ce^{+3} and Ce^{+4}.

There are a number of reports in literature where the substitution of a (critical) rare-earth with cerium results in anomalies in the structural and magnetic properties of the material. Scattered lattice parameters and an abnormal increase of the coercivity was observed by substituting 20 at% of Ce in NdFeB magnet [152]. The reason for this behaviour was attributed to the variation in the valence state of Ce in these alloys. Thus, it is important to determine the valency of cerium ions in the films. Note that in the case of

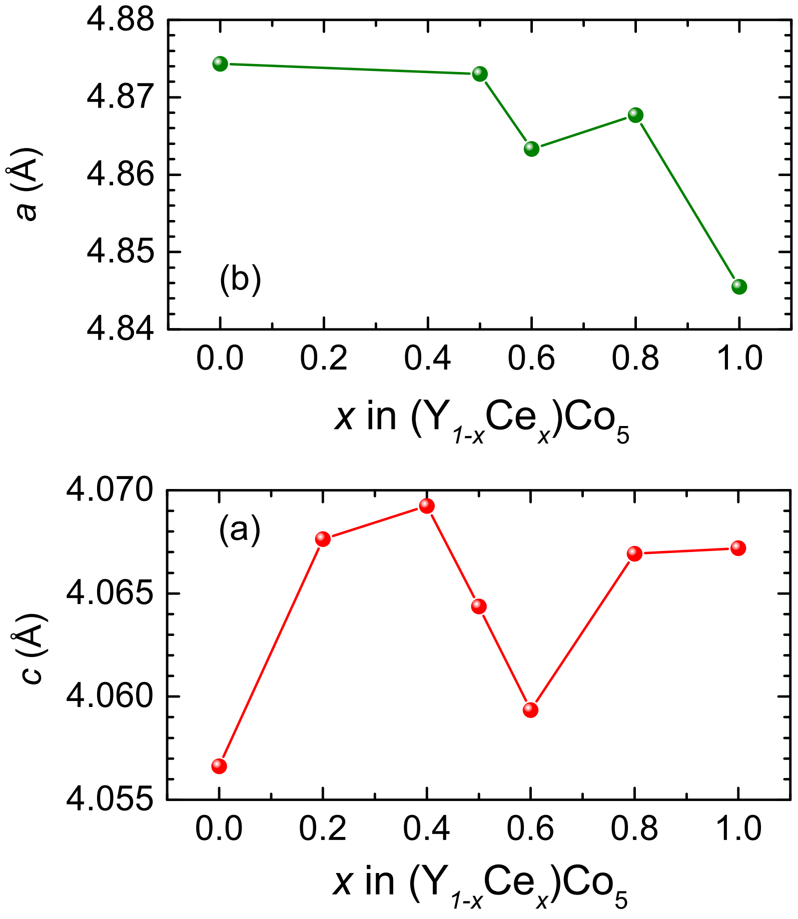

Figure 8.2: The variation of (a) a lattice parameter, and (b) c lattice parameter as a function of x in $(\mathrm{Y}_{1-x}\mathrm{Ce}_x)\mathrm{Co}_5$ thin films.

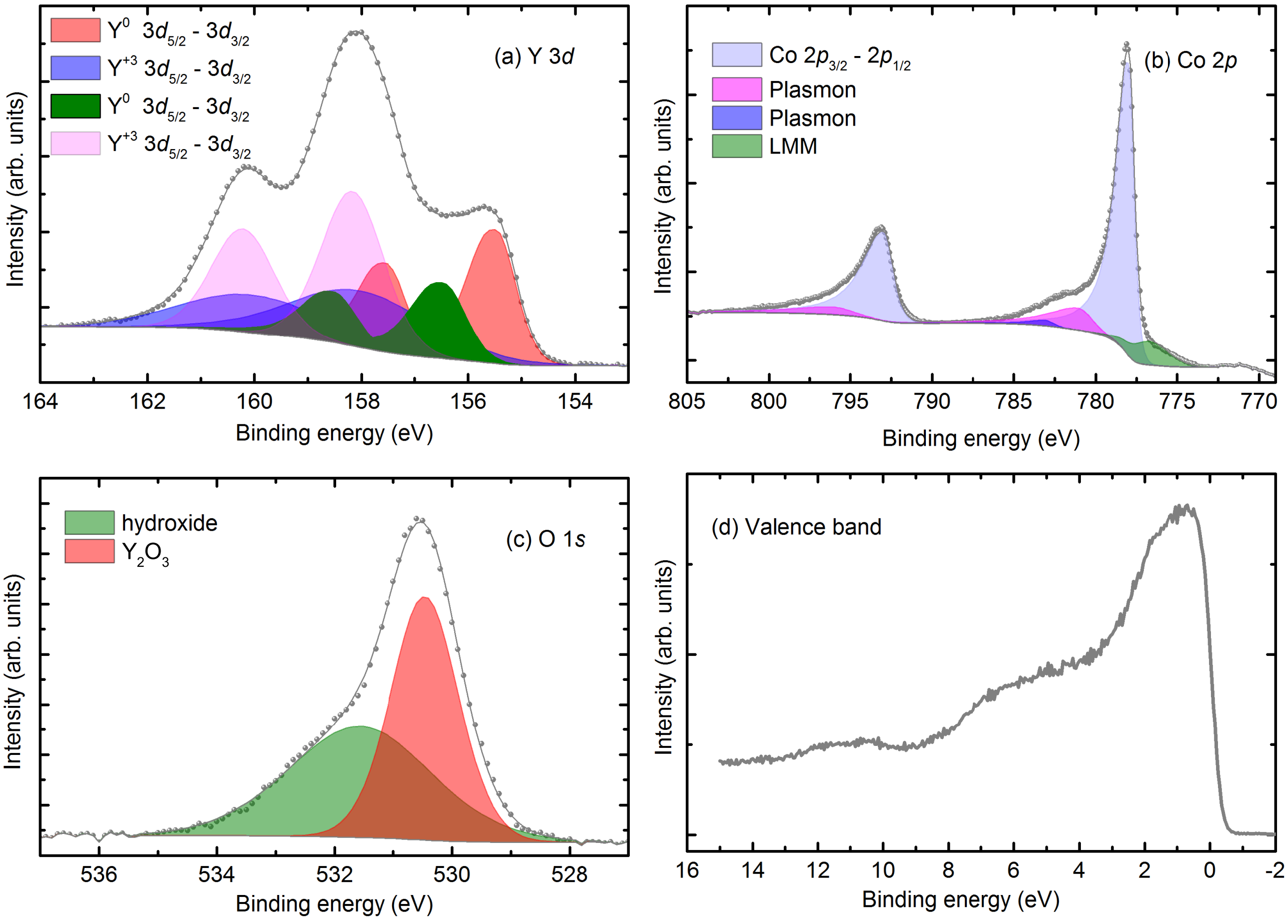

Figure 8.3: X-ray photoelectron spectra of (a) Y 3d, (b) Co 2p, (c) O 1s levels and the (d) valence band spectrum measured for YCo_5 film.

Ce one has to consider the change of the electronic structure and number of electrons within the f-shell itself during the photoemission experiment, making results less conclusive as compared to other rare-earth elements [153].

The chemical environment of different elements of the film was investigated using PULSE Dynamic XPS system in which a multi-channel analyser with in-vacuum feedback electronics allows faster acquisition of a high resolution spectra. It was important to record the photoelectron spectra using this method because the rare-earths, yttrium and especially cerium are prone to oxidation. In order to accurately determine the valency of cerium and yttrium in the intermetallics, it is crucial to prevent their oxidation while recording the spectra which usually takes several hours for each element in the PHI system. Thus, the film was sputtered with Ar ions until no oxygen is observed in the survey spectra and then the high resolution spectra of Ce and Y was recorded immediately.

8.2.1 YCo_5 film

The yttrium $3d$ photoelectron spectra comprises of four spin-orbit doublets, $3d_{5/2}$ - $3d_{3/2}$ as shown in Fig. 8.3(a). The peaks corresponding to both metallic (shown in red and green) as well as oxidized state of yttrium (shown in pink and blue) with different chemical environment are observed. (i) $Y^0 3d_{5/2}$ - $Y^0 3d_{3/2}$ at 155.48 eV - 157.53 eV; (ii) $Y^{3+} 3d_{5/2}$ - $Y^{3+} 3d_{3/2}$ at 158.01 eV - 160.06 eV; (iii) $Y^0 3d_{5/2}$ - $Y^0 3d_{3/2}$ at 156.47 eV - 158.52 eV; and (iv) $Y^{3+} 3d_{5/2}$ - $Y^{3+} 3d_{3/2}$ at 158.01 eV - 160.06 eV.

The peaks corresponding to the metallic state of Y are fit using Gaussian-Lorentzian distribution function, GL(30) with an asymmetricity of T(1.5) while the peaks corresponding to the oxidized state of yttrium are fit using GL(30) function without any asymmetricity.

Fig. 8.3(b) shows the Co $2p$ photoelectron spectrum with spin-orbit doublets, $2p_{3/2}$ at 778.01 eV and $2p_{1/2}$ at 792.98 eV and a splitting of 14.97 eV. The peaks are fit with Lorentzian asymmetric function given by LA(1.2,5,5) as described in [97]. The peak shape and position are characteristic of metallic Co (Co^0) [145]. Additionally, two plasmon loss peaks at 3.0 eV and 5.0 eV higher binding energy than the main peak corresponding to the surface and bulk plasmons, respectively, and the Auger $L_3M_{23}M_{45}$ peak at 776.72 eV are also observed in the spectra [97, 98].

The O $1s$ spectrum is shown in Fig. 8.3(c) It is made up of two components with binding energies at 531.56 eV and 530.46 eV. The peak with higher binding energy of 531.5633 eV (green) corresponds to oxygen in the form of hydroxide due to adsorption of water molecules by yttrium most likely during the acquisition of the spectra in the DXPS system as the chamber was not baked. The other component with lower binding energy of 530.46 eV corresponds to Y_2O_3

The valence band of the YCo_5 film is shown in Fig. 8.3(d). Y contributes three ($4d^1 5s^2$) electrons and Co contributes about nine ($4s^2 3d^7$) electrons per atom to the conduction band. Thus, primarily the d electrons contribute to the spectra from 0-5 eV.

The atomic content of yttrium bonded to cobalt in the intermetallic compound was estimated from the total area under the peak/(RSF × T × MFP). For the quantification, area of the metallic peaks of yttrium (shown in green in Fig. 8.3(d)) and Co $2p_{1/2}$ component was used. The atomic percent of yttrium was calculated to be 21.63 % which is well agreement to YCo_5 stoichiometry.

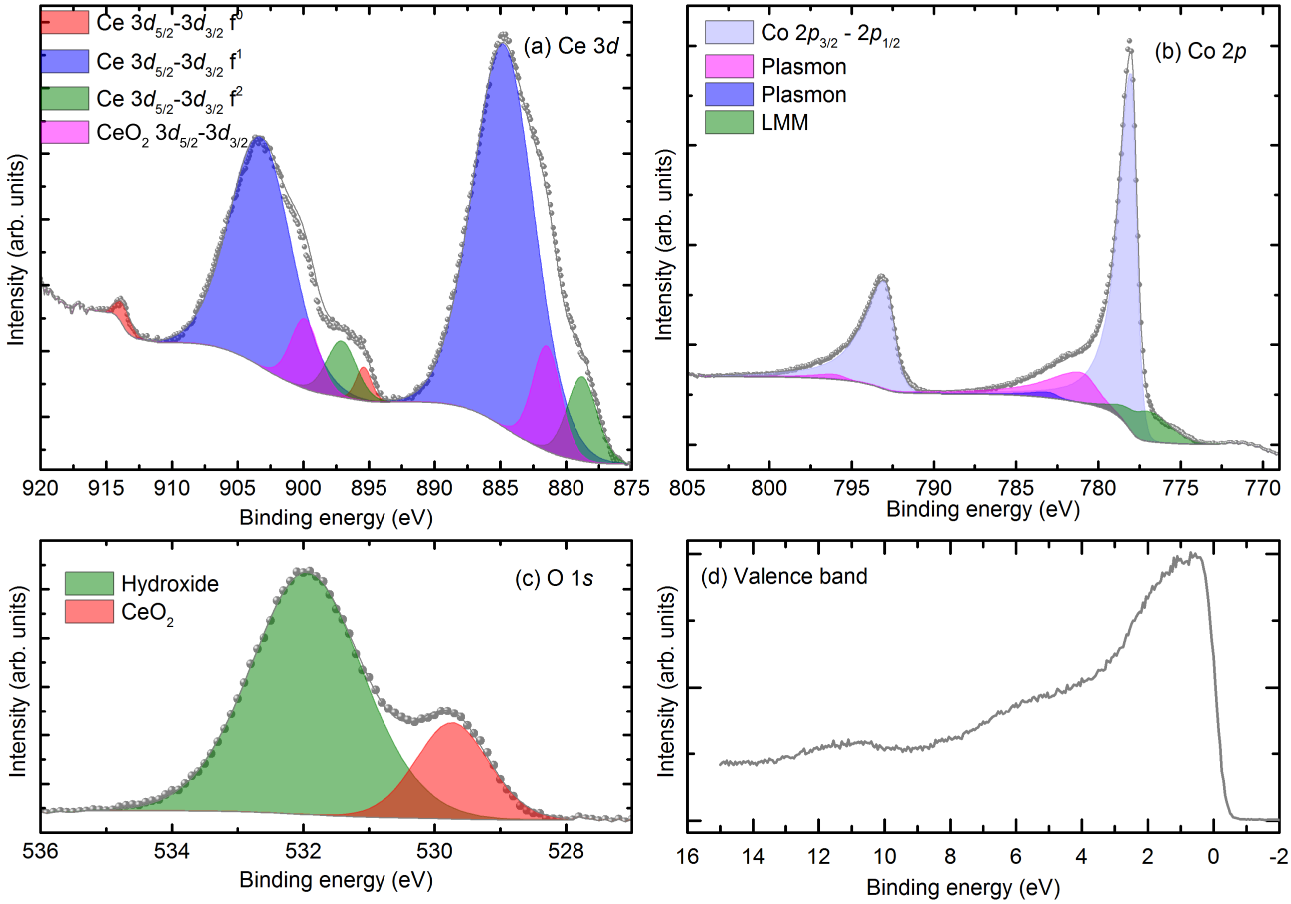

Figure 8.4: X-ray photoelectron spectra of (a) Ce $3d$, (b) Co $2p$, (c) O $1s$ levels and the (d) valence band spectrum measured for CeCo$_5$ film.

8.2.2 $CeCo_5$ film

The $3d$ photoelectron spectra of cerium is shown in Fig. 8.4(a). As a result of the hole created at the $3d$ level because of the photoemission process, the Ce $3d$ spectrum is a superposition of three final states corresponding to $3d^94f^0$, $3d^94f^1$ and $3d^94f^2$ with their spin-orbit doublets, $3d_{5/2}$ - $3d_{3/2}$. (i) $Ce^03d_{5/2}$ - $Ce^03d_{3/2}$ f^0 at 895.39 eV - 913.69 eV with a splitting of 18.30 eV; (ii) $Ce^03d_{5/2}$ - $Ce^03d_{3/2}$ f^1 at 884.74 eV - 903.26 eV with a splitting of 18.52 eV; (iii) $Ce^03d_{5/2}$ - $Ce^03d_{3/2}$ f^2 at 878.78 eV - 897.08 eV with a splitting of 18.30 eV; and (iv) $Ce^{+4}3d_{5/2}$ - $Ce^{+4}3d_{3/2}$ at 881.46 eV and 899.88 eV with a splitting of 18.42 eV.

The Co $2p$ photoelectron spectrum is shown in Fig. 8.4(b). It comprises of spin-orbit doublets, $2p_{3/2}$ at 778.01 eV and $2p_{1/2}$ at 792.98 eV with a splitting of 14.97 eV. The peaks are fit with Lorentzian asymmetric function given by LA(1.2,5,5) as described in [97]. Two plasmon loss peaks at 3.0 eV and 5.0 eV higher binding energy than the main peak corresponding to the surface and bulk plasmons, respectively, and the Auger $L_3M_{23}M_{45}$ peak at 776.97 eV are also observed in the spectra.

The O $1s$ spectrum shown in Fig. 8.4(c) comprises of two components. The peak with higher binding energy at 531.95 eV arises because of $Ce(OH)_3$. The formation of hydroxide is due to adsorption of water molecules by cerium most likely due to the ex situ processing during the acquisition of the spectra in the DXPS system as the chamber was not baked. The other component at lower binding energy at 529.73 eV corresponds to CeO_2 [154, 155]. A detailed investigation by Vescovo *et al.* showed that the oxidation of epitaxial cerium thin films proceeds through three distinct stages (i) ordered surface adsorption of oxygen; (ii) formation of an ordered Ce_2O_3-like oxide; and (iii) gradual conversion to CeO_{2-x} [156]. Gasgnier *et al.* reported that metallic cerium thin films upon exposure to atmosphere were converted to $Ce(OH)_3$, which oxidized to CeO_2; however, in some experiments, Ce_2O_3 was also observed [157, 158].

The valence band of the film is shown in Fig. 8.4(d). The region from 0-5 ev, is mainly dominated by the d electrons from cobalt and cerium.

The stoichiometry of the Ce-Co intermetallic compound in the film was estimated from the total area under the peak/(RSF × T × MFP). Since we observed, a significant amount of cerium hydroxide and cerium oxide in the O $1s$ spectra, it is necessary to exclude their contribution from the total Ce content in the film. The area under the CeO_2 peak was, thus, not used for the quantification. The amount of cerium that would combine in the form of $Ce(OH)_3$, as determined from the area of the hydroxide peak, was also subtracted from the total Ce content. The Co $2p_{1/2}$ component was used as it does not have any Auger peak. The cerium to cobalt atomic percent was calculated to be 29.2 %.

8.2.3 $(Y_{0.2}Ce_{0.8})Co_5$ film

The $3d$ photoelectron spectra of yttrium is comprised of four spin-orbit doublets, $3d_{5/2}$ - $3d_{3/2}$ as shown in Fig. 8.5(a). The peaks corresponding to both metallic as well as oxidised state of yttrium with different chemical environment are observed. The metallic state of Y is fit to Gaussian-Lorentzian distribution, GL(30) with an asymmetricity of T(1.5). The peaks corresponding to the oxidized state of yttrium was fit to GL(30) function. (i) $Y^03d_{5/2}$ - $Y^03d_{3/2}$ at 155.45 eV - 157.50 eV splitting of 2.05 eV; (ii) $Y^{3+}3d_{5/2}$ - $Y^{3+}3d_{3/2}$ at 158.26 eV - 160.31 eV splitting of 2.05 eV; (iii) $Y^03d_{5/2}$ - $Y^03d_{3/2}$ at 156.26 eV - 158.31 eV; and (iv) $Y^{3+}3d_{5/2}$ - $Y^{3+}3d_{3/2}$ at 159.19 eV - 161.24 eV

The $3d$ photoelectron spectra of cerium is comprised of four spin-orbit doublets, $3d_{5/2}$ - $3d_{3/2}$ as shown in Fig. 8.5(b). (i) $Ce^03d_{5/2}$ - $Ce^03d_{3/2}$ f^0 at 895.49 eV - 913.79 eV with a splitting of 18.30 eV; (ii) $Ce^03d_{5/2}$ - $Ce^03d_{3/2}$ f^1 at 884.07 eV - 902.72 eV with a splitting of 18.65 eV; (iii) $Ce^03d_{5/2}$ - $Ce^03d_{3/2}$ f^2 at 878.69 eV -

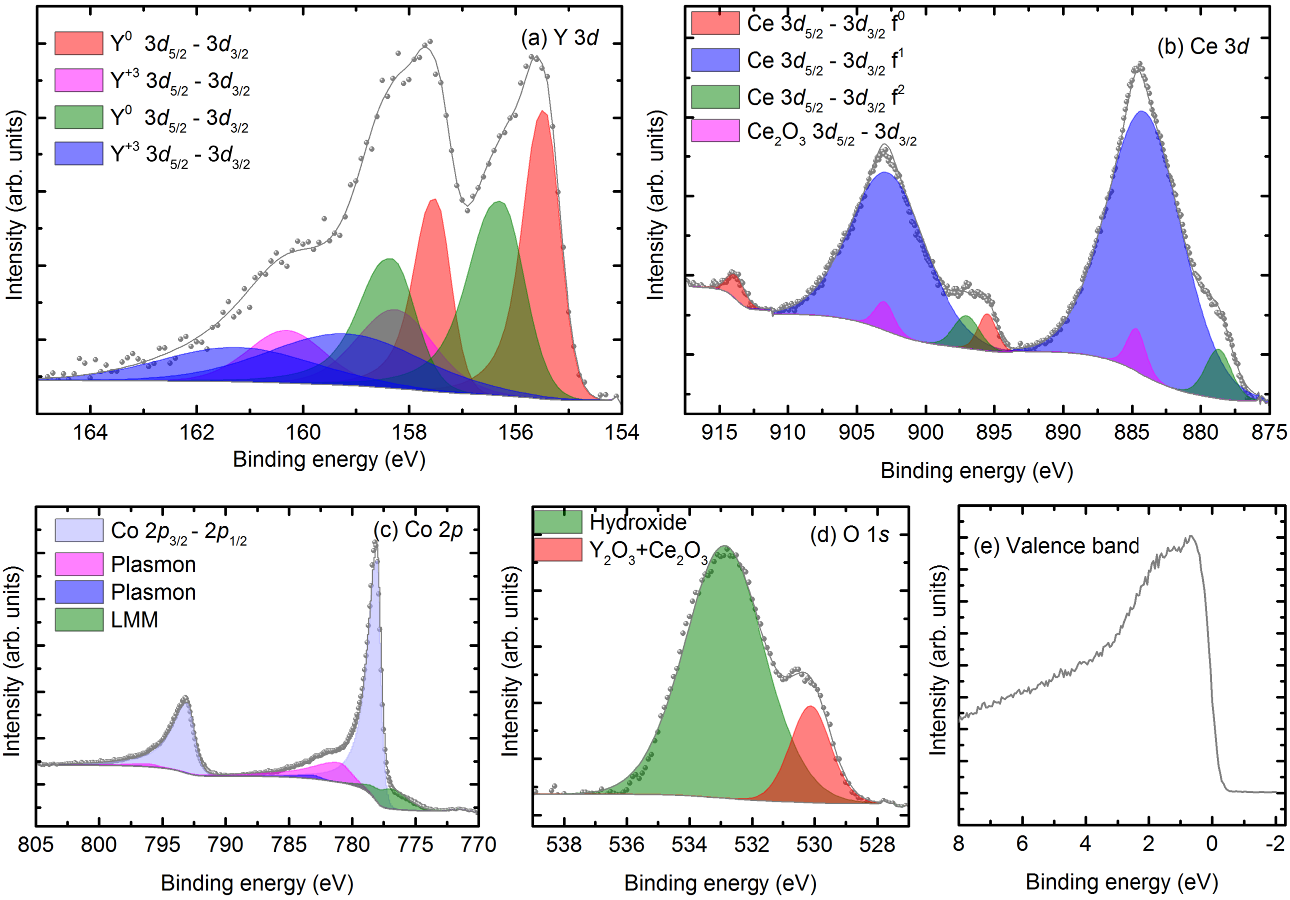

Figure 8.5: X-ray photoelectron spectra of (a) Y 3d, (b) Ce 3d, (b) Co 2p, (c) O 1s levels and the (d) valence band spectrum measured for (Y$_{0.2}$Ce$_{0.8}$)Co$_5$ film.

896.99 eV with a splitting of 18.30 eV; and (iv) $Ce^{+3}3d_{5/2}$ - $Ce^{+3}3d_{3/2}$ at 884.67 eV and 902.99 eV with a splitting of 18.32 eV.

Fig. 8.5(c) shows the Co $2p$ photoelectron spectrum with spin-orbit doublets, $2p_{3/2}$ at 778.0894 eV and $2p_{1/2}$ at 793.06 eV and a splitting of 14.97 eV. The peaks are fit with Lorentzian asymmetric function given by LA(1.2,5,5) as described in [97]. Additionally, two plasmon loss peaks at 3.0 eV and 5.0 eV higher binding energy than the main peak corresponding to the surface and bulk plasmons, respectively, and the Auger $L_3M_{23}M_{45}$ peak at 776.97 eV are also observed in the spectra.

The O $1s$ spectrum is shown in Fig. 8.5(d). It comprises of two components with binding energies at 532.88 eV (red), corresponding to the hydroxide, and at 530.12 eV (green) corresponding to sesquioxides, Ce_2O_3 and Y_2O_3.

The valence band spectrum of the film is shown in Fig. 8.5(e). The conduction electrons from cerium ($5d^16s^2$), yttrium ($4d^15s^2$) and cobalt ($4s^23d^7$) mainly contribute to the spectra near to the Fermi level.

The film was grown at evaporation rate of Y was 0.04 Å/s and Ce of 0.16 Å/s yielding Y to Ce evaporation rate ratio of 0.25. After subtracting the contribution of Y and Ce to the hydroxide, the Y to Ce ratio from the XPS analysis was calculated to be 0.24 which is close to th expected value. This shows that the calibration was accurate in terms of stoichiometry transfer from the source to the film. Thus, we rely on the experimental evaporation rate ratio used for the growth of the films.

8.2.4 $(Y_{0.5}Ce_{0.5})Co_5$ film

The $3d$ photoelectron spectra of yttrium is comprised of four spin-orbit doublets, $3d_{5/2}$ - $3d_{3/2}$ as shown in Fig. 8.6(a). The components corresponding to both metallic as well as oxidised state of yttrium with different chemical environment are observed. (i) $Y^03d_{5/2}$ - $Y^03d_{3/2}$ at 155.4377 eV - 157.4877 eV splitting of 2.05 eV; (ii) $Y^{3+}3d_{5/2}$ - $Y^{3+}3d_{3/2}$ at 158.2096 eV - 160.2596 eV splitting of 2.05 eV; (iii) $Y^03d_{5/2}$ - $Y^03d_{3/2}$ at 156.4386 eV - 158.4886 eV. The peaks corresponding to the metallic state of yttrium are fit to Gaussian-Lorentzian distribution, GL(30) with an asymmetricity of T(1.5). The peaks corresponding to the oxidized state of yttrium are fit to GL(30) function.

The cerium $3d$ photoelectron spectra is comprised of four spin-orbit doublets, $3d_{5/2}$ - $3d_{3/2}$ as shown in Fig. 8.6(b). (i) $Ce^03d_{5/2}$ - $Ce^03d_{3/2}$ f^0 at 895.34 eV - 913.64 eV with a splitting of 18.30 eV; (ii) $Ce^03d_{5/2}$ - $Ce^03d_{3/2}$ f^1 at 884.02 eV - 902.67 eV with a splitting of 18.65 eV; (iii) $Ce^03d_{5/2}$ - $Ce^03d_{3/2}$ f^2 at 878.58 eV - 896.88 eV with a splitting of 18.30 eV; and (iv) $Ce^{+3}3d_{5/2}$ - $Ce^{+3}3d_{3/2}$ at 884.47 eV and 903.10 eV with a splitting of 18.63 eV. corresponding to Ce_2O_3

Fig. 8.6(c) shows the Co $2p$ photoelectron spectrum with spin-orbit doublets, $2p_{3/2}$ at 777.97 eV and $2p_{1/2}$ at 792.94 eV and a splitting of 14.97 eV. The shape and position of the peaks are characteristic of metallic state of cobalt and are fit using Lorentzian asymmetric function given by LA(1.2,5,5) [97]. Two plasmon loss peaks at 3.0 eV and 5.0 eV higher binding energy than the main peak corresponding to the surface and bulk plasmons, respectively, and the Auger $L_3M_{23}M_{45}$ peak at 776.8853 eV are also observed in the spectra.

The O $1s$ spectrum shown in Fig. 8.6(d) comprises of two components: the one at higher binding energy of 532.0551 eV corresponds to the hydroxide and the other component at 530.0479 eV corresponds to the sesquioxides, Ce_2O_3 and Y_2O_3. After subtraction of the contribution of cerium in the form of hydroxide, the cerium to cobalt ratio was calculated to be 0.14 which slightly exceeds the targeted ratio of 1. However, we can see that even after the best possible fitting of the spectrum using all the constraints, the intensity of

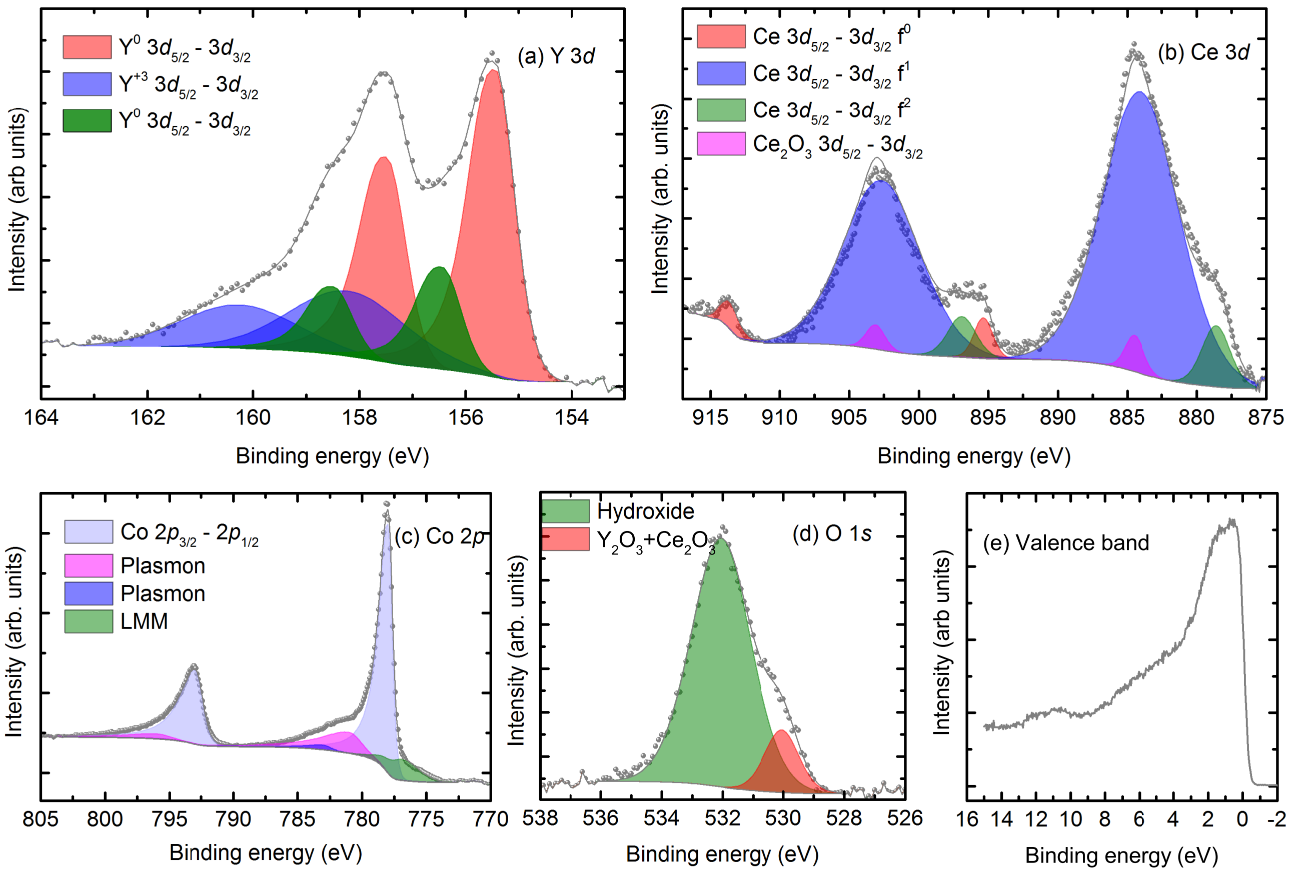

Figure 8.6: X-ray photoelectron spectra of (a) Ce 3d, (b) Co 2p, (c) O 1s levels and the (d) valence band spectrum measured for $(Y_{0.5}Ce_{0.5})Co_5$ film.

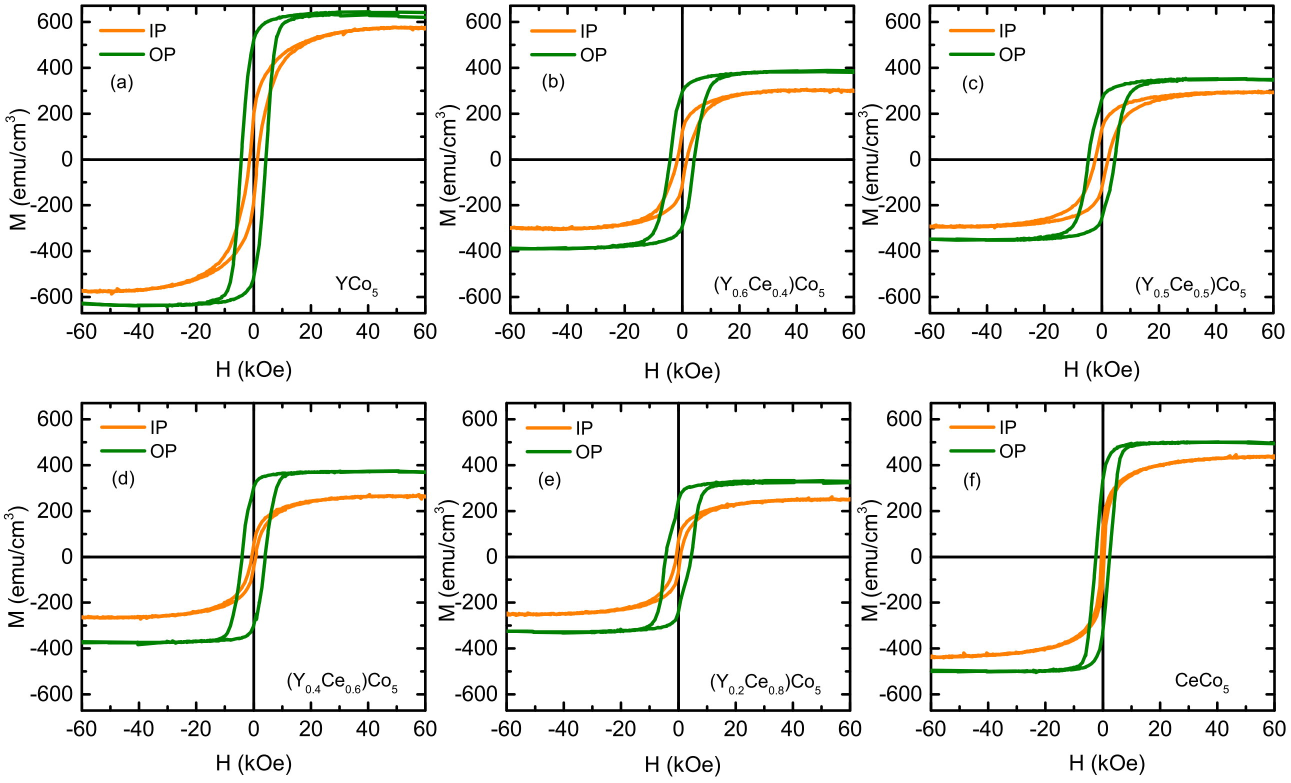

Figure 8.7: Room temperature hysteresis curves of the (Y$_{1-x}$Ce$_x$)Co$_5$ films measured perpendicular (out-of-plane, OP) and parallel (in-plane, IP) to the film plane.

the Ce^{0}3$d_{3/2}$ f^1 is overestimated. Thus, we rely on the experimental evaporation rate ratio used for the growth of the films.

The valence band spectrum of the film is shown in Fig. 8.6(e). As for all other compositions, the conduction electrons from cerium (5$d^1$6s^2), yttrium (4$d^1$5s^2) and cobalt (4$s^2$3d^7) mainly contribute to the spectra.

The ionized 3d final state, 3d^9(5d6s)^{2}4f^2, arises as a result of photoemission process from a mixed-valent compound confirming the mixed-valency of Ce ions for all the compositions, (Y$_{1-x}$Ce$_x$)Co$_5$ [159].

8.3 Magnetic properties

The magnetic hysteresis curves of the (Y$_{1-x}$Ce$_x$)Co$_5$ films measured at room temperature, perpendicular (out-of-plane, green) and parallel (in-plane, orange) to the film plane are shown in Fig. 8.7. For all the compositions, the hysteresis curve measured perpendicular to the film is larger than the in-plane hysteresis curve and has a higher remanence and coercivity indicating that the major component of magnetization is normal to the film plane.

A plot of the saturation magnetization of the films as a function of x is shown in Fig. 8.8. The saturation magnetization of the (Y$_{1-x}$Ce$_x$)Co$_5$ films shows a U-shape type of behavior on increasing x from YCo$_5$ to CeCo$_5$. Similar trend of the magnetization has been observed for bulk single crystals in an unpublished work. The decrease in the saturation magnetization from YCo$_5$ to CeCo$_5$ is not linear. This non-linear

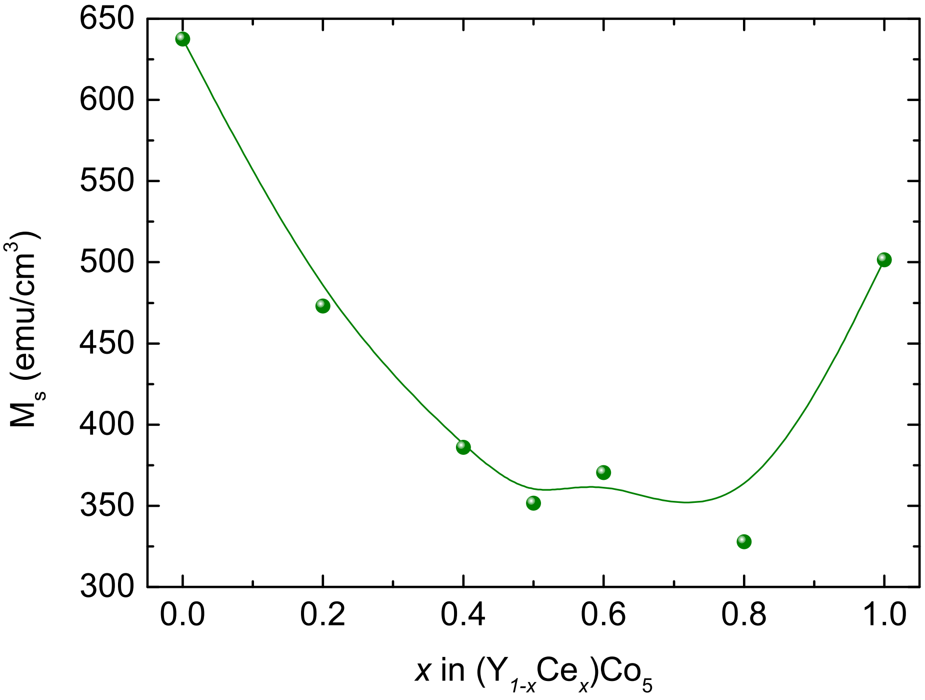

Figure 8.8: Saturation magnetization, M_s, of the $(Y_{1-x}Ce_x)Co_5$ films as a function of x.

change could arise due to the varying amount of Ce^{+3} and Ce^{+4} with increasing Ce concentration, as the tetravalent state of Ce has no magnetic moment.

The anisotropy of the $(Y_{1-x}Ce_x)Co_5$ films was derived from magnetic torque measurement. The anisotropy measured at room temperature as a function of *x* is shown in Fig. 8.9. Ideally, the torque measurement gives an accurate measure of the uniaxial-anisotropy (K_u) for perfectly aligned single crystals. However, a slight deviation from the perfect *c*-axis texture of the film is indicated by the small coercivity in the in-plane hysteresis curve. In this case, K_1 is a measure of the perpendicular component of the anisotropy of the films which, indeed, is larger than the shape anisotropy of the film.

The anisotropy of the $(Y_{1-x}Ce_x)Co_5$ films shows a non-linear variation with increasing Ce content. There are no reports on (Y,Ce)Co_5 films available in the literature and it is for the first time that we study these compositions experimentally. It is important to analyze the trend of anisotropy in the bulk single crystal which is still under investigation. In this way, we can exclude the effects due to texture or the microstructure of the films which influences the anisotropy. Nevertheless, we propose that the non-linear variation of the structural and magnetic properties in (Y,Ce)Co_5 intermetallics could arise due to the mixed-valency of Ce ions and the relative stability of a mixed composition than the parent compounds which needs to be confirmed from the density functional theory (DFT) calculations.

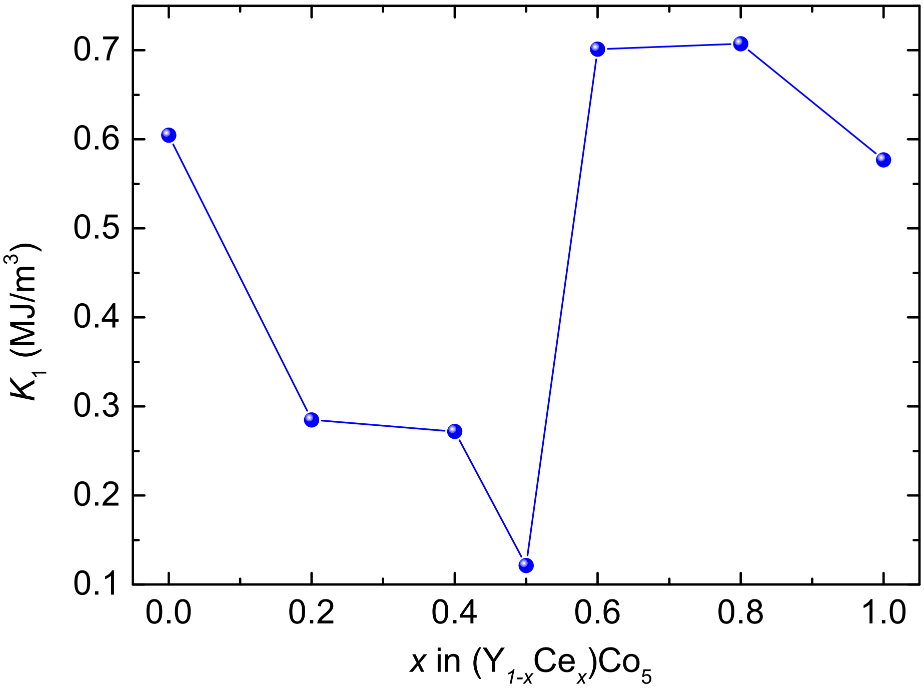

Figure 8.9: The perpendicular anisotropy of the $(\mathrm{Y}_{1-x}\mathrm{Ce}_x)\mathrm{Co}_5$ films as a function of x.

9 Conclusions

9.1 Y-Co thin films

According to the equilibrium phase diagram of the binary Y-Co system, the Y_2Co_{17} phase is formed first followed by the YCo_5 phase with decreasing cobalt or increasing yttrium content, which in molecular beam epitaxy can be obtained by the manipulation of evaporation rates. On decreasing the cobalt evaporation rate, we observed a gradual transition from Co, to Y_2Co_{17} and finally to YCo_5 phase. At the same deposition temperature, pure Co phase is stabilized in its hexagonal symmetry on the *c*-cut Al_2O_3 substrate. This hexagonal crystal structure is maintained throughout the entire range of Y and Co rates. With decreasing Co rate, the Co atoms are removed from the hexagonal crystal lattice such that the Y_2Co_{17} phase gives way to the YCo_5 phase.

On the other hand, on increasing the evaporation rate of yttrium, at intermediate compositions and temperature, a natural phase decomposition during the film growth results in separation and simultaneous stabilization of both Y_2Co_{17} and YCo_5 phases. The (001)-oriented Al_2O_3 substrate imposes a crystalline order onto the nanocomposite film such that crystallographic *c*-axes of Y_2Co_{17} and YCo_5 phases are parallel to each other, favoring a coherent growth. Self-assembly of the nanocomposite is facilitated by the closely matching lattice constants, atomic species and crystal symmetry. Such nanoscale architecture and coherent precipitation leads to enhanced energy products, without additional elements.

The Y_2Co_{17} phase in the thin film is stabilized with the magnetization and anisotropy matching well to the bulk single crystals. It is characterized by a soft ferromagnetic behavior with easy-axis of magnetization in the film plane. The YCo_5 film is magnetically hard and exhibits a perpendicular anisotropy, although it is not perfect. The origin of perpendicular anisotropy is considered to be uniaxial magnetocrystalline anisotropy associated with the *c*-axis textured growth of YCo_5 normal to the film plane. The microstructure of the film reveals stacking faults in the film growth direction. A narrow thermodynamic stability of YCo_5 phase, epitaxial and/or thermal strain, accompanied by a strong oxygen affinity of yttrium leads to the growth of defect rich YCo_5 phase.

The nanocomposite films also show perpendicular anisotropy as a result of exchange-coupling of the Y_2Co_{17} phase to the YCo_5 phase. While the magnetization reversal in the YCo_5 film takes place by coherent or incoherent rotation process, the coercivity of the Y_2Co_{17}-YCo_5 is governed by a pinning-type mechanism. The concentration and anisotropy gradients in the nanocomposite film, hinders the domain-wall motion and imparts magnetic hardness.

9.2 Y_2Co_{17} - YCo_5 bilayers

Thin-film growth allows artificial designing of microstructure as a bottom-up approach and thereby, provides a pathway to overcome the limitations of the equilibrium phase diagram. In this work, bilayers of Y_2Co_{17} and YCo_5 phases were fabricated and their magnetic properties were investigated as a proof of concept. We observed that the magnetic properties depend strongly on the order of growth of the two phases on the Al_2O_3 substrate and the thickness of the soft magnetic phase. When Y_2Co_{17} is grown initially on the Al_2O_3

substrate and then the YCo_5 layer on top, the bilayers show an overall in-plane anisotropy. On the other hand, when YCo_5 phase is grown first on the Al_2O_3 substrate, then the bilayers exhibit a perpendicular anisotropy. Our speculation is that the growth of c-axis textured YCo_5 phase is facilitated by the substrate. When it is grown on top of the Y_2Co_{17} layer, the phase is formed, however, it is not oriented along its c-axis. In order to confirm this model, it is important to investigate the microstructure of the films. The hysteresis curves of the bilayers are smooth and continuous and no kink is observed upon magnetization reversal indicating a strong exchange interaction between the two phases. As exchange is a short range interaction, the anisotropy of the bilayers depends on the thickness of the soft magnetic Y_2Co_{17} phase. The magnetization of the entire Y_2Co_{17} layer is coupled to the YCo_5 layer when its thickness is less than the exchange length.

9.3 Ce-Co thin films

To explore thin-film phase diagram of the binary Ce-Co system, the films were grown by co-evaporation of cerium and cobalt by electron-beam. In the Ce-Co system, only the compositions, Ce_2Co_{17} and $CeCo_5$ are ferromagnetic at room temperature which enables in the identification of the phases. The (001)-Al_2O_3 substrate promotes the growth of (00l) oriented films without the use of any additional metallic underlayer. The c-axis textured growth of high anisotropic phase of $CeCo_5$ results in a perpendicular anisotropy of $0.44\,\mathrm{MJ/m^3}$. The strong affinity of cerium to oxygen leads to formation of oxide inclusions in the film which can affect the magnetic properties of the films. Inspite of this, a saturation magnetization of $500\,\mathrm{emu/cm^3}$, an anisotropy of $0.44\,\mathrm{MJ/m^3}$ and coercivity of 2.74 kOe are the highest reported so far for the thin films.

9.4 Sm-Co thin films

In this work, we were able to an achieve extremely large perpendicular anisotropy of $1.67\,\mathrm{MJ/m^3}$ in $SmCo_5$ thin film. The atomic structure of the film revealed that the films grow perfectly c-axis oriented on the (001)-Al_2O_3 substrate without the use of additional buffer layers. In literature, the highest anisotropy reported for $SmCo_5$ thin films with perpendicular anisotropy is $7.6\,\mathrm{MJ/m^3}$. Note that this particular film was grown onto a Ru (20 nm) buffer layer [75]. Sayama et al. achieved a uniaxial anisotropy of $4.0\,\mathrm{MJ/m^3}$ in an intricate film structure made up of 35 alternate sublayers of Sm (0.31 nm) and Co (0.41 nm) on a Cu (100 nm)/Ti (25 nm) dual underlayer [66]. From this perspective, the outcome of a strong perpendicular anisotropy obtained in single layer is advantageous for magnetic storage devices and spintronic applications. However, still the perpendicular anisotropy of the film is less than the uniaxial magnetocrystalline anisotropy known for the single crystal. The atomic scale structure of the film resembles either the $SmCo_5$, or the Sm_2Co_{17} or a combination of the two phases. At $30\,^{\circ}$ direction from the previous orientation, the atomic arrangement of the first nine monolayers of the film match perfectly to $SmCo_5$ phase, however, above that traces of Sm_2Co_{17} structure could be observed. The presence of other Sm-Co phases can be excluded as these have either a zig-zag, or a non-linear stacking or doubling of Sm atoms. The presence of Sm_2Co_{17} phase would explain the lowered total anisotropy of the film. However, STEM imaging can only provide information about a localized region in the sample. According to our understanding, there seems to be a trade off between perfect texture and phase purity. The Sm-Co film exhibiting the highest anisotropy is perfectly oriented, however, it is not entirely made up of $SmCo_5$ phase. The nature of arrangement of the Sm_2Co_{17} and the $SmCo_5$ phase at a unit cell level, is still open for discussion. Adding to that, the film which exhibits the largest coercivity could only contain $SmCo_5$ phase, however, without any texture. In order to confirm this model, the atomic structure of the highly-coercive Sm-Co film will be investigated.

9.5 (Y,Ce)Co_5 thin films

In view of enhancing the magnetocrystalline anisotropy of a compound by strain introduced by chemical substitution, yttrium substituted cerium (Y,Ce)Co_5 intermetallics are investigated. A combined study of the thin films and bulk single crystals are performed, although, in this work, the results obtained for only the thin films are shown. We observed that the structural and magnetic properties of $(Y_{1-x}Ce_x)Co_5$ films show a non-linear dependence on Ce content, x. The absolute values vary, but a similar trend in the lattice parameters and magnetization is also observed in the bulk single crystals. The different factors which influence the crystal structure and thus, the magnetocrystalline anisotropy are the ionic size, chemical valence and the site where the substitution takes place. As the tetravalent state of Ce has no magnetic moment, a varying concentration of Ce^{+3} and Ce^{+4} can also lead to a change in the magnetization of the films. The mixed-valent state of the Ce ion for all the compositions was confirmed using XPS measurements. However, the quantification of the Ce^{+3} and Ce^{+4} components is not possible using XPS technique as it provides information about the final states after the photoemission process.

In general, this work highlights the importance of thin film epitaxy in controlling and designing of materials at the nanoscale, understanding the magnetic hardness mechanisms and developing new strategies for rational design of more sustainable magnetic systems.

10 Outlook

There are some important lessons learnt from this work which opens up possibilities for improvements, new ideas and research directions.

(i) In this work, we were able to achieve a perpendicular anisotropy in YCo_5 and $CeCo_5$ films without the use of additional buffer layers, although it was not perfect. The growth of these phases is affected by a narrow thermodynamic stability, epitaxial and/or thermal strain as well as their strong affinity towards oxygen. To avoid the problem of oxidation, better vacuum conditions and use of an appropriate buffer layer are advisable. The buffer layer should be such that it can serve as a barrier between the film and the substrate and at the same time maintain the epitaxy of the substrate. A layer of ruthenium is a good option as it grows $(00l)$ oriented on the (001)-Al_2O_3 substrate and does not interfere with the magnetic properties of the film.

(ii) Magnetic force microscopy can be utilized to observe the domain patterns in these R-Co films. The technique can provide important insights into the magnetization reversal process and determine experimentally if the coercivity is controlled by nucleation of reverse domains or pinning of the domain walls.

(iii) In the Y_2Co_{17}-YCo_5 bilayers, we observed that the structural and magnetic parameters depend strongly on the order of growth of the two phases on the Al_2O_3 substrate and the thickness of the soft magnetic phase. Our explanation of these properties is based on a layered architecture of the Y_2Co_{17} and YCo_5 phases. It is important to confirm the microstructure of the bilayers, if these are grown layer-by-layer or as nanostructured grains of the two phases. In order to understand the effect of thickness, experimental studies on a broad range of layer thickness will be advantageous. As a future research direction, the thin film epitaxy method can be used to artificially fabricate the ordered nanostructure of the prototype, pinning type $Sm_2(Co, Fe, Cu, Zr)_{17}$-magnet which is formed by the natural phase decomposition reactions. The artificial designing of the microstructure could provide a pathway to overcome the limitations of the equilibrium phase diagrams.

(iv) The introduction of strain by partial substitution of a rare-earth with another rare-earth of different atomic size is considered to be a potential way to an enhance the magnetocrystalline anisotropy energy. Keeping this in view, we investigated the effect of substitution of yttrium with cerium in $(Y,Ce)Co_5$ intermetallics. Among all the rare-earths cerium is one of the lowest priced and mined anyhow abundantly as part of the rare earth basket, thus, its use in applications is advisable. We observed a non-linear variation of the structural and magnetic properties in $(Y_{1-x}Ce_x)Co_5$ films with Ce content, x. The interpretation of the results is based on the mixed-valent nature of Ce ion and the final states of cerium formed as a result of photoemission process. In this regard, the measurement of the XANES spectra of the film can provide information on the valence state of the compounds. Additionally, it is also important to confirm the minimum energy or the most stable structures of the mixed composition using the DFT calculations. Finally, we propose that in order to investigate the influence of size of the substituting atom, a series of $(Y,La)Co_5$ and $(Y,Sm)Co_5$ could be investigated so that the effects due to mixed-valent state of the rare-earth ion could be avoided.

List of Figures

2.1 Plot of inverse susceptibility with temperature for (a) diamagnetic, (b) paramagnetic, (c) antiferromagnetic, (d) ferromagnetic, and (e) ferrimagnetic materials. 4

2.2 The development of maximum energy density of the hard magnetic materials developed in the twentieth century. Image adapted from [5]. 9

2.3 The different types of magnetic nanocomposites: (a) a decoupled nanocomposite, (b) an exchange-spring magnet, (c) an exchange-coupled magnet. 10

2.4 A schematic illustration of the (a) Frank-van der Merwe, (b) Volmer-Weber and (c) Stranski-Krastanov growth modes of thin films. 15

3.1 Equilibrium phase diagram of Y-Co system. Adapted from [34]. 18

3.2 Equilibrium phase diagram of Ce-Co system. Adapted from [41]. 19

3.3 Equilibrium phase diagram of Sm-Co system. Adapted from [44]. 20

3.4 (a) The unit cell of RCo$_5$ compound with CaCu$_5$ structure where R at $1a$ site is shown in grey, Co at $2c$ site in red and Co at $3g$ site in green. (b) A schematic representation of the same CaCu$_5$ unit cell. 21

3.5 Schematic representation of the two types of stacking modes for R_2M$_{17}$ derived from (a) RM$_5$, hexagonal CaCu$_5$ structure. (b) The two possible stacking modes leading to hexagonal and rhombohedral structure types of the R_2M$_{17}$ intermetallic compounds. 22

3.6 (a) The Th$_2$Ni$_{17}$-type hexagonal, and the Th$_2$Zn$_{17}$-type rhombohedral, structures of R_2Co$_{17}$. The R at $1a$ site is shown in grey, Co at $2c$ site in red, Co at $3g$ site in green and the Co dumbbell in blue. 23

3.7 Schematic representation of (a) RM$_5$ unit cells with a and c lattice constants and the different stacking arrangements which lead to the (b) hexagonal and rhombohedral, R_2M$_7$, (c) hexagonal and rhombohedral, RM$_3$, and (d) cubic RM$_2$ structure. 24

3.8 Crystal structure of rhombohedral, RCo$_3$, derived from the unit cell of RCo$_5$ with CaCu$_5$ structure. The R at $1a$ site is shown in grey, Co at $2c$ site in red, Co at $3g$ site in green and Co at $2a$ site of MgZn$_2$ structure in purple. 25

3.9 Crystal structure of hexagonal, R_2Co$_7$, derived from the unit cell of RCo$_5$ with CaCu$_5$ structure. The R at $1a$ site is shown in grey, Co at $2c$ site in red, Co at $3g$ site of CaCu$_5$ in green and Co at $2a$ site of MgZn$_2$ in purple. 26

4.1 Schematic of molecular beam epitaxy unit used in this work. 32

4.2 Schematic of the valve board of the MBE unit including corresponding vacuum guages, ion guage (IG) and pirani vacuum guage (VG). 34

4.3 (a) The geometric relationship between incident and diffracted X-rays from the atomic planes with a spacing d, representing the Bragg's law. (b) The sample stage of the horizontal sample mount goniometer with all the possible movements along different axes. 35

4.4 Schematic of electron emission processes in solids: (a) Auger process (b) photoemission process, upon irradiation with an X-ray photon. 42

4.5 (a) Schematic of a DC SQUID. (b) $I - V$ curve showing the bias current (I_B) that puts the operational point midway between the superconducting (SC) and resistive regions. (c) Periodic change in voltage with externally applied flux at a constant bias current. 43

4.6 A schematic of torque-lever-chip used to measure magnetic torque. Image taken from Quantum Design PPMS torque magnetometer option user's manual [105]. 47

4.7 A schematic showing the different types of interactions of electrons with a thin sample. . . 49

4.8 Comparison of TEM and STEM modes of operation. In TEM mode, (a) direct or (b) scattered electrons are selected using aperture forming BF and DF images, respectively. In STEM mode, an (c) on-axis or (d) off-axis annular detector is used to perform equivalent operations. 51

5.1 XRD patterns of 30 nm Y-Co films deposited at a rate of Y of 0.05 Å/s and Co rate of 0.08 Å/s with increasing growth (set) temperature from 400 °C to 750 °C. 54

5.2 XRD patterns of 30 nm Y-Co films, deposited at a constant rate of Y of 0.05 Å/s and Co rate decreasing (a) from 0.19 Å/s to 0.10 Å/s and (b) from 0.09 Å/s to 0.01 Å/s 55

5.3 (a) The cross-sectional BF image of the YCo_5 film grown on (001)-oriented Al_2O_3 substrate. The inset shows the fast fourier transformation (FFT) map of YCo_5 grain. 56

5.4 (a) X-ray diffraction patterns of Y-Co thin films grown onto (001)-oriented Al_2O_3 substrates at 590 °C. The evaporation rate of Y is increased from 0.18 Å/s to 0.25 Å/s while the Co rate is fixed at 0.25 Å/s. (b) Magnified view of the film peaks between 42.9° and 46° with fitting using Gaussian distribution function. The positions of the 004 Y_2Co_{17} (2:17) and 002 YCo_5 (1:5) Bragg reflections are marked by vertical dashed lines. 56

5.5 X-ray diffraction patterns of Y-Co thin films grown onto (001)-oriented Al_2O_3 substrates with increasing temperature from 490 °C to 660 °C for Y:Co of 1. (b) Magnified view of the film peaks between 42.9° and 46° with fitting using Gaussian distribution function. The positions of the 004 Y_2Co_{17} (2:17) and 002 YCo_5 (1:5) Bragg reflections are marked by vertical dashed lines. 58

5.6 (a) The cross-sectional high resolution HAADF-STEM image of the Y-Co film grown on (001)-oriented Al_2O_3 substrate. Multislice simulations of a 15 nm slab of (b) YCo_5 crystal viewed along the [100] direction, (c) Y_2Co_{17} crystal along [210] viewing direction, and (d) a supercell of combined YCo_5 [100] and Y_2Co_{17} [210] cells. (e) Experimental atomic-resolution HAADF-STEM image of the crystalline area marked in (a). 59

5.7 The atomic arrangement of (a) four unit cells of Y_2Co_{17} and (b) seven unit cells of YCo_5 in the ab plane upon seven unit cells of Al_2O_3 substrate. 60

5.8 (a) ϕ-scan of 222 reflection of Y_2Co_{17} (red) with respect to 104 reflection of Al_2O_3 substrate (black). 61

5.9 (a) ϕ-scan of 201 reflection of YCo_5 (orange) with respect to 104 reflection of Al_2O_3 substrate (grey). (b) Pole figure measurement of 201 reflection of YCo_5 where the film peaks are shown in orange and the less intense background in grey. 62

5.10 RHEED patterns of an (001)-oriented Al_2O_3 substrate along [11-20] azimuth, and 30 nm thick films of (b) Y_2Co_{17} and (c) YCo_5 along the same azimuth. 63

5.11 Room temperature hysteresis curves measured perpendicular ($\perp$, orange spheres) and parallel ($\|$, grey diamonds) to the plane of (a) Y_2Co_{17}, (b) YCo_5 and (c) Y_2Co_{17} and YCo_5 films grown at 590 °C. The corresponding initial magnetization curves are shown in the inset. 64

5.12 Torque measurement of a 30 nm YCo_5 thin film showing the actual data points and the refined curve, at 14 T and 300 K. 65

5.13 Coercive field, H_c, and maximum energy product, $(BH)_{max}$, versus ratio of evaporation rates of Y to Co. The three regions correspond to the growth of Y_2Co_{17}, YCo_5 and a nanocomposite of Y_2Co_{17} and YCo_5 phases. 67

5.14 Coercive field, H_c, and maximum energy product, $(BH)_{max}$, versus the growth temperatures from 490 °C to 660 °C of Y-Co thin films grown at Y to Co ratio of 1. 68

5.15 The arrangement of unit cells of YCo_5 and Y_2Co_{17} on Al_2O_3 in the bilayers: (a) $YCo_5 \parallel Y_2Co_{17} \parallel Al_2O_3$, (b) $YCo_5 \parallel Y_2Co_{17} \parallel Al_2O_3$ 69

5.16 (a) $\theta - 2\theta$ scans of Y_2Co_{17} - YCo_5 bilayers with Y_2Co_{17} grown directly on Al_2O_3 substrate and then YCo_5 layer on top. (b) Magnified view of the Y-Co film peaks with vertical dashed lines indicating the Bragg angle of 004 Y_2Co_{17} (2:17) and 002 YCo_5 (1:5) phases. 70

5.17 Room temperature hysteresis curves of Y_2Co_{17} - YCo_5 bilayers measured perpendicular (orange) and parallel (grey) to substrate with thicknesses: (a) Y_2Co_{17} (5 nm) and YCo_5 (25 nm), (b) Y_2Co_{17} (10 nm) and YCo_5 (20 nm), and (c) Y_2Co_{17} (15 nm) and YCo_5 (15 nm). 70

5.18 (a) X-ray diffraction scans of YCo_5 - Y_2Co_{17} bilayer stack with YCo_5 grown directly on Al_2O_3 substrate and then Y_2Co_{17} layer on top. (b) Magnified view of the Y-Co film peaks with vertical dashed lines indicating the Bragg angle of 004 Y_2Co_{17} (2:17) and 002 YCo_5 (1:5) phases. 71

5.19 Room temperature hysteresis curves measured perpendicular ($\perp$, orange spheres) and parallel ($\|$, grey diamonds) to the bilayers: (a) YCo_5 (10 nm) - Y_2Co_{17} (2 nm) (b) YCo_5 (20 nm) - Y_2Co_{17} (2 nm). The corresponding virgin magnetization curves are shown in the insets. 72

6.1 X-ray diffraction pattern of a 30 nm (001)-oriented $CeCo_5$ film grown onto a (001) Al_2O_3 substrate at 500 °C. The evaporation rates of Ce and Co were 0.10 Å/s. The inset (a) shows the rocking curve of the 002 Bragg peak, and (b) shows the RHEED pattern of the corresponding film at the end of deposition along the Al_2O_3 [11-20] azimuth. 74

6.2 ϕ-scans of the 201 $CeCo_5$ and the 104 Al_2O_3 reflections. 75

6.3 Magnetization, M, versus applied field, H, measured perpendicular (solid blue spheres) and parallel (open green diamonds) to the film plane at (a) 5 K and (b) 300 K. 76

6.4 Temperature dependence of coercivity, perpendicular (solid blue spheres) and parallel (open green diamonds) to the film plane. 77

6.5 Angular dependence of torque per unit volume measured at 300 K and 14 T with actual data points (open black circles) and fit (red line). 78

6.6 Magnetic phase diagram with saturation magnetization and coercivity of Ce-Co thin films (*TF*) as a function of rate ratio of Ce to Co [134]. The magnetization of bulk (*B*) $CeCo_5$ and Ce_2Co_{17} single crystals are marked with red arrows on magnetization axis (y-axis). The calculated ratio for $CeCo_5$ phase is marked with red arrow on ratio axis (x-axis). 79

7.1 X-ray diffraction patterns of Sm-Co thin films grown onto (001)-oriented Al_2O_3 substrate at temperatures from 300 °C to 700 °C at evaporation rate of Sm of 0.10 Å/s and Co rate of 0.165 Å/s. 82

7.2 Room temperature M-H curves measured perpendicular (green spheres) and parallel (blue diamonds) to the plane of Sm-Co films deposited at growth temperatures increasing from (a) 500°C (b) 600°C, and (c) 700°C. 82

7.3 X-ray diffraction patterns of Sm-Co thin films grown onto (001)-oriented Al_2O_3 substrates at $600\,^\circ\mathrm{C}$. The evaporation rate of Sm is fixed at 0.1 Å/s while the Co rate is decreased from 0.28 Å/s to 0.05 Å/s. 83

7.4 X-ray diffraction patterns of Sm-Co thin films grown onto (001)-oriented Al_2O_3 substrates at $540\,^\circ\mathrm{C}$. The evaporation rate of Sm is increased from 0.04 Å/s to 0.75 Å/s while the Co rate is fixed at 0.25 Å/s. 84

7.5 2θ value of the (00l) type reflection around 44° for Sm-Co thin films as a function of Sm rate. 85

7.6 (a) X-ray diffraction pattern of Sm-Co thin film grown onto (001)-oriented Al_2O_3 substrate at 540°C. The film is grown at evaporation rate of Sm of 0.16 Å/s and Co rate of 0.25 Å/s. (b) $\theta - 2\theta$ measurement showing the 002 Sm-Co reflection with Laue oscillations and the corresponding rocking curve shown inset. (c) ϕ scans of 104 reflection of Al_2O_3 substrate (grey) and 201 reflection of $SmCo_5$ (green). (d) Pole figure measurement of 201 $SmCo_5$ reflection. 86

7.7 Room temperature M-H curves measured perpendicular ($\perp$, green spheres) and parallel ($\|$, purple, diamonds) to the plane of Sm-Co films deposited with increasing Sm rate from 0.04 Å/s (a) to 0.75 Å/s (l) and a fixed Co rate of 0.25 Å/s. 88

7.8 The saturation magnetization, M_s, of Sm-Co thin films and their respective first anisotropy constant, K_1, at 300 K, as a function of Sm rate. The magnetization of bulk (B) Sm_2Co_{17} and $SmCo_5$ are marked. 89

7.9 Magnetic torque curves measured for Sm-Co thin films deposited at Sm rate of 0.08 (a), 0.16 (b), 0.20 (c), and 0.50 Å/s (d) and Co rate of 0.25 Å/s at 14 T and 300 K. 90

7.10 X-ray photoelectron spectra of (a) Sm 3d, (b) Co 2p, (c) O 1s levels and the (d) valence band spectrum measured for $SmCo_5$ film. 91

7.11 The HAADF-STEM image showing the overview of the Sm-Co film grown on (001)-oriented Al_2O_3 substrate. 93

7.12 (a) The crystallographic directions in the real space (grey) and reciprocal space (orange) for hexagonal unit cell mapped for the Sm-Co thin film sample. (b) A schematic of the thin film sample with corresponding crystallographic orientations. (c) Scanning electron microscopy image with the position and orientation of lamella 1 on the surface of the sample. 93

7.13 The cross-sectional high resolution HAADF-STEM image of the Sm-Co film in two directions, 1 and 2 at 30° to each other as indicated in Fig. 7.12(a). 94

8.1 X-ray diffraction pattern of a 30 nm ($00l$)-oriented ($Y_{1-x}Ce_x$)Co_5 thin films grown at 575°C onto a (001)-oriented Al_2O_3 substrate. 96

8.2 The variation of (a) a lattice parameter, and (b) c lattice parameter as a function of x in ($Y_{1-x}Ce_x$)Co_5 thin films. 97

8.3 X-ray photoelectron spectra of (a) Y 3d, (b) Co 2p, (c) O 1s levels and the (d) valence band spectrum measured for YCo_5 film. 98

8.4 X-ray photoelectron spectra of (a) Ce 3d, (b) Co 2p, (c) O 1s levels and the (d) valence band spectrum measured for $CeCo_5$ film. 100

8.5 X-ray photoelectron spectra of (a) Y 3d, (b) Ce 3d, (b) Co 2p, (c) O 1s levels and the (d) valence band spectrum measured for ($Y_{0.2}Ce_{0.8}$)Co_5 film. 102

8.6 X-ray photoelectron spectra of (a) Ce 3d, (b) Co 2p, (c) O 1s levels and the (d) valence band spectrum measured for ($Y_{0.5}Ce_{0.5}$)Co_5 film. 104

8.7 Room temperature hysteresis curves of the ($Y_{1-x}Ce_x$)Co_5 films measured perpendicular (out-of-plane, OP) and parallel (in-plane, IP) to the film plane. 105

8.8 Saturation magnetization, M_s, of the ($Y_{1-x}Ce_x$)Co_5 films as a function of x. 106

8.9 The perpendicular anisotropy of the ($Y_{1-x}Ce_x$)Co_5 films as a function of x. 107

List of Tables

3.1 Binary *R*-*M* intermetallic compounds with lattice structure and symmetry 18

3.2 Crystallographic parameters of the $CaCu_5$ structure 21

3.3 Comparison of saturation magnetization, M_s, remanent magnetization, M_r, coercive field, H_c, in perpendicular direction, and first anisotropy constant, K_1, for YCo_5 thin films. . . . 27

3.4 Review of growth parameters and magnetic properties of Sm-Co thin films. 29

5.1 Average grain size of Y_2Co_{17} ($d_{2:17}$) and YCo_5 ($d_{1:5}$) in the Y-Co films in the nanocomposite films. 57

Bibliography

[1] C. Kittel. Physical theory of ferromagnetic domains. *Rev. Mod. Phys.*, 21(4):541–583, 1949.

[2] E. C. Stoner. LXXX. Atomic moments in ferromagnetic metals and alloys with non-ferromagnetic elements. *London, Edinburgh, Dublin Philos. Mag. J. Sci.*, 15(101):1018–1034, 1933.

[3] B. T. Shirk and W. R. Buessem. Temperature dependence of M_s and K_1 of $BaFe_{12}O_{19}$ and $SrFe_{12}O_{19}$ single crystals. *J. Appl. Phys.*, 40(3):1294–1296, 1969.

[4] J. J Becker. Permanent magnets based on materials with high crystal anisotropy. *IEEE Trans. Magn.*, 4:239–249, 1968.

[5] O. Gutfleisch, M. A. Willard, E. Brück, C. H. Chen, S. G. Sankar, and J. P. Liu. Magnetic materials and devices for the 21st century: Stronger, lighter, and more energy efficient. *Adv. Mater.*, 23:821–842, 2011.

[6] E. C. Stoner and E. P. Wohlfarth. A mechanism of magnetic hysteresis in heterogeneous alloys. *Philos. Trans. R. Soc. A*, 240(826):599–642, 1948.

[7] K. Skokov and O. Gutfleisch. Hysteresis in Magnetic Materials SoSe 2019, lecture 04 : Coherent rotation of magnetization, Stoner – Wohlfarth model and Brown' s paradox, 2019.

[8] H. Kronmüller, K.-D. Durst, and M. Sagawa. Analysis of the magnetic hardening mechanism in RE-FeB permanent magnets. *J. Magn. Magn. Mater.*, 74(3):291–302, 1988.

[9] D. Goll. Micromagnetism – microstructure relations and the hysteresis loop. In H. Kronmüller and S. Parkin, editors, *Handb. Magn. Adv. Magn. Mater.*, number 2, pages 1–36. John Wiley and Sons, Ltd., 2007.

[10] D. Goll and H. Kronmüller. High-performance permanent magnets. *Naturwissenschaften*, 87:423–438, 2000.

[11] R. Ramesh, G. Thomas, and B. M. Ma. Magnetization reversal in nucleation controlled magnets. II. Effect of grain size and size distribution on intrinsic coercivity of Fe-Nd-B magnets. *J. Appl. Phys.*, 64(11):6416–6423, 1988.

[12] E. A. Nesbitt, R. H. Willens, R. C. Sherwood, E. Buehler, and J. H. Wernick. New permanent magnet materials. *Appl. Phys. Lett*, 12(11):361, 1968.

[13] A. E. Ray. Metallurgical behavior of $Sm(Co,Fe,Cu,Zr)_z$ alloys. *J. Appl. Phys.*, 55(6):2094–2096, 1984.

[14] M. Duerrschnabel, M. Yi, K. Uestuener, M. Liesegang, M. Katter, H.-J. Kleebe, B. Xu, O. Gutfleisch, and L. Molina-Luna. Atomic structure and domain wall pinning in samarium-cobalt-based permanent magnets. *Nat. Commun.*, 8(1):54, 2017.

[15] H. Sepehri-Amin, J. Thielsch, J. Fischbacher, T. Ohkubo, T. Schrefl, O. Gutfleisch, and K. Hono. Correlation of microchemistry of cell boundary phase and interface structure to the coercivity of $Sm(Co_{0.784}Fe_{0.100}Cu_{0.088}Zr_{0.028})_{7.19}$ sintered magnets. *Acta Mater.*, 126:1–10, 2017.

[16] P. Bruno and J. P. Renard. Magnetic surface anisotropy of transition metal ultrathin films. *Appl. Phys. A Solids Surfaces*, 49(5):499–506, 1989.

[17] P. Poulopoulos and K. Baberschke. Magnetism in thin films. *J. Phys. Condens. Matter*, 11(48):9495–9515, 1999.

[18] B. N. Engel, C. D. England, R. A .V. Leeuwen, M. H. Wiedmann, and C. M. Falco. Interface magnetic anisotropy in epitaxial superlattices. *Phys. Rev. Lett.*, 67(14):1910–1913, 1991.

[19] B. Schulz and K. Baberschke. Crossover from in-plane to perpendicular magnetization in ultrathin Ni/Cu(001) films. *Phys. Rev. B*, 50(18):13467–13471, 1994.

[20] C. W. Chen. Fabrication and characterization of thin films with perpendicular magnetic anisotropy for high-density magnetic recording - Part I A review. *J. Mater. Sci.*, 26(7):1705–1728, 1991.

[21] A. Moser, K. Takano, D. T. Margulies, M. Albrecht, Y. Sonobe, Y. Ikeda, S. Sun, and E. E. Fullerton. Magnetic recording: advancing into the future. *J. Phys. D. Appl. Phys.*, 35(19):R157–R167, 2002.

[22] D. Weller, A. Moser, L. Folks, M. E. Best, W. Lee, M. F. Toney, M. Schwickert, J. U. Thiele, and M. F. Doerner. High K_u materials approach to 100 Gbits/in^2. *IEEE Trans. Magn.*, 36(1):10–15, 2000.

[23] M. T. Johnson, P. J. H. Bloemen, F. J. A den Broeder, and J. J. de Vries. Magnetic anisotropy in metallic multilayers. *Reports Prog. Phys.*, 59(11):1409–1458, 1999.

[24] S. Hashimoto, Y. Ochiai, and K. Aso. Perpendicular magnetic anisotropy and magnetostriction of sputtered Co/Pd and Co/Pt multilayered films. *J. Appl. Phys.*, 66(10):4909–4916, 1989.

[25] N. Nakajima, T. Koide, T. Shidara, H. Miyauchi, H. Fukutani, A. Fujimori, K. Iio, T. Katayama, M. Nývlt, and Y. Suzuki. Perpendicular magnetic anisotropy caused by interfacial hybridization via enhanced orbital moment in Co/Pt multilayers: magnetic circular X-ray dichroism study. *Phys. Rev. Lett.*, 81(23):5229–5232, 1998.

[26] S. Ikeda, K. Miura, H. Yamamoto, K. Mizunuma, H. D. Gan, M. Endo, S. Kanai, J. Hayakawa, F. Matsukura, and H. Ohno. A perpendicular-anisotropy CoFeB – MgO magnetic tunnel junction. *Nat. Mater.*, 9:721–724, 2010.

[27] A. D. Kent. Spintronics: Perpendicular all the way. *Nat. Mater.*, 9:699–700, 2010.

[28] H. X. Yang, M. Chshiev, B. Dieny, J. H. Lee, A. Manchon, and K. H. Shin. First-principles investigation of the very large perpendicular magnetic anisotropy at Fe|MgO and Co|MgO interfaces. *Phys. Rev. B*, 84(5):054401–1–5, 2011.

[29] Z. Zhang and M. G. Lagally. Atomistic processes in the early stages of thin-film growth. *Science*, 276(5311):377–383, 1997.

[30] H. Brune. Epitaxial growth of thin films. In K. Wandelt, editor, *Surf. interface Sci. Solid-solid interfaces thin Film.*, pages 421–491. Wiley-VCH Verlag GmbH & Co. KGaA, first edition, 2014.

[31] R. Eason, editor. *Pulsed Laser Deposition of Thin Films*. Wiley -Interscience, 2006.

[32] K. H. J. Buschow. Intermetallic compounds of rare-earth and 3d transition metals. *Reports Prog. Phys.*, 40(10):1179–1256, 1977.

[33] A. R. Miedema, R. Boom, and F. R. De Boer. On the heat of formation of solid alloys. *J. Less-Common Met.*, 41:283–298, 1976.

[34] C. H. Wu and Y. C. Chuang. The Co-Y (Cobalt-Yttrium) system. *J. Phase Equilibria*, 12(5):587–592, 1991.

[35] G. Hoffer and K. Strnat. Magnetocrystalline anisotropy of YCo_5 and Y_2Co_{17}. *IEEE Trans. Magn.*, 2(3):487–489, 1966.

[36] G. Asti, F. Bolzoni, D. Melville, and S. Rinaldi. Anisotropy Constants of RCo_5 compounds. *IEEE Trans. Magn.*, 11(5):1437–1439, 1975.

[37] K. J. Strnat and R. M. W. Strnat. Rare earth-cobalt permanent magnets. *J. Magn. Magn. Mater.*, 100(1-3):38–56, 1991.

[38] M. I. Bartashevich, T. Goto, R. J. Radwanski, and A. V. Korolyov. Magnetic anisotropy and high-field magnetization process of $CeCo_5$. *J. Magn. Magn. Mater.*, 131(1-2):61–66, 1994.

[39] H. P. Klein, A. Menth, and R.S. Perkins. Magnetocrystalline anisotropy of light rare-earth cobalt compounds. *Phys. B*, 80(1-4):153–163, 1975.

[40] K. H. J. Buschow. Magnetic properties of $CeCo_3$, Ce_2Co_7 and $CeNi_3$ and their ternary hydrides. *J. Less-Common Met.*, 72(2):257–263, 1980.

[41] E. A. Nesbitt and J. H. Wernick. *Rare earth permanent magnets*. Academic Press, Inc., 1973.

[42] K. H. J. Buschow and A. S. Van der Goot. Intermetallic compounds in the system samarium-cobalt. *J. Less Common Met.*, 14:323–328, 1968.

[43] E. Burzo, A. Chelkowski, and H. R. Kirchmayr. Magnetic properties of metals. In H. P. J. Wijn, editor, *Landolt-Börnstein, Numer. data Funct. relationships Sci. Technol.*, pages 1–116. Springer-Verlag, 1990.

[44] K.H.J. Buschow and A. S. Van der Goot. NIMS AtomWork, Intermetallic compounds in the system samarium-cobalt, 1967.

[45] K. Balkis Ameen and M.L. Bhatia. Stability regime of the $CaCu_5$ structure. *J. Alloys Compd.*, 347(1-2):165–170, 2002.

[46] K. Momma and F. Izumi. Vesta: a three-dimensional visualization system for electronic and structural analysis. *J. Appl. Crystallogr.*, 41(3):653–658, 2008.

[47] J. Wernick and S. Geller. Transition element-rare earth compounds with Cu_5Ca structure. *Acta Crystallogr.*, 12:662–665, 1959.

[48] K. H. J. Buschow. Intermetallic compounds of rare earth elements and Ni, Co, or Fe. *Phys. Status Solidi*, 7(1):199–210, 1971.

[49] R. Skomski and D. J. Sellmyer. Anisotropy of rare-earth magnets. *J. Rare Earths*, 27(4):675–679, 2009.

[50] R. Lemaire, D. Paccard, R. Pauthenet, and J. Schweizer. Magnetic behavior of cobalt and of nickel in compounds with rare earth metals. *J. Appl. Phys.*, 39(2):1092–1093, 1968.

[51] Y. Suzuki, S. Takayama, F. Kirino, and N. Ohta. Single ion model for perpendicular magnetic anisotropy in RE-TM amorphous films. *IEEE Trans. Magn.*, 23(5):2275–2277, 1987.

[52] R. L. Streever. Individual Co site contributions to the magnetic anisotropy of RCo_5 compounds and related structures. *Phys. Rev. B*, 19(5):2704–2711, 1979.

[53] Z. Kakol, H. Figiel, and K. Turek. Local Co anisotropy in Y-Co compounds. *IEEE Trans. Magn.*, 20(5):1605–1607, 1984.

[54] D. Givord, J. Laforest, R. Lemaire, and Q. Lu. Cobalt magnetism in RCo_5-intermetallics: Onset of 3d magnetism and magnetocrystalline anisotropy (R=rare earth or Th). *J. Magn. Magn. Mater.*, 31-34(Part 1):191–196, 1983.

[55] J. Deportes, D. Givord, J. Schweizer, and F. Tasset. Different contributions of the two cobalt sites to the magnetocrystalline anisotropy of YCo_5 and related compounds. *IEEE Trans. Magn.*, 12(6):1000–1002, 1976.

[56] J. Schweizer and F. Tasset. Polarised neutron study of the RCo_5 intermetallic compounds. I. The cobalt magnetisation in YCo_5. *J. Phys. F Met. Phys*, 10:2799–818, 1980.

[57] L. Nordstrom, M. S. S. Brooks, and B. Johansson. Calculation of orbital magnetism and magnetocrystalline anisotropy energy in YCo_5. *J. Phys. Condens. Matter*, 4(12):3261–3272, 1992.

[58] J. E. Greedan and V. U. S. Rao. An analysis of the rare earth contribution to the magnetic anisotropy in RCo_5 and R_2Co_{17} compounds. *J. Solid State Chem.*, 6(3):387–395, 1973.

[59] Y. Kubota, Y. Fu, X. Wu, and T. F. Ambrose. High anisotropy Y-Co films on thin Cu underlayer. *IEEE Trans. Magn.*, 43(6):2998–3000, 2007.

[60] M. Yamada, Y. Hotta, M. Ohtake, M. Futamoto, F. Kirino, and N. Inaba. Preparation of YCo_5 and $GdCo_5$ ordered alloy epitaxial thin films on Cu(111) underlayer. *J. Magn. Soc. Japan*, 40(5):132–136, 2016.

[61] J. C. Tellez-Blanco, R. Grossinger, R. Sato Turtelli, and E. Estevez-Rams. Magnetic and structural properties of $YCo_{5-x}Cu_x$. *IEEE Trans. Magn.*, 36(5):3333–3335, 2000.

[62] G. Li, Q. Ke, G. Liu, and Y. Tong. Studies on the electrodeposition of Ce–Co rare earth alloy thin films in Urea-DMSO systems. *J. Electrochem. Soc.*, 153(6):C411–C416, 2006.

[63] M. Ohtake and M. Futamoto. Determination of crystallographic phase and estimation of order degree for rare earth-transition metal alloy films with hexagonal structures. *J. Magn. Soc. Japan*, 39(5):205–212, 2015.

[64] J. J. Zhang, H. M. Gao, Y. Yan, X. Bai, F. Su, W. Q. Wang, and X. B. Du. Morphology and magnetic properties of $CeCo_5$ submicron flakes prepared by surfactant-assisted high-energy ball milling. *J. Magn. Magn. Mater.*, 324(20):3272–3275, 2012.

[65] L. Lu, Y. Yan, X. B. Du, W. Q. Wang, B. Zhang, F. Su, Z. S. Zhang, S. F. Li, F. Wang, H. M. Jin, and H. Xia. The crystallographic texture and magnetic anisotropy of melt-spun $CeCo_{5.4}$ ribbon. *J. Magn. Magn. Mater.*, 321(15):2382–2385, 2009.

[66] J. Sayama, K. Mizutani, T. Asahi, and T. Osaka. Thin films of $SmCo_5$ with very high perpendicular magnetic anisotropy. *Appl. Phys. Lett.*, 85(23):5640–5642, 2004.

[67] E. M. T. Velu and D. N. Lambeth. High density recording on SmCo/Cr thin film media. *IEEE Trans. Magn.*, 28(5):3249–3254, 1992.

[68] J. Sayama, K. Mizutani, Y. Yamashita, T. Asahi, and T. Osaka. $SmCo_5$ -based thin films with high magnetic anisotropy for perpendicular magnetic recording. *IEEE Trans. Magn.*, 41(10):3133–3135, 2005.

[69] A. Morisako and X. Liu. Sm-Co and Nd-Fe-B thin films with perpendicular anisotropy for high-density magnetic recording media. *J. Magn. Magn. Mater.*, 304(1):46–50, 2006.

[70] A. Walther, C. Marcoux, B. Desloges, R. Grechishkin, D. Givord, and N. M. Dempsey. Micro-patterning of NdFeB and SmCo magnet films for integration into micro-electro-mechanical-systems. *J. Magn. Magn. Mater.*, 321(6):590–594, 2009.

[71] A. Walther, D. Givord, N. M. Dempsey, K. Khlopkov, and O. Gutfleisch. Structural, magnetic, and mechanical properties of 5μm thick SmCo films suitable for use in microelectromechanical systems. *J. Appl. Phys.*, 103(4):043911–1–5, 2008.

[72] L. Peng, H. Zhang, Q. Yang, Y. Li, Y. Song, and J. Shen. Correlation between sputtering parameters and composition of SmCo-based films for microelectromechanical system applications. *J. Appl. Phys.*, 105(6):063915–1–6, 2009.

[73] T. Budde and H. H. Gatzen. Thin film SmCo magnets for use in electromagnetic microactuators. *J. Appl. Phys.*, 99(8):08N304–1–4, 2006.

[74] S. Takei, A. Morisako, and M. Matsumoto. Fabrication of Sm–Co films with perpendicular magnetic anisotropy. *J. Magn. Magn. Mater.*, 272-276:1703–1705, 2004.

[75] M. Seifert, V. Neu, and L. Schultz. Epitaxial $SmCo_5$ thin films with perpendicular anisotropy. *Appl. Phys. Lett.*, 94(2):1–4, 2009.

[76] L.N. Zhang, J.F. Hu, J.S. Chen, and J. Ding. A study on magnetic properties and structure of $SmCo_5$ thin films on Ni–W underlayers. *J. Magn. Magn. Mater.*, 322(23):3737–3741, 2010.

[77] L.N. Zhang, J.F. Hu, J.S. Chen, and J. Ding. Microstructure and magnetic properties studies of $SmCo_5$ thin films grown on MgO and glass substrates. *J. Magn. Magn. Mater.*, 321(17):2643–2647, 2009.

[78] A. Singh, V. Neu, R. Tamm, K. S. Rao, S. Fähler, W. Skrotzki, L. Schultz, and B. Holzapfel. Growth of epitaxial $SmCo_5$ films. *Appl. Phys. Lett.*, 87(7):072505–1–3, 2005.

[79] L. N. Zhang, J. F. Hu, J. S. Chen, and J. Ding. Seed layer effect on texture and magnetic properties of $SmCo_5$ thin films. *J. Appl. Phys.*, 105(7):07A743–1–6, 2009.

[80] J. Sayama, T. Asahi, K. Mizutani, and T. Osaka. Newly developed $SmCo_5$ thin film with perpendicular magnetic anisotropy. *J. Phys. D. Appl. Phys.*, 37(1):L1–L4, 2004.

[81] V. Neu, J. Thomas, S. Fähler, B. Holzapfel, and L. Schultz. Hard magnetic SmCo thin films prepared by pulsed laser deposition. *J. Magn. Magn. Mater.*, 242-245:1290–1293, 2002.

[82] J. J. Romero, F. J. Palomares, F. Pigazo, R. Cuadrado, F. Cebollada, A. Hernando, and J. M. Gonzalez. Crystallization and magnetic hardening of SmCo thin films. *J. Non. Cryst. Solids*, 353(8-10):786–789, 2007.

[83] J. Sayama, K. Mizutani, T. Asahi, J. Ariake, K. Ouchi, and T. Osaka. Origin of perpendicular magnetic anisotropy of $SmCo_5$ thin films with Cu underlayer. *J. Magn. Magn. Mater.*, 301(1):271–278, 2006.

[84] M. Benaissa, K. M. Krishnan, E. E. Fullerton, and J. S. Jiang. Magnetic anisotropy and its microstructural origin in epitaxially grown SmCo thin films. *IEEE Trans. Magn.*, 34(4):1204–1206, 1998.

[85] Y. K. Takahashi, T. Ohkubo, and K. Hono. Microstructure and magnetic properties of $SmCo_5$ thin films deposited on Cu and Pt underlayers. *J. Appl. Phys.*, 100(5):053913–1–6, 2006.

[86] E. E. Fullerton, C. H. Sowers, J. E. Pearson, S. D. Bader, J. B. Patel, X. Z. Wu, and D. Lederman. Structure and magnetism of epitaxial rare-earth–transition-metal films. *J. Appl. Phys.*, 81(8):5637–5639, 1997.

[87] J. R. Arthur. Molecular beam epitaxy. *Surf. Sci.*, 500(1-3):189–217, 2002.

[88] B. D. Cullity. *Elements of X-ray diffraction*. Addison-Wesley Publishing Company, Inc., 1956.

[89] K. Inaba. X-ray thin-film measurement techniques I. Overview. *Rigaku J.*, 24:10–15, 2008.

[90] *X-ray diffraction analysis for thin film samples: Training textbook*. Application Laboratory Rigaku Corporation, 2009.

[91] T. Mitsunaga. X-ray thin-film measurement techniques II. Out-of-plane diffraction measurements. *Rigaku J.*, 25:7–12, 2009.

[92] M. Yasaka. X-ray thin-film measurement techniques V. X-ray reflectivity measurement. *Rigaku J.*, 26:1–9, 2010.

[93] S. Kobayashi. X-ray thin-film measurement techniques IV. In-plane XRD measurements. *Rigaku J.*, 26:3–11, 2010.

[94] G. Wang and T. Lu. *RHEED Transmission Mode and Pole Figures*. Springer Science + Business Media NewYork, 2014.

[95] N. J. C. Ingle. Electron diffraction techniques for studying thin film growth in situ. In G. Koster and G. Rijnders, editors, *In situ characterization of thin film growth*, pages 29–51. Woodhead Publishing Limited, Cambridge, UK, 2011.

[96] J. F. Moulder, W. F. Stickle, P. E. Sobol, and K. D. Bomben. *Handbook of X-ray Photoelectron Spectroscopy*. Physical Electronics, Inc., Eden Prairie, Minnesota 55344, USA, 1995.

[97] M. C. Biesinger, B. P. Payne, A. P. Grosvenor, L. W. M. Lau, A. R. Gerson, and R. St. C. Smart. Resolving surface chemical states in XPS analysis of first row transition metals, oxides and hydroxides: Cr, Mn, Fe, Co and Ni. *Appl. Surf. Sci.*, 257(7):2717–2730, 2011.

[98] P. Steiner, H. Höchst, and S. Hüfner. Analysis of the plasmon structure in XPS experiments of simple metals. *Phys. Lett. A*, 61(6):410–412, 1977.

[99] G. Garreau, V. Schorsch, E. Beaurepaire, J. Parlebas, O. Speder, P. Rennert, and JC Parlebas. Core-level XPS spectra of supported 3d-metal ultrathin layers : experimental and theoretical studies. *J. Phys. IV Colloq.*, 4:C9–127–C9–130, 1994.

[100] B. D. Josephson. The discovery of tunnelling supercurrents. *Rev. Mod. Phys.*, 46(2):251–254, 1974.

[101] J. Bardeen, L. N. Cooper, and J. R. Schrieffer. Theory of superconductivity. *Theory Supercond.*, 108(5):1175–1204, 1957.

[102] C. Kittel. *Introduction to solid state physics*. John Wiley and Sons, Inc., eighth edition, 2005.

[103] R. L. Fagaly. Superconducting quantum interference device instruments and applications. *Rev. Sci. Instrum.*, 77:101101–1–45, 2006.

[104] Quantum Design: MPMS MultiVu application user's manual. Technical report, 2004.

[105] Quantum Design, Physical property measurement system: Torque magnetometer option user's manual. Technical report, 1999.

[106] J. Worst, J.C. Lodder, and T. Wielinga. R.f.-sputtered Co-Cr layers for perpendicular magnetic recording: II: Magnetic anisotropy. *Thin Solid Films*, 101(1):75–81, 1983.

[107] D. B. Williams and C. Barry Carter. *Transmission Electron Microscopy: A textbook for Material Science*. Springer Science + Business Media, LLC, 233 Spring Street, New York, NY 10013, USA.

[108] J. Barthel. Dr. Probe: A software for high-resolution STEM image simulation. *Ultramicroscopy*, 193:1–11, 2018.

[109] International Centre for Diffraction Data, Y_2Co_{17}, document no. 04-001-1972. 2015.

[110] International Centre for Diffraction Data, $Y_{0.9}Co_{5.2}$, document no. 04-003-5259. 2015.

[111] S. Sharma, E. Hildebrandt, S. U. Sharath, I. Radulov, and L. Alff. $YCo_{5\pm x}$ thin films with perpendicular anisotropy grown by molecular beam epitaxy. *J. Magn. Magn. Mater.*, 432:382–386, 2017.

[112] International Centre for Diffraction Data, YCo_5, document no. 04-002-8224. 2016.

[113] X. K. Sun, J. Zhang, Y. Chu, W. Liu, B. Cui, and Z. Zhang. Dependence of magnetic properties on grain size of α-Fe in nanocomposite $(Nd, Dy)(Fe, Co, Nb, B)_{5.5}/\alpha$-Fe magnets. *Appl. Phys. Lett.*, 74:1740, 1999.

[114] W. Borchardt-Ott. *Crystallography : An Introduction*. Springer-Verlag Berlin Heidelberg, third edition, 2011.

[115] F. Robaut, P. Milkulik, N. Cherief, O. F. K. McGrath, D. Givord, T. Baumbach, and J. Y. Veuillen. Epitaxial growth and characterization of Y_2Co_{17} (0001) thin films deposited on $W(110)$. *J. Appl. Phys.*, 78(2):997–1003, 1995.

[116] T. Shima, K. Takanashi, Y. K. Takahashi, and K. Hono. Coercivity exceeding 100 kOe in epitaxially grown FePt sputtered films. *Appl. Phys. Lett.*, 85:2571–2573, 2004.

[117] C. Behler, V. Neu, L. Schultz, and S. Fähler. Magnetically and thermally induced switching processes in hard magnets. *J. Appl. Phys.*, 112:083919, 2012.

[118] J. M. Alameda, J. Deportes, D. Givord, R. Lemaire, and Q. Lu. Large magnetization anisotropy in uniaxial YCo_5 intermetallic. *J. Magn. Magn. Mater.*, 15-18:1257–1258, 1980.

[119] J. M. Alameda, D. Givord, R. Lemaire, and Q. Lu. Co energy and magnetization anisotropies in RCo_5 intermetallics between 4.2 K and 300 K. *J. Appl. Phys.*, 52(3):2079–2081, 1981.

[120] E. R. Callen. Anisotropic magnetization. *J. Appl. Phys.*, 31(5):149S–150S, 1960.

[121] E. R. Callen and H. B. Callen. J. Phys. Chem. Solids. *J. Phys. Chem. Solids*, 16(3-4):310–328, 1960.

[122] H. Rosner, D. Koudela, U. Schwarz, A. Handstein, M. Hanfland, I. Opahle, K. Koepernik, M. D. Kuz'min, K.-H. Müller, J. A. Mydosh, and M. Richter. Magneto-elastic lattice collapse in YCo_5. *Nat. Phys.*, 2:469–472, 2006.

[123] L. Pareti, M. Solzi, and G. Marusi. Phenomenological analysis of the magnetocrystalline anisotropy of the Co sublattice in some rhombohedral and hexagonal intermetallic structures derived from the $CaCu_5$ unit cell. *J. Appl. Phys.*, 72(7):3009–3012, 1992.

[124] J. D. Livingston and M. D. McConnell. Domain-wall energy in cobalt-rare-earth compounds. *J. Appl. Phys.*, 43:4756, 1972.

[125] E. F. Kneller and R. Hawig. The exchange-spring magnet: a new material principle for permanent magnets. *IEEE Trans. Magn.*, 27(4):3588–3600, 1991.

[126] R. Skomski and J. M. D. Coey. Giant energy product in nanostructured two-phase magnets. *Phys. Rev. B*, 48(21):15812–15816, 1993.

[127] H. W. Chang, W. C. Ou, Y. I. Lee, C. W. Shih, W. C. Chang, C. C. Yang, and C. C. Shaw. Magnetic property enhancement of melt spun YCo_5 ribbons by Fe and C Doping. *IEEE Trans. Magn.*, 53(11):2100504, 2017.

[128] P. Tozman, M. Venkatesan, G.A. Zickler, and J. M. D Coey. Enhanced energy product in Y-Co-Fe magnets intermediate between Nd-Fe-B and ferrite. *Appl. Phys. Lett.*, 107(2015):032405–1–5, 2015.

[129] E. F. Kneller and F. E. Luborsky. Particle size dependence of coercivity and remanence of single-domain particles. *J. Appl. Phys.*, 34(3):656–658, 1963.

[130] International Center for Diffraction Data, $CeCo_5$, document no. 03-065-8886. 2017.

[131] International Center for Diffraction Data, $Ce_{0.9}Co_{5.2}$, document no. 04-003-5257. 2017.

[132] Y. Zhang, D. Givord, and N. M. Dempsey. The influence of buffer/capping-layer-mediated stress on the coercivity of NdFeB films. *Acta Mater.*, 60(9):3783–3788, 2012.

[133] S. N. Piramanayagam, M. Matsumoto, A. Morisako, and S. Takei. Studies on NdFeB thin films over a wide composition range. *J. Alloys Compd.*, 281(1):27–31, 1998.

[134] S. Sharma, E. Hildebrandt, M. Major, P. Komissinskiy, I. Radulov, and L. Alff. $CeCo_5$ thin films with perpendicular anisotropy grown by molecular beam epitaxy. *J. Magn. Magn. Mater.*, 452:80–85, 2018.

[135] International Centre for Diffraction Data, Sm_2O_3, document no. 00-015-0813. 2017.

[136] S. Sharma, I. Radulov, M. Major, and L. Alff. Evolution of magnetic anisotropy with Sm Contents in Sm-Co thin films. *IEEE Trans. Magn.*, 54(11):1–5, 2018.

[137] International Centre for Diffraction Data, Co, document no. 01-089-4308. 2016.

[138] International Centre for Diffraction Data, Sm_2Co_{17}, document no. 04-007-7820. 2018.

[139] International Centre for Diffraction Data, $SmCo_5$, document no. 04-001-0410. 2017.

[140] International Centre for Diffraction Data, $Sm_{0.9}Co_{5.2}$, document no. 04-003-5261. 2017.

[141] K. Strnat, G. Hoffer, J. Olson, W. Ostertag, and J. J. Becker. A family of new cobalt-base permanent magnet materials. *J. Appl. Phys.*, 38:1001–1002, 1967.

[142] T. Nishizawa and K. Ishida. The Co (cobalt) system. *Bull. Alloy Phase Diagrams*, 4(4):387–390, 1983.

[143] B. D. Cullity and C. D. Graham. *Introduction to Magnetic Materials*. IEEE Press, second edition, 2009.

[144] S. Iwasaki and K. Ouchi. Co-Cr recording films with perpendicular magnetic anisotropy. *IEEE Trans. Magn.*, 14:849–851, 1978.

[145] C. R. Brundle, T. J. Chuang, and D. W. Rice. X-ray photoemission study of the interaction of oxygen and air with clean cobalt surfaces. *Surf. Sci.*, 60(2):286–300, 1976.

[146] A. Laslo, R. Dudric, M. Neumann, O. Isnard, M. Coldea, and V. Pop. Effects of M=Si, Ga and Al for Co substitution on the electronic properties of RCo_4M as probed by XPS. *Solid State Commun.*, 199:43–46, 2014.

[147] O. Akdogan, H. Sepehri-Amin, N. M. Dempsey, T. Ohkubo, K. Hono, O. Gutfleisch, T. Schrefl, and D. Givord. Preparation , characterization , and modeling of ultrahigh coercivity Sm-Co thin films. *Adv. Electron. Mater.*, 1:1500009–1–8, 2015.

[148] S.-Y. Jekal, M. Charilaou, and J. F. Löffler. Pushing the limits of magnetic anisotropy in the Sm-Co system. *arXiv:1807.09257 [cond-mat.mtrl-sci]*, pages 1–8, 2018.

[149] R. A. Neifeld, M. Croft, T. Mihalisin, C. U. Segre, M. Madigan, M. S. Torikachvili, M. B. Maple, and L. E. Delong. Chemical environment and Ce valence: Global trends in transition-metal compounds. *Phys. Rev. B*, 32(10):6928–6931, 1985.

[150] D. Gignoux, F. Givord, and R. Lemaire. Valence state of cerium in the hexagonal CeM_5 compounds with the transition metals. *J. Phys.*, 43(1):173–180, 1982.

[151] M. Croft, R. Neifeld, C. U. Segre, S. Raaen, and R. D. Parks. Ce valence variation in intermetallic alloys: L_{III} absorption spectroscopy results. *Phys. Rev. B*, 30(8):4164–4169, 1984.

[152] M. Yang, H. Wang, Y. Hu, L. Yang, A. Maclennan, and B. Yang. Increased coercivity for Nd-Fe-B melt spun ribbons with 20 at.% Ce addition: The role of compositional fluctuation and Ce valence state. *J. Alloys Compd.*, 710:519–527, 2017.

[153] G. Krill, J. P. Kappler, A. Meyer, L. Abadli, and M. F. Ravet. Surface and bulk properties of cerium atoms in several cerium intermetallic compounds: XPS and X-ray absorption measurements. *J. Phys. F Met. Phys.*, 11(8):1713–1725, 1981.

[154] K. B. Sundaram, P. F. Wahid, and O. Melendez. Deposition and x-ray photoelectron spectroscopy studies on sputtered cerium dioxide thin films. *J. Vac. Sci. Technol. A Vacuum, Surfaces, Film.*, 15(1):52–56, 1997.

[155] A. M. Salvi, F. Decker, F. Varsano, and G. Speranza. Use of XPS for the study of cerium-vanadium (electrochromic) mixed oxides. *Surf. Interface Anal.*, 31(4):255–264, 2001.

[156] E. Vescovo and C. Carbone. Oxidation of epitaxial Ce films. *Phys. Rev. B*, 53(7):4142–4147, 1996.

[157] M. Gasgnier, J. Ghys, G. Schiffmacher, Ch. Henry La Blanchetais, P. E. Caro, C. Boulesteix Ch. Loier, and B. Pardo. Rare-earth hydrides and rare-earth oxides in and from thin films of rare-earth metals. *J. Less Common Met.*, 34(1):131–142, 1974.

[158] M. Gasgnier, G. Schiffmacher, D. R. Svoronos, and P. E. Caro. Electron beam impact: a new route to unusual stoichiometry and rare earth intermediate oxides. *Inorganica Chim. Acta*, 140:79–82, 1987.

[159] J. M. Lindquist and J. C. Hemminger. CO chemisorption effects on cerium initial and final states in the core level photoelectron spectrum of $CeIr_2$. *J. Phys. Chem.*, 91(22):5535–5537, 1987.

Academic Contributions

Publications

1. Evolution of magnetic anisotropy with Sm contents in Sm–Co thin films

   IEEE Transactions on Magnetics 54 (2018) 1-5

   Shalini Sharma, Iliya Radulov , Márton Major, and Lambert Alff
2. $CeCo_5$ thin films with perpendicular anisotropy grown by molecular beam epitaxy

   Journal of Magnetism and Magnetic Materials 452 (2018) 80-85

   Shalini Sharma, Erwin Hildebrandt, Márton Major, Philipp Komissinskiy, Iliya Radulov, and Lambert Alff
3. $YCo_{5\pm x}$ thin films with perpendicular anisotropy grown by molecular beam epitaxy

   Journal of Magnetism and Magnetic Materials 432 (2017) 382-386

   Shalini Sharma, Erwin Hildebrandt, S. U. Sharath, Iliya Radulov, and Lambert Alff

Conference contributions

Oral presentations

1. Tuning magnetic anisotropy in $(Y_{1-x}Ce_x)Co_{5\pm y}$ thin films grown by molecular beam epitaxy

   Joint MMM-Intermag 2019, Washington DC, USA
2. YCo_5 and $CeCo_5$ thin films with perpendicular magnetic anisotropy grown by molecular beam epitaxy

   Intermag 2018, Singapore
3. Magnetic properties of $(Y_{1-x}Ce_x)Co_5$ thin films and bulk single crystals

   JEMS 2018, Mainz, Germany
4. Epitaxial YCo_5 thin films with perpendicular anisotropy

   DPG 2017, Dresden, Germany
5. Magnetic properties of YCo_5 epitaxial thin films

   DPG 2016, Regensburg, Germany

Poster presentations

1. Magnetic properties of $(Y_{1-x}Ce_x)Co_5$ and $(Y_{1-x}Sm_x)Co_5$ thin films grown by molecular beam epitaxy

   JEMS 2019, Uppsala, Sweden
2. Magnetism of YCo_5 and Y_2Co_{17} epitaxial thin films

   REPM 2016, Darmstadt, Germany

Acknowledgements

I express my sincere gratitude to Prof. Dr. Lambert Alff for believing in me and giving me this opportunity to carry out my doctoral studies at the Advanced Thin Film Technology group. I would always be grateful to him for his motivation to develop one’s own ideas and his willingness to discuss these at all times. I am thankful to him for his encouragement to present my work in several conferences and truly appreciate his efforts to help me improve the presentations before each conference. I consider myself extremely fortunate to be guided by his supervision during the PhD time and beyond.

I am grateful to Prof. Dr. Oliver Gutfleisch for his valuable time to review this dissertation. I thank him for sharing his knowledge, scientific developments and being a source of inspiration. I extend my gratitude to the members of the examination committee, Prof. Dr. Wolfgang Donner and Prof. Dr. Barbara Albert for their precious time and kindly agreeing to evaluate my PhD defense. I thank Prof. Donner for providing the recommendation letters for the extension of DAAD scholarship, every year.

I wholeheartedly thank Dr. Erwin Hildebrandt, Dr. Márton Major, Dr. Philipp Komissinskiy, Dr. Leopold Diop, Dr. Iliya Radulov and Dr. Konstantin Skokov for sharing their expertise, providing useful insights and able guidance. I am grateful to them for all the fruitful discussions and immense support throughout these years. I thank Dr. Katharina Ollefs, Dr. Leopoldo Molina-Luna, Jun. Prof. Dr. Hongbin Zhang and Prof. Dr. Bai-Xiang Xu for their scientific contributions and collaborations. I also acknowledge Dr. Christian Kaiser and Burkhard Krömker for supporting with PULSE system dynamic XPS measurements.

I thank Gabi Haindl, Jürgen Schreeck and Michael Weber for assistance with technical issues and supporting the laboratory work; and Ulrike Kunz for preparing the lamella by focused ion beam.

I am grateful to Dr. Stefan Petzold, Dr. Dominik Gölden, Dr. Sharath Ulhas and Dr. Soumya Ray for introducing and teaching me to operate the MBE system. Thanks to them and the current MBE users, Tobias Vogel, Nico Kaiser, Robert Eilhardt and Eszter Piros for a great team-work during chamber opening times on Fridays. I thank Alexander Zintler for his efforts in dealing with ‘hard ’thin film samples for TEM; and Dominik Ohmer for supporting with micromagnetic simulations.

I take this opportunity to thank all the members of the ATFT group for their kind co-operation and a memorable time spent here. I am thankful to Marion Bracke for supporting with the administrative work, which could be challenging for a foreigner. I appreciate the help from Thorsten Schneider with the German translation of the thesis abstract. Special thanks to my former and present colleagues; Juliette Cardoletti, Eszter Piros, Patrick Salg, Lukas Zeinar, Supratik Dasgupta, Tobias Vogel, Nico Kaiser, Dr. Stefan Petzold, Dr. Sareh Sabet and Dr. Vikas Shabadi for their friendship, support and companionship through my PhD life. I wish great success to the entire ATFT group!

The journey so far would not have been possible without the unconditional love, support and encouragement of my parents, Dr. Shukdev Sharma and Rashmi Sharma. I wholeheartedly thank them and my brother, Dr. Amar Prakash, for standing by me at all times and at every stage of life.

I am thankful to the Deutscher Akademischer Austauschdienst (DAAD) for providing this great platform to students from across the world to be a part of Germany’s strong scientific research foundation. I also acknowledge the German federal state of Hessen through its excellence program LOEWE RESPONSE for the financial support.

Above all, I am grateful to God for this life and being my source of light through the dark times.

Curriculum Vitae

Shalini Sharma, born on 21st of March, 1990 in Meerut, India

Education

2015 - present	Doctoral studies at Advanced Thin Film Technology, Institute of Materials Science, Technische Universität Darmstadt, Germany
2008 - 2014	Master of Technology (Nanotechnology)-Integrated, Amity University, India
2013 - 2014	Trainee researcher at Luxembourg Institute of Science and Technology, Luxembourg
2008	All India Senior School Certificate Examination, India
2006	All India Secondary School Examination, India

Scholarships

2014 -2019	DAAD Graduate School Scholarship Programme at Technische Universität Darmstadt, Germany
2012	Summer Research Fellowship Programme at National Chemical Laboratory, Pune, India

Awards

2014	Shree Baljit Shastri Award for the best in Human and Traditional values at Amity Institute of Nanotechnology, batch 2008-2014
2014	Silver medal for Second in academic performance at Amity Institute of Nanotechnology, Amity University, batch 2008-2014